A STUDY OF PION-PROTON BACKWARD ELASTIC SCATTERING IN THE CENTRE OF MASS ENERGY RANGE 2.1 to 2.4 GeV.

Thesis

Submitted by

DAVID CLARKSON LOWE

for the degree of

DOCTOR OF PHILOSOPHY

Department of Physics,

University of Edinburgh

SEPTEMBER, 1982.

CONTENTS

CONTENTS (Contd.)

CONTENTS (Contd.)

ABSTRACT

This thesis describes an experiment to study the reactions $\pi^+p \rightarrow K^+\Sigma^+$ and $\pi^+p \rightarrow \pi^+p$ at 26 incident pion momenta between 1.27 GeV/c and 2.48 GeV/c. A total of approximately 17 million events were collected by the experiment. In this thesis backward elastic scattering differential cross sections are presented at 13 momenta at the top end of the momentum range. The angular range of the data is $-0.97 \leq \cos\theta^* \leq -0.11$. Comparisons are made with the results of previous experiments and also with partial wave analyses.

DECLARATION

I declare that this thesis has been written and composed entirely by myself.

The experiment described in this thesis was performed by a team of physicists and as a result my responsibility was for only a small part of it. Despite this it was necessary for me to be familiar with most aspects of the experiment.

I was directly responsible for the analysis of the channel presented in this thesis.

FIGURE CAPTIONS

FIGURE CAPTIONS (Contd.)

FIGURE CAPTIONS (Contd.)

FIGURE CAPTIONS (Contd.)

FIGURE CAPTIONS (Contd.)

TABLE CAPTIONS

CHAPTER 1

INTRODUCTION

1.1 Introductory Remarks

This thesis describes an experiment to study the interaction of "elementary" particles. The experiment was performed at the Rutherford Laboratory's Nimrod accelerator by a team of approximately twenty physicists from Edinburgh University, Westfield College and the Rutherford Laboratory. Two reactions were studied in the experiment ($\pi^+p \rightarrow \pi^+p$ and $\pi^+p \rightarrow K^+\Sigma^+$) with the ultimate aim of studying the Δ^{++} states which can be formed in these reactions. Preliminary results on the $\pi^+p \rightarrow \pi^+p$ reaction are presented in this thesis and compared with the results of previous experiments and analyses.

The first chapter of the thesis contains a description of the historical development of particle physics and gives an indication of this experiment's position within the field. In the second chapter the mass spectrum of the strongly interacting particles known as baryons (of which the Δ^{++} states are members) is discussed. Both the experimental determination of the spectrum and the theoretical model which best describes the spectrum (as they apply to the Δ^{++} states) are discussed. The chapter concludes with a justification of the experiment described in the thesis. The third chapter deals with the experimental set up used in the experiment and the fourth chapter deals with the techniques used to reconstruct individual scattering events from the measured data. In the fifth chapter the selection of elastic scattering events (i.e. events of the type $\pi^+p \rightarrow \pi^+p$) and the calculation of the elastic scattering differential cross section are described. In Chapter Six preliminary differential cross sections at 13 momenta are presented and compared with the results of previous experiments and partial wave analyses. Finally, in Chapter Seven, the conclusions which may be drawn from these results are discussed and summarized.

1.2 Historical Perspective

Throughout man's history one feature of his character has set him apart from other creatures. This is his desire to control the environment to suit his own specific needs. This desire led man to develop a deeper understanding of his environment in order to gain control over it. As he discovered more about nature the belief grew in him that the world was basically simple and could be "explained" by some underlying structure which awaited discovery. The search for this structure has so intrigued man through the ages that it has become an end in itself and the control of the environment has, to some extent, become a by product of the search[1].

Perhaps the first important idea in this search was the concept of small indivisible particles from which all matter was constructed. This idea was originally proposed by the Greeks who gave their "elementary" particles the name atoms. The idea of atoms remained little more than an idea for many centuries until the early 1800's when John Dalton began to formulate a theory to explain the observation that chemical elements combine in fixed ratios by weight. Dalton suggested that this could be explained by supposing that each chemical element consisted of atoms. He proposed that the atoms of a particular element were all identical and had a fixed mass characteristic of the element. He further proposed that in the formation of a compound from the elements the atoms combined in a fixed ratio to form molecules. Thus Dalton's theory "explained" the observed way in which the elements combined.

As the number of known elements increased, it was noticed that some of the elements had similar properties. Dmitri Mendeleev arranged the known elements in a table in order of increasing mass in such a way that elements with similar properties occurred in the same column. In order to place some of the elements in their "correct" columns he had to leave gaps in his table. He correctly interpreted these gaps as being due to undiscovered elements. Thus an underlying symmetry of the elements had been discovered, although as yet there existed no explanation of this symmetry.

In 1897 J.J. Thomson discovered the electron as a constituent particle of the atom and with this discovery the idea that atoms were indivisible elementary particles was shattered. The electron is negatively charged and thus to maintain the electrical neutrality of the atom there also had to be positively charged constituents. In 1911 Ernest Rutherford proposed a model for the atom in which the bulk of the matter was contained in a central positively charged nucleus around which the electrons orbitted. This model was based upon the results of scattering experiments performed by Rutherford in which positively charged α particles (helium nuclei) were scattered by a thin gold foil. Despite the success of Rutherford's model in describing the results of the scattering experiments a theoretical difficulty remained. From known electromagnetic theory the orbitting electrons should have continuously emitted energy and so spiralled down into the nucleus. Niels Bohr resolved this difficulty by suggesting that the electrons could only orbit the nucleus in fixed energy states and that when the electrons were in such a state they did not emit energy. This idea provided an explanation of the observed spectra of atoms, which consisted of discrete spectral lines of fixed frequency, by supposing that energy was emitted from atoms in fixed amounts when electrons jumped from higher to lower energy states.

Bohr's ideas were extended with the development of quantum mechanics and the shell model of the atom and with these extensions Mendeleev's underlying symmetry of the elements was finally understood.

For many years after the discovery of the nucleus it seemed as "elementary" as the atom had once been. One of the theoretical problems with splitting the nucleus into component particles was the fact that nuclei did not have a fixed mass to charge ratio. This fact was inexplicable to scientists in the early 1930's who believed that matter was built from electrically charged particles. However with the discovery of the neutron by James Chadwick in 1932 this theoretical difficulty was overcome and a model of the nucleus emerged in which it consisted of two types of particle - the zero charge neutron and the positively charged proton.

Thus a fairly simple picture of nature had been constructed in which matter was built from three "elementary" particles - the proton, neutron and electron. However a problem still remained in this model. Atoms consisted of a charged nucleus, consisting of protons and neutrons, which was bound electromagnetically to a "cloud" of orbitting electrons. The protons in the nucleus, by virtue of their positive electric charge, repel each other and the attractive gravitational force between the nucleons (a generic name for protons and neutrons) is not strong enough to overcome this repulsion. Thus the question arose as to why the nucleus was stable. There had to exist some attractive force which could overcome the electromagnetic repulsion of the protons and hold the nucleus together. In 1935 Hideki Yukawa suggested that this strong interaction which held the nucleons together in the nucleus could be mediated by the exchange of a particle intermediate in mass between the electron and the nucleons. Yukawa based his model on the successful theory of the electromagnetic interaction in which the interaction is mediated by the exchange of photons. He was able to estimate the mass of the new exchange particle and subsequently a particle with approximately the correct mass was discovered. Unfortunately it soon became apparent that this particle - which was named the muon (μ) - could not be the particle predicted by Yukawa's theory since it interacted weakly with matter and thus could not be responsible for the strong binding force between nucleons. Yukawa's predicted particle was later discovered and named the pion (π).

In the late 1940's and early 1950's several new strongly interacting particles were discovered in cosmic ray experiments and, with the advent of particle accelerators, many more such particles were detected. With the discovery of these particles the number of "elementary" particles had increased drastically and the simple picture of matter based on the proton, neutron and electron had been lost. Physicists were unhappy with the increasing number of "elementary" particles and in an effort to simplify the situation Gell-Mann and Ne'eman suggested that the observed hadrons (strongly interacting particles) were composite. They proposed the existence of a basic triplet of fractionally charged particles which Gell-Mann named quarks. The three quark types were denoted by u, d and s (up, down and strange). The observed hadrons could then be accounted for by assuming that only 3 quark systems and quark anti-quark pairs existed in nature. Subsequently the existence of a fourth type of quark was predicted from symmetry considerations and also to provide a mechanism for the suppression of unwanted strangeness - changing neutral currents in the theory of the weak interaction. This quark was named the charmed quark (c). The discovery in 1974 of the J/ψ particle by Ting and Richter confirmed the presence of the c quark and provided striking confirmation of the quark model.

Once again the basic structure of matter was beginning to look aesthetically pleasing with only a few "elementary" particles being necessary to construct all known matter. The new "elementary" particles were of two types - the strongly interacting quarks and the weakly interacting leptons. The quarks consisted of two quark doublets $\binom{u}{d}$ and $\binom{c}{s}$ and the leptons consisted of two lepton doublets $\binom{\nu_e}{e^-}$ and $\binom{\nu_\mu}{\mu^-}$. The quark-lepton model has received further support recently with the discovery of a new heavy lepton - the τ particle - and evidence for a fifth type of quark - the bottom quark b. These particles are predicted to have associated particles - the τ neutrino ν_τ and the top quark t - which will form a third quark and lepton doublet to maintain the overall symmetry of the model.

The problem of constructing the basic force laws by which the quarks and leptons interact has also made some progress. The most successful theory of all the interactions is that of the electromagnetic interaction - Quantum Electro-dynamics (QED). Thus in an attempt to explain the strong and weak interactions the theory of QED was used as a guide. This has led to the development of a theory (by Weinberg, Salam and Glashow) which combines the weak and electromagnetic interactions into two aspects of a single interaction, the Electro-weak interaction. In this theory the weak interaction is mediated by three vector particles - the $W^\pm$ and the Z^o. One great success of the model was the prediction of weak neutral currents (i.e. weak scattering processes of the type $\nu e \to \nu e$) mediated by Z^o exchange which were subsequently observed experimentally. The masses of the Z^o and the $W^\pm$ were predicted by the Weinberg-Salam theory, provided the one free parameter of the theory (the Weinberg angle) was known. Several experiments have measured this angle and if their measurements are correct the W's and Z should soon be discovered in $\overline{p}p$ collisions at the CERN SPS. The observation of these particles will be a crucial test of the Weinberg-Salam theory.

A candidate theory of the strong interactions has also been developed. In this theory the strong interaction between quarks is due to their having a property known as "colour". Colour is the strong interaction's equivalent of the electromagnetic interaction's charge. The theory is known as Quantum Chromo-dynamics (QCD). In QCD the strong interaction between quarks occurs via the exchange of 8 massless vector particles known as gluons. Unlike the electromagnetic case where the particle which mediates the interaction is not electrically charged, the gluons carry a colour charge. This means that gluons can interact with each other and this leads to QCD being a non-abelian theory unlike QED.

The unification of the electromagnetic and weak interactions has encouraged theorists to attempt to unify the new electro-weak theory with QCD in what have become known as Grand Unified Theories (GUT's). Although this work is very tentative one prediction has come from several of these theories - that of proton decay - and several experiments are being planned to try and observe this phenomenon.* The unification of the gravitational interaction with the other interactions is also an area of research which many theorists are actively involved in. These theories are known as Supergravity theories.

As has been mentioned previously in this section the observation of the intermediate vector bosons (the $W^{\pm}$ and the Z^{o}) will be a crucial test of the Weinberg-Salam theory of the electro-weak interaction. The situation in the strong interaction case is more complicated.

---

*Note that since the time of writing some of these experiments have actually started running and four proton decay candidates were presented at the XXI High Energy Physics Conference in Paris, 1982.

One of the reasons for this is the observation that quarks appear to be permanently confined within hadrons. This has meant that the inter-quark force can only be studied indirectly by studying the properties of the hadrons. Despite this difficulty there has been some indirect evidence in support of QCD in high energy experiments (e.g. scaling violations in deep inelastic scattering). The situation at lower energies is more confused since the perturbation theory approach to QCD breaks down at such energies. This has meant that QCD cannot (at present) be used to predict the hadron mass spectrum. In order to gain further insight into the nature of the strong interaction phenomenological models of the hadrons (some of which are based upon ideas taken from QCD) have been constructed which can predict the spectrum. To test the validity of these models the hadron spectrum must be known. The experiment described in this thesis was designed to study the mass spectrum of the Δ^{++} states (and thus provide more data on the hadron spectrum) for this purpose.

The Grand Unified theories are considered by many physicists to be highly speculative since the simpler theories of Weinberg-Salam and QCD are still awaiting rigorous experimental verification. However, the observation of proton decay would greatly enhance the acceptance of Grand Unified theories and the subsequent study of such decay processes could help to select the correct Grand Unified theory from the many candidates. The Supergravity theories are considered to be even more speculative than the Grand Unified theories and are not yet amenable to experimental verification.

CHAPTER 2

THE BARYON SPECTRUM

2.1 Introduction

This chapter contains a description of the strongly interacting particles known as baryons. The discussion is limited to those particles which may be formed from the three lightest quarks (u, d and s) since all of the particles involved in the experiment described in this thesis were of this type.

Section 2.2 contains a more detailed description of the quark model(2) and its motivation than that given in Chapter 1. Section 2.3 discusses the harmonic oscillator quark model and its extension by Nathan Isgur and Gabriel Karl(3). Section 2.4 describes the experimental determination of the masses of resonance particles by means of partial wave analysis(4) and finally section 2.5 discusses the motivation for the experiment described in this thesis(5).

2.2 The Quark Model

In the late 1940's and early 1950's several new strongly interacting particles were discovered. Initially these discoveries were made in cosmic ray experiments. However, with the advent of particle accelerators the experimental emphasis shifted towards accelerator experiments.

Using accelerators it was possible to produce beams of particles of a specific type with a precise energy. These beams could then be allowed to impinge upon a fixed target and the resulting scattering processes could be studied. Two types of scattering processes were observed to occur in these experiments - elastic scattering and inelastic scattering. In an elastic scattering process the final state particles are identical, in type and number, to the initial state particles (e.g. $\pi^+p \to \pi^+p$ or $pp \to pp$) whereas in an inelastic scattering process new particles are produced in the final state which did not exist in the initial state (e.g. $\pi^+p \to \pi^+p\pi^o$ or $\pi^+p \to K^+\Sigma^+$). The analysis of these early accelerator experiments led to the discovery of many new strongly interacting particles with lifetimes several orders of magnitude smaller than previously discovered particles ($\tau \sim 10^{-23}$ seconds). These particles were named resonance particles.

Many of the resonance particles were discovered in formation experiments. In these experiments the beam particle "combined" in some way with the target particle to form a resonance particle. This particle then decayed to produce the final state particles of the scattering process. Such resonance particles were observed initially as "bumps" in the total cross section when it was plotted as a function of centre of mass energy. The mass of the resonance particle was given by the centre of mass energy at which the "bump" occurred. The development of partial wave analysis allowed the separation of scattering processes via different angular momentum states and this has led to the discovery of even more resonance particles. The very short lifetimes of these particles have proved impossible to measure. However, due to Heisenberg's Uncertainty Principle, a short lifetime corresponds to a large energy "width" and the widths of these particles could be measured. Thus the resonance particles were assigned widths instead of lifetimes.

The newly discovered strongly interacting particles were found to exhibit several new properties and symmetries. These features were superficially explained by the assignment of several new quantum numbers to the particles and the introduction of new conservation laws associated with some of these quantum numbers. Three of these quantum numbers - baryon number B, strangeness S and the third component of isotopic spin I_3 - were found to be related to the electric charge of the particle Q (as a multiple of the electric charge on the proton) via equation (2.2.1)

$$Q = I_3 + \tfrac{1}{2}(S + B) \quad . \tag{2.2.1}$$

The rapid increase in the number of known "elementary" particles and the observed symmetries of the strongly interacting particles led Gell-Mann and Ne'eman to suggest that the hadrons were composite. They proposed the existence of a basic triplet of particles, which Gell-Mann named quarks, based upon the mathematical group SU(3). The quantum numbers of the three quark types (or flavours) u, d and s are shown in Table 2.2.1. The quark model proposed that baryons consisted of 3 quarks and mesons consisted of a quark anti-quark pair. The combination of quarks in this manner via the underlying SU(3) group led to an extension of the idea of isospin multiplets to SU(3) multiplets. If SU(3) was an exact symmetry of the strong interaction all particles within a particular multiplet would have the same mass. However this is not the case since SU(3) is a broken symmetry.

Quark Type	u	d	s
B	$\frac{1}{3}$	$\frac{1}{3}$	$\frac{1}{3}$
S	0	0	-1
I	$\frac{1}{2}$	$\frac{1}{2}$	0
I_3	$+\frac{1}{2}$	$-\frac{1}{2}$	0
Q	$+\frac{2}{3}$	$-\frac{1}{3}$	$-\frac{1}{3}$

Table 2.2.1

The quantum numbers of the three lightest quarks.

The fundamental representation of SU(3) is denoted by a $\{3\}$ which represents the basic quark triplet. For the baryon multiplets three quarks are combined to obtain:

$$\{3\} \times \{3\} \times \{3\} = \{10\} + \{8\} + \{8\} + \{1\} \qquad (2.2.2)$$

and for the mesons a quark and an anti-quark are combined to obtain:

$$\{3\} \times \{\bar{3}\} = \{8\} + \{1\} \quad . \qquad (2.2.3)$$

Thus the quark model predicts that mesons only exist in singlets and octets whereas baryons exist in singlets, octets and decuplets. It was found that the low mass hadrons with identical spins and intrinsic parities (J^P) could in fact be assigned to such multiplets. One of the early successes of this model was the prediction of a particle with $S = -3$ which was necessary to complete the $J^P = \frac{3}{2}^+$ decuplet. This particle was subsequently discovered and named the Ω^-. In the quark model the higher mass hadrons were assumed to be excited states of the lower mass ground state hadrons.

In order to reproduce the correct spin for the observed hadrons quarks were hypothesised to be spin $\frac{1}{2}$ objects. This led to an inconsistency in the quark model. The $J^P = \frac{3}{2}^+$ ground state baryon decuplet contains a hadron made from 3 u quarks (the Δ^{++}). The quarks in this hadron are totally symmetric in space, spin and flavour. This contravenes the Pauli exclusion principle which states that fermion wavefunctions must be totally anti-symmetric. This problem was overcome by postulating that quarks had an extra (hidden) degree of freedom in which the baryon wavefunction was anti-symmetric. This extra degree of freedom was named "colour". In order to construct anti-symmetric baryon wavefunctions quarks were hypothesised to come in three colours - red, green and blue. It was proposed that baryons contained a quark of each colour and hence the baryons were "white" and the colour degree of freedom was hidden. Similarly mesons were made from a colour anti-colour pair and were also white. Further evidence for the existence of colour came from measurements of the ratio R where:

$$R = \frac{\sigma(e^+e^- \to \mathrm{HADRONS})}{\sigma(e^+e^- \to \mu^+\mu^-)} \quad . \tag{2.2.4}$$

If it is assumed that the $e^+e^- \to$ HADRONS interaction occurs via the mechanism $e^+e^- \to q\bar{q}$ (i.e. a quark and an anti-quark) and the $q\bar{q}$ pair then fragment into hadrons, it can be shown that:

$$R = \sum_{\substack{\text{all} \\ \text{quarks}}} (Q_i)^2 \tag{2.2.5}$$

where Q_i is the charge of the i-th quark. To obtain agreement between experiment and theory a factor of 3 must be included to take account of the colour degree of freedom.

The quark model led to a much deeper understanding of the observed hadron spectrum. However, it was not clear initially whether quarks actually existed as real hadron constituents or whether they were simply a mathematical construction. Many experiments were conducted to search for free quarks in cosmic rays and high energy scattering experiments. Despite this effort no evidence for fractionally charged particles was found. One experiment which claimed to observe free fractionally charged particles was that of Fairbank et al.[6] who performed a Millikan type experiment using Niobium balls. The results of this experiment have, however, been treated with some scepticism due to the difficulties of interpreting the data. There is some theoretical indication from QCD that quarks may be permanently confined within hadrons. This, coupled with the apparent experimental failure to observe free quarks, has given much support to the idea of quark confinement.

Experiments to observe the effects of constituent particles within hadrons have met with a much greater degree of success. The main evidence for the existence of point-like constituents within hadrons has come from deep inelastic scattering experiments in which non-strongly interacting particles (leptons), such as electrons, muons and neutrinos, collide with protons. If the energy of the colliding particles is high enough the incident lepton can probe the internal structure of the proton and scatter from an individual proton constituent rather than from the proton as a whole. This leads to an increased probability of observing scatters in which a large amount of momentum is transferred from the lepton. The observation of such collisions supports the proposition that protons contain discrete scattering centres. These scattering centres have become known as partons. The question still remained as to whether these partons could be identified as quarks. Further scattering experiments have shown that the partons within the proton appear to be of two types - spin $\frac{1}{2}$ particles which have been identified with quarks and spin 1 particles which have been identified with the vector gluons of QCD. These conclusions have also received support from the observed "jet" structure of the hadrons produced in e^+e^- collisions.

2.3 Baryon Models

Current theory and experimental data suggest that the baryons are bound states of three quarks. The interaction which binds the quarks together in such a system is believed to be described by the theory of Quantum Chromo-dynamics (QCD). Due to the difficulty of performing calculations using QCD it has so far proved impossible to calculate rigorously the energies (masses) of such systems. Thus QCD cannot predict the mass spectrum of the baryons. In an effort to gain further insight into the nature of the strong interaction, attempts have been made to construct phenomenological models of the baryons (under the assumption that they consist of quarks) which can be used to predict baryon masses.

In the standard quark model baryons consist of three coloured spin $\frac{1}{2}$ quarks. The wavefunction for such a system can be split into 4 distinct component wavefunctions as shown in equation (2.3.1).

$$|qqq\rangle = \underset{O(3)}{\psi_{SPACE}} \times \underset{SU(2)}{\chi_{SPIN}} \times \underset{SU(3)}{\phi_{FLAVOUR}} \times \underset{SU(3)_{\bar{c}}}{f_{COLOUR}} \quad . \qquad (2.3.1)$$

The group structure of these component wavefunctions is indicated below them. As mentioned in section 2.2 the colour wavefunction for baryons is hypothesised to be anti-symmetric. Thus the remaining component wavefunctions must combine to give a symmetric wavefunction to maintain the required total anti-symmetry of the system. The spin and flavour components may be combined to give an SU(6) structure. The fundamental representation of SU(6) is denoted by a $\{6\}$ which represents the basic quark triplet in each of its two possible spin states. For the baryon multiplets three of these basic representations are combined to obtain:

$$\{6\} \times \{6\} \times \{6\} = \{56\} + \{70\} + \{70\} + \{20\} \quad . \qquad (2.3.2)$$

The SU(6) wavefunction is then combined with the spatial wavefunction to obtain a wavefunction which is totally symmetric in spin, space and flavour leading to SU(6) × O(3) supermultiplets. Thus, for example, if we consider the ground state spatial wavefunction which is symmetric and has $L = 0$ (where L is the orbital angular momentum of the system) only combinations of the spin and flavour wavefunctions which give a symmetric SU(6) wavefunction will be allowed. This leads to a $[56,0^+]$ SU(6) × O(3) supermultiplet (where the 56 is the SU(6) dimensionality and the 0^+ means $L = 0$ and positive parity) which can be identified with the well known low lying $J^P = \frac{3^+}{2}$ decuplet and the $J^P = \frac{1^+}{2}$ octet of SU(3).

To proceed further it is necessary to choose a particular form for the potential confining the quarks in the baryon. A common choice for this potential is a spin independent, flavour independent, two body harmonic potential[7]. With such a potential the three quark system can be treated as two independent harmonic oscillators (the so called $\underline{\rho}$ and $\underline{\lambda}$ oscillators - see Figure 2.3.1). The Hamiltonian for such a system can be solved exactly to obtain the expected energy levels. If the three quarks are assumed to have equal masses this leads to a spectrum which consists of a series of equally spaced levels to which the SU(6) × O(3) supermultiplets are assigned. Each of these levels is characterised by the value of a single quantum number N which is just the total number of excitations of the $\underline{\rho}$ and $\underline{\lambda}$ oscillators. The supermultiplet structure for the first 3 levels is shown in Figure 2.3.2.

This spectrum is not observed experimentally on two counts. Firstly the supermultiplets at the $N = 2$ level are not degenerate in mass and secondly the particles within a supermultiplet are not degenerate in mass. Thus the harmonic oscillator model cannot, by itself, describe the observed baryon spectrum. There have been several attempts to extend this model to obtain better agreement with experiment. I shall only discuss the most successful of these models, which is that due to Nathan Isgur and Gabriel Karl[3].

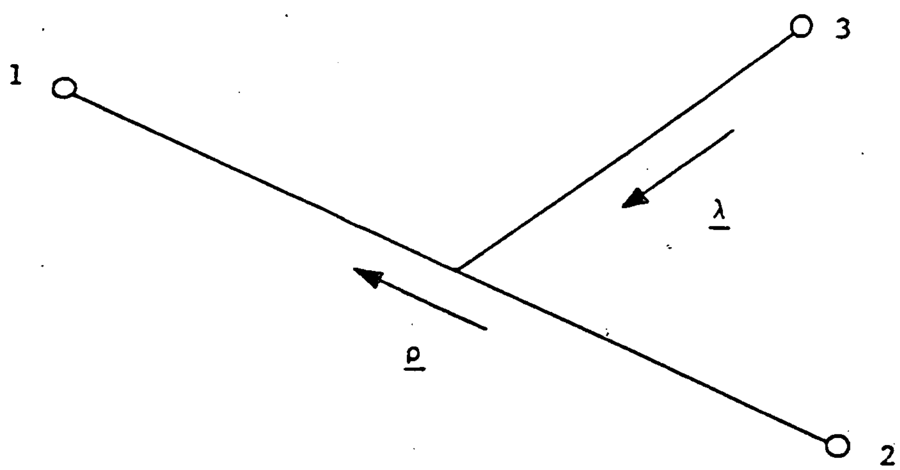

$$\underline{\rho} = \frac{1}{\sqrt{2}} (\underline{r}_1 - \underline{r}_2)$$

$$\underline{\lambda} = \frac{1}{\sqrt{6}} (\underline{r}_1 + \underline{r}_2 - 2\underline{r}_3)$$

FIGURE 2.3.1: The $\underline{\rho}$ and $\underline{\lambda}$ oscillators of the harmonic oscillator quark model of baryons.

$N = 2$ ——— $[\underline{56},2^+]$, $[\underline{70},2^+]$, $[\underline{20},1^+]$, $[\underline{56},0^+]$, $[\underline{70},0^+]$

$N = 1$ ——— $[\underline{70},1^-]$

$N = 0$ ——— $[\underline{56},0^+]$

FIGURE 2.3.2: The SU(6) × O(3) supermultiplet structure for the first three levels of the harmonic oscillator quark model with equal mass quarks.

Isgur and Karl assumed that the confining potential was not exactly harmonic. They added an arbitrary central potential (U, say) which was spin and flavour independent and which comprised pairwise interactions only (i.e. no three body interactions) to the harmonic potential. They then proceeded to perform first order perturbation theory in this potential using the harmonic oscillator states as basis states. This procedure split the degeneracy of the $N = 2$ supermultiplets and furthermore the pattern of splitting was found to be independent of the specific form of the potential U [8].

Although this solved part of the degeneracy problem, states within a supermultiplet were still degenerate in mass in this model. In order to resolve this difficulty Isgur and Karl introduced a spin dependent short range force which would be expected to arise from one gluon exchange. This interaction is a colour magnetic dipole-colour magnetic dipole (or hyperfine) interaction which is the QCD analogue of ordinary magnetic dipole-magnetic dipole interactions in QED. The addition of this extra term to the Hamiltonian not only split the degeneracy within supermultiplets, it also produced mixing between the supermultiplets to produce the observed physical states. The results of this model for the $S = 0$ positive parity excited baryons are shown in Figure 2.3.3. The open boxes show the regions in which the experimentally observed resonances lie. These boxes contain the "star" rating of the resonances as defined by reference (9). The resonances predicted by Isgur and Karl are denoted by solid bars whose lengths indicate their predicted visibility. The results of the model are seen to be in good agreement with experiment.

Isgur and Karl have also carried through their analysis in the strange sector where the quarks have unequal masses and again found good agreement with the experimentally observed states.

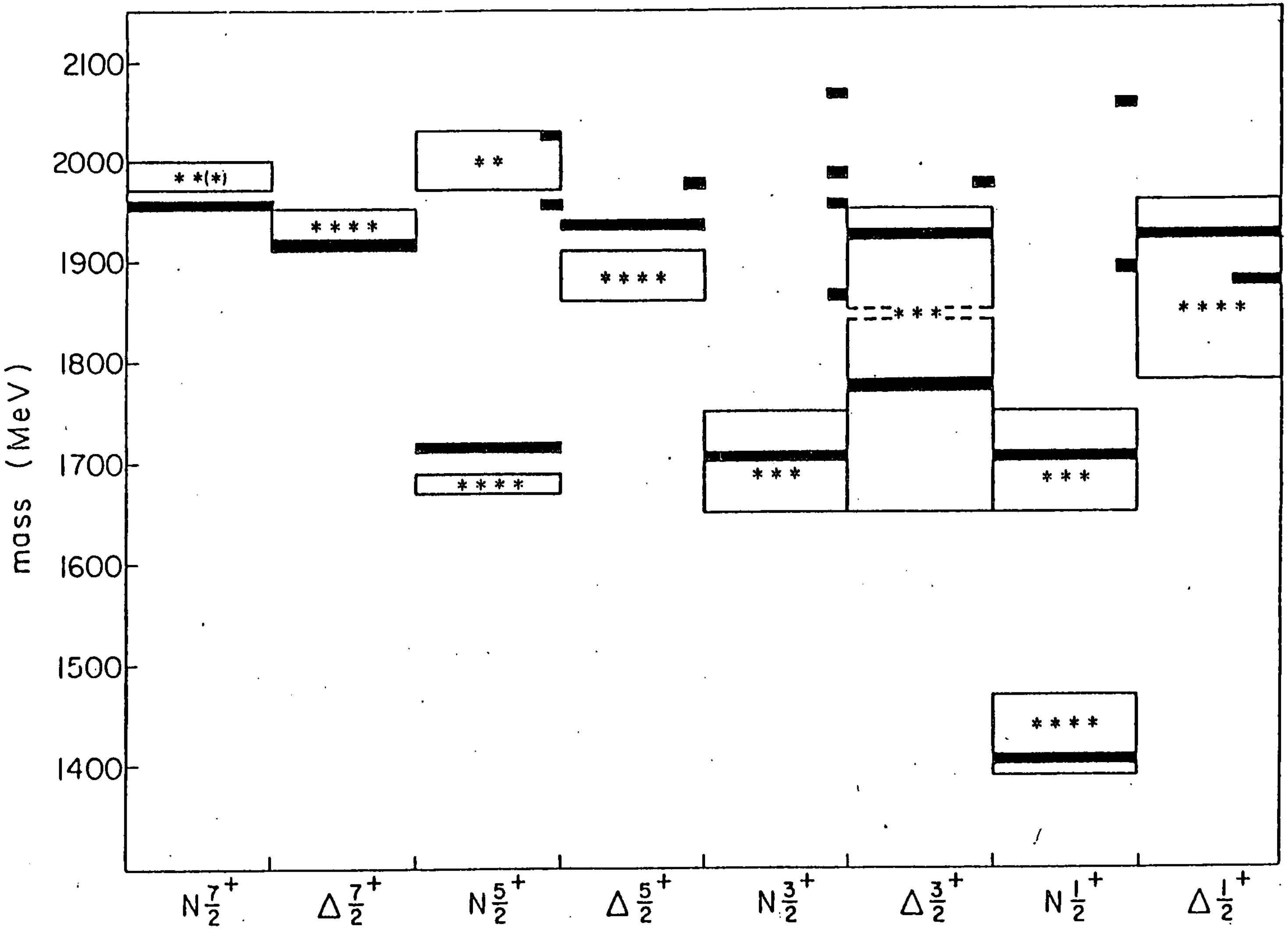

FIGURE 2.3.3: The mass spectrum of the S = 0, positive parity, excited baryons as calculated by Isgur and Karl.

2.4 Experimental Determination of Resonance Parameters

In this section the experimental determination of resonance parameters(4) as it relates to π^+p elastic scattering is described.

For simplicity consider firstly the scattering of two spin zero particles. In this case the scattering process can be described by a single complex scattering amplitude, $f(\theta,k)$, which is a function of the scattering angle θ and the centre of mass momentum k. This amplitude is related to the differential cross section, $\frac{d\sigma}{d\Omega}$, by equation 2.4.1.

$$\frac{d\sigma}{d\Omega} = f^*f \quad . \tag{2.4.1}$$

The scattering amplitude f may be expanded in an infinite series of "partial waves", $\{T_\ell, \ \ell = 0,1,2, \ldots\}$, of definite angular momentum ℓ as shown in equation 2.4.2.

$$f(\theta,k) = \frac{1}{k} \sum_{\ell=0}^{\infty} (2\ell+1)T_\ell(k)P_\ell(\cos\theta) \tag{2.4.2}$$

where the P_ℓ are Legendre functions.

The scattering of a spin zero particle by a spin ½ particle is more complicated. In this case the scattering amplitude f of the spin zero case is replaced by two amplitudes f and g (the so-called spin non-flip and spin flip amplitudes, respectively). The partial wave amplitudes T_ℓ are also replaced by two amplitudes - T_ℓ^+ corresponding to $J = \ell+\frac{1}{2}$ and T_ℓ^- corresponding to $J = \ell-\frac{1}{2}$. Formulae for f and g in terms of the partial wave amplitudes are quoted in equations 2.4.3 and 2.4.4.

$$f(\theta,k) = \frac{1}{k} \sum_{\ell=0}^{\infty} \left[(\ell+1)T_\ell^+(k) + \ell T_\ell^-(k)\right] P_\ell(\cos\theta) \tag{2.4.3}$$

$$g(\theta,k) = \frac{1}{k} \sum_{\ell=1}^{\infty} \left[T_\ell^+(k) - T_\ell^-(k)\right] P_\ell^{\,1}(\cos\theta) \tag{2.4.4}$$

where the P_ℓ^1 are associated Legendre functions. The differential cross section $\frac{d\sigma}{d\Omega}$ is now given by:

$$\frac{d\sigma}{d\Omega} = ff^* + gg^* \quad . \tag{2.4.5}$$

The introduction of spin also leads to three new measurable quantities (the polarisation P and the spin rotation parameters A and R), which, like $\frac{d\sigma}{d\Omega}$, are bilinear functions of the amplitudes f and g. The experimental determination of these new quantities in pion nucleon elastic scattering is extremely difficult, requiring a polarised target to measure P and the combination of a polarised target with a double scattering experiment to measure A and R.

To determine resonance parameters it is necessary to extract the complex partial wave amplitudes $\{T_\ell^{\pm}\}$ from the measured physical quantities. This extraction process is known as partial wave analysis. Due to the experimental difficulties of measuring P, A and R in pion-nucleon elastic scattering few such measurements have been made. This leads to ambiguities in the partial wave analysis. That is to say that there exists more than one set of $\{T_\ell^{\pm}\}$ which describe the measured data. If the partial wave expansion is infinite there is in fact a continuum ambiguity (i.e. there exists an infinite set of $\{T_\ell^{\pm}\}$ all of which describe the data equally well). By truncating the partial wave expansion, at some $\ell = \ell_{MAX}$ say, the continuum ambiguity can be reduced to a set of discrete ambiguities. Two distinct types of partial wave analyses may be performed - energy independent partial wave analysis or energy dependent partial wave analysis.

In energy independent partial wave analyses data at each energy is analysed independently. Usually each partial wave amplitude is allowed to vary freely (subject only to unitarity constraints) over a wide range to find the best fits to the data. At the end of this analysis a choice is then made between the discrete solutions which have been found, usually on the basis of energy continuity.

In energy dependent partial wave analyses data at different energies are fitted simultaneously by assuming some particular energy dependent parameterisation for the amplitudes. Several such parameterisations have been attempted. One of the early such attempts was the parameterisation of the amplitudes by a slowly varying polynomial background with or without some Breit-Wigner resonance terms. Another approach is to use dispersion relations to provide constraints between the real and imaginary parts of the amplitudes.

Having found the "true" solution the problem still remains of deciding whether particular partial waves are resonant or not and of extracting resonance parameters from those waves which are believed to be resonant. A criterion for resonance within a partial wave is that the complex amplitude $T_\ell^{\pm}$ should be described by the Breit-Wigner resonance formula (2.4.6)

$$T_\ell^{\pm} = \frac{\Gamma_e/2}{(M - E - i\Gamma/2)} \qquad (2.4.6)$$

where Γ_e and Γ are the elastic and total resonance widths respectively, M is the resonance mass and E is the centre of mass energy. The resonance elasticity x_e is defined as:

$$x_e = \frac{\Gamma_e}{\Gamma} \quad . \qquad (2.4.7)$$

The Breit-Wigner formula describes a circle in the complex T plane which is centred on $(0,x_e/2)$ and is of radius $x_e/2$. In practice this formula is modified in many ways (e.g. the widths may vary with energy, it may be necessary to include a slowly varying background term, etc.) to obtain a good fit to the observed amplitudes. Many different forms have been used to parameterise the amplitudes, based essentially on the simple Breit-Wigner formula. This has led to the discovery of many resonances (with varying degrees of certainty) and to the prediction of resonance parameters (Γ, x_e and M) for these resonances.

2.5 Justification for this Experiment

The experiment described in this thesis was designed to study the following two reactions:

1) $\pi^+ p \to K^+ \Sigma^+$ where the Σ^+ subsequently decayed into a proton and a neutral pion ($\Sigma^+ \to p\pi^o$).
2) $\pi^+ p \to \pi^+ p$ elastic scattering in the "backward" direction (i.e. $\cos\theta^* \lesssim 0.2$).

From the data collected in the experiment $\frac{d\sigma}{d\Omega}$ could be extracted for both reactions and the polarisation P could be extracted for the $K\Sigma$ reaction (by observation of the proton from the Σ^+ decay). These quantities could then be used to obtain information on the formation of Δ^{++} resonances (via the processes $\pi^+ p \to \Delta^{++} \to K^+ \Sigma^+$ and $\pi^+ p \to \Delta^{++} \to \pi^+ p$) in the mass range from 1.8 to 2.4 GeV/c^2.

The experiment was designed primarily to study the $K\Sigma$ reaction. This channel is the only two body inelastic final state channel in $\pi^+ p$ scattering. By performing a partial wave analysis of the channel an independent measurement of the Δ^{++} resonances could be carried out. In addition, the data could be used to study the phases of partial wave amplitudes in a pure isospin ($I = \frac{3}{2}$) inelastic channel.

It was realised at an early stage of the experiment that backward elastic scattering data could be collected simultaneously with the KΣ data, with no loss in the KΣ signal. In principle forward elastic scattering data could also be collected. However, due to the large forward elastic peak and the limited beam time available to perform the experiment, the collection of this data would have seriously reduced the KΣ reaction statistics. For this reason a large downstream threshold Cerenkov counter was used to veto forward elastic events. Despite the large amount of data collected by previous experiments in the elastic channel the analysis of the elastic data was felt to be worthwhile for several reasons. Firstly, the elastic scattering events could be used to check the analysis programs. The KΣ data was not as suitable for this purpose, since there is only one previous high statistics KΣ experiment to compare with and it only made measurements at one momentum. Secondly, many of the previous elastic experiments were old low statistics bubble chamber experiments. Thirdly, the more recent higher statistics counter experiments were in disagreement with each other (especially in the backward scattering region). Fourthly, the vast majority of the high statistics data from previous experiments was at beam momenta below 2.3 GeV/c and thus this experiment could provide new high statistics data in the momentum range from 2.3 to 2.5 GeV/c. Thus it was hoped that the analysis of the elastic scattering data collected in this experiment would help to resolve some of the discrepancies between previous experiments in the low energy region and would also provide new high statistics data in the region above 2.3 GeV/c.

CHAPTER 3

EXPERIMENTAL SET UP

3.1 Introduction

This chapter contains a description of the apparatus used in this experiment. A more detailed description may be found in Dr. L.R. Scotland's doctoral thesis[10].

Section 3.2 outlines the experimental method used in the experiment and gives a brief overview of the apparatus. Sections 3.3 to 3.6 give a more detailed discussion of individual components of the apparatus. In particular section 3.3 discusses the beam, 3.4 the target, 3.5 the trigger and 3.6 the measurement system. The running conditions of the experiment are discussed in section 3.7 and finally, in section 3.8, the data collected by the experiment is described.

3.2 Experimental Method and Apparatus

The initial aim of this experiment was the extraction of polarisation and differential cross section measurements for the reaction $\pi^+p \rightarrow K^+\Sigma^+$ and differential cross section measurements (in the backward direction) for the reaction $\pi^+p \rightarrow \pi^+p$. This process required the observation and measurement of many individual scattering events of each reaction type.

In the experiment a beam of particles, containing positively charged pions, impinged upon a stationary hydrogen target of known length and density. The number of π^+'s in the beam, incident on the target, was measured by a system of scintillation counters and a

Cerenkov counter. Many interactions occurred between the beam π^+'s and the protons in the hydrogen target. A set of scintillation and Cerenkov counters was used to preferentially select $K\Sigma$ and backward elastic scattering events. This was done by combining the signals from these counters to define a trigger signal. For events which "passed" the trigger, measurements of event parameters were made. The trajectories of the charged particles involved in the interaction were measured, using multi-wire proportional chambers (MWPC's) and wire spark chambers. The majority of these chambers were situated inside a large volume open spectrometer magnet to enable the measurement of particle momenta from the curvature of trajectories. In addition to these measurements some of the trigger counters provided time of flight information which could be used to aid particle identification.

The apparatus used in the experiment was known collectively as the Rutherford Multi-particle Spectrometer (or RMS for short). A plan view of the apparatus (not to scale) is shown in Figure 3.2.1. The RMS reference frame, which is used throughout this thesis, is also illustrated on this diagram. Four types of particle detector are shown in the diagram.

1) Scintillation Counters

These counters were used to define a trigger and also to provide time of flight information.

C3, C2, CO, A2 and AO

C3, C2 and CO were small circular counters which were situated in

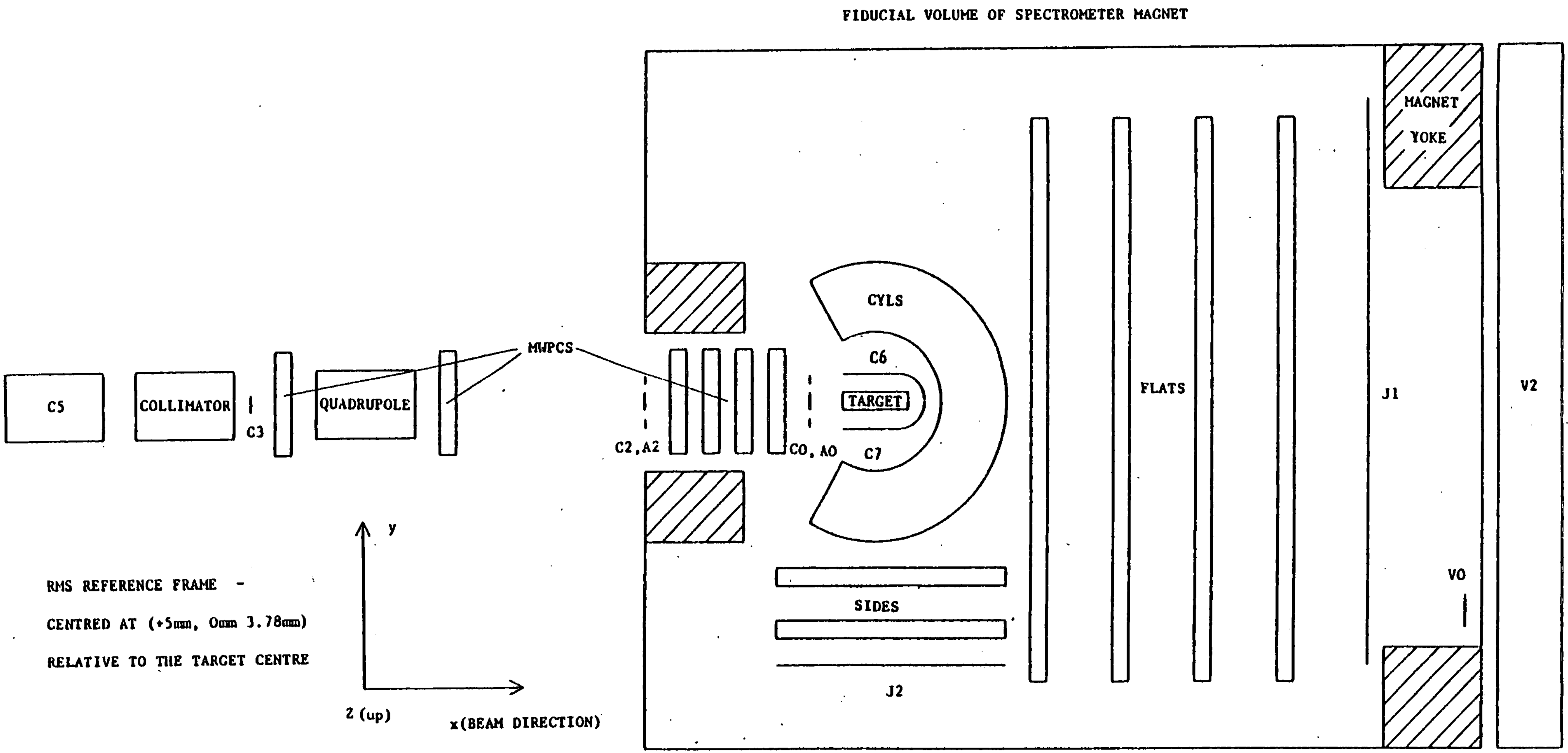

FIGURE 3.2.1: Plan view of the experimental apparatus used in this experiment.

the beam. A2 and A0 were annular counters surrounding C2 and C0 respectively. These counters were used in the trigger and, in addition, C3 and C2 provided time of flight information.

C6, C7, A3 and A4

C6 and C7 were counters which lay on either side of the target and curved round to meet in front of the target. C6 was 20 mm high and C7 was 50 mm high. A3 and A4 were flat counters which lay above and below the target and which abutted the straight sections of C6 and C7 (Note that A3 and A4 are not shown in Figure 3.2.1). These counters were used in the trigger.

V0

This was a small (100 mm) square counter, inserted just in front of the large downstream Cerenkov counter V2, for use in the trigger.

J1

This was a large downstream hodoscope. It consisted of three separate scintillation counters, each 2.3 metres long by 0.25 metres high, with a photomultiplier tube at each end. J1 was used in the trigger and also to provide time of flight information.

J2

This was a large hodoscope situated to one side of the target. It consisted of four scintillation counters, each 1.2 metres long by 0.15 metres high, with a photomultiplier tube at one end. J2 was used solely to provide time of flight information.

2) Cerenkov Counters

There were two Cerenkov counters used in this experiment, both of which formed part of the trigger.

C5

This was a medium pressure threshold Cerenkov counter which was situated in the beam.

V2

This was a large downstream threshold Cerenkov counter which had 18 photo-tubes and was filled with Freon 12 to a pressure of 7.8 atmospheres.

3) Multi Wire Proportional Chambers

There was a total of six MWPC modules used in this experiment. Each module consisted of two chambers - one to provide horizontal information and one to provide vertical information. These chambers were situated in the beam to measure the beam particles' momenta and trajectories. All the MWPC's had a wire spacing of 1 mm.

4) Spark Chambers

The wire spark chambers used in this experiment measured the outgoing particles' momenta and trajectories. The chambers, which were equipped with capacitative read out on both the high and low voltage planes, were arranged in three groups:-

a) Seven concentric cylindrical chambers (CYLS) which had their axis in the vertical (Z) direction. These chambers were closest to the target and were 1 metre high with radii from 0.17 to 0.48 metres.

b) Four double gap flat chambers (FLATS) in the region between the CYLS and the hodoscope J1. These chambers were 2 metres wide by 1 metre high.

c) Two double gap flat chambers (SIDES) in the region between the CYLS and the hodoscope J2. These chambers were 1 metre high by 1 metre wide.

The CYLS and SIDES had a wire spacing of 1 mm and 1.5 mm, respectively, with the high voltage planes vertical and the low voltage planes inclined at (+ or −) 14° to the vertical. The FLATS had a wire spacing of 1 mm with the high and low voltage planes inclined at $\pm 15^{\circ}$ to the vertical.

All of the spark chambers and four of the six MWPC modules lay within the fiducial volume of the spectrometer magnet which had a useful volume of approximately 4 m × 2 m × 1 m.

3.3 The Beam

The experiment used the $\pi 13$ beam line at the Rutherford Laboratory's proton synchrotron accelerator (NIMROD). This was a conventional three stage beam line, transporting positive particles, which produced an unseparated beam with a small momentum bite ($\frac{\Delta p}{p} \sim 0.4\%$). Pions in the beam were identified by two different techniques. Above 1.9 GeV/c beam momentum the beam Cerenkov C5 was used to veto K^+'s and protons and accept π^+'s, μ^+'s and e^+'s. The small contamination from μ^+'s and e^+'s was measured and corrected for. Below 1.9 GeV/c π^+'s were identified by their time of flight between the two beam scintillation counters C3 and C2. In this mode the beam Cerenkov C5 was used to veto e^+'s. The method used to count the number of π^+'s in the beam, incident on the target, is described in section 3.5.

3.4 The Target

The target used in the experiment was a cylinder 150 mm long, of diameter 25 mm, which was filled with liquid hydrogen. The liquid hydrogen used in the target was boiling at a vapour pressure between 16.2 and 16.6 pounds per square inch. This corresponded to a temperature in the range 20.59K to 20.67K and a density of $(7.067 \pm 0.005) \times 10^{-2}$ gm. cm^{-3}.

3.5 The Trigger

The purpose of the trigger was to reject, at an early stage, events which did not satisfy certain topological constraints satisfied by the reactions under study. Such events came from many sources (e.g. interactions outside the target, competing reaction channels - $\pi^+p \rightarrow \pi^+p\pi^o$, $\pi^+p \rightarrow n\pi^+\pi^+$ etc.). Figure 3.5.1 shows a plan view of the trigger counters used in the experiment illustrating their position relative to a "typical" elastic event.

In this experiment the trigger imposed five constraints on the events.

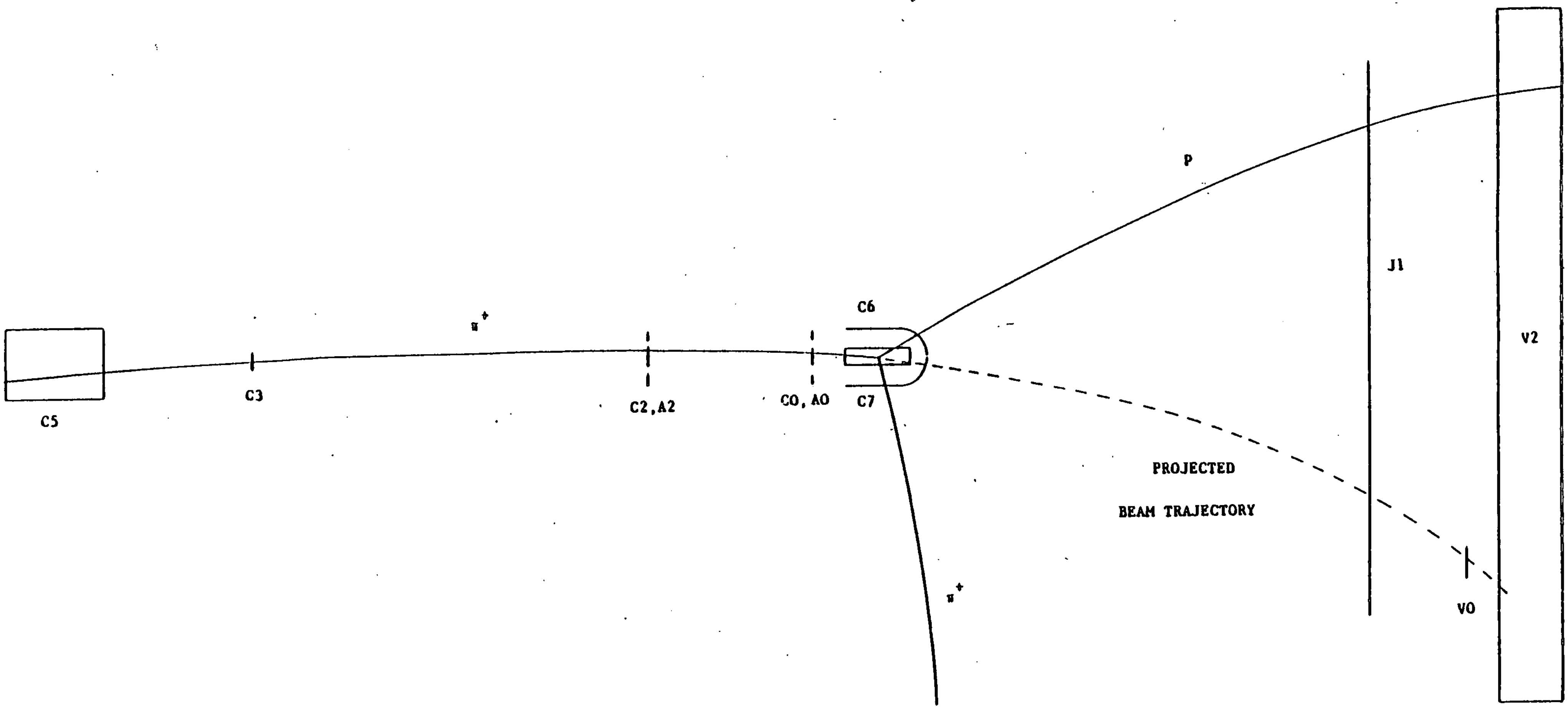

FIGURE 3.5.1: Plan view of the trigger counters used in this experiment.

Constraint 1

This constraint was that a beam π^+ had to enter the hydrogen target. Beam π^+'s were identified by the technique described in section 3.3. These particles were constrained to enter the hydrogen target by demanding a "hit" in the two small circular scintillation counters (C2 and CO) and no hit in the annular counters (A2 and AO) which were situated immediately in front of the target to form a beam "telescope". The combination of all these conditions was used to define a "good" beam π^+ and a counter (known as R3) was incremented whenever all these conditions were met to count the number of π^+'s incident on the target.

Constraint 2

This constraint was that no outgoing beam particle should be observed. This condition was met by demanding no signal from the Cerenkov counter V2 and no signal from the scintillation counter VO. V2 had a threshold for pions of about 1.0 GeV/c and an efficiency of greater than 95% above 1.3 GeV/c. Events with non-interacting beam tracks which did not "fire" V2 (due to its small inefficiency) were vetoed by VO.

Constraint 3

This constraint was that two, and only two, outgoing, charged particles should be observed and these particles should be approximately coplanar with the beam. In addition, the event plane was constrained to lie approximately in the horizontal plane.

The elastic scattering reaction obviously has two outgoing charged particles. These particles must be coplanar with the beam in order to conserve momentum. The $K\Sigma$ reaction also has two outgoing charged particles - the K^+ and the proton from the Σ^+ decay ($\Sigma^+ \rightarrow p\pi^o$). Due to the proton mass being a large fraction of the Σ^+ mass the laboratory opening angle between the Σ^+ and the proton is generally small and thus the K^+ and the proton are approximately coplanar with the beam. The condition that events should lie approximately in the horizontal plane ensured the best momentum measurement accuracy since the major magnetic field component was in the vertical direction.

This constraint was met by demanding a count in both the scintillation counters C6 and C7 (on either side of the target) and no count in A3 and A4 (above and below the target).

Constraint 4

This constraint was that one of the outgoing particles should travel in the forward direction in the laboratory. This ensured that at least one of the observed final state particles would be well measured since most of the outgoing track measurement chambers were "downstream" of the target. The constraint was met by demanding a hit in the downstream hodoscope J1.

Constraint 5

This constraint was that the event should not be a forward elastic event (for the reason discussed in section 2.5). The constraint was automatically met by previous demands. In particular, the fast forward π^+ from such events fired the downstream Cerenkov V2, thus causing the events to be vetoed.

One further feature of the trigger was a 50 nanosecond past and future protection on (A2 + C2).(AO + CO)*. This prevented any mis-calculation of the beam flux due to beam tracks being very close together in time.

3.6 The Measurement System

For those events which "passed" the trigger, some means of measuring the particle momenta and trajectories was necessary.

Particle momenta could be calculated from the observed curvature of trajectories within the magnetic field of the spectrometer magnet, provided the field was well known. The current through the spectrometer magnet coils was varied with the beam momentum to produce similar event topologies at each momentum. The current varied from 1541 amps at the lowest momentum to 4400 amps at the highest momentum, giving a field at the target centre of between 6-10 K. gauss. The magnetic field within the useful volume of the magnet was measured at three current values throughout the range and magnetic field maps were constructed at all current values by interpolation[10]. Thus the problem of momentum measurement was reduced to the measurement of particle trajectories.

The beam particle trajectories were measured by the MWPC's and the outgoing particle trajectories were measured by the wire spark chambers. The MWPC's could be continuously read out, however the spark chambers had to be pulsed. The spark chambers were "fired" by the trigger pulse. After firing and reading out a D.C. clearing field removed the remaining ionisation and the read-out capacitors were discharged. This resulted in the chambers being "dead" for approximately 10 milliseconds after recording an

*Note that the peak instantaneous beam rate was $\sim 10^6$ particles per second.

event. During this time no new events could be recorded and hence the trigger was inhibited. The chamber dead time was the limiting factor in the data taking rate.

3.7 Running Conditions

During data taking the following conditions were maintained as closely as possible:-

a) The beam flux was maintained at an approximately constant level ($\sim$ 50K beam pions/Nimrod burst) by adjustment of collimator settings.

b) The spark chamber efficiencies were maintained at approximately 85% with cluster sizes $\sim$ 6 on the low voltage planes and $\sim$ 4 on the high voltage planes. This was achieved by adjustment of the high tension voltages applied to the chambers.

c) The MWPC efficiencies were maintained at approximately 99% by adjustment of their applied voltages. In practice, these chambers required very little adjustment.

In addition, the gas mixtures to the chambers, the two Cerenkovs' operating conditions and the currents through the beamline elements were monitored at least once per eight hour shift.

3.8 Data Collected

Approximately 17 million triggers were recorded at 26 beam momenta in the range from 1.25 GeV/c to 2.50 GeV/c at a spacing of approximately 0.05 GeV/c. The data collected at each momentum is shown in

Figure 3.8.1. The hatched region shows the momenta for which results are presented in this thesis.

In addition to data taken with the "standard" trigger and under normal running conditions, several specialised data tapes were also collected:-

a) A "target empty" run was collected at every second momentum. In these runs the target was filled with gaseous hydrogen. These runs were collected to allow a determination of the interaction rate from the experimental apparatus.

b) A "Cerenkov off" run was collected at 4 momenta throughout the range. In these runs the large downstream Cerenkov (V2) was removed from the trigger. These runs enabled the efficiency of the Cerenkov and its random veto rate to be calculated.

c) Several "Straight Track" tapes were collected at momenta throughout the range. For these tapes the spectrometer magnet was switched off. This data was used by the Survey Program to accurately determine the chamber positions.

d) A "beam track" tape was collected at every momentum. These tapes had a "non interacting beam track trigger" and they were used in the beam momentum calibration process (see section 4.4).

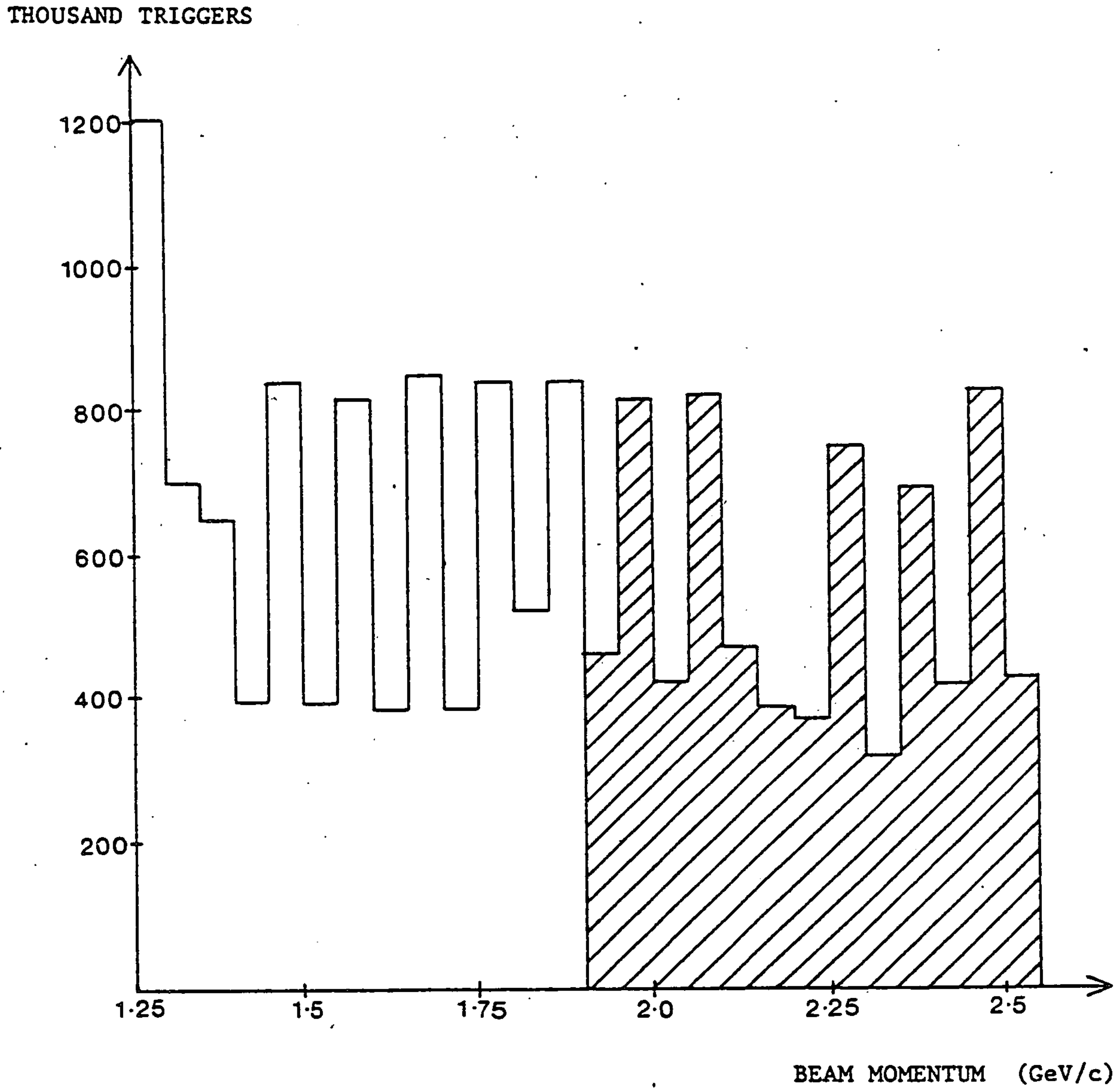

FIGURE 3.8.1: Data collected at each momentum.

CHAPTER 4

EVENT RECONSTRUCTION

4.1 Introduction

The data collected in this experiment consisted of events which passed the trigger. Each event was represented by the data acquisition system (DAS) information which was divided into four sections. The first section was a "header" section which contained the date, run number, event number and trigger code. The second section recorded the scaler information for the event. This information fell into three categories - TDC's and ADC's (for time of flight measurement), trigger logic scalers per event (e.g. R3's per event) and cumulative trigger logic scalers. The third section contained MWPC information which consisted of a list of MWPC wire numbers which recorded a signal for the event. The fourth section contained spark chamber information which consisted of a list of spark chamber wire numbers (in coded form) which recorded a signal for the event.

The aim of event reconstruction was to calculate, from the DAS information, all relevant event parameters. The wire numbers were translated into 3-D coordinate points (and errors). These points were systematically searched for particle tracks. Points which lay on tracks were then used to determine particle momenta and subsequently an interaction vertex. The ADC and TDC information was combined to produce times of flight which could be used to identify particle types. All of this information was then combined to identify particular types of events (e.g. elastic scattering events).

A description of the event reconstruction techniques used in this experiment is given in sections 4.2 to 4.6. (A more detailed description may be found in Dr. L.R. Scotland's doctoral thesis[10]). In section 4.2 the organisation of the RMS event reconstruction program is described. Section 4.3 describes the track finding technique and section 4.4 describes the track fitting procedure. In section 4.5 the time of flight information is discussed. Section 4.6 describes the event fitting procedure and finally in section 4.7 the quality of the reconstructed events is discussed.

4.2 The Reconstruction Program

The RMS event reconstruction program was split into three main sections:-

1) REAP which found particle tracks.
2) STRIP which fitted these tracks to obtain particle momenta and trajectories.
3) GKIN which carried out a geometrical and kinematic fit to the event as a whole.

The program, which was known as RSG, was run on the Rutherford laboratory's dual IBM 360/195 computers.

RSG used the HYDRA[11] memory management system which was written at CERN. In this system the program was split into self contained sets of subroutines, known as processors, which performed specific tasks. The calling of these processors was controlled by a steering program (STEER) which was split into three stages. Each requested processor was called during each stage. Stage 1 contained all the initialisation necessary to prepare the program for event processing. Stage 2 contained the event processing loop. This stage of each requested processor was called once per event. Stage 3 terminated the program and produced a summary of the analysed events characteristics.

The HYDRA system used blank common as a storage space. The information required by the processors to analyse events was stored here as was the processed event data. The information was stored in a "tree structure" of data blocks which were known as banks. These banks were linked to each other to enable easy access to the stored information.

The techniques used by the analysis program to reconstruct events will now be discussed.

4.3 Track Finding

The first stage of the track finding process was the translation of the digital spark chamber and MWPC readout into a set of 3-D spatial coordinates with corresponding errors.

Each chamber in the system was represented by a surface. In the case of the spark chambers, this surface corresponded to the mid-point of the spark gap (i.e. mid-way between the high and low voltage wire planes). For the MWPC's the surface corresponded to the plane of the anode sense wires. There were two types of surface - planar and cylindrical.

The information from the spark chambers and the MWPC's was different. The spark chambers gave positional information from two planes (high and low voltage) whereas the MWPC's only gave information from the anode sense planes. Also in the spark chambers clusters of wires gave a signal when a charged particle traversed the chamber (with a typical cluster size ~ 5 wires), whereas in the MWPC's only one (or occasionally two) wire(s) gave a signal. In the spark chambers all cluster intersections (from both planes) corresponded to possible spark positions. This could lead to "ghost images" of real sparks as illustrated in Figure 4.3.1. These ghost sparks did not, in general, line up throughout the chambers and hence "ghost tracks" were not a problem. Knowledge of the chamber positions and construction allowed the 3-D spatial coordinates of hits to be calculated from the DAS information.

The next stage in the track finding process was to search systematically through the set of reconstructed 3-D coordinate points to find which of these points lay on particle tracks. The method used differed for the spark chambers (which measured the outgoing particle tracks) and the MWPC's (which measured the beam tracks). The technique used in the beam track case combined track fitting and track finding into one process and hence it will be discussed in section 4.4 on track fitting.

The general approach used in the outgoing track case was to search for track segments in the CYLS, FLATS and SIDES independently. Segments of the same track were then merged. Any track segments remaining unmatched were then extrapolated to search for more sparks lying on the track.

Track segment searches were carried out by means of linear extrapolation from the last two sparks on the segment into the next chamber. (Initially the linear extrapolation was from the target centre and a spark on the first chamber into the second chamber). If no spark was found on the next chamber close* to the intersection point of the line with the chamber the candidate track segment was rejected. All track segments found by this process were fitted using a "pseudo helix" fit (i.e. a circle in the x-y plane and a line in the R-Z plane). Segments were then selected, based on the mean squared residuals of this fit, and all sparks on selected segments were flagged to exclude from further

*The road width within which sparks were accepted depended upon the extrapolation distance and was typically ~ 5 mm.

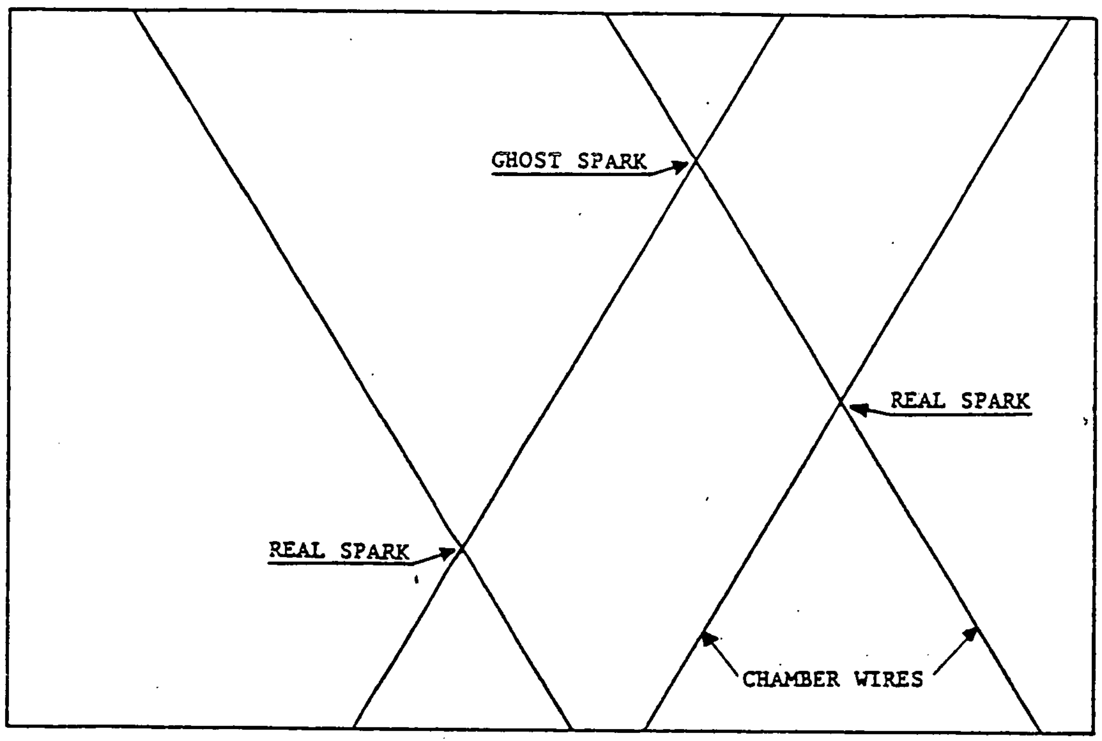

FIGURE 4.3.1: Illustration of "ghost" spark formation.

track finding. The segment search was then repeated, looking for segments with one, two, three and four sparks missing for the CYLS and FLATS and with one spark missing for the SIDES. At the end of this process track segments with four or more sparks in the CYLS and FLATS and with three or more sparks in the SIDES had been found.

An attempt was then made to merge track segments from each of the three chamber groups. Each track segment was extrapolated, using the pseudo helix fit to a reference cylinder just outside the last cylinder. The positions, directions and curvatures of the segments at this cylinder were then calculated. A weighted sum of the squared residuals in these five parameters was then formed for all track segment combinations (within limits). Mutually exclusive combinations were then accepted in order of increasing residual. Any remaining unmatched track segments were extrapolated into the other chambers to search for more sparks which lay on the track. At the end of this process a set of tracks had been defined.

The efficiency of the track finding portion of the analysis program was estimated by the visual scanning of events and found to be $\sim 96\%$.

4.4 Track Fitting

In this section the calculation of track parameters by fitting to the measured track points is discussed[12]. This process was carried out for both the outgoing and the beam tracks.

Outgoing Track Fitting

The outgoing particles travelled through a magnetic field. The equation of motion for such a particle is given by:

$$\frac{d^2\underline{r}}{dt^2} = \frac{q}{\gamma m}\frac{d\underline{r}}{dt} \times \underline{B} \tag{4.4.1}$$

where $\underline{r}$ is the position vector (x, y, z)

t is time

γm is the particle mass

and $\underline{B}$ is the magnetic field vector.

This equation may be rewritten (in component form) in terms of the particle momentum p and the derivatives

$y'(=\frac{dy}{dx})$, z' $(=\frac{dz}{dx})$, $y''(=\frac{d^2y}{dx^2})$ and $z''(=\frac{d^2z}{dx^2})$ as shown in

equations (4.4.2) and (4.4.3).

$$py'' = q(1 + y'^2 + z'^2)^{\frac{1}{2}}(z'B_x + y'z'B_y - (1 + y'^2)B_z) \equiv Y(x) \tag{4.4.2}$$

$$pz'' = q(1 + y'^2 + z'^2)^{\frac{1}{2}}(-y'B_x - z'y'B_z + (1 + z'^2)B_y) \equiv Z(x) \tag{4.4.3}$$

If y' and z' are known then the right hand sides of these equations can be calculated and the resulting functions $Y(x)$ and $Z(x)$ may be described by a cubic spline approximation.* This may then be integrated twice analytically so that the track model becomes:

$$y(x) = y_o + y_o'x + \frac{1}{p}\int\int Y(x)dx^2 \tag{4.4.4}$$

$$z(x) = z_o + z_o'x + \frac{1}{p}\int\int Z(x)dx^2 \;. \tag{4.4.5}$$

The trajectory is described by the five parameters y_o, y_o', z_o, z_o' and $\frac{1}{p}$. In this model the cubic spline description of $Y(x)$

*Note that, before performing track fitting, the coordinate axes were rotated to ensure that Y(x) and Z(x) were single valued functions of x.

and $Z(x)$ is essentially being used to describe the magnetic field in an analytically convenient form. The fit is a quintic spline fit to the trajectory since it has discontinuities at the fifth derivative.

The method relies upon y' and $\ddot{z}'$ being known (at least approximately). These quantities were obtained from an initial prefit to the trajectory using a cubic spline model. The five parameters of the model were fitted, using a least squares fit. The fit was then iterated using the previous iteration to give better estimates of $\ddot{y}'$ and $\dot{z}'$ at the measured points. The fit converged typically within 3 to 4 iterations.

The charged particles lost energy as they traversed the detection chambers. This effect was taken into account in the fit by replacing p by $p_o(1 - e(s))$ where $e(s)$ is the fractional momentum loss as a function of arc length, s. The basic algorithm was changed to:

$$\bar{y}(x) = \bar{y}_o + \dot{y}_o{}' x + \frac{1}{p_o} \int\int (1 + e(s))Y(x)dx^2 \qquad (4.4.6)$$

and similarly for $z(x)$. The fit then proceeded as described previously.

Beam Track Fitting

The techniques used in finding and fitting the beam tracks were different from those used for the outgoing tracks.

Using non-interacting beam track data the momentum (as calculated by the outgoing track technique) was parameterised as a function of the Y positions on some of the beam MWPC's. Since information was not always available from all the MWPC's, several parameterisations were constructed and a hierarchical order of preference for beam momentum reconstruction was set up.

The reconstruction of beam track trajectories in "normally" triggered events was carried out as follows. A list of all "hits" in the Y MWPC's was constructed and each possible combination of these hits was used to try and reconstruct a beam track. The momentum of the track was calculated using the best possible parameterisation in the hierarchical structure and an "ideal" trajectory was then calculated, using this momentum. The ideal trajectory was subtracted from the observed points and a straight line was then fitted to the points. Tracks were rejected if their residuals were too large. For tracks which were not rejected, a full quintic spline fit to the trajectory was performed. Tracks were then rejected if the fit probability was too low or if the track did not pass through C0 and C2. Only events in which the beam track was identified unambiguously were considered further.

4.5 Time of Flight Information

Time of flight information could be obtained from the scintillation counters C3, C2, J1 and J2. The positions of these counters in relation to a typical event are illustrated in Figure 4.5.1. The following times of flight were measured, using these counters:

1) C3 → C2
2) C2 → J1
3) C2 → J2 .

Each of the photomultipliers joined to these counters was connected to a TDC (time to digital converter). The start pulse for all the TDC's was the trigger pulse and the stop pulse was the appropriate

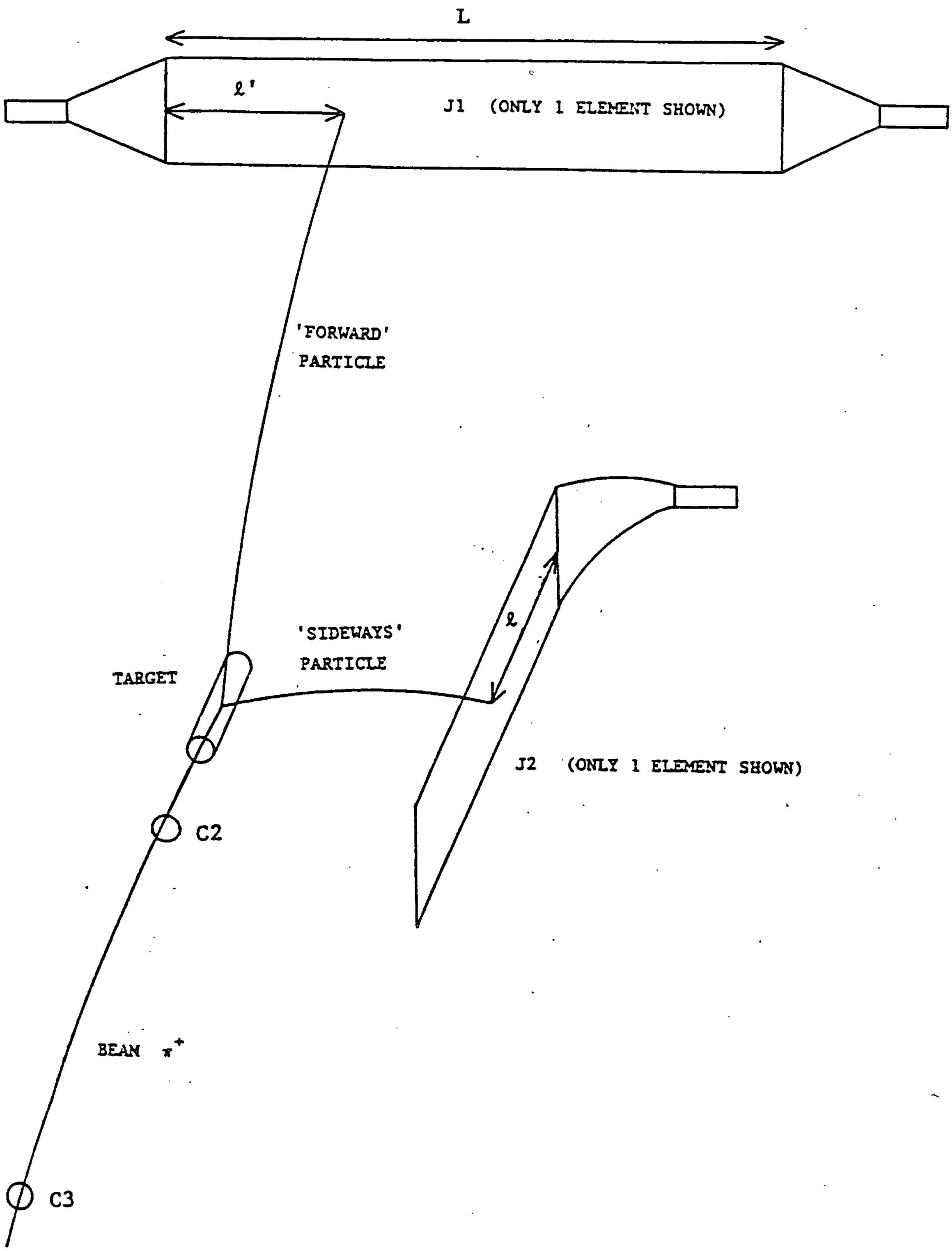

FIGURE 4.5.1: Time of flight counters in relation to a typical event.

counter pulse suitably delayed.

The time of flight from some reference counter, R, say, to a generic counter G is given by :

$$TOF_{R\to G} = TDC_G\,\alpha_G - TDC_R\,\alpha_R - \frac{\ell}{v} - K \qquad (4.5.1)$$

where TDC_i ≡ the TDC reading for counter i

α_i ≡ the conversion factor from TDC counts to time for TDC_i

ℓ ≡ the distance travelled by the light in the generic counter G

v ≡ the velocity of the light in the generic counter G

and K ≡ the delay due to cables and electronics of G's signal relative to R's.

In RMS C2 was used as the reference counter. The term $\frac{\ell}{v}$ in equation (4.5.1) was negligible in the C3 → C2 time of flight and hence it was ignored in this case. In the C2 → J1 measurements two expressions for the time of flight could be obtained since there were two photomultipliers joined to each element of J1. These expressions could be combined to eliminate the dependence on the hit position in the hodoscope (ℓ' in Figure 4.5.1) or alternatively, they could be used to predict ℓ' by elimination of the unknown time of flight.

To calculate times of flight the unknown parameters α, K and v had to be determined for all scintillation counters involved in time of flight measurement. This calibration process was carried out using elastic scattering events (which had been selected on kinematic grounds) in which the particles associated with all tracks were known.

The measured times of flight from an event were used to try and identify particle types. This process was carried out by forming a chi-squared (χ^2) where:-

$$\chi^2 = \frac{(TOF_m - TOF_c)^2}{\sigma_m^2} \qquad (4.5.2)$$

with TOF_m ≡ the measured time of flight

TOF_c ≡ the calculated time of flight assuming a particular particle type (π, K or p)

and σ_m ≡ the counter resolution.

Three such χ^2's were formed for each outgoing track for the three particles π, K and p. The χ^2's were then converted to probabilities.

At high momenta no separation between particle types was possible using TOF information, since the differences between the times of flight for the three particle types were smaller than the counter resolution (e.g. a 1.9 GeV/c forward particle had a TOF of 9.03 ns if it was a π and 10.04 ns if it was a p whereas the counter resolution was $\sim$1.7 ns (FWHM)). At lower momenta some useful information could be obtained (e.g. a 1.25 GeV/c forward particle had a TOF of 9.06 ns if it was a π and 11.3 ns if it was a p).

4.6 Event Fitting

The final stage of event reconstruction is to combine the reconstructed information for each observed track to try and identify the event type and its parameters. Each event had a "primary" vertex where the interaction of the beam π^+ with the target proton occurred. Events could also have "secondary" vertices if any of the outgoing particles decayed. To reconstruct an event fully the position of these vertices, the momenta of the particles at the vertices and the type of particle associated with each track had to be determined.

One method of reconstructing events is to perform a full geometrical and kinematic fit to the event. The parameters to be determined by this technique (P_o, say) are:-

1) The primary vertex coordinates
2) Any intermediate track lengths (to decay vertices)
3) The track parameters (P_x, P_y, P_z or P, $\tan\lambda$, ψ)* at the vertices.

The track reconstruction procedure gave the momenta and positions of the observed tracks at pre-determined reference surfaces. For beam tracks this surface was chosen to be at $x = -125$ mm and for the outgoing tracks it was chosen to be a cylinder just inside the first CYL which recorded a hit. The momenta and positions at these surfaces are the "measured" quantities (P_m, say). A χ^2 may be formed as shown below:-

$$\chi^2 = (P - P_m)^T G(P - P_m) \qquad (4.6.1)$$

where the P are the track parameters to be compared with the measured quantities P_m and G is the inverse error matrix.

The quantities P are functions of the quantities to be determined (P_o). Initial values for the quantities P_o were estimated from the fitted tracks and, by Runge Kutta tracking[12] to the reference planes, the quantities P were determined. Using the method of Lagrange multipliers χ^2 was minimised subject to energy-momentum conservation at the interaction vertices to obtain the best fit to the event.

In using this technique a specific event type had to be assumed initially and then, if the event was topologically compatible with the assumed event type, a fit could be attempted. This procedure led to some events fitting as more than one event type and for such events a choice had to be made based on the probabilities of the fits or on some

*See FIGURE 5.2.9.

external information (such as time of flight information).

This method of event fitting was not used in the reconstruction of elastic scattering events. There were several reasons for this. Firstly elastic scattering events are relatively uncomplicated events in that they have only one vertex (the π^+ lifetime is relatively long and hence π^+ decays were not a problem in this experiment) and only two outgoing particles. This means that such events are highly constrained and thus they can be identified fairly easily without recourse to full geometrical and kinematic fitting. This was not the case with the $K\Sigma$ reaction due to the unobservable Σ^+ and π^o particles and thus the geometrical and kinematic fitting technique was used for such events. Secondly, the geometrical and kinematic fitting technique was very time consuming (approximately 250 milliseconds CPU time per good event) and since an alternative method was available for the elastic events it was used.

In the reconstruction of elastic scattering events each outgoing track was independently intersected with the beam track. This was done by an iterative procedure which used the measured track parameters at the reference surfaces. In each iteration the distances from the track positions on the reference surfaces to the "best" previous vertex position were calculated. (Note that the initial "best" vertex position was taken to be the target centre.) Using fourth order Runge Kutta tracking the tracks were stepped through these distances and then linearly extrapolated to find the point at which the distance between the two tracks was a minimum. This point was then taken as the "best" vertex position and the process was repeated until it converged. When this happened the vertex position and the momenta at the vertex were given by the Runge Kutta algorithm. These quantities were used in the identification of elastic scattering events by the calculation of elastic scattering angular correlations and missing masses. The details of this selection process are discussed in section 5.2.

4.7 Reconstruction Quality

The quality of the reconstructed momenta and trajectories depended ultimately upon the measurement of the positions at which particle trajectories intersected the detection chambers (i.e. upon the measured point precision). This point precision was influenced by several factors, some of which were track dependent and some of which were track independent.

The three main track independent effects were:-

1) Wire spacing
2) The address boundary effect (CYLS 1-4 only)
3) Chamber distortion (CYLS only).

Effect 1) defines the best possible point precision that can be obtained by any given chamber. If it is assumed that particles traversed the chambers normal to the chamber gap then the distribution of hits about the true hit position will be a rectangular distribution orthogonal to the wire direction and of full width d, where d is the wire spacing. The variance of this distribution is given by:-

$$\sigma^2 = \frac{d^2}{12} \quad . \tag{4.7.1}$$

Knowledge of the wire spacings and angles for all chambers allowed σ_H^2 and $\sigma_V{}^2$ (the horizontal and vertical variances) to be calculated for each chamber type. The results of these calculations are shown in Table 4.7.1.

Effect 2) is due to the fact that, for the CYLS, it was noticed

Chamber Type	d(mm)	Wire Angles	σ_H(mm)	σ_v (mm)
CYLS	1.0	$(0^\circ, \pm 14^\circ)$	0.29	1.63
SIDES	1.5	$(0^\circ, \pm 14^\circ)$	0.43	2.45
FLATS	1.0	$(-15^\circ, +15^\circ)$	0.20	0.82
MWPCS	1.0	0° or 90°	0.29	0.29

TABLE 4.7.1: Point variances due to chamber construction.

that certain regions of the chambers were inefficient. The spark chambers were read out in groups of 32 wires (known as addresses) and the inefficient regions were at the edges of addresses (hence the name "address boundary effect"). The problem was solved during setting up for the outer cylinders by additional screening of the readout cables. However, CYLS 1-4 could not be reached without dismantling the whole system. Thus for the first four CYLS the problem had to be solved at the analysis stage. Although this was an efficiency problem its effect was to shift sparks near the address boundary rather than lose them altogether. This was due to the fact that a spark set off a cluster of wires and the inefficiency near the address boundary led to the "loss" of wires from one side of the cluster, thus leading to a displacement of the cluster centre. This problem was resolved by finding out how much, on average, the central positions of clusters were shifted as a function of spark position, using straight track data. The shift near the boundary was found to be ~ 0.5 mm. A correction was applied to cluster positions to correct for this effect based on the results obtained from the straight track data.

Effect 3) was noticed when straight tracks were being used to determine the chamber positions. Large discrepancies were found in the cylindrical chambers as a function of angle around the chambers. These discrepancies were consistent at several momenta and this supported the theory that they were inherent in the chamber construction. This effect was also corrected for by moving cluster positions using the discrepancies measured by the straight track data.

The four main track dependent effects were:-

1) The track angle effect.
2) The $\underline{E} \times \underline{B}$ effect.
3) The cluster size effect.
4) Multiple Coulomb scattering.

The track angle effect was due to the fact that tracks did not, in general, traverse the detection chambers normally to the chamber plane. This meant that, in the spark chambers, some of the ionisation from the track was swept away by the clearing field before the chambers fired and this resulted in a displacement of the sparks as illustrated in Figure 4.7.1.

The $\underline{E} \times \underline{B}$ effect was a similar type of effect to the track angle effect. The track ionisation moved perpendicular to the wire planes under the influence of the clearing field initially and then in the opposite direction as the chamber HT's began to build up. Due to the vertical magnetic field, a Lorentz force was induced which caused the ionisation to acquire a velocity component parallel to the wire planes and hence produced a spark displacement. The Lorentz force was in opposite directions under the influence of the clearing

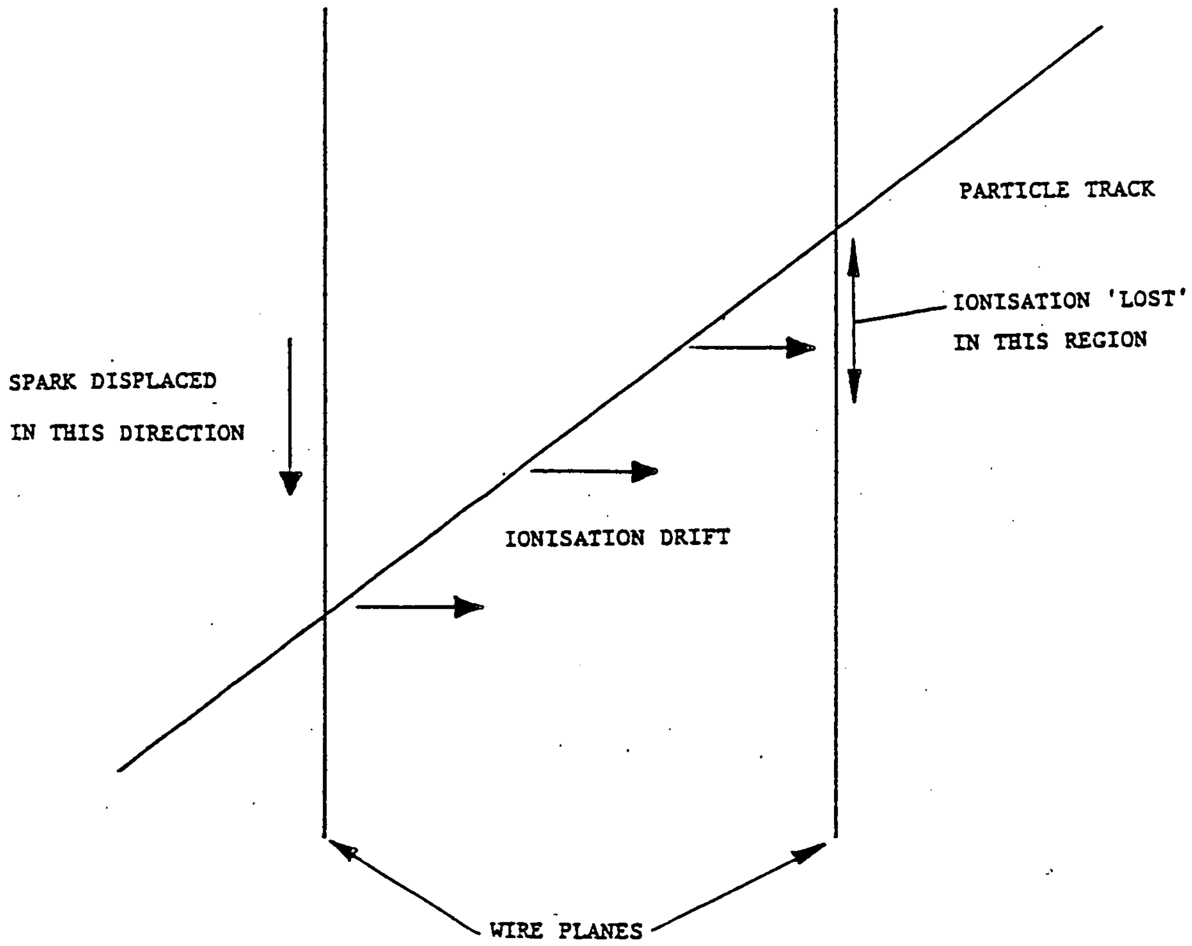

FIGURE 4.7.1: Displacement of sparks due to the track angle effect.

field and the chamber HT and thus some cancellation occurred. The $\underline{E} \times \underline{B}$ effect and the track angle effect were dependent upon many factors (e.g. timing, chamber HT's, HT pulse shapes, clearing fields, etc.) and hence it was impossible to calculate them exactly at all stages of the experiment. These effects were parameterised empirically and fitted to. The fitting process was re-calculated every 25,000 events. This gave a good set of constants provided conditions were slowly varying. These constants were used to shift the observed spark positions to correct for the track angle and $\underline{E} \times \underline{B}$ effects.

The cluster size effect stemmed from the fact that very large and very small cluster sizes gave larger residuals than medium sized clusters. This was believed to be due to variations in pulse shape with cluster size coupled with variations in the thresholds on the spark chamber wires. The effect was taken into account by increasing the point error on very large and very small clusters.

The multiple scattering of particles by many independent small angle Coulomb scatters with the nuclei in the detection chambers also affected the point precision. This was taken account of by adding a term to the error matrix, based upon the expected multiple scattering from "previous" chambers, before performing the track fitting procedure.

Thus the final point variance was calculated by combining three components:-

1) The intrinsic error due to chamber construction.
2) The multiple scattering error.
3) "Jitter" in the $\underline{E} \times \underline{B}$ and related effects.

Typically the horizontal point error was ~ 0.8 mm and the vertical point error was ~ 2.9 mm for the spark chambers. The point errors on the beam MWPC's were dominated by multiple Coulomb scattering due to the wide spacing of the MWPC's and the presence of the beam scintillation counters. Typically the horizontal and vertical point errors for these chambers were ~ 2 mm.

The track fitting procedures transformed the point errors to errors on the fitted quantities - the momentum p, the track direction parameters $\tan\lambda$ and ψ and the position at the reference planes Z and θ or Y. Typical values for these errors for forward tracks, sideways tracks and beam tracks are shown in Table 4.7.2.

Track Type	$\Delta p/p$	$\Delta\tan\lambda$	$\Delta\psi$	ΔZ(mm)	$\Delta\theta$	ΔY(mm)
BEAM	0.002	0.001	0.001	0.45	-	0.4 mm
FORWARD	0.01	0.003	0.003	1.2	0.002	-
SIDEWAYS	0.03	0.007	0.006	1.6	0.002	-

TABLE 4.7.2: Typical errors on the fitted track parameters.

It can be seen from this table that the beam tracks were more accurately measured than the outgoing tracks. This arose mainly from the fact that the beam momentum was measured very accurately by the Y hit position on the furthest upstream MWPC module. It can also be seen that the forward tracks were more accurately measured than the sideway tracks. This was due to the fact that there were more detection chambers spread over a larger distance in the forward direction as compared to the sideways direction.

The fitted quantities were used to calculate interaction vertices and momenta at these vertices. Missing masses, at the vertices, were then calculated and used, as the primary selection procedure, in the selection of elastic scattering events. Typically the errors on the missing masses were $\sim 0.03\ (\mathrm{GeV}/c^2)^2$ on the missing mass squared to the forward track and $\sim 0.1\ (\mathrm{GeV}/c^2)^2$ on the missing mass squared to the sideways track.

CHAPTER 5

CALCULATION OF DIFFERENTIAL CROSS SECTIONS

5.1 Introduction

In this chapter the method used to calculate the elastic scattering differential cross section, at each beam momentum, is described. This process required the selection of elastic events and the construction of a $\cos\theta^*$ distribution for these events. The selected events were arranged into $\cos\theta^*$ bins and the cross section in each bin was calculated independently using formula (5.1.1).

$$\left(\frac{d\sigma}{d\Omega}\right)_i = N \left(\frac{D_i}{A_i}\right) \qquad (5.1.1)$$

where $\left(\frac{d\sigma}{d\Omega}\right)_i$ is the differential cross section in the i-th $\cos\theta^*$ bin.

N is an overall normalisation factor which is independent of $\cos\theta^*$.

D_i is the number of selected data events in the i-th $\cos\theta^*$ bin.

and A_i is the experimental acceptance in the i-th $\cos\theta^*$ bin.

Thus the calculation of differential cross sections split naturally into three parts -

1) Event selection and $\cos\theta^*$ distribution calculation

2) Acceptance calculation

3) Normalisation calculation.

These three processes are described in sections 5.2, 5.3 and 5.4 respectively. Section 5.5 discusses the calculation of errors on the differential cross sections.

5.2 Event Selection and $\cos\theta^*$ Distribution Calculation

Introduction

The reconstructed data consisted of events from the various kinematically allowed channels (e.g. $\pi^+p \rightarrow \pi^+p$; $\pi^+p \rightarrow K^+\Sigma^+$; $\pi^+p \rightarrow \pi^+p\,\pi^o$; $\pi^+p \rightarrow n\,\pi^+\pi^+$) and background events which occurred from various sources (e.g. interactions in the target walls, interactions in the particle detectors, stray cosmic rays etc.). The first step in the construction of a differential cross section was the isolation of π^+p elastic scattering events and the construction of their $\cos\theta^*$ distribution. A set of cuts were developed to isolate elastic scattering events. These cuts were largely momentum independent since the magnetic field was scaled with beam momentum to give similar event topologies at all momenta. The plots shown in this chapter were taken from a sample beam momentum (2.10 GeV/c) unless otherwise indicated.

Elastic Event Configuration

Every elastic scattering event can be characterised by two angles - $\cos\theta^*$ (the cosine of the centre of mass scattering angle) and ϕ (the azimuthal angle which is a measure of the orientation of the scattering plane around the beam direction). These angles are illustrated, relative to the RMS coordinate system, in Figure 5.2.1. Elastic events occur over the full angular range (i.e. from $\cos\theta^* = -1.0$ to $\cos\theta^* = +1.0$ and from $\phi = -\pi$ to $\phi = +\pi$). However the elastic scattering events observed in this experiment were confined to a limited angular range by the experimental apparatus. Figure 5.2.2 shows the angular regions in which elastic events were detected by this experiment at a beam momentum of 2.29 GeV/c. The four regions shown in this figure were

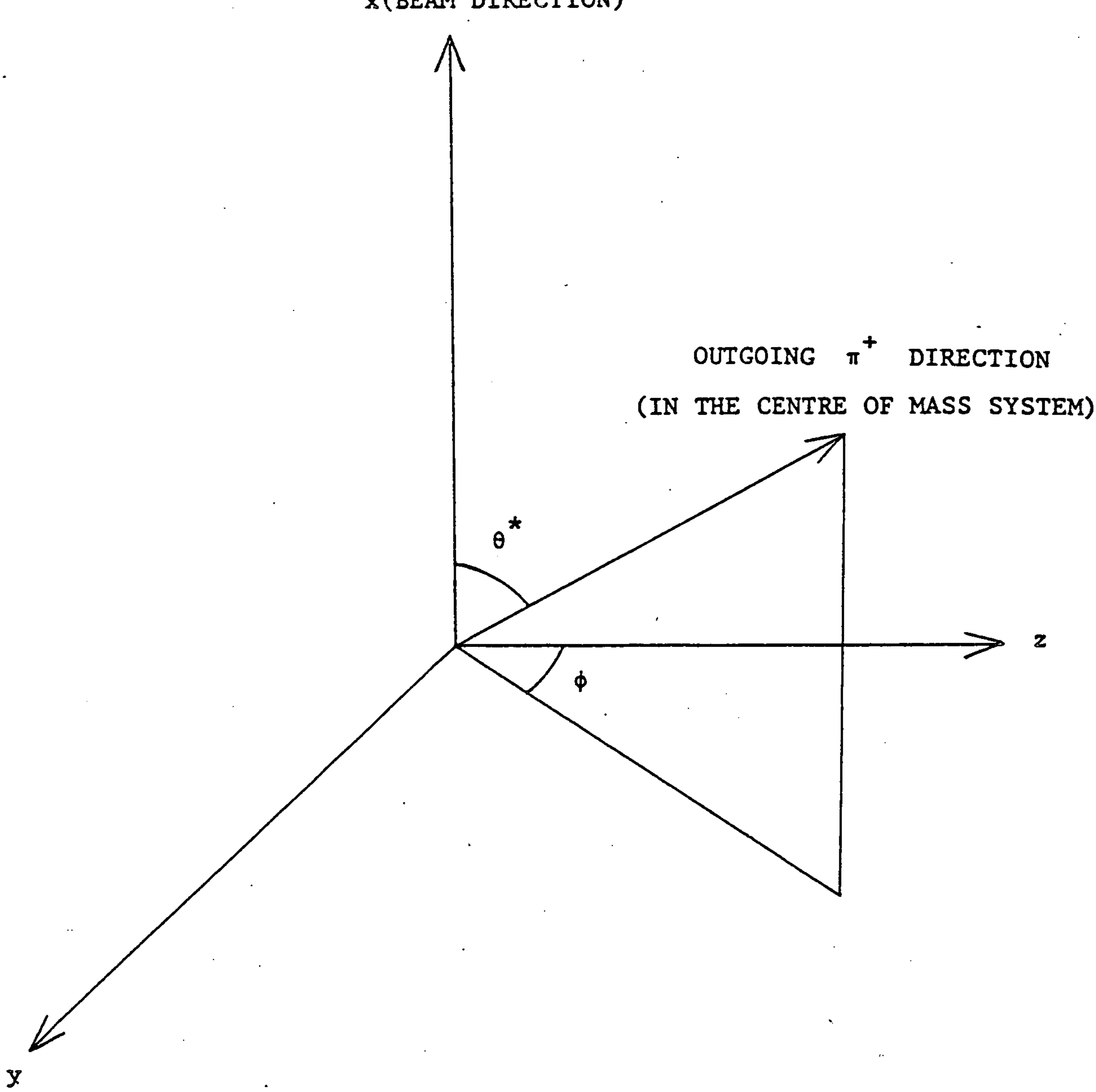

<u>FIGURE 5.2.1</u>: θ^* and ϕ relative to the RMS coordinate system.

observed at all momenta although their limits were momentum dependent. Figure 5.2.3 shows the approximate configuration of the events (in each angular region of Figure 5.2.2) relative to the RMS coordinate system. The angular regions within which elastic events were detected in this experiment were defined by the trigger chambers. In particular the scintillation counters C6, C7 and J1 defined the angular ranges.

The ϕ ranges were defined by the heights of the scintillation counters C6, C7 and J1. Two ϕ ranges were "picked out" by these counters corresponding to the proton going to positive $Y(\phi < 0.0)$ and the π^+ going to positive $Y(\phi > 0.0)$. Each of the two ϕ regions was subdivided into two $\cos\theta^*$ regions with limits again defined by the counters C6, C7 and J1. The configuration of events, at the extremes of each $\cos\theta^*$ region, in relation to these counters is shown in Figure 5.2.4.

Configuration (1) type events were limited in $\cos\theta^*$ by the forward proton missing J1 to give an upper $\cos\theta^*$ limit and by the sideways π^+ missing C6 to give a lower $\cos\theta^*$ limit.

Configuration (2) type events were limited in $\cos\theta^*$ by the forward π^+ missing J1 to give a lower limit and by the sideways proton missing C7 to give an upper limit. Many configuration (2) type events were vetoed by the downstream Cerenkov counter V2 (Note that the effect of V2 is not shown in Figure 5.2.2). An appreciable number of configuration (2) type elastic events were observed only at the extreme $\cos\theta^*$ limits of region (2). At the high $\cos\theta^*$ limit this was due to the large forward peak in the elastic cross section coupled with the fact that V2 was not 100% efficient. At the low $\cos\theta^*$ limit this was due to the fact that the forward π^+ was absorbed by the iron magnet yoke (see Figure 5.2.4) and thus did not reach V2 to provide a veto signal.

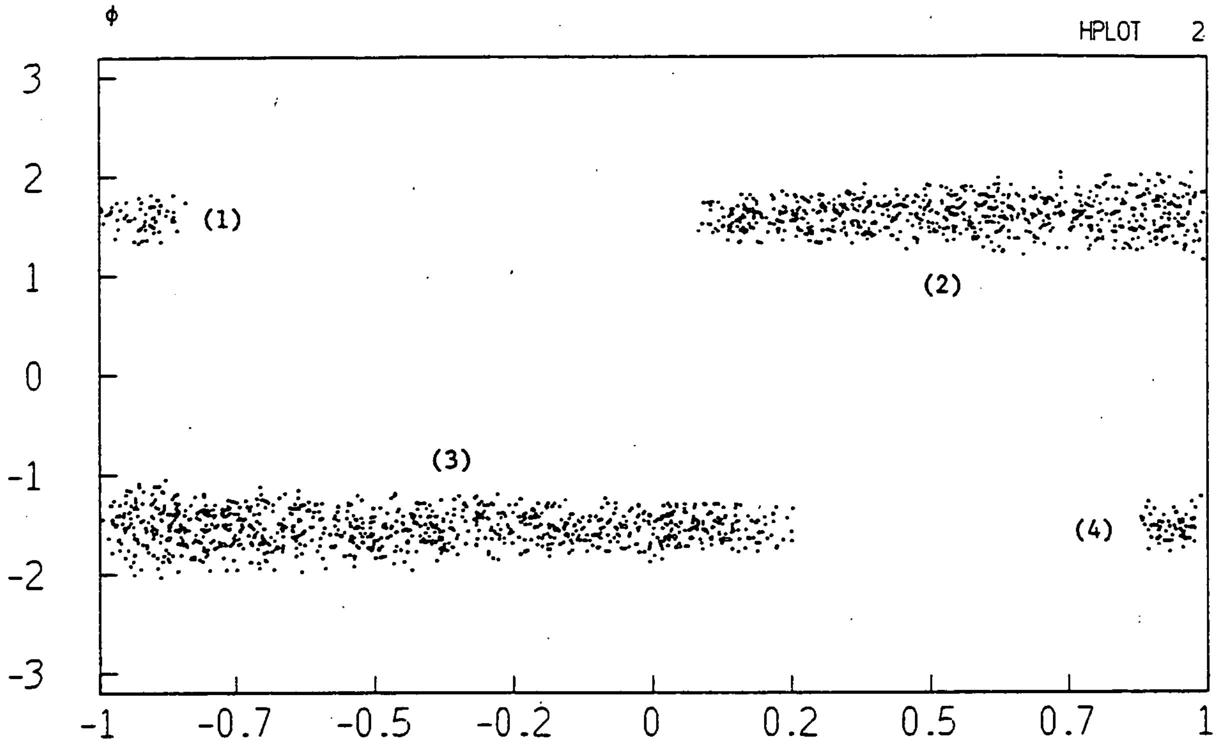

FIGURE 5.2.2: cos θ^* versus ϕ for triggered Monte Carlo events at 2.29 GeV/c.

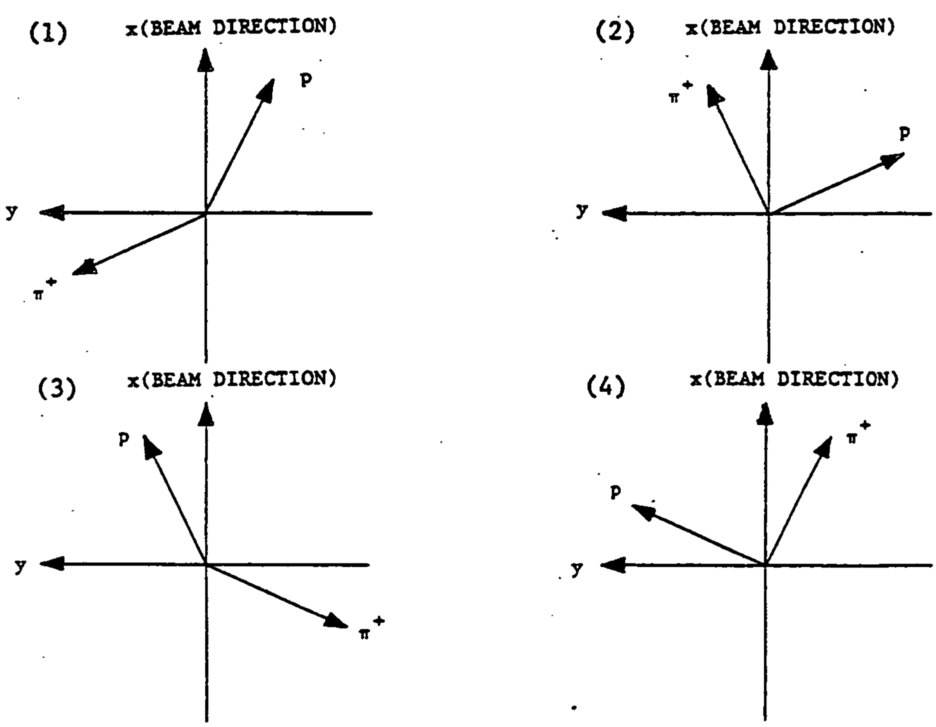

FIGURE 5.2.3: Approximate configuration of elastic events observed in this experiment relative to the RMS coordinate system.

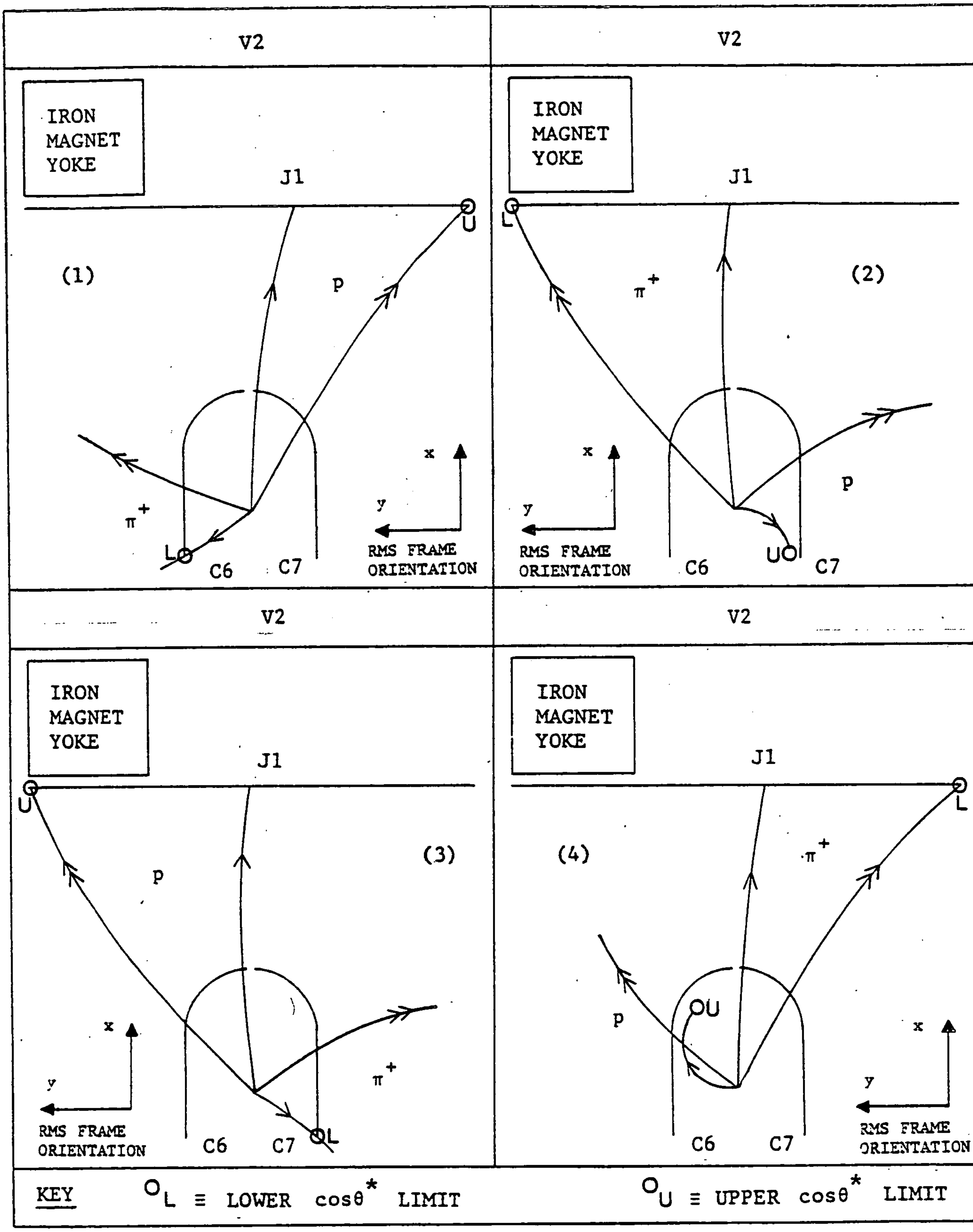

FIGURE 5.2.4: Configuration of elastic events relative to the apparatus. Note that, for the purposes of clarity, many detection chambers have been omitted from this figure and the relative dimensions of the counters which are shown have been greatly distorted (in particular the dimensions of C6 and C7 have been greatly exaggerated relative to J1).

Configuration (3) type events were limited in $\cos\theta^*$ by the forward proton missing J1 to give an upper limit and by the sideways π^+ missing C7 to give a lower limit.

Configuration (4) type events were limited in $\cos\theta^*$ by the forward π^+ missing J1 to give a lower limit and by the sideways proton missing C6 to give an upper limit. As in the case of configuration (2) type events many configuration (4) type events were vetoed by the Cerenkov counter V2. An appreciable number of configuration (4) type events were observed only at the upper $\cos\theta^*$ limit of region (4) due to the large forward elastic peak and the inefficiency of V2.

Configuration (1) and (4) type events covered rather limited $\cos\theta^*$ ranges. In addition the calculation of a differential cross-section for events of type (2) and (4) was very difficult since the effect of the Cerenkov counter V2 would have had to be known to a high degree of accuracy. For these reasons it was decided to reconstruct the elastic differential cross section only for configuration (3) type events.

Outline of Selection Method

The aim of the event selection procedure was to isolate those elastic scattering events in which the proton travelled to positive Y and hit the hodoscope J1 and the π^+ travelled to negative Y (i.e. configuration (3) type events). Such events have two outgoing charged particles. Over most of the angular range both of the outgoing particles passed through sufficient detection chambers for track reconstruction to be possible. However in the extreme backward region the slow sideways π^+ did not pass through the spark chambers and only the fast forward proton track could be reconstructed. Also forward tracks were more accurately measured than sideway tracks (see section

4.7). For these reasons it was decided to try and isolate configuration (3) type events by searching for the forward proton track and only using sideway tracks to reject events which were definitely inconsistent with the "backward" elastic hypothesis.

Event Pre-Selection

Backward elastic scattering candidates were selected from the full data sample using the missing mass technique.

The incoming beam particle was taken to be a π^+ and the scatter was assumed to be off a free proton. Then, under the hypothesis that the outgoing forward particle was a proton, the missing energy and momentum, which must have been carried away from the interaction by other particles, could be calculated. These quantities were then used to calculate an effective missing mass for the "unobserved" particles.

Due to details of the processing technique a saving in computing time could be achieved by making an initial pre-selection of backward elastic scattering events based on these missing masses. Only events with a forward track (i.e. a track with a "hit" in one of the two furthest downstream FLATS) whose missing mass squared, when assumed to be a proton, was within 6 standard deviations of the π^+ mass squared were selected. To reduce the number of events satisfying this condition due to poor event measurement a cut was also applied to the error on the missing mass squared. Events with an error on the missing mass squared to the forward track greater than 0.25 $(GeV/c^2)^2$ were rejected. This cut was safe since the width of the elastic missing mass squared peak was ~ 0.04 $(GeV/c^2)^2$.

Time of Flight Weight

In the electronic logic of the downstream hodoscope (J1) a time of flight cut was applied to reject forward tracks with very long times of flight. This was thought to have no effect on real elastic events, however it was later discovered that this cut did reject some backward elastic events at the high end of the $\cos\theta^*$ range ($\cos^* \gtrsim -0.3$). This occurred because the J1 - R3 coincidence had been set up using beam pions which had much shorter times of flight than the protons from high $\cos\theta^*$ elastic events.

In order to correct for this effect a time of flight weight was calculated for Monte Carlo events and a correction applied in the acceptance calculation. To calculate the weight real elastic events were used to obtain the distribution of the measured time of flight minus the calculated (from the tracks momentum and length) time of flight. For events whose calculated time of flight (T_c) was close to the cut value (T_{cut}) the origin of this distribution was re-centred on T_c. The probability (p) of the events measured time of flight exceeding the cut value T_{cut} (thus leading to the loss of the event) could then be calculated by taking the ratio of the hatched area in Figure 5.2.5 to the total area under the distribution. The time of flight weight was then defined as the inverse of the probability of observing the event -

$$TOF_{weight} = \frac{1.0}{(1.0 - p)} \quad . \qquad (5.2.1)$$

Time of flight weights were calculated for real data events and also for the Monte Carlo events used in the acceptance calculation. A correction factor (of $1.0/TOF_{weight}$) was applied only to the Monte Carlo events since the real data already had the effect applied by the J1 electronics.

Events with very high time of flight weights (corresponding to very

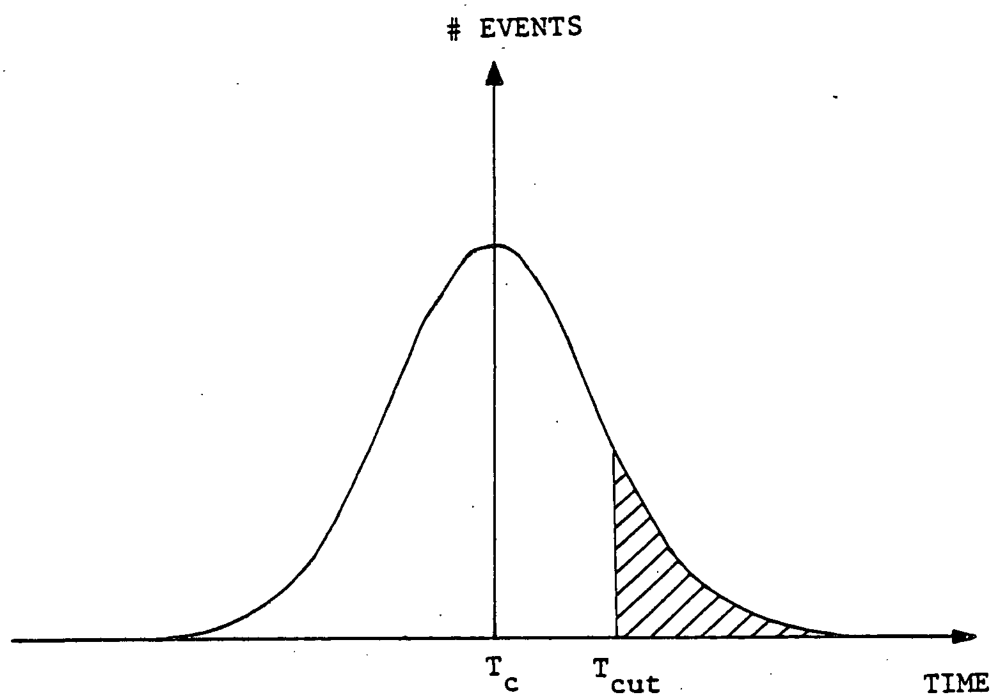

FIGURE 5.2.5: Measured minus calculated time of flight distribution (re-centred on T_c).

low probabilities of being observed) could have caused the introduction of large errors into the acceptance calculation. To prevent this events with a time of flight weight greater than 4.0 (corresponding to a probability of being observed less than 0.25) were rejected. In order to maintain comparability between the data and the Monte Carlo this cut was applied to both.

Missing Mass Technique

Figure 5.2.6 shows the missing mass squared to the forward track treated as a proton for all forward tracks in a raw data sample. There is a peak in this plot in the region of the π^+ mass squared due to the presence of backward elastic scattering events. This peak is shifted slightly from the π^+ mass squared due to small systematic errors in the missing mass calculation (due to such things as systematics in the vertex reconstruction and magnetic field reconstruction). Another, somewhat larger peak is also visible at a higher missing mass squared. This peak is due to the presence of forward elastic events which the downstream Cerenkov V2 did not veto. For these events the forward particle was a π^+ and by treating it as a proton when calculating the missing mass squared the second peak was obtained. This peak has a long tail which extends under the backward elastic peak. The nature of this "contamination" was confirmed by plotting the missing mass squared to the forward particle under the assumption that it was a π^+. When this was done a peak was obtained in the region of the proton mass squared (see Figure 5.2.7). In both these missing mass squared plots there is also a background from other types of event.

It would have been possible to select backward elastic scattering events simply by placing a cut on the missing mass squared to the forward particle treated as a proton. However the sample of events selected

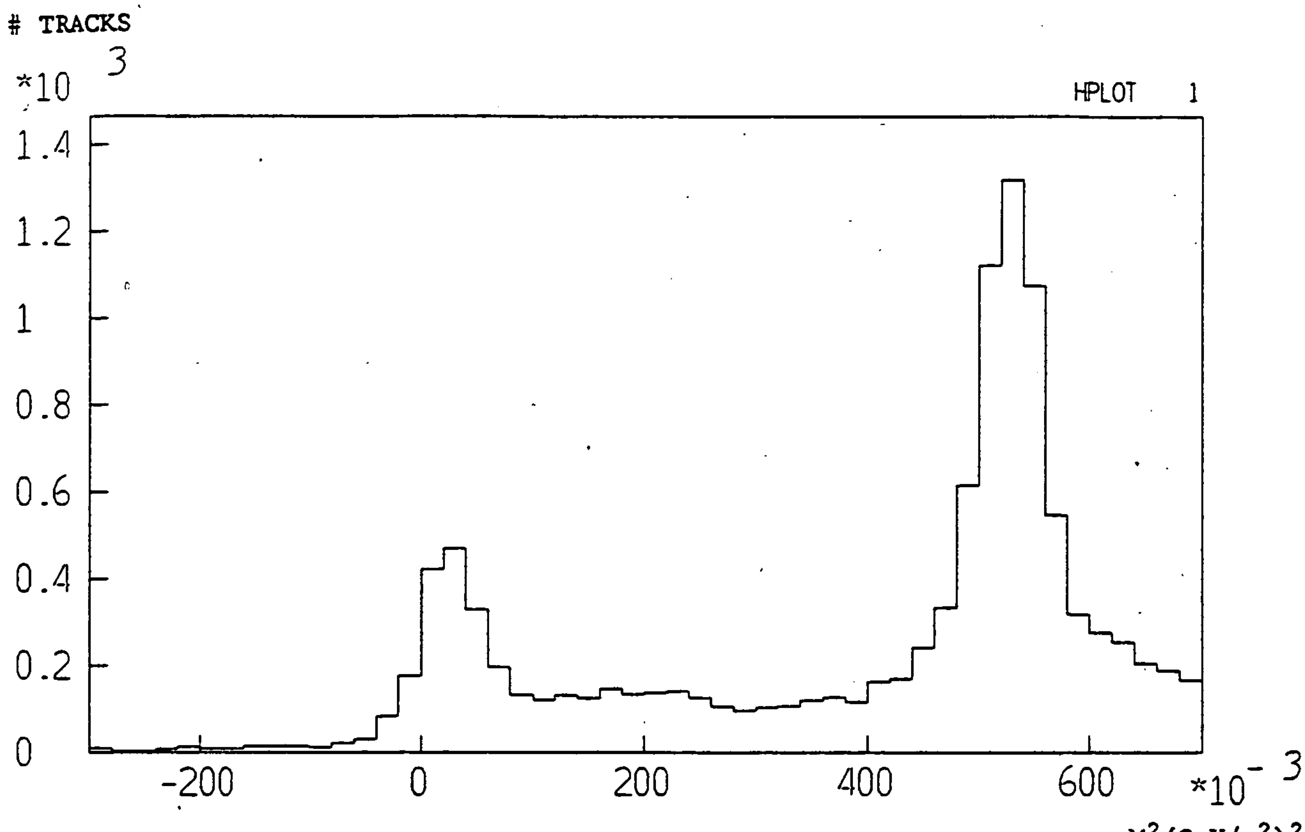

FIGURE 5.2.6: Missing mass squared to the forward track treated as a proton for all forward tracks.

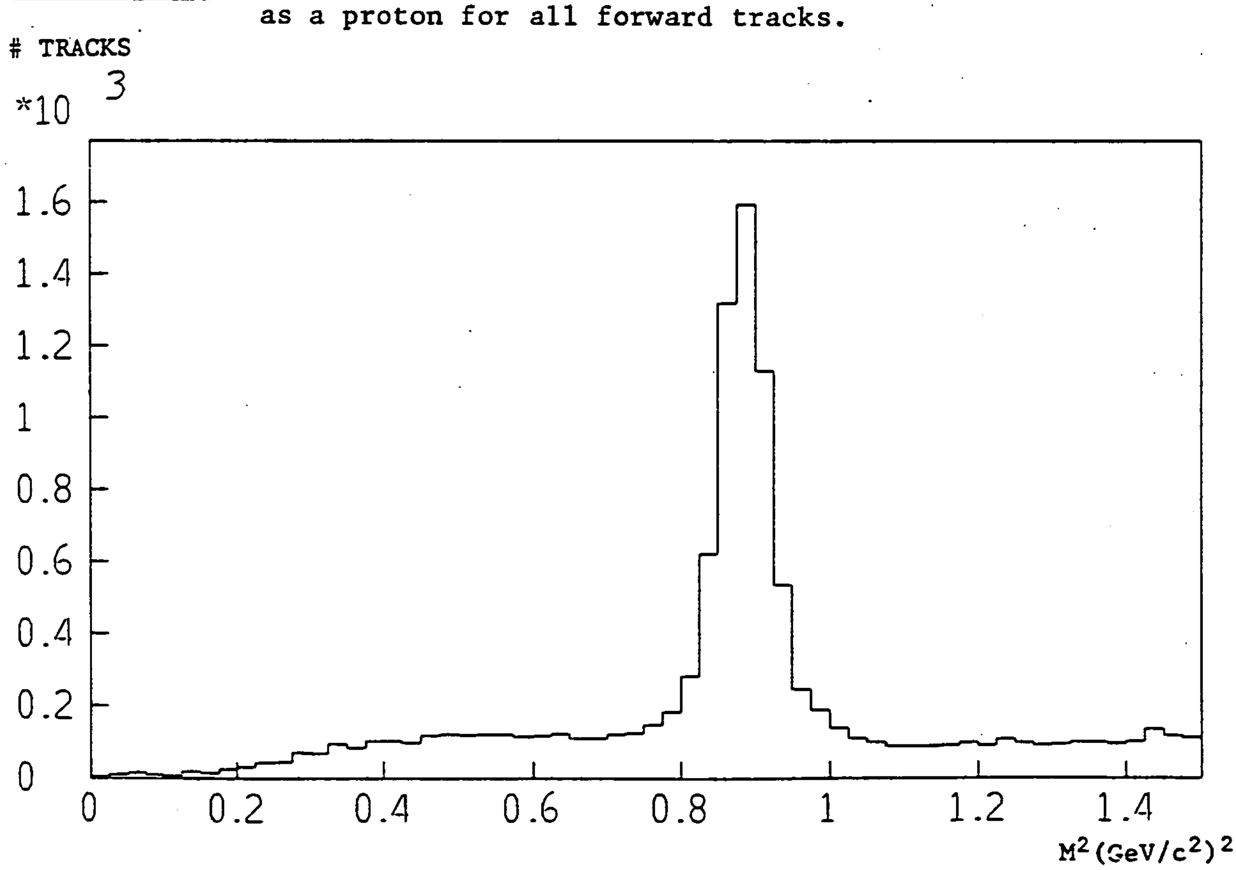

FIGURE 5.2.7: Missing mass squared to the forward track treated as a π^+ for all forward tracks.

by this means would have contained not only real backward elastic events but also background contamination. Thus other cuts were developed to reduce this contamination to a minimum before applying a missing mass squared cut.

Target Position Cut

One of the first criteria for an elastic scattering event is that the incident beam π^+ must scatter off a free proton. In this experiment this essentially meant that the interaction vertex had to lie within the hydrogen target which was positioned between $x = -80$ mm and $x = +70$ mm with a radius of 12.5 mm.

The intersection point of the forward track with the beam track was taken as a measure of the interaction vertex position. The x-coordinate of this point and its radial distance from the target axis, R, are shown in Figure 5.2.8 for both real data and Monte Carlo events. It can be seen from this figure that most real data vertices lie radially in or near the target. However the real data x distribution shows the presence of two clusters of interaction vertices downstream from the target at $x \approx +85$ mm and $x \approx +120$ mm. The small cluster at $x \approx +85$ mm is due to interactions in the thin mylar window at the downstream end of the target vessel and the larger cluster at $x \approx +120$ mm is due to interactions in the scintillation counters C6 and C7 which surrounded the target. It can also be seen that the events in the target region overflow the absolute edges of the target to some extent. There are two reasons for this. Firstly there is the effect of interactions within the target walls and secondly there is the effect of the vertex position resolution.

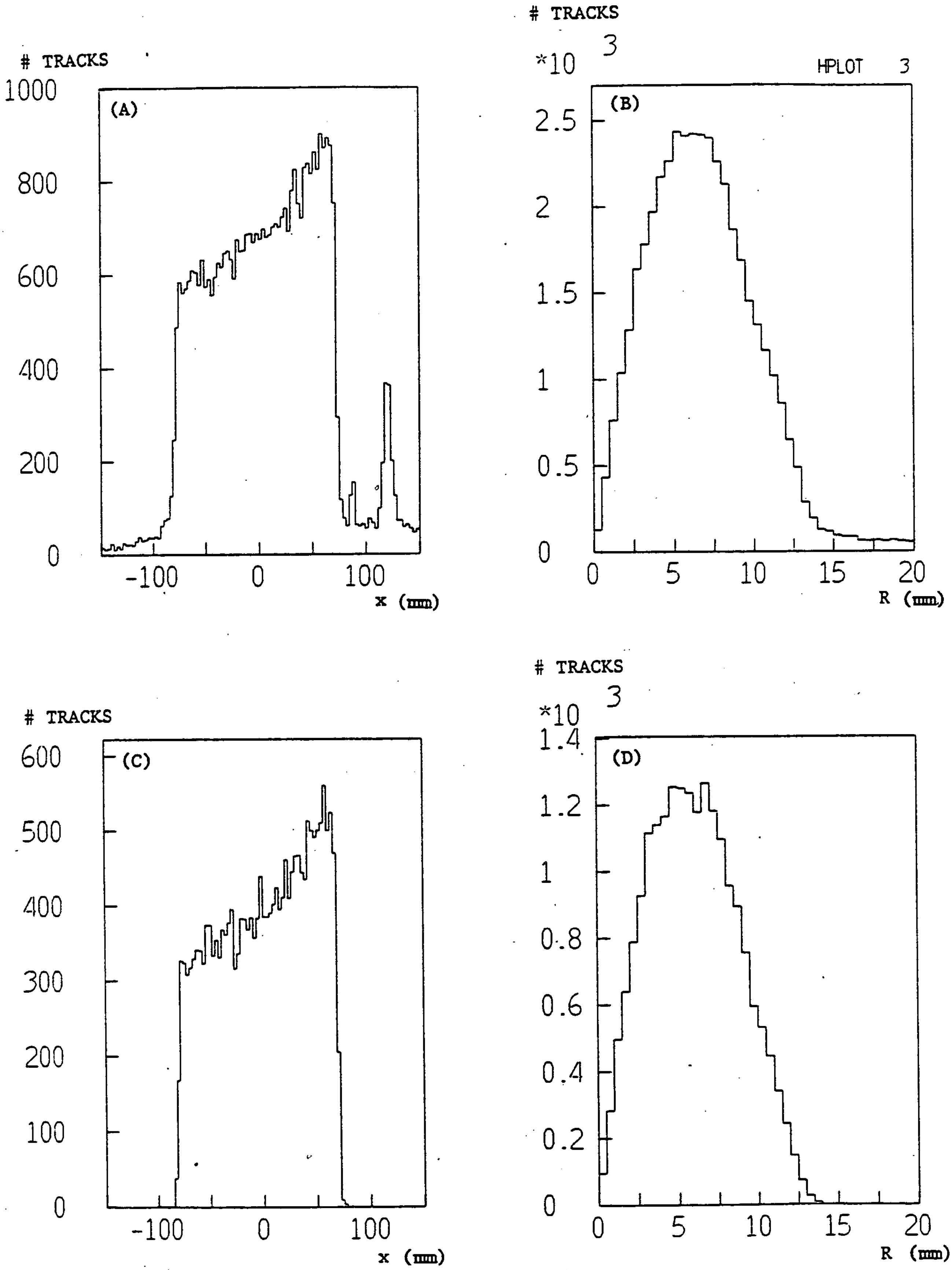

FIGURE 5.2.8: Interaction vertex parameters. Plots (A) and (B) show x and R for real data events and plots (C) and (D) show the corresponding quantities for Monte Carlo events.

A target position cut was applied to the data. This cut only retained events which had a forward track whose x and R variables satisfied -

$$-95 \text{ mm} < x < 90 \text{ mm}$$

$$R < 17.5 \text{ mm}$$

This cut had a negligible effect on the Monte Carlo events and it rejected real data events with interactions in the scintillation counters C6 and C7.

Proton Direction Cut

The spherical polar angles of the forward track at the interaction vertex (relative to the RMS coordinate system) were calculated by the analysis program. These angles are illustrated in Figure 5.2.9. Figure 5.2.10 shows $\tan\lambda$ versus ψ for real data events and for triggered Monte Carlo events. It can be seen from these plots that the data events cover a wider range in ψ than would be expected for backward elastic scattering events. This suggested that a ψ cut could be applied to remove some of the background events. A cut was also applied on $\tan\lambda$ although its effect was much smaller than the ψ cut. These cuts rejected events which had no track satisfying -

$$|\tan\lambda| < 0.18 \quad \text{and} \quad |\psi - 0.4| < 0.36 \quad .$$

This rejected configuration (1) and configuration (4) type events.

Second Track Cuts

To reduce the background further the sideways track information was used.

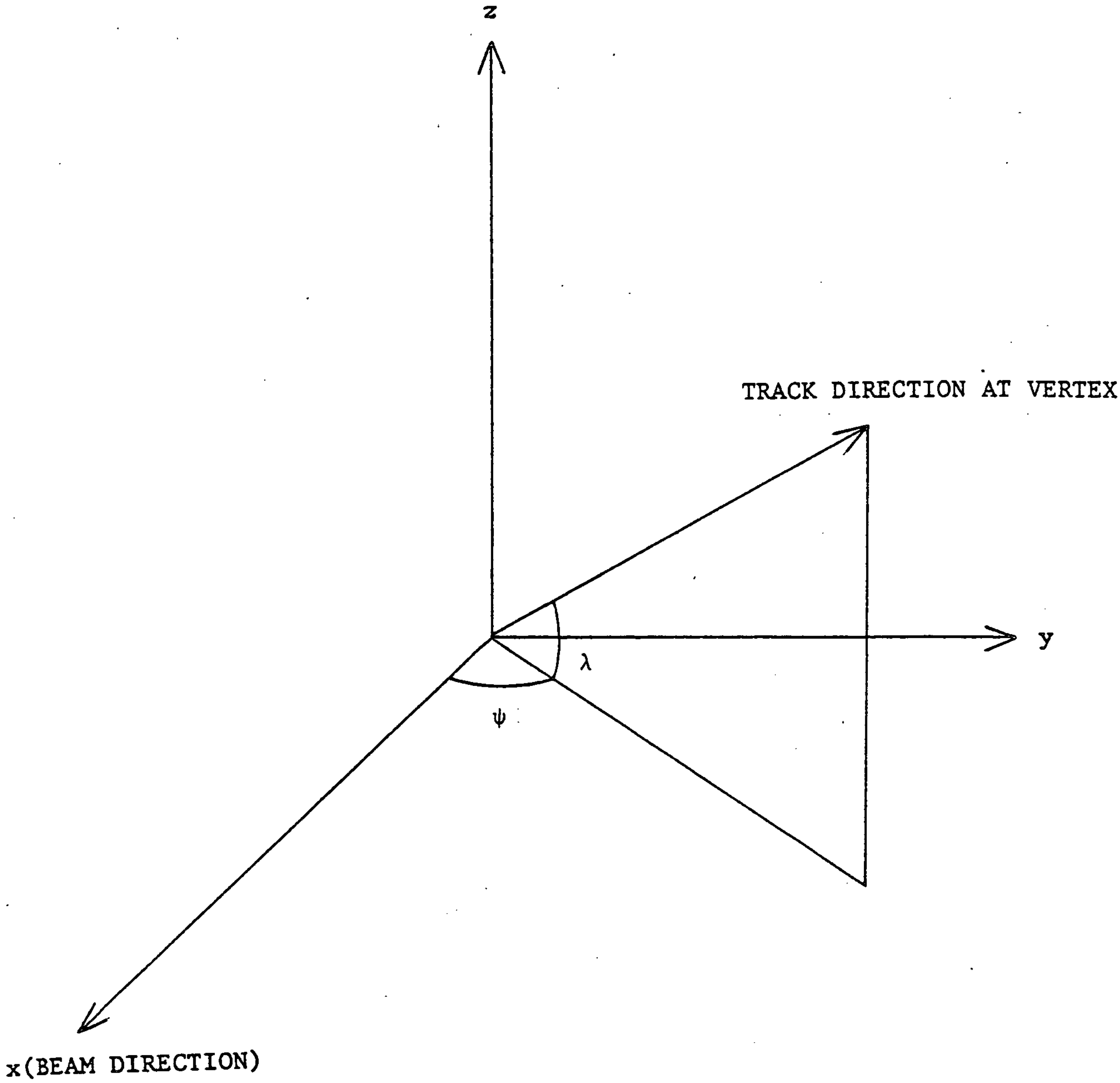

FIGURE 5.2.9: Track angle parameters λ and ψ relative to the RMS coordinate system.

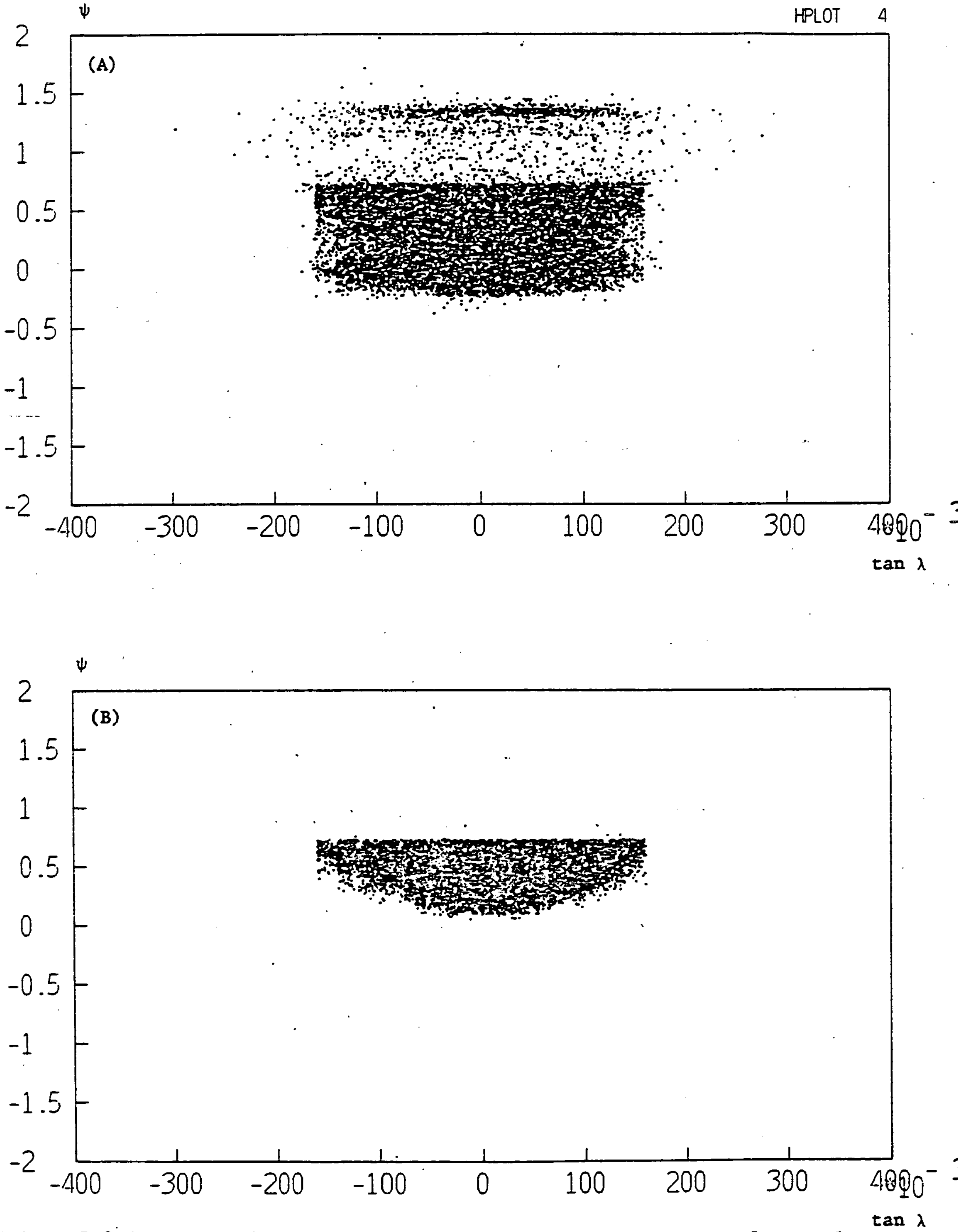

FIGURE 5.2.10: Track angle parameters - tanλ versus ψ - for real data events (plot (A)) and for Monte Carlo events (plot (B)).

The first stage in this process was to split the data into events with a second track which was associated with the forward track and those with no associated second track. This was achieved by comparison of the intersection points of both tracks with the beam and also their closing distances from the beam. This ensured that both tracks came from the same interaction point and also that this interaction point was close to the incident beam trajectory.

GKIN fitted backward elastic events were used to help define a quantity V to cut on as follows -

$$V = \frac{|X_D - B_X|}{A_x} + \frac{|Y_D - B_Y|}{A_y} + \frac{|Z_D - B_Z|}{A_z} \qquad (5.2.2)$$

where X_D, Y_D, Z_D ≡ the differences in x, y and z coordinates between the intersection points of the forward and sideway tracks with the beam track and the A's and B's were constants determined from the widths and central positions of the X_D, Y_D and Z_D distributions plotted for GKIN fitted backward elastics.

$$\text{Thus} \qquad A_X = \sigma_{X_D} \qquad (5.2.3)$$

$$\text{and} \qquad B_X = \overline{X}_D \qquad (5.2.4)$$

and analogously for A_Y, B_Y and A_Z, B_Z. The values of these constants are shown in Table (5.2.1).

V and $\frac{d}{2}$ (where $\frac{d}{2}$ is the closing distance to the beam track) for forward and sideway tracks are shown for both real data and Monte Carlo events in Figures 5.2.11 and 5.2.12. Events were defined as having an associated second track if $V \leq 10.0$ and $\frac{d}{2} \leq 7.5$ mm for both tracks.

For those events with an associated second track two quantities - coplanarity C and opening angle difference $\Delta\theta$ - were defined as follows. Firstly a set of axes was defined using the momentum of the

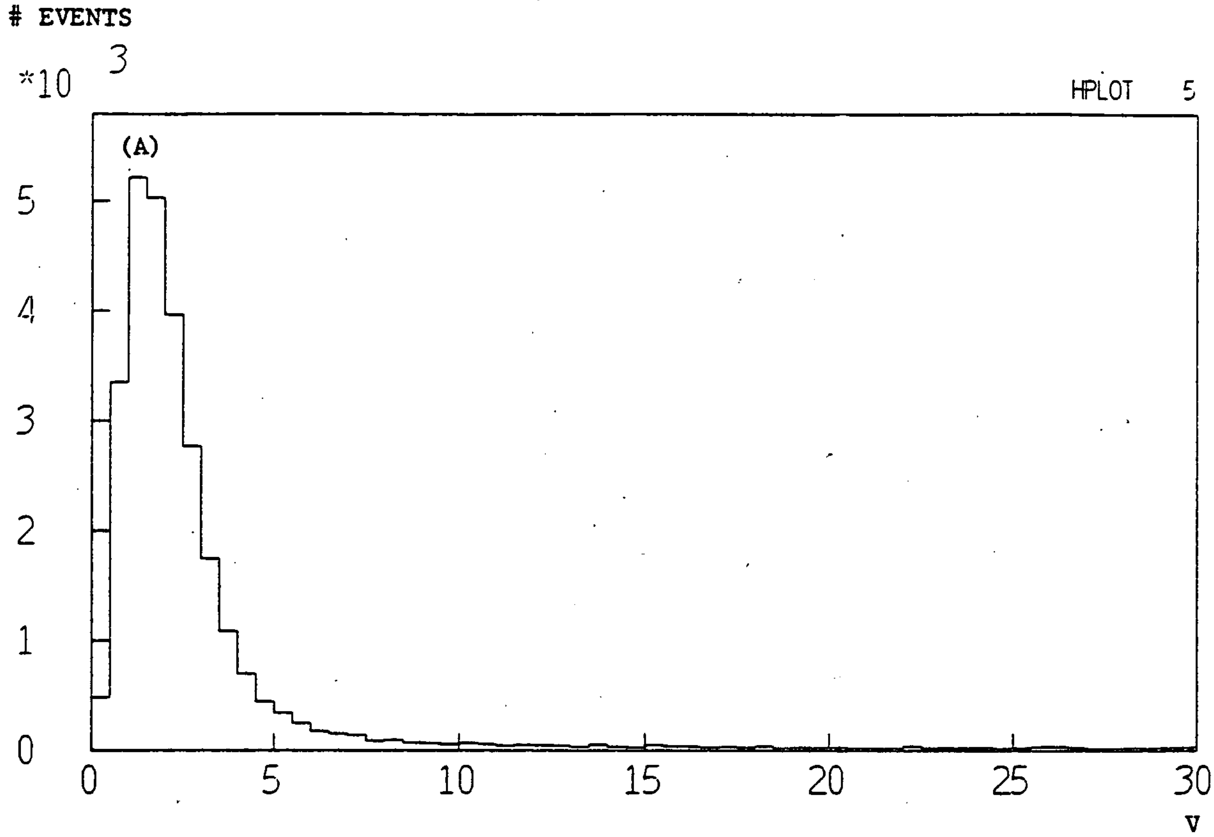

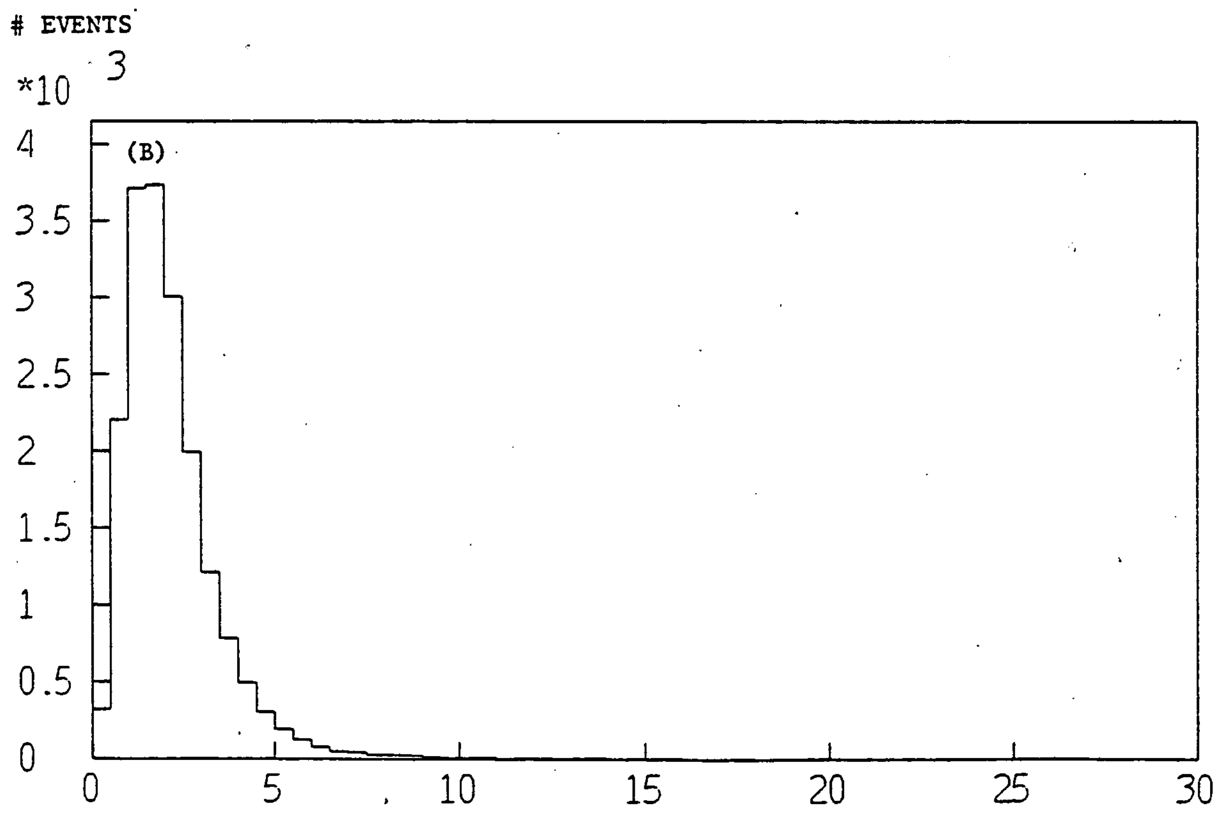

FIGURE 5.2.11: The vertex parameter, V, for real data events (plot (A)) and for Monte Carlo events (plot (B)).

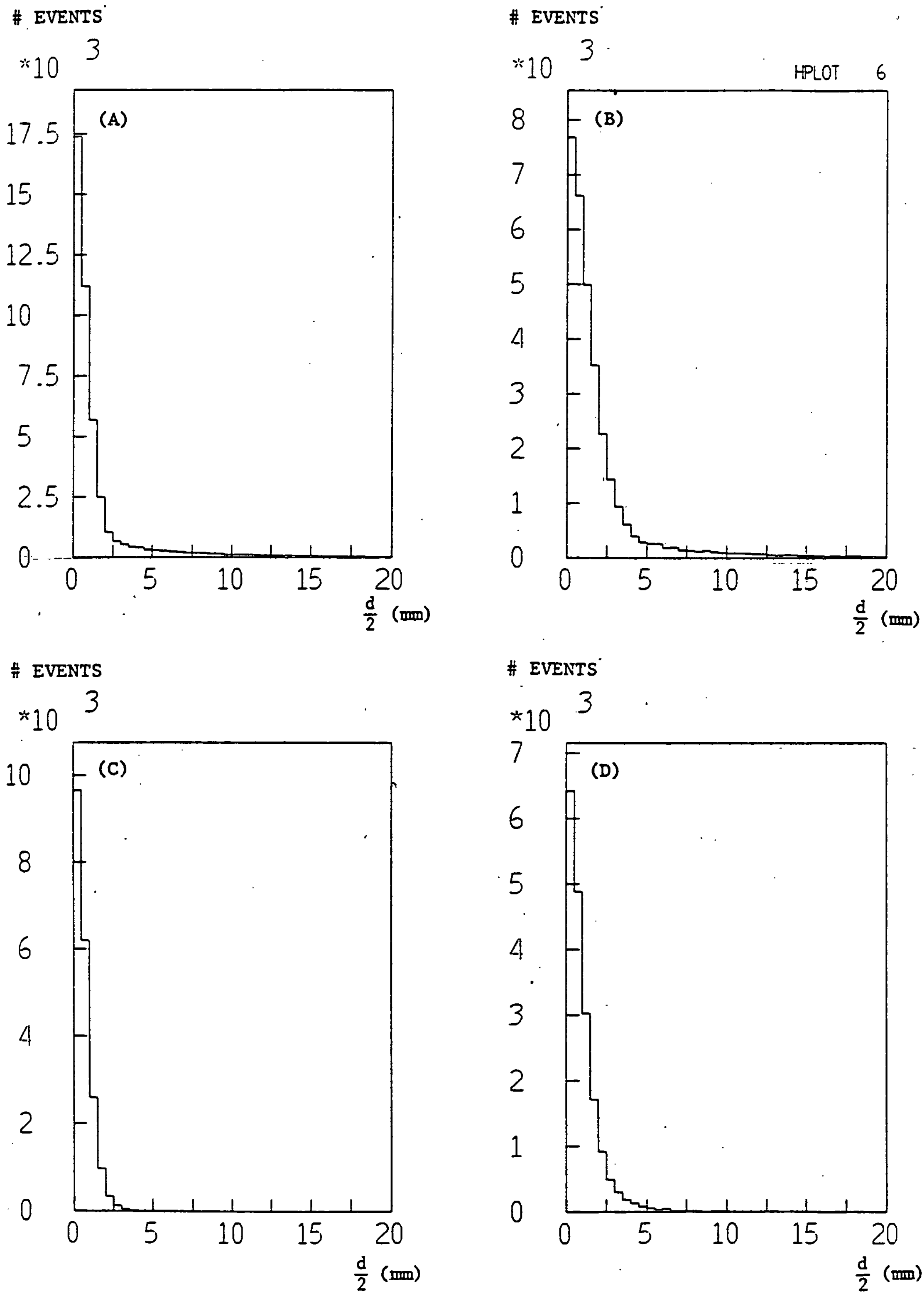

FIGURE 5.2.12: Closing distance - $\frac{d}{2}$. Plots (A) and (B) show this quantity for sideways and forward tracks respectively for real data events. Plots (C) and (D) show the corresponding quantities for Monte Carlo events.

A_x	+ 3.84 mm
B_x	- 2.52 mm
A_y	+ 0.33 mm
B_y	+ 0.07 mm
A_z	+ 1.86 mm
B_z	+ 0.74 mm

TABLE 5.2.1

Values of the constants used in the definition of the vertex parameter V.

forward track, $\underline{P}_F$, and the momentum of the sideways track, $\underline{P}_S$, at the interaction vertex as shown below -

$$\hat{\underline{x}} = \frac{\underline{P}_F}{|\underline{P}_F|} \qquad (5.2.5)$$

$$\hat{\underline{z}} = \frac{\underline{P}_S \times \underline{P}_F}{|\underline{P}_S \times \underline{P}_F|} \qquad (5.2.6)$$

$$\hat{\underline{y}} = \hat{\underline{z}} \times \hat{\underline{x}} \qquad (5.2.7)$$

The coplanarity C was then defined as follows -

$$C = \frac{\underline{P}_B \cdot \hat{\underline{z}}}{|\underline{P}_B|} \qquad (5.2.8)$$

where $\underline{P}_B$ was the beam momentum at the interaction vertex. The coplanarity C is a measure of how closely the beam and the two outgoing tracks are to being coplanar. The opening angle θ is the angle between the forward and sideways tracks. It was defined as follows -

$$\theta = \arctan \left[\frac{\hat{\underline{P}}_S \cdot \hat{\underline{y}}}{\hat{\underline{P}}_S \cdot \hat{\underline{x}}} \right] \tag{5.2.9}$$

If the event was assumed to be an elastic scattering event the "expected" opening angle θ_E could be calculated by using the beam and forward track momenta and momentum conservation to calculate the "expected" sideways track momentum $\underline{P}_{SE}$. θ_E was then defined by -

$$\theta_E = \arctan \left[\frac{\hat{\underline{P}}_{SE} \cdot \hat{\underline{y}}}{\hat{\underline{P}}_{SE} \cdot \hat{\underline{x}}} \right] \tag{5.2.10}$$

and $\Delta\theta$ was defined by -

$$\Delta\theta = \theta - \theta_E \; . \tag{5.2.11}$$

For real elastic scattering events both the coplanarity C and the opening angle difference $\Delta\theta$ should equal zero (within measurement errors). Figure 5.2.13 shows plots of coplanarity versus opening angle difference for both real data and Monte Carlo events. Cuts were placed on these quantities as illustrated in this figure.

The "2-prong" events which survived the coplanarity and opening angle difference cuts were subjected to a 2-prong missing mass squared chi-squared (χ^2) cut to reject forward elastic events (i.e. configuration (2) and configuration (4) type events). Two χ^2's were defined as follows -

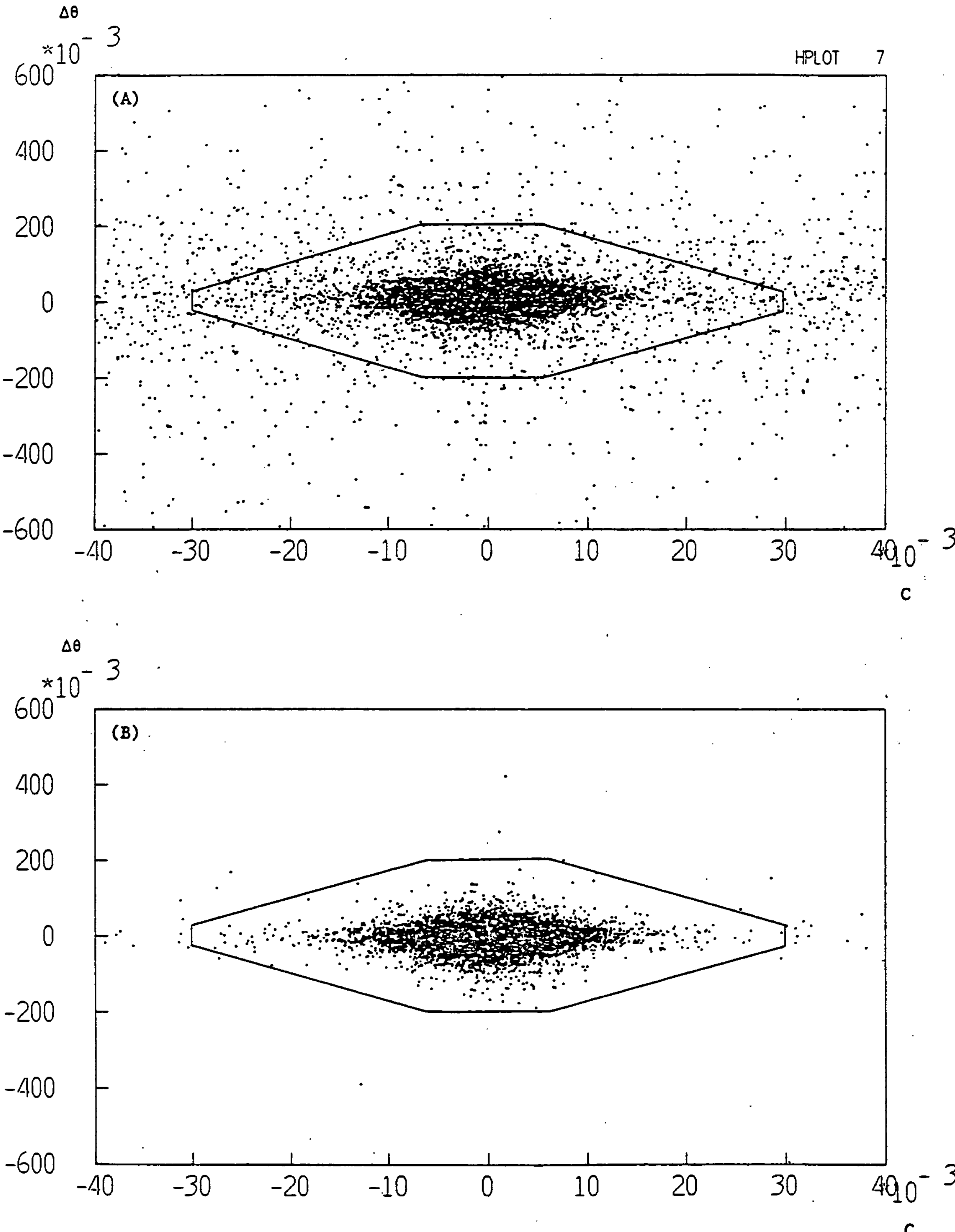

FIGURE 5.2.13: Coplanarity versus opening angle difference for real data events (plot (A)) and for Monte Carlo events (plot (B)).

$$\chi^2_{FE} = \frac{(mm^2_{F\pi} - m_p{}^2)^2}{(\Delta(mm^2_{F\pi}))^2} + \frac{(mm^2_{SP} - m_\pi{}^2)^2}{(\Delta(mm^2_{SP}))^2} \tag{5.2.12}$$

$$\chi^2_{BE} = \frac{(mm^2_{FP} - m_\pi{}^2)^2}{(\Delta(mm_{FP}{}^2))^2} + \frac{(mm^2_{S\pi} - m_P{}^2)^2}{(\Delta(mm_{S\pi}{}^2))^2} \tag{5.2.13}$$

where χ^2_{FE} is the χ^2 for the event being a forward elastic event

χ^2_{BE} is the χ^2 for the event being a backward elastic event

m_π is the π^+ mass

m_p is the proton mass

and mm^2_{IJ} is defined as the missing mass squared to the forward (I = F) or sideways (I = S) track assumed to be a proton (J = P) or a $\pi^+ (J = \pi)$

From these χ^2's probabilities were then calculated. These probabilities are shown in Figure 5.2.14 for both real data and Monte Carlo events. Events were rejected only if the forward elastic probability was greater than 0.04 and, for the same event, the backward elastic probability was less than 0.02.

Single Track Missing Mass Squared χ^2 Cut

For those events with no associated second track the coplanarity and opening angle difference variables could not be calculated. However single track missing mass squared χ^2's could be calculated using the forward track only. Thus χ^2_{FE} and χ^2_{BE} for these events were defined as follows -

$$\chi^2_{FE} = \frac{(mm^2_{F\pi} - m_p{}^2)^2}{(\Delta(mm_{F\pi}{}^2))^2} \tag{5.2.14}$$

$$\chi^2_{BE} = \frac{(mm^2_{FP} - m_\pi{}^2)^2}{(\Delta(mm^2_{FP}))^2} \tag{5.2.15}$$

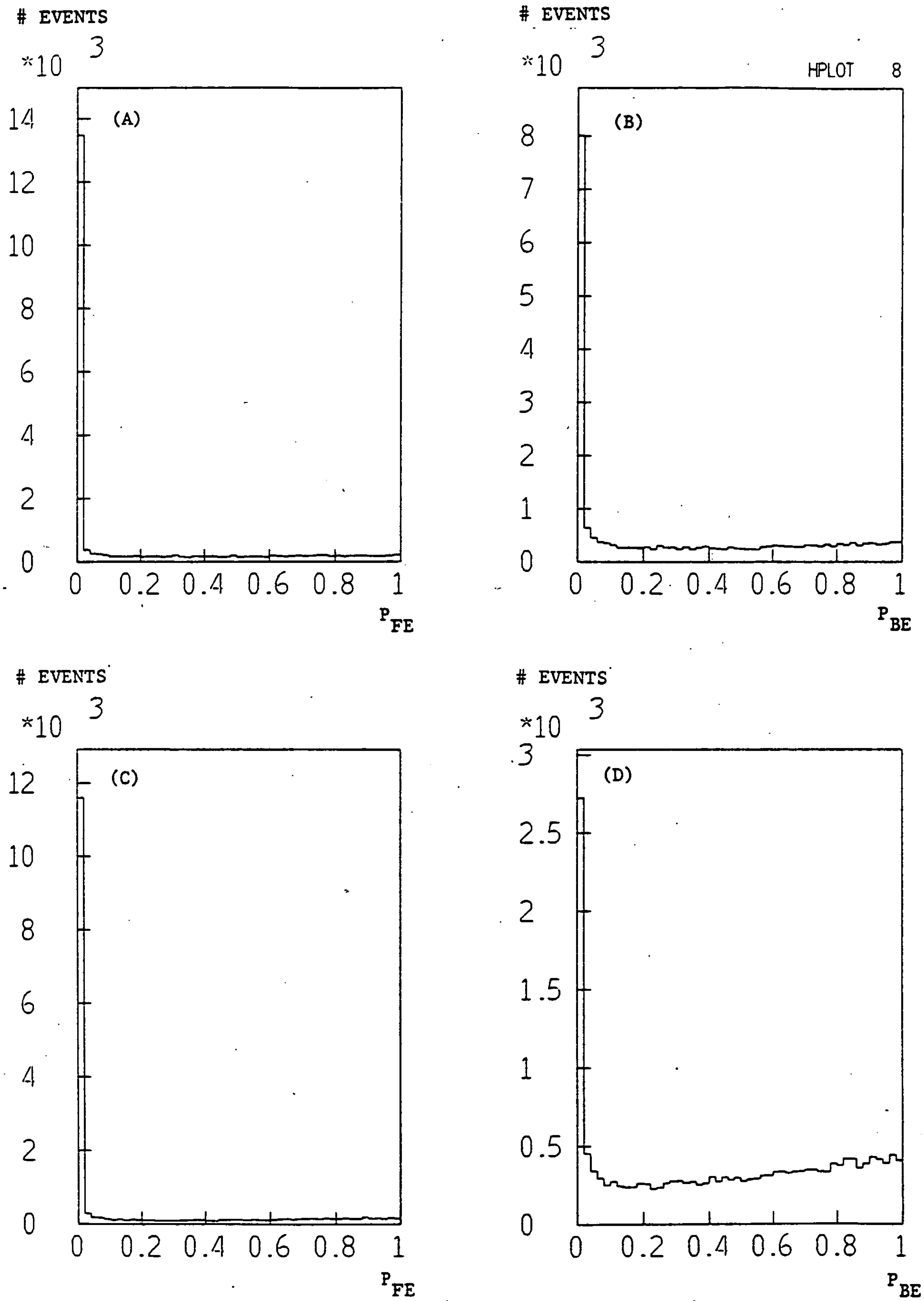

<u>FIGURE 5.2.14</u>: Two-prong missing mass squared χ^2 probabilities. Plots (A) and (B) show the forward elastic and backward elastic probabilities respectively for real data events. Plots (C) and (D) show the corresponding quantities for Monte Carlo events.

where the notation is the same as that used in the definition of the two prong missing mass squared χ^2's. The probabilities calculated from these χ^2's are shown in Figure 5.2.15 for both real data and Monte Carlo events. Events were rejected only if the forward elastic probability was greater than 0.04 and the backward elastic probability was less than 0.02 for the same event.

Y at J1 Cut

A cut was placed on the Y position of the forward track at the hodoscope J1.

In the Monte Carlo events were vetoed if the forward track hit a plane at $Y = + 1260$ mm before reaching J1. This provided a quick and easy means of vetoing events in which the forward track left the fiducial volume of the spectrometer. To ensure that the real data and the Monte Carlo were being treated in an identical manner a cut was placed on Y at J1, in both cases, such that events whose forward track had $Y > 1250$ mm were rejected.

Background

Figure 5.2.16 shows the missing mass squared to the forward track treated as a proton for real data and Monte Carlo events which survived all the cuts described in previous sections. It can be seen from this figure that, despite all efforts, some background still remains in the real data distribution.

The data distribution at every second momentum was fitted (over a limited region around the backward elastic peak) using the Monte Carlo distribution plus a linear background term (for details of this fit see

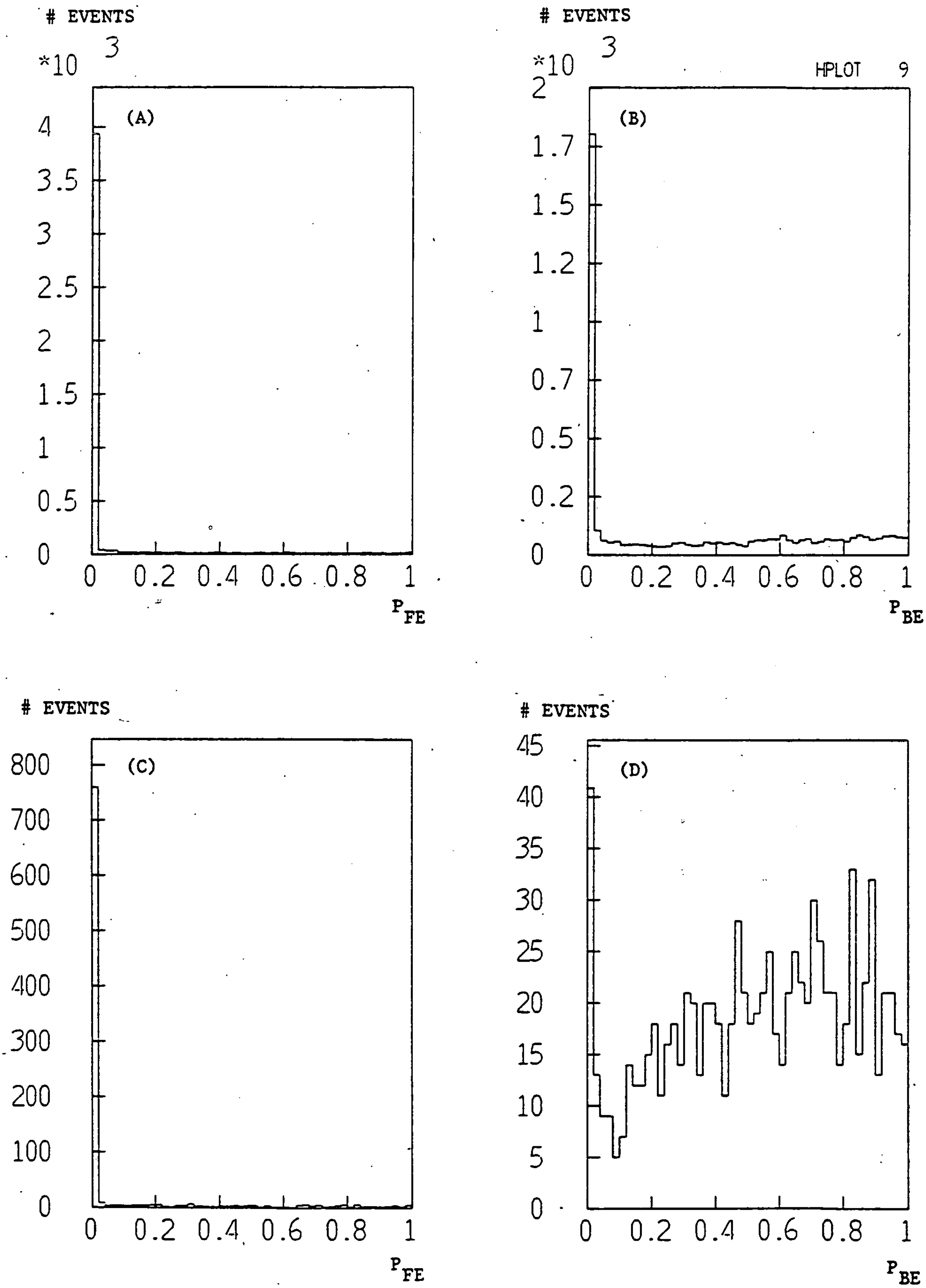

FIGURE 5.2.15: One-prong missing mass squared χ^2 probabilities. Plots (A) and (B) show the forward elastic and backward elastic probabilities respectively for real data events. Plots (C) and (D) show the corresponding quantities for Monte Carlo events.

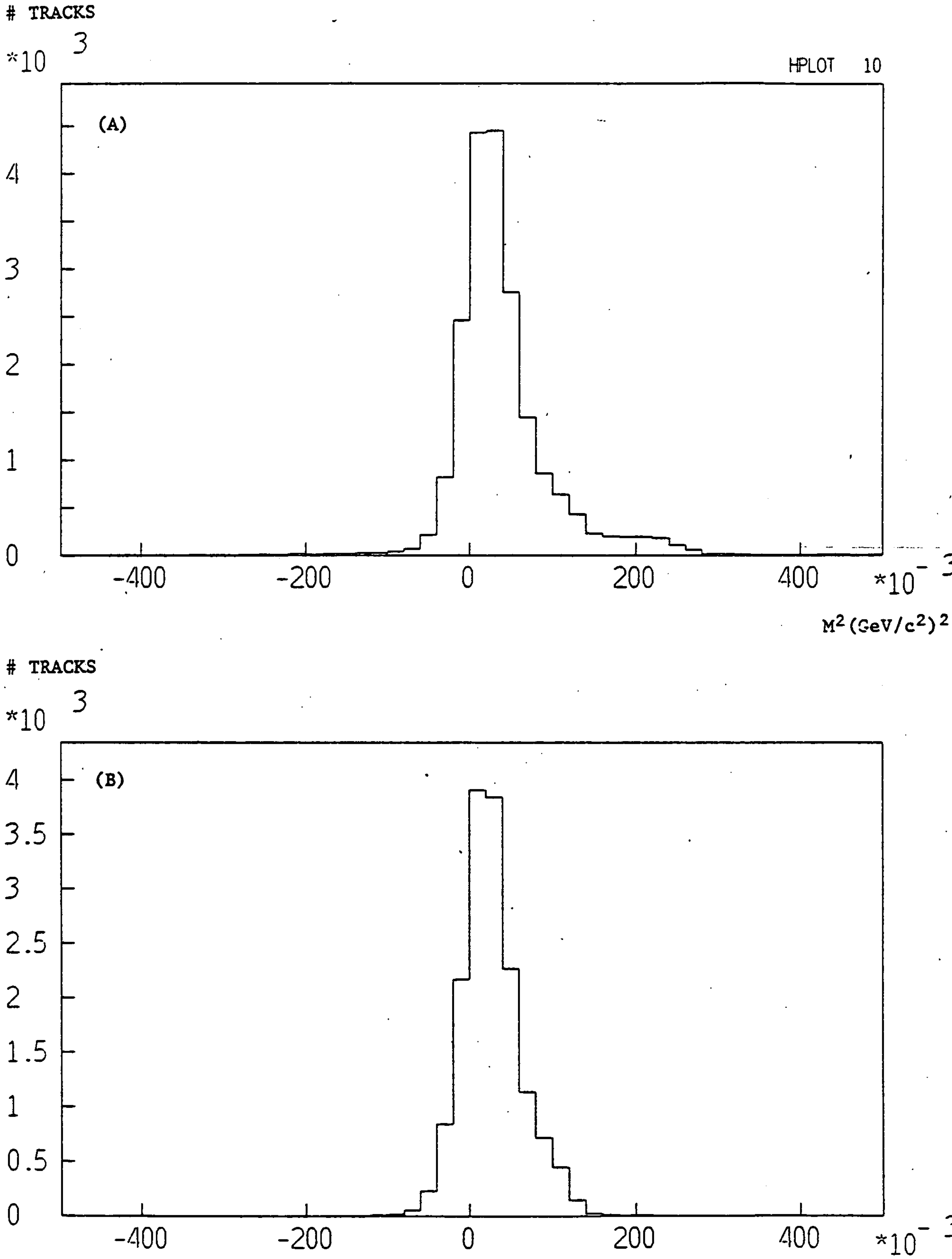

FIGURE 5.2.16: Missing mass squared to the forward track treated as a proton for events surviving the cuts (excluding the missing mass squared cut). Plot (A) shows this quantity for real data events and plot (B) shows the corresponding quantity for Monte Carlo events.

Appendix 1). This provided a good fit to the data at all momenta with χ^2's per degree of freedom in the range 0.75 to 1.09 thus suggesting that the background was linear to a good approximation.

The background was believed to consist mainly of $\pi^+ p \to \pi^+ p\ \pi^o$ events in which the π^o was slow moving in the laboratory. The expected background from this source, adjacent to the backward elastic missing mass squared peak, was estimated at three beam momenta using Monte Carlo generated $\pi^+ p \to \pi^+ p\ \pi^o$ events. The main elastic selection cuts were applied to these events to estimate the number which would survive the elastic selection process. The observed and expected (from $\pi^+ p \to \pi^+ p\ \pi^o$ events) backgrounds were found to be in reasonable agreement (see Table 5.2.2). In addition the cos θ^* distribution of the observed background events was similar in shape to the cos θ^* distribution of the $\pi^+ p \to \pi^+ p\ \pi^o$ events which survived the elastic selection cuts. Both of these distributions had a large backward peak at cos $\theta^* \lesssim -0.9$.

Momentum (GeV/c)	Observed Background	Background expected from $\pi^+ p \to \pi^+ p\ \pi^o$ events
2.48	8.6%	11.0%
2.20	7.4%	10.0%
1.91	3.7%	5.3%

TABLE 5.2.2

Observed and expected (from $\pi^+ p \to \pi^+ p\ \pi^o$ events) backgrounds.

This was due to the loss of the "sideways" track information at such scattering angles resulting in an inability to apply coplanarity and opening angle difference cuts. The missing mass squared distribution of the $\pi^+p \to \pi^+p\,\pi^o$ events which survived the elastic selection cuts was not linear and it did not extend completely under the backward elastic peak. In contrast the observed background was well fitted by a linear approximation which extended completely under the backward elastic peak. This suggested that, while $\pi^+p \to \pi^+p\,\pi^o$ events were probably the major component of the background (based upon the results shown in Table 5.2.2) they were not the only source of background events.

It was decided to correct for the background contamination by performing a linear background subtraction (details of which are given later). Possible deviations of the background from linearity were estimated, based upon the deviation of the $\pi^+p \to \pi^+p\,\pi^o$ background, and used to increase the errors on the data $\cos\theta^*$ distribution (see section 5.5). The possible deviations of the background from linearity had a negligible effect on the final cross sections over most of the $\cos\theta^*$ range with an appreciable effect only being observed in the extreme backward region $(\cos\theta^* \lesssim -0.9)$ where the background was higher.

<u>Missing Mass Squared Cut</u>

A cut was applied to the missing mass squared to the forward track treated as a proton. This cut varied with beam momentum since the central positions and widths of the missing mass distributions varied slightly with beam momentum. The cut rejected events which satisfied -

$$|mm^2 - C| > W$$

where mm^2 is the missing mass squared and C and W are constants defining the position and width of the cut respectively. The values of the constants C and W at each beam momentum are shown in Table 5.2.3.

This cut isolated a sample of events which consisted of backward elastic scattering events and also some background events.

Momentum (GeV/c)	C $(GeV/c^2)^2$	W $(GeV/c^2)^2$
1.91	0.034	0.108
1.99	0.026	0.110
2.01	0.024	0.112
2.08	0.048	0.113
2.10	0.020	0.115
2.16	0.022	0.117
2.20	0.018	0.118
2.25	0.030	0.120
2.29	0.032	0.122
2.34	0.030	0.123
2.38	0.028	0.125
2.43	0.036	0.127
2.48	0.036	0.128

TABLE 5.2.3

Missing mass squared cut parameters

The Kinematic Ambiguity

At each beam momentum there exists an event configuration for which it is kinematically impossible to identify which of the outgoing particles is the proton and which is the π^+. Such events have the configuration shown in Figure 5.2.17. For these events the missing mass to particle 1 treated as a π^+ equals the proton mass and simultaneously the missing mass to particle 1 treated as a proton equals the π^+ mass

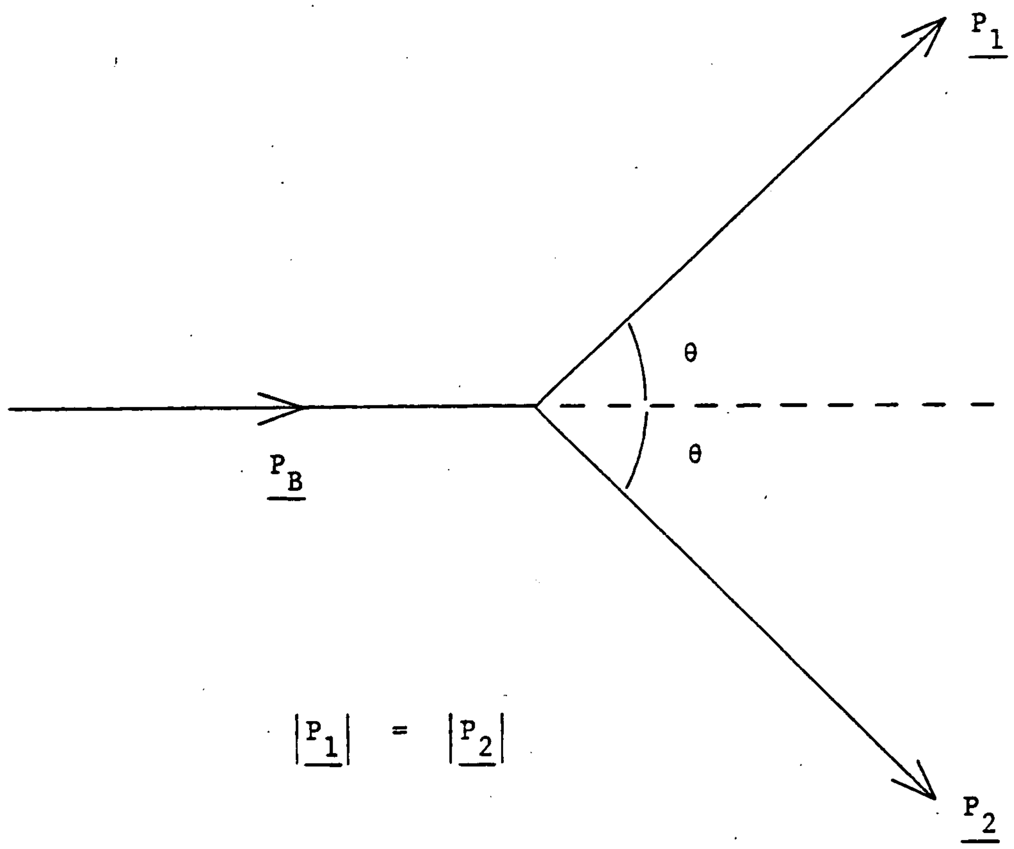

FIGURE 5.2.17: Configuration of kinematically ambiguous elastic events.

(and similarly for particle 2). These events are ambiguous in that there is no kinematic way of deciding whether particle 1 is a proton or a π^+. At a particular beam momentum the kinematic ambiguity occurs at a fixed $\cos\theta^*$ value. Figure 5.2.18 shows how the ambiguity moves in $\cos\theta^*$ as a function of beam momentum. For the higher momenta analysed in this experiment (i.e. the ones presented in this thesis) the kinematic ambiguity occurred in or near the $\cos\theta^*$ ranges of configuration (2) and configuration (3) type events (as defined in Figure 5.2.4). Furthermore the ambiguity was in such a position that configuration (2) type events near the ambiguity were not vetoed by the downstream Cerenkov V2 due to the presence of the iron magnet yoke. Due to measurement error configuration (2) type events which lay near the kinematic ambiguity in $\cos\theta^*$ could not be distinguished kinematically from configuration (3) type events. The time of flight information could in principle be used to resolve this ambiguity however in practice the time of flight resolution was not good enough to distinguish between the two event types. Similarly the mass dependent features of the track fitting process (i.e. energy loss and multiple Coulomb scattering) were too weak to resolve the ambiguity. Thus it was impossible to isolate totally configuration (3) type events in the region of the ambiguity without also selecting some configuration (2) type events. In an effort to correct for this effect Monte Carlo events of configuration type (2) were generated in the region of the ambiguity to simulate the effect of such events in the real data. It was discovered that the reconstructed cross sections in this region were strongly dependent upon the missing mass squared and the missing mass squared χ^2 cuts which were applied. This was believed to be due to slight differences between the Monte Carlo and real data missing mass squared distributions which led

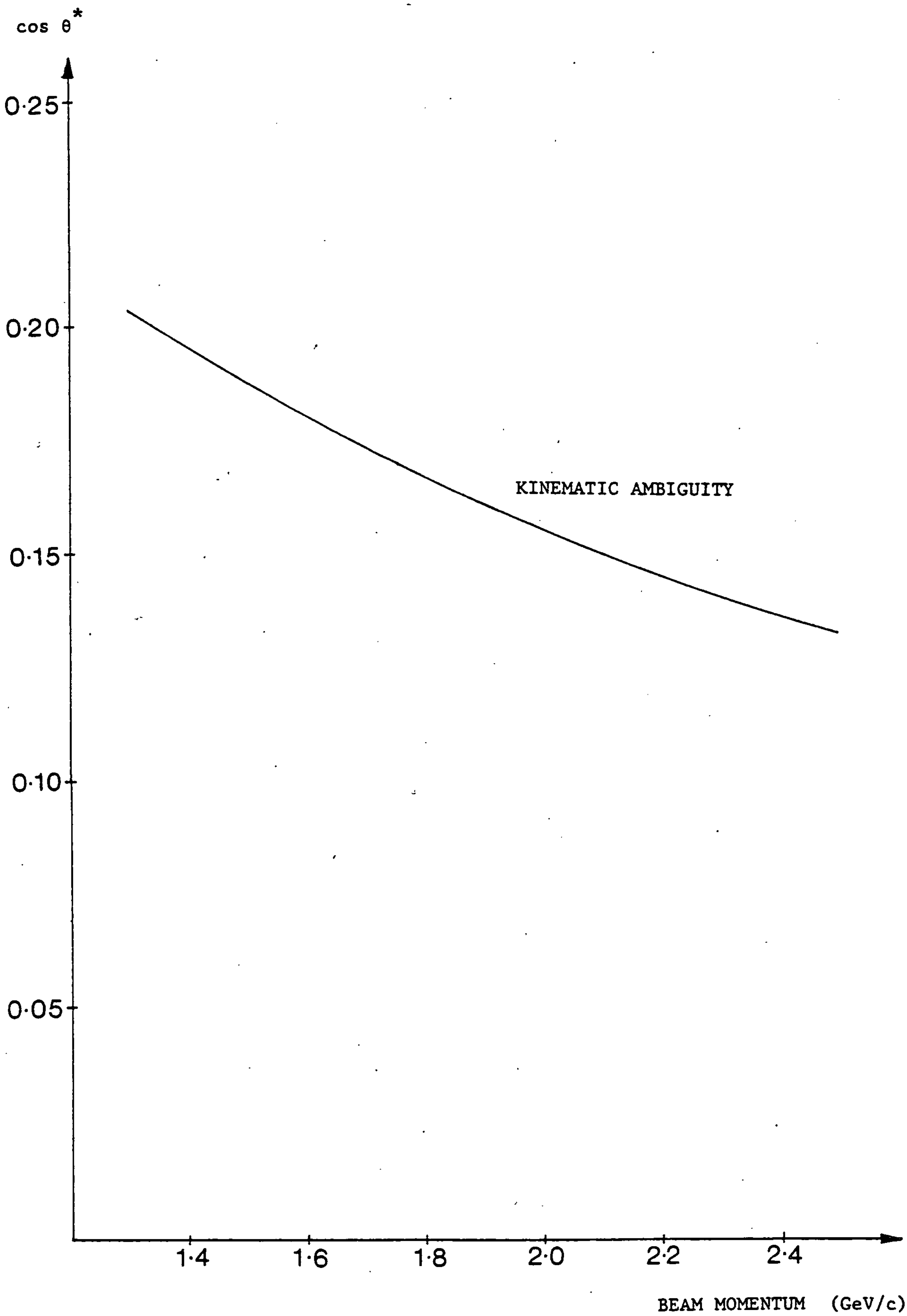

FIGURE 5.2.18: Variation of the kinematic ambiguity position in $\cos\theta^*$ with beam momentum.

to large differences in the number of configuration (2) type events which passed the cuts in each case. Even when the Monte Carlo distributions were transformed to make them look more like the data (see Appendix 1) the cross sections in this region were still very sensitive to the missing mass squared and the missing mass squared χ^2 cuts. Thus the Monte Carlo configuration (2) type events were simply used to determine the $\cos\theta^*$ region where the cross sections were unstable and the Monte Carlo and data $\cos\theta^*$ distributions were truncated to cut out this region.

$\text{Cos}\theta^*$ Distribution Calculation

For those events which passed all the cuts preceding the missing mass squared cut $\cos\theta^*$ was calculated under the assumption that the forward track was a proton. The momenta of the beam π^+, $\underline{P_B}$, and the forward proton, $\underline{P_F}$, at the interaction vertex were transformed to the centre of mass system giving $\underline{P_B}^*$ and $\underline{P_F}^*$ respectively. $\cos\theta^*$ was then defined as -

$$\cos\theta^* = \frac{-\underline{P_F}^* \cdot \underline{P_B}^*}{|\underline{P_F}^*|\,|\underline{P_B}^*|} \qquad (5.2.16)$$

$\cos\theta^*$ distributions were built up for each of the three hodoscope elements of J1. This allowed three cross sections to be calculated at each momentum, thus providing a useful internal consistency check on the data. The cross sections obtained for each hodoscope element at the sample momentum (2.10 GeV/c) are shown in Figure 5.2.19. These cross sections were found to be in reasonable agreement at all momenta.

Two $\cos\theta^*$ distributions were constructed for each hodoscope

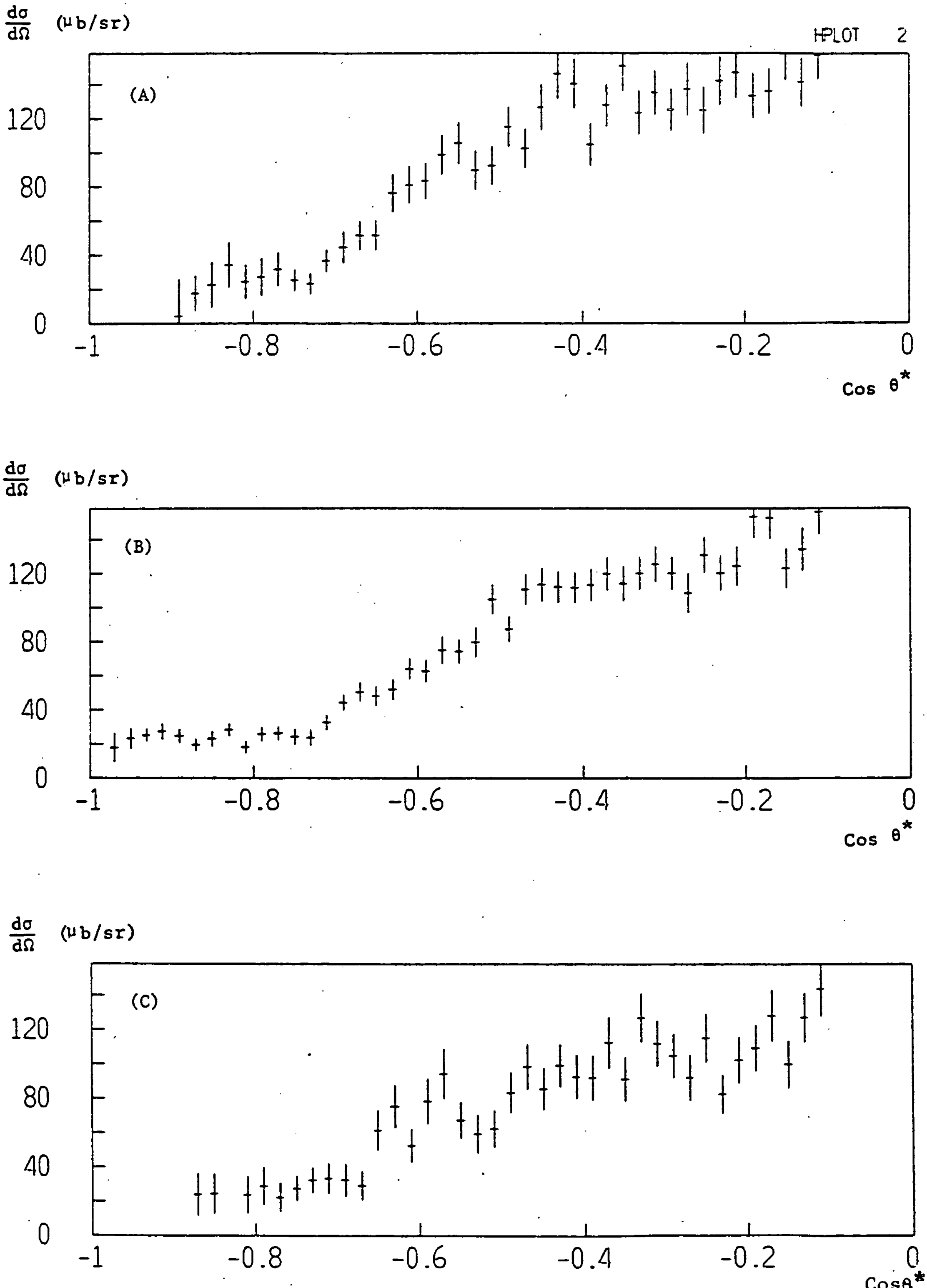

FIGURE 5.2.19: Differential cross sections at 2.10 GeV/c for the three elements of hodoscope J1. Plot (A) corresponds to the top element, (B) to the middle element and (C) to the bottom element.

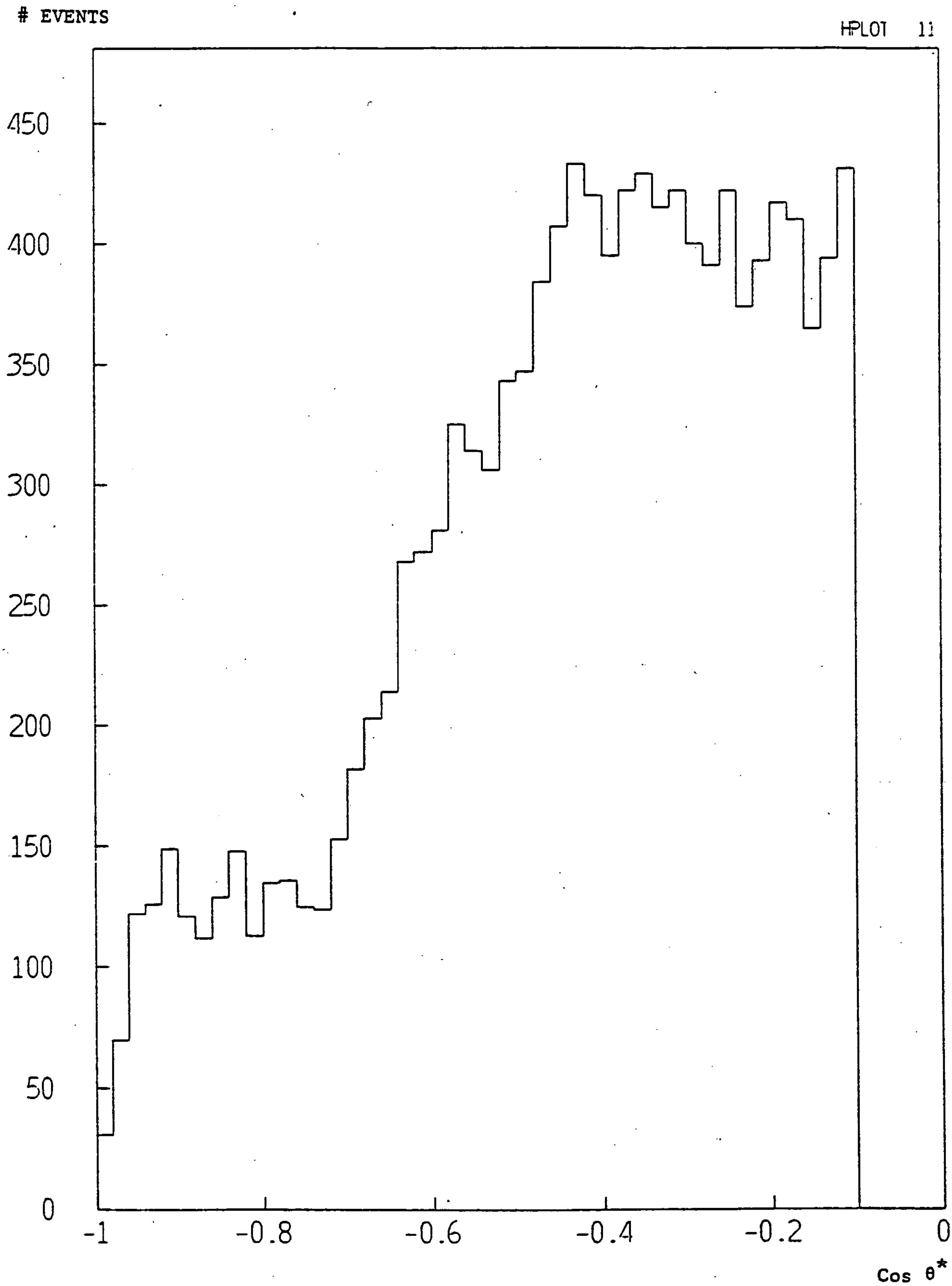

FIGURE 5.2.20: Final data cos θ^* distribution at 2.10 GeV/c.

element - a "signal" distribution and a "background" distribution. The missing mass squared to the forward track treated as a proton, mm^2 say, was used to assign events to these distributions. Thus if the missing mass squared cut was defined by a central value C and a half width W events were placed in the "signal" distribution if $|mm^2 - C| \leqslant W$ and in the "background" distribution if $W < |mm^2 - C| \leqslant 2W$. Events which lay outwith both these ranges were rejected.

A final $\cos\theta^*$ distribution was obtained by the following method. Firstly events in the region of the kinematic ambiguity were rejected by applying a $\cos\theta^*$ cut (at $\cos\theta^* = -0.1$). The "background" distributions were then subtracted from the "signal" distributions to correct for the effect of the linear background. Finally the distributions for each element of J1 were added together to obtain an overall $\cos\theta^*$ distribution for the experiment. This distribution was the one used in the calculation of differential cross sections. A typical final $\cos\theta^*$ distribution for this experiment is shown in Figure 5.2.20.

5.3 Acceptance Calculation

The $\cos\theta^*$ distribution obtained in the previous section is not the true distribution of elastic scattering events. It has been distorted by the imperfect measurement and reconstruction processes. In order to determine the true distribution from the observed one it was necessary to calculate the efficiency of the detection system as a function of $\cos\theta^*$. This efficiency is known as the acceptance.

The problem of acceptance calculation is essentially the calculation of the fraction of elastic events in each $\cos\theta^*$ bin which were detected by the apparatus and identified by the analysis programs. There were three main factors which determined the overall acceptance of this experiment -

1) The geometric acceptance
2) The chamber efficiencies
3) The software efficiency.

The geometric acceptance takes account of the fact that the experimental apparatus only detected events within specific $\cos\theta^*$ and ϕ ranges. The chamber efficiency factor takes account of the fact that the detection chambers were not 100% efficient and this led to the loss of some elastic scattering events. The software efficiency factor takes account of the imperfect event reconstruction algorithms.

The three components of the acceptance were not calculated separately. Instead Monte Carlo techniques were used to calculate the overall acceptance of the experiment for elastic scattering events. In this process random number generators were used to generate elastic scattering events with random $\cos\theta^*$'s and ϕ's and a random vertex position within the hydrogen target. The generated vertex and beam parameters distributions were based upon the observed data distributions.

The true distribution of elastic scattering events as a function of the azimuthal angle ϕ will be flat since there is nothing to define a preferential orientation around the beam direction. Thus a flat ϕ distribution was generated in the Monte Carlo. A realistic $\cos\theta^*$ distribution was generated based upon the differential cross sections obtained from the partial wave analysis amplitudes of the Helsinki-Karlsruhe group[13]. This reduced the distortion, caused by events being reconstructed in the wrong $\cos\theta^*$ bin (due to measurement errors), to a minimum. Events were not generated over the full $\cos\theta^*$ and ϕ ranges since it was known that the experimental apparatus had a zero acceptance over much of these ranges. Since the ϕ distribution was flat the generation of events over a limited ϕ range, within a particular $\cos\theta^*$ bin, could be corrected for by weighting events in that bin by a ϕ weight, ϕ_{w_i} say, defined by -

$$\phi_{w_i} = \frac{2\pi}{\phi_i} \qquad (5.3.1)$$

where ϕ_i is the generated ϕ range in the i'th $\cos\theta^*$ bin. The limited $\cos\theta^*$ range of the data simply meant that differential cross sections could not be calculated over the full $\cos\theta^*$ range and thus it was not necessary to generate Monte Carlo events over the full range. Events were generated in two $(\cos\theta^*, \phi)$ ranges corresponding to region (3) type events (in Figure 5.2.2) and also to region (2) type events in the vicinity of the kinematic ambiguity.

For each generated event the beam and outgoing particles were tracked through the magnetic field to determine whether the event passed the trigger conditions. For those events which passed the trigger "hits" were recorded on the detection chambers, where the tracks traversed them, based upon the measured chamber efficiencies. The events were then passed through the same reconstruction and selection programs as the real data events.

There were two main differences between the Monte Carlo and real data analyses. Firstly there was no measured time of flight information in the Monte Carlo case. This meant that the final Monte Carlo $\cos\theta^*$ distribution had to be weighted, with the time of flight weights described in section 5.2, to correct for the time of flight cut on the J1 electronics. Secondly it was noticed that the Monte Carlo missing mass distributions had slightly different widths and central positions from the data distributions. This was believed to be due to magnetic field measurement errors in the beam region. Using the missing mass squared to the forward track treated as a proton distribution (before the missing mass squared cut) the data distribution was fitted by a linear background plus a transformed Monte Carlo distribution. The basic equation used in the fit was -

$$D(m^2) \quad = \quad p + qm^2 + rM(s(m^2 + t)) \qquad (5.3.2)$$

where m^2 is the missing mass squared to the forward track treated as a proton

D is the real data distribution

M is the Monte Carlo distribution

p and q are linear background parameters

r is a relative normalisation factor between the real data and the Monte Carlo.

s is a parameter describing the relative widths of the two distributions

and t is a parameter describing the relative displacement of the two distributions.

The fit was linearised and using $s = 1$, $t = p = q = 0$ as starting values it was iterated until it converged. Details of the fit can be found in Appendix 1. The results of the fit for the 7 momenta where Monte Carlo data existed are shown in Table 5.3.1. The parameters s and t were used to transform the Monte Carlo missing masses in an appropriate manner before applying missing mass squared and missing mass squared χ^2 cuts. This procedure ensured that equivalent cuts were applied to the data and the Monte Carlo. The differential cross sections were insensitive to small changes in the parameters s and t

Momentum (GeV/c)	s	t $(GeV/c^2)^2$	χ^2/NDF
1.91	0.996	0.0008	0.98
2.01	1.000	0.0103	0.75
2.10	1.058	0.0126	0.77
2.20	0.968	0.0145	1.01
2.29	1.004	0.0018	1.09
2.38	1.053	0.0072	0.87
2.48	1.036	-0.0008	0.88

TABLE 5.3.1

Results of the missing mass squared fitting procedure.

except in the region of the kinematic ambiguity. Since events in this region were ultimately rejected this sensitivity did not matter.

The acceptance was calculated by taking the ratio of the final Monte Carlo reconstructed $\cos\theta^*$ distribution to the ϕ weighted generated distribution -

$$A_i = \frac{W_i}{\phi_{w_i} G_i} \tag{5.3.3}$$

where A_i is the acceptance in the i'th $\cos\theta^*$ bin

ϕ_{w_i} is the ϕ weight in the i'th $\cos\theta^*$ bin

G_i is the number of generated events in the i'th generated $\cos\theta^*$ bin

W_i is the number of (time of flight weighted) reconstructed events which passed all cuts in the i'th reconstructed $\cos\theta^*$ bin.

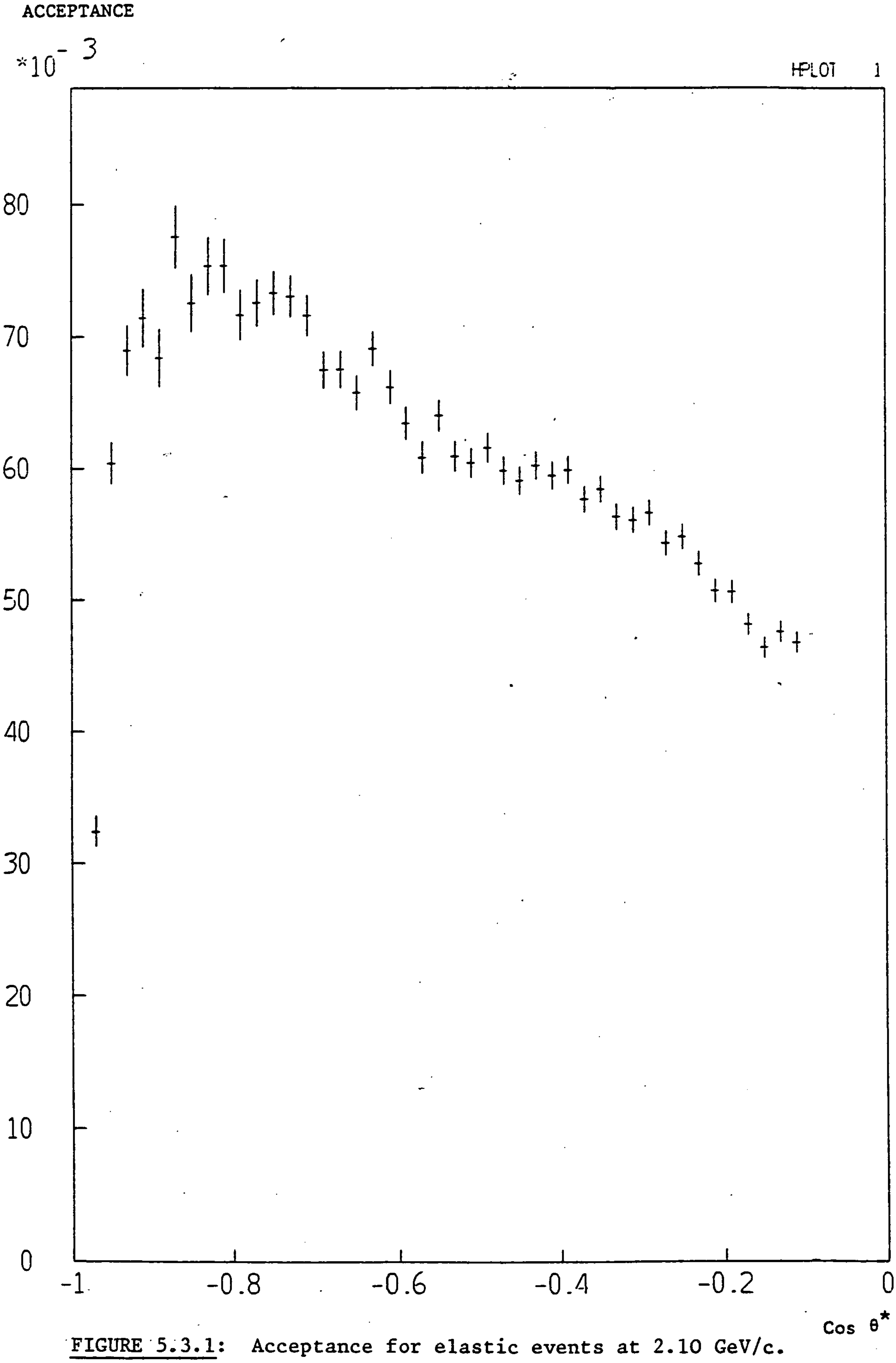

FIGURE 5.3.1: Acceptance for elastic events at 2.10 GeV/c.

A detailed derivation of this formula for the acceptance can be found in Appendix 2.

Monte Carlo data was only generated at every second momentum since the acceptance was expected to vary smoothly with momentum thus enabling interpolation to intermediate momenta. It was discovered that the integrated (over $\cos\theta^*$) acceptance did not vary smoothly with momentum but fluctuated slightly due to the sensitivity of the experiment to the beam position. This introduced an overall normalisation error into the acceptance (and subsequently into the differential cross section) which was estimated to be ±3%. Despite these fluctuations a good fit to the acceptance, as a function of momentum, was obtained by assuming a smooth variation. The acceptance in each $\cos\theta^*$ bin was assumed to vary linearly with momentum and a least squares fit was performed. This fit was used to estimate the acceptance at each momentum. A typical acceptance (at the sample momentum of 2.10 GeV/c) is shown in Figure 5.3.1.

5.4 Normalisation Calculation

Introduction

To calculate the differential cross section, at a particular beam momentum, it only remained to calculate the $\cos\theta^*$ independent normalisation factor, N, in equation (5.1.1). This factor has four main components as shown in equation (5.4.1) -

$$N = G\, E \left(\frac{1}{N_p}\right)\left(\frac{1}{N_{\pi^+}}\right) \qquad (5.4.1)$$

where G is a geometric factor

E is an efficiency and random veto factor

N_p is the number of proton scattering centres in the target (per unit area) and N_{π^+} is the number of beam π^+'s which passed through the target.

Geometric Factor

This factor is simply the element of inverse solid angle defined by each $\cos\theta^*$ bin. It is given by -

$$G = \frac{1}{2\pi\delta} \tag{5.4.2}$$

where δ is the $\cos\theta^*$ binwidth ($\delta = 0.02$).

Efficiency and Random Veto Factor

This factor consists of several components. The majority of these components take account of the fact that the trigger elements were not 100% efficient and also those elements used to veto events sometimes gave random signals(14).

1) C6/C7 efficiency

These efficiencies were not directly measured, however the plateau curves of both photomultipliers looked good and indicated an efficiency of greater than 99% each. The efficiency of both combined was estimated to be 0.99 ± 0.01.

2) J1 efficiency

This was measured using beam triggers in which J1 was not part of the trigger. Its efficiency was found to be 0.98 ± 0.01.

3) A3 + A4 random veto

This correction factor was estimated from the fraction of the beam seen by these counters, the data taking rate and the veto pulse width to be 0.99 ± 0.01.

4) V0 random veto

This correction factor was measured to be 0.992 ± 0.010.

5) V2 random veto

This factor was measured using "Cerenkov off" data tapes in which the Cerenkov, V2, was not part of the trigger. By selecting a sample of backward elastic events in which the proton entered the Cerenkov and looking at the number of such events for which the Cerenkov gave a "count" the V2 random veto correction factor was estimated to be 0.994 ± 0.001.

6) Outgoing track finding efficiency

The loss of outgoing tracks due to chamber inefficiency was simulated in the Monte Carlo. Tracks could also be lost if random noise produced sparks which "confused" the track finding program. This random noise was simulated crudely in the Monte Carlo. Visual scanning of data and Monte Carlo events gave comparable track finding efficiencies for both (95% for real data and 97.5% for Monte Carlo data) and hence a correction factor of 1.0 ± 0.03 was estimated.

7) Loss of events due to secondary interactions

Due to the method of event selection the secondary interactions of the sideways π^+ were unimportant since the loss of this track simply meant that the event was treated as a one-prong. The secondary interaction of the forward proton could have one of three effects. Either the interaction could cause the event to fail the trigger and be lost or the event could pass the trigger but fail to be identified as an elastic event or it could pass the trigger and, despite the secondary interaction still be correctly identified as an elastic event. The fraction of protons which would be expected to undergo a secondary interaction was estimated using a selected sample of backward elastic events. The mean effective length of liquid hydrogen traversed by the forward track was estimated and then, using a total pp cross section of 47 mb[15] (which remained fairly constant in our momentum region), the fraction of secondary interactions, f, was calculated using equation (5.4.3) -

$$f = \sigma \rho L N_A / A \qquad (5.4.3)$$

where σ is the pp total cross section

ρ is the density of liquid hydrogen

L is the effective length of liquid hydrogen traversed by the forward proton

N_A is Avogadro's number

and A is the atomic weight of hydrogen.

Thus $f = 47 \times 10^{-27} \times 0.07065 \times 10.3 \times 6.022 \times 10^{23}/1.007$

$= 0.0205.$

Not all of the events which underwent a secondary interaction were lost and hence a correction factor of 0.99 ± 0.01 was applied.

8) <u>Interactions in the target walls</u>

Some of the beam π^+'s interacted in the walls of the target en. Some fraction of these

c to pass all the selection

for this effect since it

subtraction would, to some

the Target (Per Unit Area)

centres in the target per unit

(5.4.4)

quid hydrogen target

length

hydrogen.

lculated to be 0.07067 ± 0.00005

.ength was calculated by intersecting

target and calculating the mean dis-

. A straight line approximation was

.nce the curvature of the track within

the ... ligible effect. The effective target length was calculated for several different samples of events (a beam track tape, a Monte Carlo tape, a raw data tape and a tape of selected elastic events). The effective target length used was that calculated using the beam track tape and the spread of lengths for the various data samples was used to estimate the error on the effective target length. This gave L = 146 ± 2 mm. Thus-

$$N_p = \frac{0.07067 \times 14.6 \times 6.02 \times 10^{23}}{1.007}$$

$$= (6.17 \pm 0.08) \times 10^{23}\ \mathrm{cm}^{-2}\ .$$

Number of Beam π^+'s Which Passed Through the Target

The number of π^+'s which passed through the target was counted by the scaler R3 which recorded the number of beam π^+'s satisfying the beam telescope trigger logic. This number had to be corrected to take into account several effects[(14)].

1) Beam reconstruction failures

Since R3 was part of the trigger logic every recorded event should have had a good beam track. A small fraction (~ 5 - 10%) of events failed in the reconstruction of a beam track. These failures were caused by either missing or extra hits in the beam MWPC's which caused the program to be unable to find one unambiguous beam track. Such events were impossible to analyse since the beam momentum and trajectory were unknown. This loss was uncorrelated in $\cos\theta^*$ and hence an overall correction factor was applied. The correction factors at each momentum are shown in Table 5.4.1.

2) e^+, μ^+ contamination at C5

There was some e^+ and μ^+ contamination in the beam which led to an overestimate of the number of π^+'s in the beam. The magnitude of this effect was measured by taking data at various C5 pressures. This data was used to calculate correction factors at five standard momenta. The correction factors were then quadratically interpolated to intermediate momenta. The correction factors at each momentum are shown in Table 5.4.1.

Effect \ Momentum (GeV/c)	1.91	1.99	2.01	2.08	2.10	2.16	2.20	2.25	2.29	2.34	2.38	2.43	2.48	Errors
Beam Reconstruction Failures	0.899	0.885	0.899	0.873	0.847	0.911	0.918	0.932	0.929	0.940	0.943	0.946	0.945	-
e^+, μ^+ Contamination at C5	0.926	0.932	0.937	0.942	0.947	0.951	0.955	0.959	0.962	0.966	0.968	0.971	0.973	± 0.010
π^+ Decay Between C5 and CO	0.985	0.985	0.986	0.986	0.986	0.986	0.987	0.987	0.987	0.987	0.988	0.988	0.988	± 0.005
π^+ Decay After CO	0.997	0.997	0.997	0.997	0.997	0.997	0.997	0.997	0.997	0.997	0.997	0.997	0.998	± 0.001
Interaction Loss After CO	0.987	0.987	0.987	0.987	0.987	0.987	0.987	0.986	0.986	0.986	0.986	0.986	0.986	± 0.005

TABLE 5.4.1

Momentum dependent normalisation factors.

3) μ^+ contamination from π^+ decays between C5 and CO

Some of the beam π^+'s decayed after passing through the beam Cerenkov, C5, and before reaching the scintillation counter CO which was situated just in front of the target. These events could still satisfy the beam trigger logic if the μ^+ from the decay passed through C2 and CO. Correction factors for this effect were calculated at several momenta using the distance between C5 and CO, the measured beam characteristics and the size of the scintillation counter CO. The correction factor was found to vary slowly with beam momentum and the correction factor at each momentum is shown in Table 5.4.1.

4) π^+ decay after CO

This factor corrects for the loss of beam π^+'s due to decay after the scintillation counter CO. It was computed explicitly at each momentum using the beam momentum and the distance from CO to the target centre. The results of these calculations are shown in Table 5.4.1.

5) Interaction loss from CO to the target centre

Some of the beam π^+'s interacted inelastically after passing through CO and were lost. Correction factors for this effect were calculated at each momentum using the total inelastic π^+p cross section and the amount of material between CO and the target centre. The results of these calculations are shown in Table 5.4.1.

6) Protons in the beam satisfying the time of flight cut

This effect was negligible and a correction factor of unity was applied.

7) Dead time losses

The number of π^+'s in the beam could be miscalculated if two passed through the beam scintillation counters very close together in time and were not resolved as two separate particles. This effect was negligible and a correction factor of unity was applied.

5.5 Error Calculation

The calculation of the differential cross sections was subject to two types of error - $\cos\theta^*$ independent errors and $\cos\theta^*$ dependent errors.

The $\cos\theta^*$ independent errors came from two main sources. Firstly there was a systematic error in the calculation of the normalisation factor N. This error was calculated by combining the measurement errors, from each factor which made up N, in quadrature. Secondly there was a systematic error in the acceptance due to uncertainties in the beam position. The magnitude of this error was estimated from the fluctuations in the integrated acceptance as a function of momentum. These two errors were combined in quadrature to give a total normalisation error of ± 6% at all momenta.

The $\cos\theta^*$ dependent errors came from four main sources, two of which contributed to the errors on the data $\cos\theta^*$ distribution (ΔD_i) and two of which contributed to the errors on the acceptance (ΔA_i).

The errors on the data $\cos\theta^*$ distribution were due to a statistical error associated with the finite number of data events and a systematic error associated with uncertainties in the background subtraction procedure. The number of data events in the i'th $\cos\theta^*$ bin was given by -

$$D_i = E_i - F_i \qquad (5.5.1)$$

where E_i was the number of selected data events in the i'th $\cos\theta^*$ bin before the background subtraction and F_i was the number of selected data events in the background in the i'th $\cos\theta^*$ bin. The error in D_i, (ΔD_i), was given by adding the errors in E_i and F_i in quadrature -

$$(\Delta D_i)^2 = (\Delta E_i)^2 + (\Delta F_i)^2 \quad . \tag{5.5.2}$$

The error in E_i was statistical and it was given by -

$$\Delta E_i = E_i^{\frac{1}{2}} \quad . \tag{5.5.3}$$

The error in F_i consisted of a statistical part $(F_i^{\frac{1}{2}})$ and a systematic part due to possible deviations of the background from linearity. This systematic error was estimated, from the deviation of the Monte Carlo generated $\pi^+ p \rightarrow \pi^+ p \pi^o$ background from linearity, to be $\sim {}^{F}i/_{3}$. Thus the total error in F_i was given by -

$$\Delta F_i = ((F_i^{\frac{1}{2}})^2 + (F_i/3)^2)^{\frac{1}{2}} \quad . \tag{5.5.4}$$

The errors on the acceptance were due to a statistical error associated with the finite number of Monte Carlo events which were generated and to the errors in the time of flight weights (which were also statistical in nature). The calculation of the acceptance errors, (ΔA_i), was much more complicated than the data $\cos\theta^*$ distribution error calculation. Details of this calculation are shown in Appendix 2.

The $\cos\theta^*$ dependent error on the differential cross section was given by combining (ΔD_i) and (ΔA_i) as in equation (5.5.5) -

$$\Delta\left(\frac{d\sigma}{d\Omega}\right)_i = N\left(\frac{(\Delta D_i)^2}{A_i^2} + \frac{D_i^2}{A_i^4}(\Delta A_i)^2\right)^{\frac{1}{2}} \tag{5.5.5}$$

The $\cos\theta^*$ independent normalisation error is not included in the errors shown on the differential cross section plots of Chapter Six. The errors shown on these plots represent the $\cos\theta^*$ dependent errors which give a measure of the errors on the cross section "shape" independent of the overall normalisation.

CHAPTER 6

RESULTS

6.1 Introduction

In this chapter the differential cross sections at the 13 momenta analysed in this thesis are presented. These cross sections are compared with the results of previous experiments and also with the two main partial wave analyses of the channel. The number of selected elastic events observed at each momentum is shown in Table 6.1.1.

Momentum (GeV/c)	Number of Selected Elastic Events
1.91	20880
1.99	29890
2.01	7401
2.08	6881
2.10	11630
2.16	9261
2.20	7864
2.25	11050
2.29	5528
2.34	11330
2.38	6558
2.43	11760
2.48	6695

TABLE 6.1.1

Number of selected elastic events.

Section 6.2 gives a brief description of the previous $\pi^+ p \rightarrow \pi^+ p$ experiments which can be compared with the results quoted in this thesis and section 6.3 gives a brief description of the partial wave analyses in this channel. In section 6.4 the differential cross sections are presented and comparisons with other experiments and with partial wave analyses are made.

6.2 Previous Experiments

The results presented in this thesis are compared with the results of four previous π^+p elastic scattering experiments.

1) Abe et al.[16]

This is a counter experiment which was performed at the Argonne ZGS (zero gradient synchrotron). Data was collected at 16 beam momenta between 1.2 and 2.3 GeV/c. Typically 50,000 events were collected at each momentum in the centre of mass angular range $-0.9 < \cos\theta^* < 0.9$. This experiment had no magnet and hence it could not measure particle momenta. Thus the selection of elastic scattering events was achieved solely by the scattering angle correlation between the two outgoing particles. Loose cuts were made on vertex quantities and on the coplanarity of the event. For events which survived these cuts the centre of mass scattering angles were calculated for both assumptions as to particle identities. The deviations of the experimentally determined scattering angles from elastic kinematics, $\Delta\theta$, were then calculated for each $\cos\theta^*$ bin. The $\Delta\theta$ distributions were characterised by two peaks - one corresponding to the correct assumption as to particle identities and the other corresponding to the incorrect assumption. These distributions were fitted using two Gaussians and a flat background. The true number of elastic scattering events in a $\cos\theta^*$ bin was then determined by subtracting the fitted background and incorrectly interpreted events in a restricted region centred on the correctly interpreted events.

2) Bardsley et al.[17]

This is a counter experiment which was performed at the Rutherford laboratory's Nimrod accelerator. It measured $\pi^{\pm}p$ elastic scattering at 51 beam momenta in the range 0.4 to 2.15 GeV/c. Approximately 15,000 to 20,000 elastic events were collected in each channel at each momentum. The angular region covered was $-0.99 < \cos\theta^* < 0.99$. Only preliminary results from this experiment are available for comparison. The experiment ran in two distinct modes - a spectrometer mode and a correlation mode. In the spectrometer mode a magnet was used to measure the momentum of the fast forward particle. This mode was used to measure scattering in the extreme backward and extreme forward regions. In the correlation mode no magnet was used and hence elastic events could only be recognised by the angular correlation between the two outgoing tracks. The method of selecting elastic events was different in the two modes. In the correlation mode events were selected based upon their vertex parameters and the correlation of the directions of the two outgoing tracks. For events which passed these cuts the triple scalar product of the unit vectors along the three track directions was formed. This quantity was plotted for each $\cos\theta^*$ bin and a well defined elastic peak was observed above a low background. A small linear background subtraction was then made in each bin to correct for the background. In the spectrometer mode the correlation between momentum and angle of the forward track was used to select elastic events.

3) Ott et al.[18]

This is a counter experiment which was performed at the Berkeley Bevatron. It measured backward differential cross sections for π^+p elastic scattering at 16 beam momenta in the range 1.25 to 1.92 GeV/c. The angular region covered was $-0.97 < \cos\theta^* < -0.46$. The experiment used a double arm telescope of scintillation counters with a magnet in one arm to provide rough momentum measurement. Three main criteria were used to select elastic scattering events. The first was the angular correlation between the two outgoing tracks which showed elastic peaks on top of a smooth background. Secondly, due to the configuration of the scintillation counters used in the experiment (with phototubes mounted on top of the proton counters and on the bottom of the pion counters), time of flight measurements could be used to impose approximate coplanarity . Finally the inelastic background was examined to ensure that it could be subtracted from the elastic data without bias.

4) Busza et al.[19]

This is a "magnetless" counter experiment which was performed at the Rutherford laboratory's Nimrod accelerator. It measured $\pi^{\pm}p$ elastic scattering at 10 beam momenta in the range 1.72 to 2.80 GeV/c. The angular region covered was $-0.94 < \cos\theta^* < 0.95$. This is an older experiment than the three previous experiments and its statistics are much lower. Elastic events were selected by imposing severe coplanarity and kinematic constraints. The data was then corrected to take account of the inelastic and target empty backgrounds.

There are several other experiments with which it would have been possible to compare the results of this experiment. The two main remaining high statistics experiments with which comparisons could be made are those of Jenkins et al.[20] and Albrow et al.[21]. No comparison was made with these experiments since in the Jenkins case the $\cos\theta^*$ overlap with this experiment was very small ($\sim$ 2 bins at all momenta) and in the Albrow case the differential cross sections were normalised to previous experiments. In addition to these two experiments there exist several older experiments (e.g. Carroll et al.[22] and Cook et al.[23]). The errors quoted by these experiments are rather large and hence no comparison was made with them.

6.3 Partial Wave Analyses

There are two main up to date partial wave analyses of the pion nucleon system. These are the analyses of the Helsinki-Karlsruhe group[13] and the Carnegie-Mellon University - Lawrence Berkeley Laboratory (CMU - LBL) group[24]. Both of these groups use as input an amalgamation of the world data on pion-nucleon scattering. As mentioned in Chapter 2 few measurements of the spin rotation parameters (A and R) and the polarisation (P) have been made. This means that partial wave analyses can only find a unique solution if additional theoretical constraints on the partial wave amplitudes are provided. Some of these constraints are common to both the main analyses (e.g. Lorentz invariance, unitarity and isospin invariance) however some are not and this is the main difference between the analyses.

The CMU-LBL group performed single energy fits to the scattering data as the first stage of their analysis. In addition to the scattering data itself unitarity and predictions from forward dispersion relations were used to constrain the amplitudes in these fits. At each energy the single energy fits obtained several solutions which were then used as input to an energy dependent analysis. This analysis employed dispersion relations along hyperbolic curves in the Mandelstam plane (hyperbolic dispersion relations) to constrain the amplitudes. The hyperbolic dispersion relation constraints were then incorporated into the single energy fits and the two fit types (single energy and energy dependent) were then alternated to arrive at a unique set of amplitudes which fitted the scattering data throughout the energy region studied.

The Helsinki-Karlsruhe group used an energy dependent partial wave analysis. In this case analyses using fixed t, fixed centre of mass angle, forward and backward dispersion relations were constrained together with an ordinary partial wave analysis and performed simultaneously. This led to a unique solution which had the approximate analyticity properties of the individual analyses.

In the case of both these analyses resonance parameters were extracted from the partial waves by fitting them using parameterisations based upon the Breit-Wigner resonance formula.

6.4 Comparison of Differential Cross Sections

Introduction

This section contains a comparison of the differential cross sections obtained in this thesis with the results of the four experiments described in section 6.2 and the two partial wave analyses described in section 6.3.

These experiments and partial wave analyses did not have data at the same momenta as the RMS experiment and hence, to make meaningful comparisons, their data was interpolated to the RMS momenta. The partial wave analyses scattering amplitudes were interpolated using an algorithm provided by the Helsinki-Karlsruhe group and differential cross sections were then reconstructed from the interpolated amplitudes. In the case of the experimental data the differential cross sections were linearly interpolated between the two closest momenta on either side of the RMS data. The linear interpolation procedure could introduce a systematic error into the interpolated differential cross sections. The magnitude of this error was estimated from a plot of the integrated cross section ($-0.85 \leq \cos\theta^* \leq -0.11$) versus momentum (see Figure 6.4.7) for three of the four experiments. The error introduced to the data of Bardsley et al. was estimated to be $\sim$ 6% and the error introduced to the data of Abe et al. to be $\sim$ 4%. The error introduced to the data of Busza et al. was somewhat larger ($\sim$ 10-15%), however this was not believed to be important since the error was comparable with the large statistical errors quoted by the experiment. The error introduced to the data of Ott et al. was believed to be negligible in comparison to the large normalisation uncertainties associated with this experiment. The interpolated differential cross sections for each experiment and for the two partial wave analyses are shown superimposed on the RMS differential cross sections in Figures 6.4.1 to 6.4.6. In these figures the RMS data points are represented by solid squares, those of Abe et al. by open squares, Bardsley et al. by triangles, Ott et al. by diamonds and Busza et al. by circles. The partial wave analyses cross sections are represented by solid curves. The error bars on the RMS data points, shown in these plots, represent the $\cos\theta^*$ dependent errors only (as described in section 5.5) and do not include the $\cos\theta^*$ independent normalisation errors. Similarly the error bars on the data points of the other experiments represent only the statistical errors on the points. The normalisation and interpolation errors are not shown in these plots but are discussed separately in the text.

In addition to the direct comparison of differential cross sections the two partial wave analyses and all of the experimental data samples, with the exception of the Ott data, were fitted by a Legendre series over a limited $\cos\theta^*$ range ($-0.85 \leqslant \cos\theta^* \leqslant -0.11$). In this fit the zero'th order coefficient, Q_o, (which is directly proportional to the integrated cross section over the limited $\cos\theta^*$ range) was not fitted to but was calculated explicitly using the trapezoidal rule. The higher order coefficients ($R_\ell \equiv Q_\ell/Q_o$ with $\ell = 1,2,\ldots, L_{max}$) were then fitted to by performing a least squares fit. A good fit to all the data samples and to the two partial wave analyses was obtained with $L_{max} = 6$. The first few of these coefficients are plotted as a function of momentum, for all the data samples, in Figures 6.4.7 to 6.4.9. In these figures the RMS coefficients are represented by solid squares, the Abe coefficients by open squares, the Busza data by circles and the Bardsley data by triangles. The Helsinki-Karlsruhe coefficients are represented by a solid curve and the CMU-LBL coefficients by a dashed curve. As in Figures 6.4.1 to 6.4.6 the error bars in these figures do not include any contribution from the $\cos\theta^*$ independent normalisation errors. Such errors only affect the zero'th order coefficients, Q_o, and their effect is discussed in the text. The higher order coefficients obtained from the experimental data ($\ell > 2$) had large errors and hence a comparison of these coefficients was not thought to be very meaningful.

The comparison of the RMS data with each of the four experiments and with the two partial wave analyses will now be discussed.

Comparison with Abe et al.[16]

The data of Abe et al. extended to an upper beam momentum of 2.30 GeV/c and hence a comparison with the data presented in this thesis could only be made at the lowest nine momentum settings. The linearly interpolated differential cross sections of Abe et al. are shown superimposed on the RMS cross sections at these nine momentum settings in Figure 6.4.1. It can be seen from this figure that there are significant differences between the two data samples at all momentum settings with the exception of the 1.99 GeV/c data. In particular there is a large discrepancy in normalisation between the two data samples which also shows up clearly in the plot of Q_o as a function of momentum (Figure 6.4.7). This discrepancy is greatest at the high end of the momentum range where Abe's data is as much as 90% higher than the RMS data and even at the lower end of the range discrepancies of the order of 30% exist (with the exception of the 1.99 GeV/c data which is only 8% higher than the RMS data). Considering the magnitude of the normalisation errors quoted by the two experiments (2-3% for the Abe experiment and 6% for the RMS experiment) and the estimated linear interpolation error on the Abe data ($\sim$ 4%) the differences between the two data samples represent a significant discrepancy over most of the momentum range. One possible source of this discrepancy is a systematic error in the measurement of beam momentum in one of the experiments. To obtain agreement between the two data samples requires a shift in momentum of $\sim$ 0.2 GeV/c at the higher end of the momentum range and of $\sim$ 0.1 GeV/c at the lower end. The possible systematic shift in beam momentum of the RMS data was estimated,

FIGURE 6.4.1: Comparison of the RMS differential cross sections with those of Abe et al.

KEY

This experiment.

Abe et al.

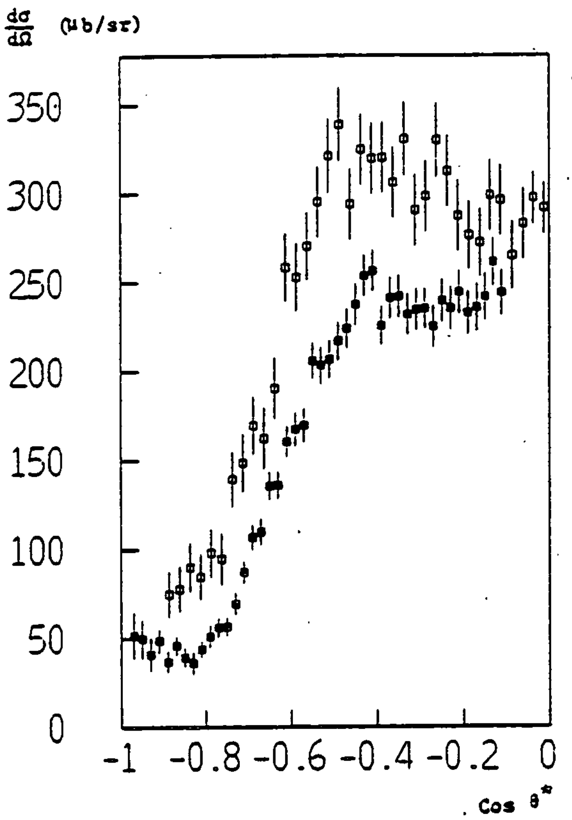

1.91 GEV/C

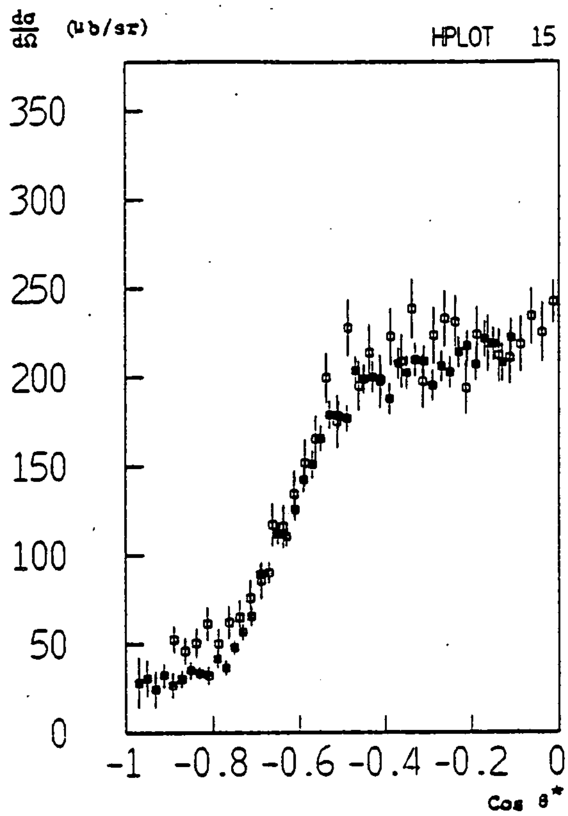

1.99 GEV/C

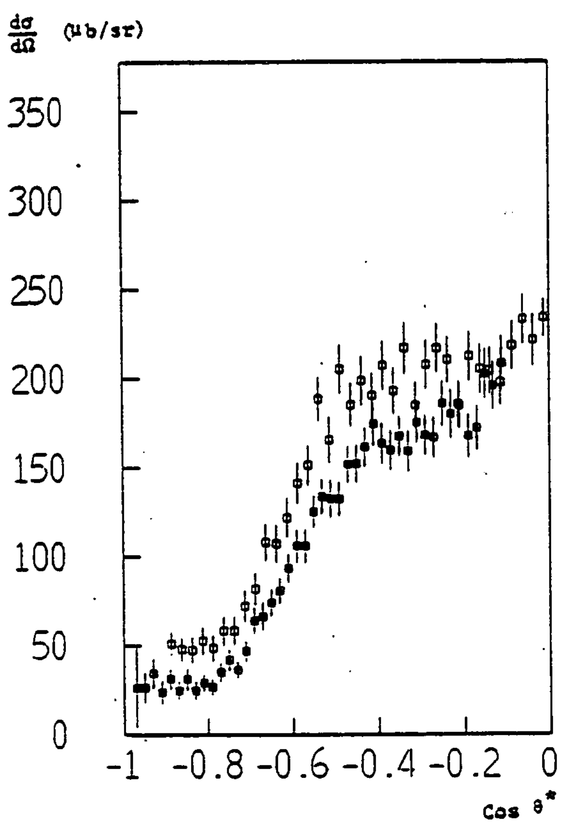

2.01 GEV/C

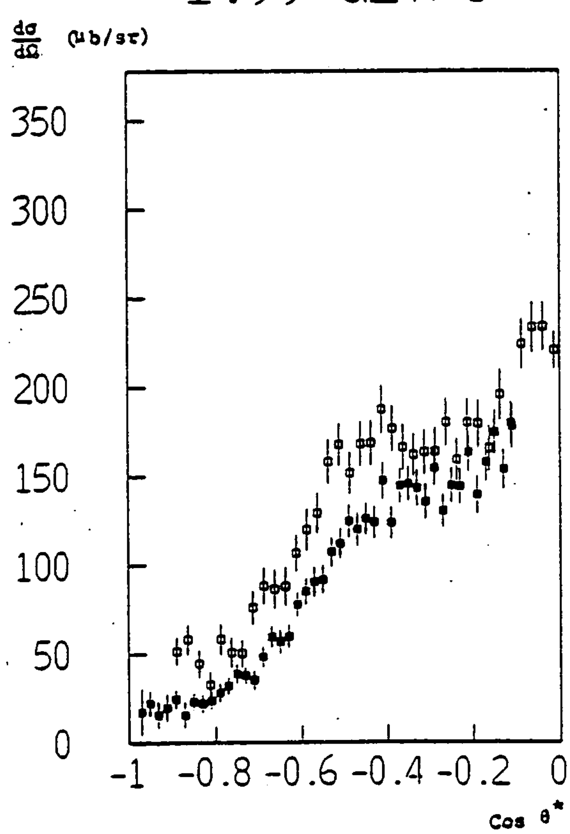

2.08 GEV/C

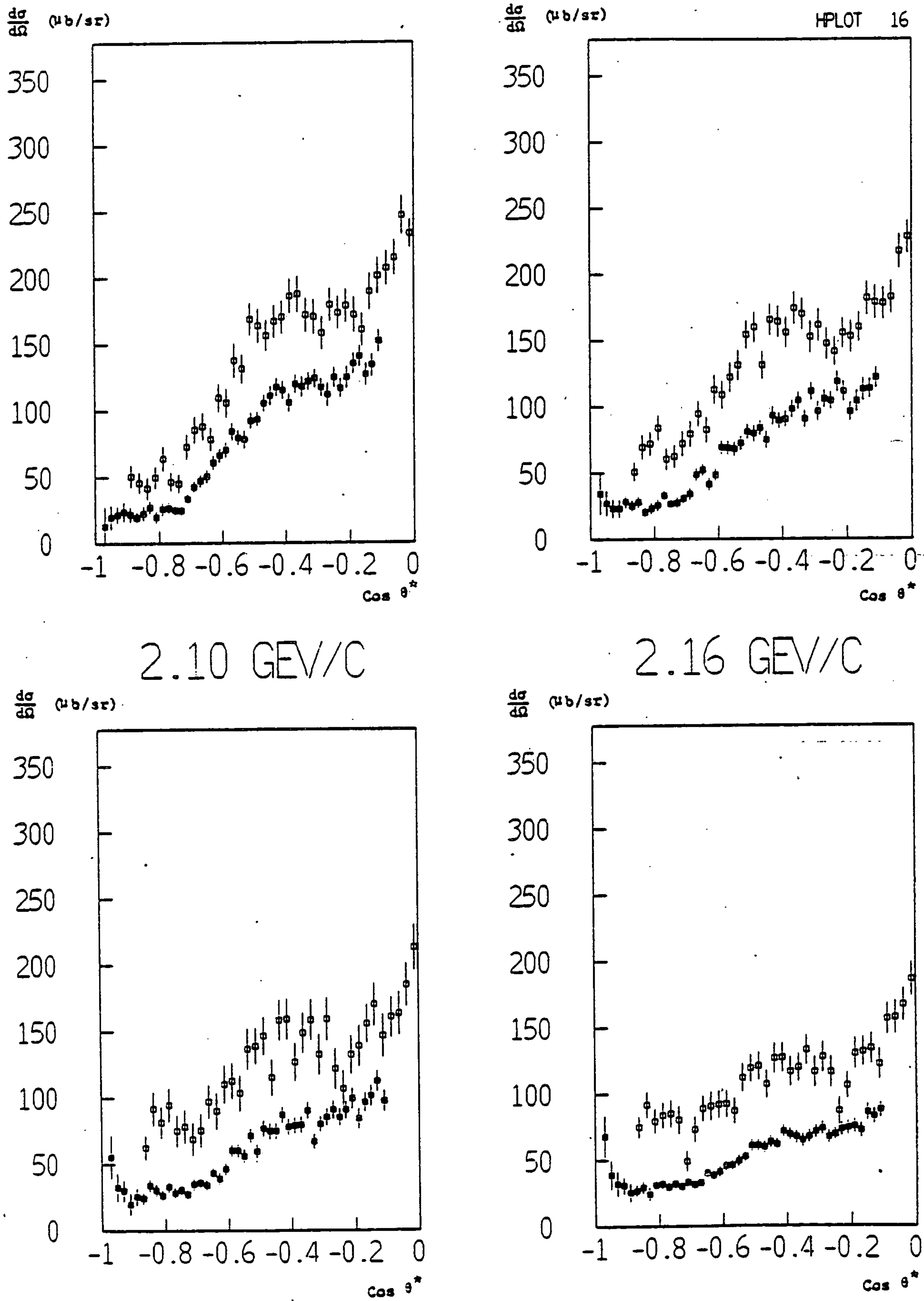

2.10 GEV/C

2.16 GEV/C

2.20 GEV/C

2.25 GEV/C

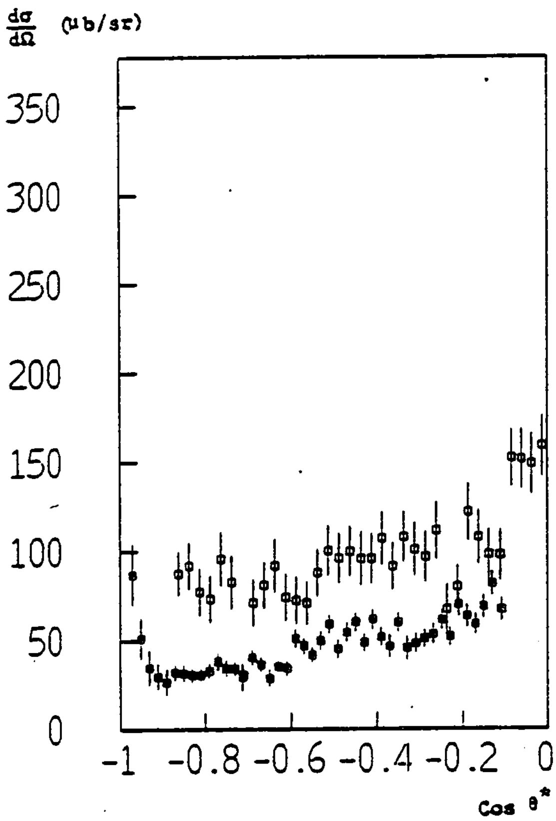

2.29 GEV/C

from the possible systematic error in the magnetic field measurement (estimated to be $\sim$ 0.5%) and the effect of possible systematic errors in the positions of the beam MWPC's (estimated to be $\sim$ 0.2%), to be $\sim$ 0.015 GeV/c which is much smaller than the required shift. The error in the central beam momentum quoted by the Abe experiment was $\sim$ 0.007 GeV/c which is also much smaller than the required shift. In addition a shift in the RMS data of the order required to obtain agreement with the Abe data would destroy the good agreement with the data of Busza et al. and Bardsley et al. (still to be discussed).

Not only was a difference in normalisation observed between these two data samples but a significant shape difference was also observed in the first order fit coefficients R_1 (see Figure 6.4.8) with the Abe coefficients being consistently lower than the RMS coefficients. Higher order coefficients were found to agree fairly well (within errors).

Comparison with Bardsley et al.[17]

The data of Bardsley et al. extended to an upper beam momentum of 2.13 GeV/c thus enabling a comparison with the differential cross sections obtained at the lowest five RMS momentum settings presented in this thesis. The linearly interpolated cross sections of Bardsley et al. at these five momenta are shown superimposed on the RMS cross sections in Figure 6.4.2. This figure shows that the two data samples are in reasonable agreement at all momenta although the Bardsley data contains several points at the two highest momenta which look "spuriously" high (at $\cos\theta^* \stackrel{\sim}{\sim} -0.5$). These points will distort the comparison of the Legendre coefficients in Figure 6.4.7 to 6.4.9 to

FIGURE 6.4.2: Comparison of the RMS differential cross sections with those of Bardsley et al.

KEY

This experiment.

Bardsley et al.

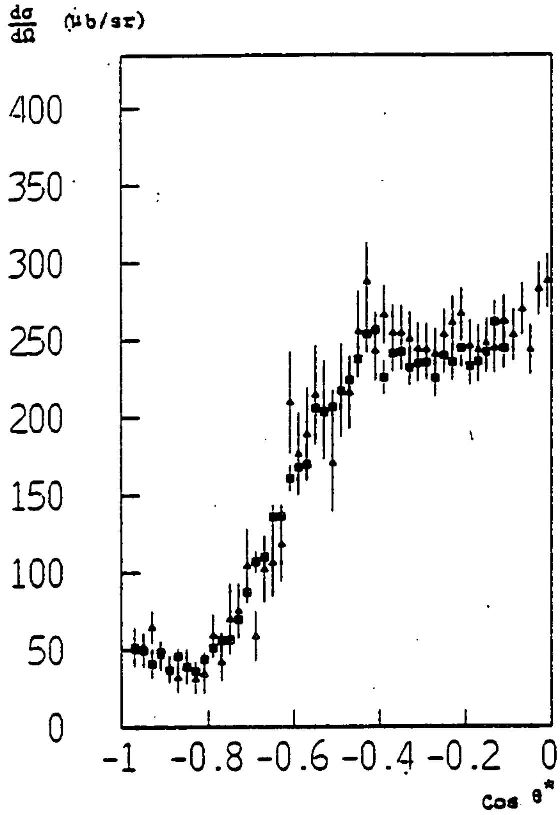

1.91 GEV/C

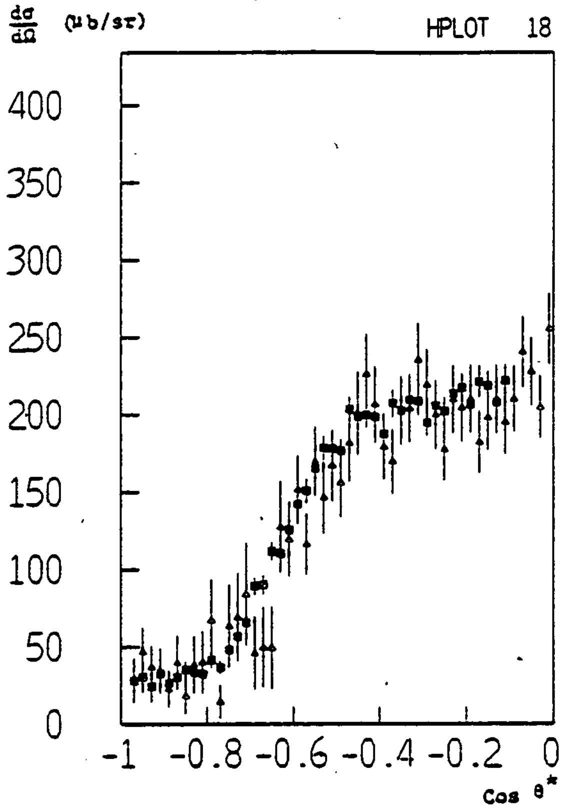

1.99 GEV/C

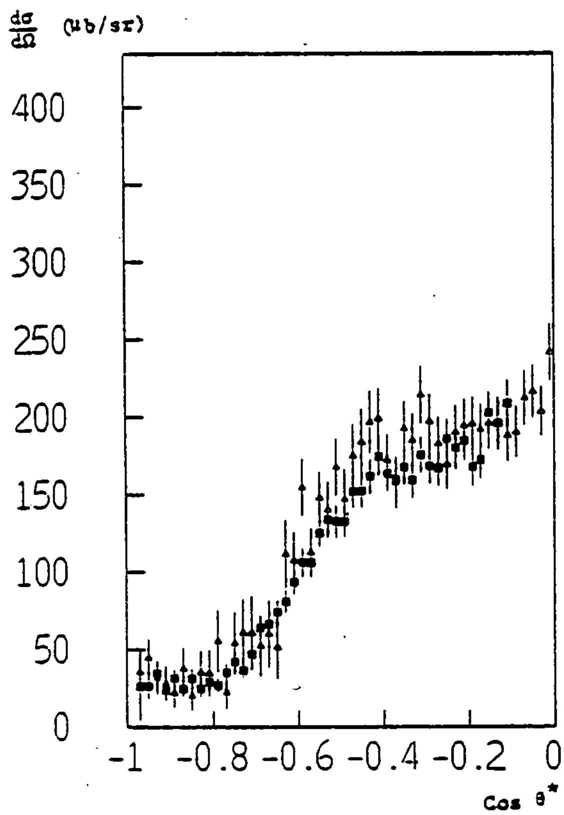

2.01 GEV/C

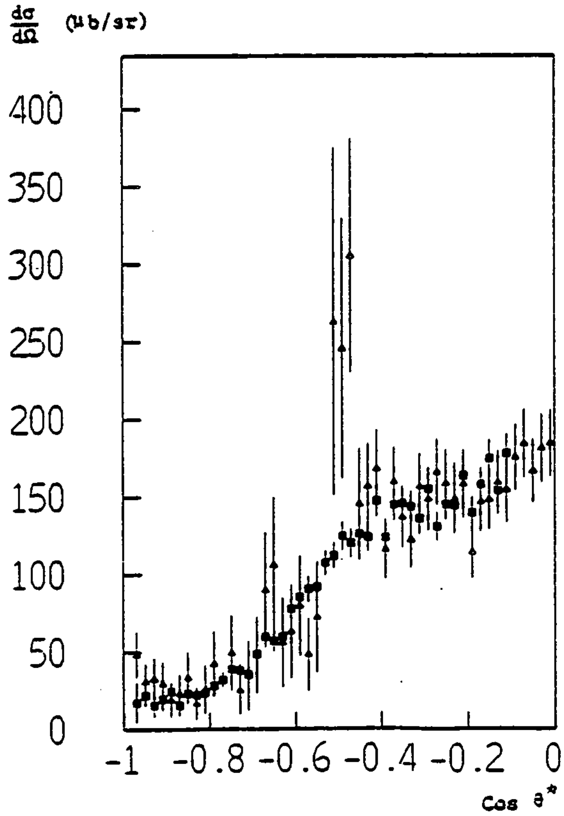

2.08 GEV/C

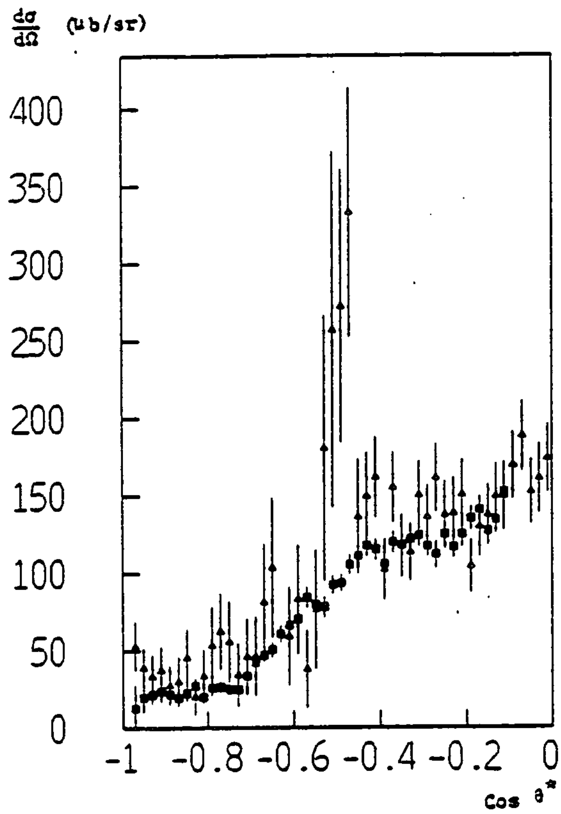

$\frac{d\sigma}{d\Omega}$ (μb/sr)
400
350
300
250
200
150
100
50
0
-1
-0.8
-0.6
-0.4
-0.2
0
Cos θ*

2.10 GEV/C

some extent. This distortion is most marked in the plot of Q_o (Figure 6.4.7) in which Bardsley's top two momentum points are significantly higher than the RMS data points. By linearly interpolating Bardsley's Q_o coefficients the data of Bardsley et al. was found to be $\sim$ 15% higher than the RMS data at 2.08 GeV/c and $\sim$ 34% higher than the RMS data at 2.10 GeV/c. If the effect of the "spuriously" high points was taken into account in the calculation of Q_o the data of Bardsley et al. was found to agree with the RMS data to within 11% at all momenta except 2.10 GeV/c where Bardsley's data was still some 26% higher than the RMS data. Due to the preliminary nature of the Bardsley data no estimate of the normalisation error on this data or of the error on the beam momentum can be given. Despite this the normalisation discrepancies between the two data samples can be accounted for fairly adequately at all momenta except 2.10 GeV/c by the normalisation errors of the RMS experiment ($\sim$ 6%) and by the estimated linear interpolation errors on the Bardsley data ($\sim$ 6%). In addition at 2.10 GeV/c the statistical errors on the Bardsley data were comparable with the observed normalisation discrepancy between the two data samples and hence care should be taken not to read too much into this discrepancy.

In addition to the good agreement in normalisation between the Bardsley and the RMS data the shapes were also found to be in reasonable agreement as can be seen from Figures 6.4.8 to 6.4.9. The only serious discrepancy in these figures is in the first order coefficient, R_1, (Figure 6.4.8) at Bardsley's highest momentum where the Bardsley coefficient is somewhat lower than the RMS data. It is, however, difficult to assess whether this discrepancy is significant or is a distortion caused by the "spuriously" high points.

Comparison with Ott et al.[18]

The data of Ott et al. extended to an upper beam momentum of 1.917 GeV/c and hence a comparison could only be made with this experiment at the lowest RMS momentum setting presented in this thesis (1.91 GeV/c). Also, due to the limited $\cos\theta^*$ range of the Ott experiment, no fit was performed to this data and hence no comparison of fit coefficients could be made. The linearly interpolated differential cross section of Ott et al. at 1.91 GeV/c is shown superimposed on the RMS cross section in Figure 6.4.3. It can be seen from this figure that there is a large normalisation difference between the two experiments with the Ott data being some 40% lower than the RMS data. This discrepancy is perhaps not too serious since the Ott experiment had difficulty in distinguishing beam pions from beam protons at the upper end of their momentum range and large corrections to the number of beam pions used in normalising the data had to be applied. These corrections were not well known and hence any systematic error in them could seriously affect the Ott normalisation.

Comparison with Busza et al.[19]

The data of Busza et al. extended from 1.72 GeV/c to 2.80 GeV/c and hence a comparison with the data presented in this thesis could be made at all thirteen momentum settings. The linearly interpolated differential cross sections of Busza et al. at these thirteen momentum settings are shown superimposed on the RMS cross sections in Figure 6.4.4. As can be seen from these plots the data of Busza et al. is subject to large statistical errors and thus care must be taken not to read too much into the comparison of this data with the RMS data. Despite this difficulty (or perhaps because of it) the Busza data is

FIGURE 6.4.3: Comparison of the RMS differential cross sections with those of Ott et al.

KEY

This experiment

Ott et al.

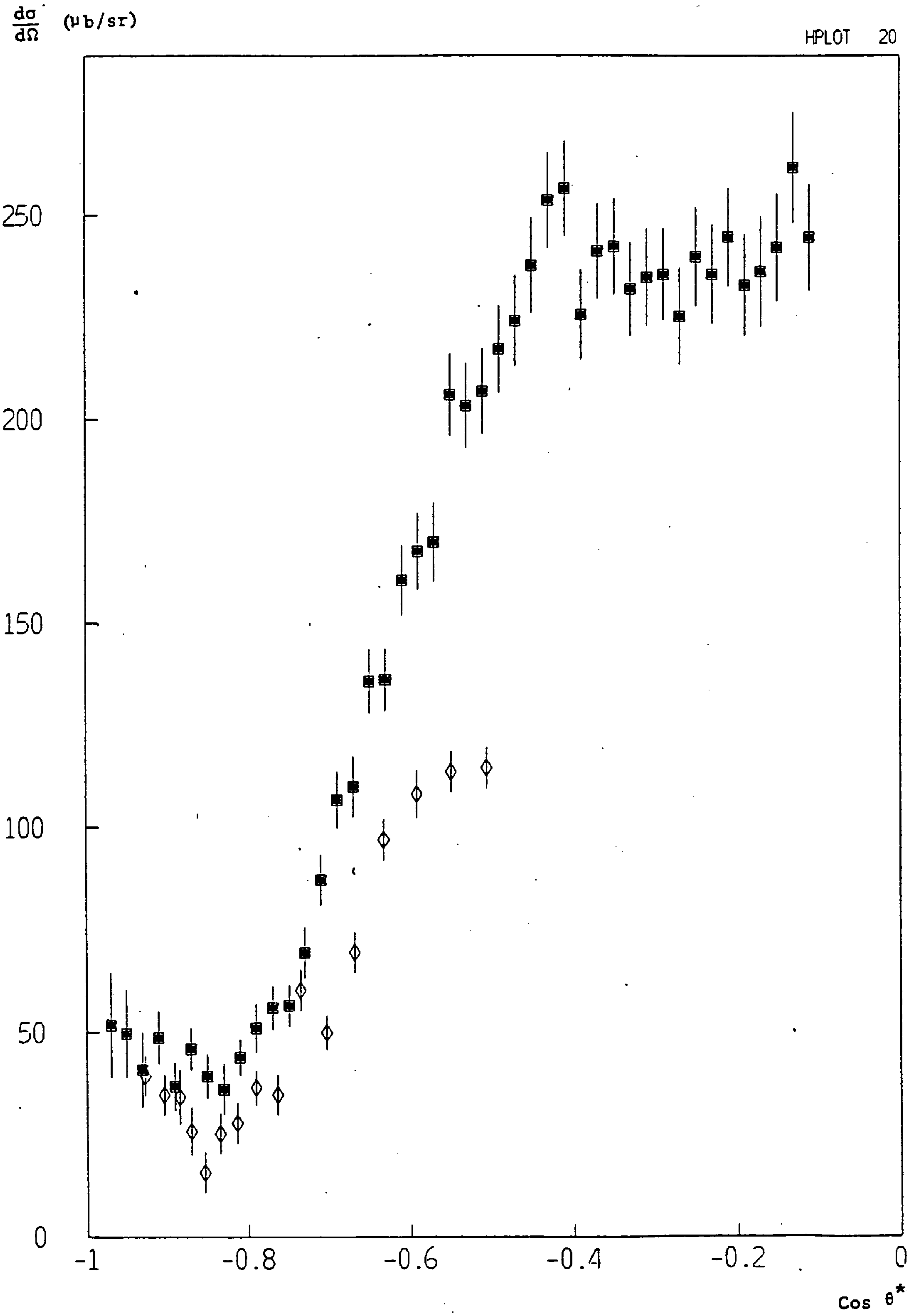
$\frac{d\sigma}{d\Omega}$ (μb/sr)
HPLOT 20
250
200
150
100
50
0
-1
-0.8
-0.6
-0.4
-0.2
0
Cos θ*

1.91 GEV/C

<u>FIGURE 6.4.4:</u> Comparison of the RMS differential cross sections with those of Busza et al.

<u>KEY</u>

This experiment

Busza et al.

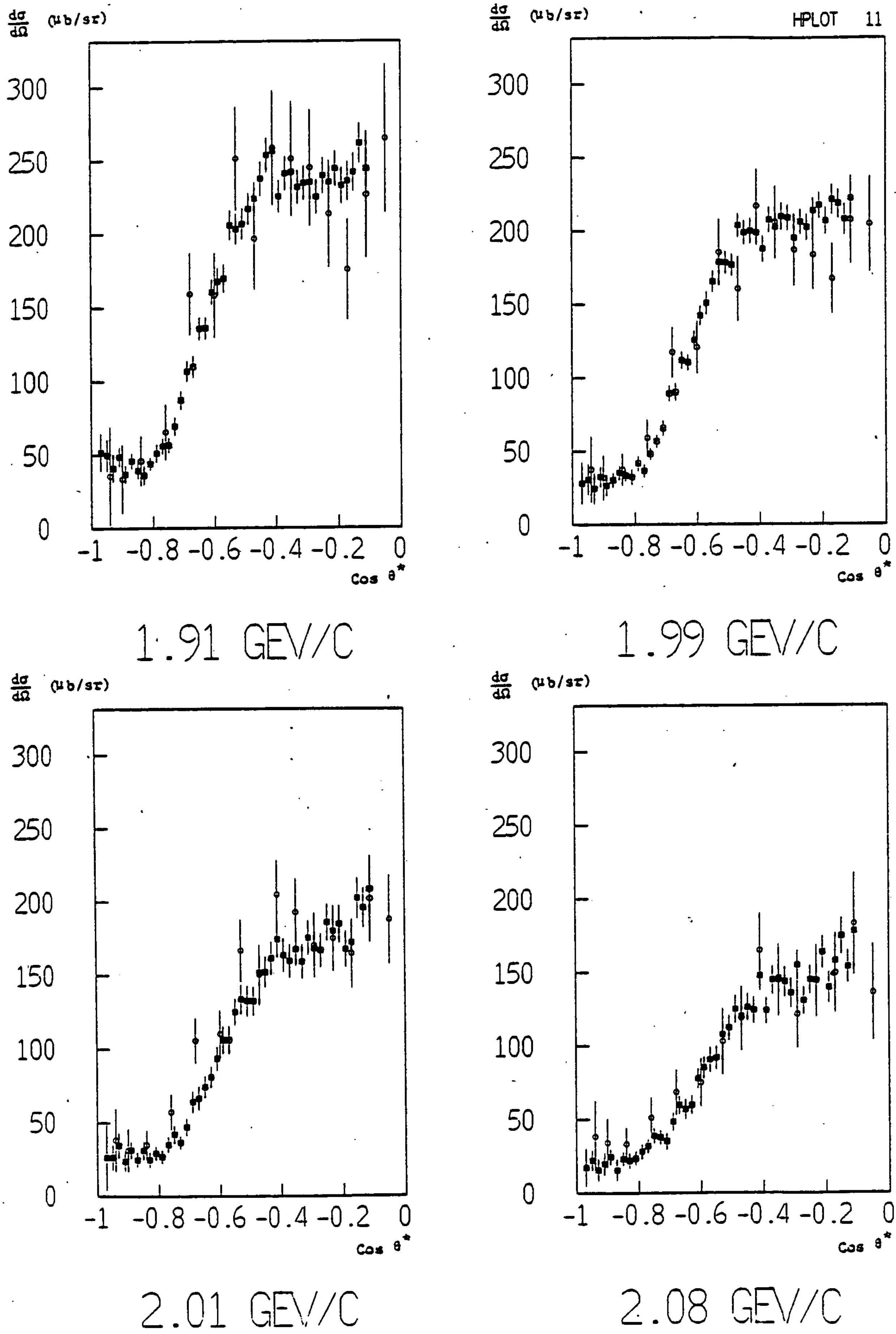
HPLOT 11
dσ/dΩ (μb/sr)
Cos θ*
1.91 GEV/C
1.99 GEV/C
2.01 GEV/C
2.08 GEV/C

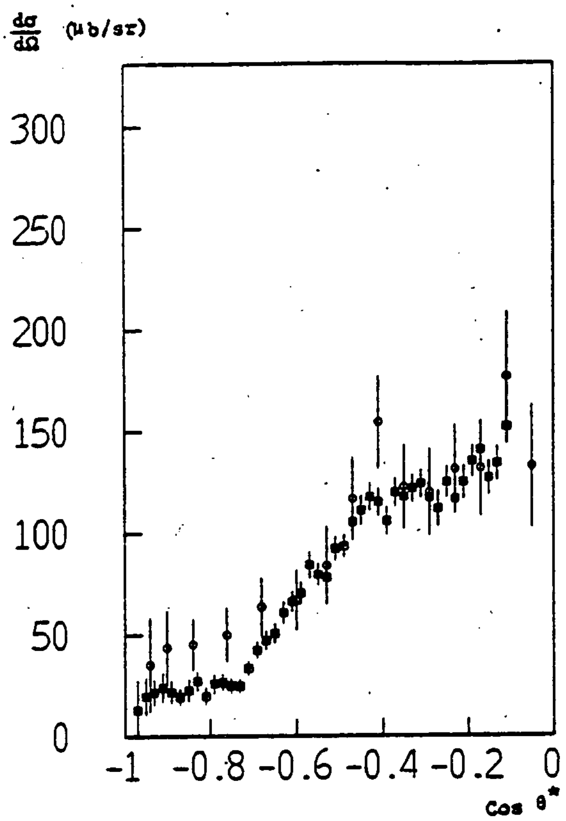

2.10 GEV/C

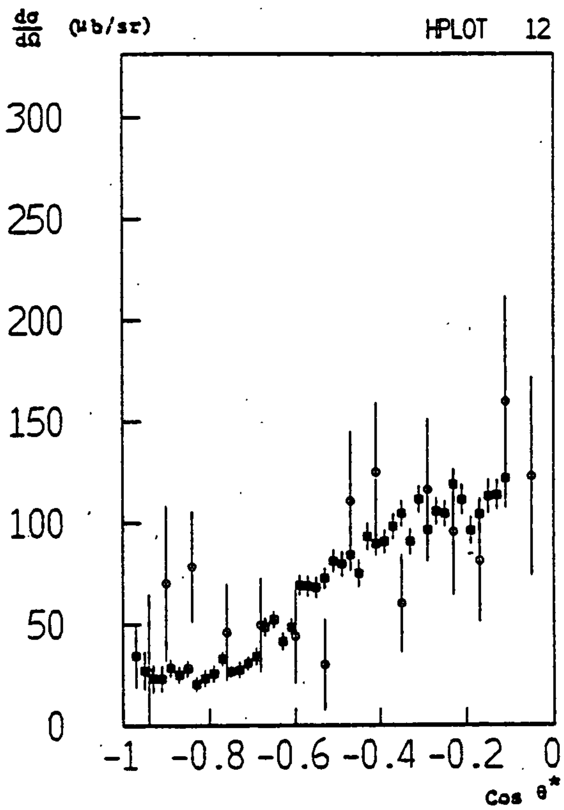

2.16 GEV/C

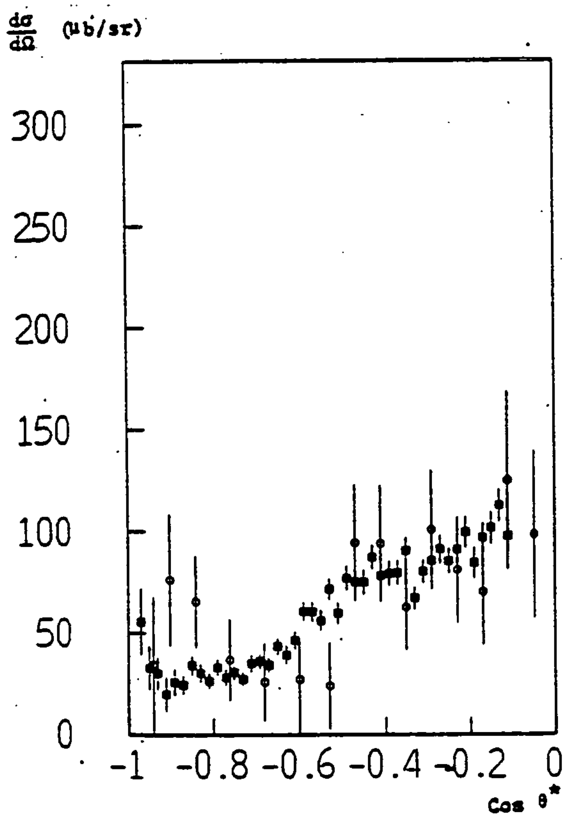

2.20 GEV/C

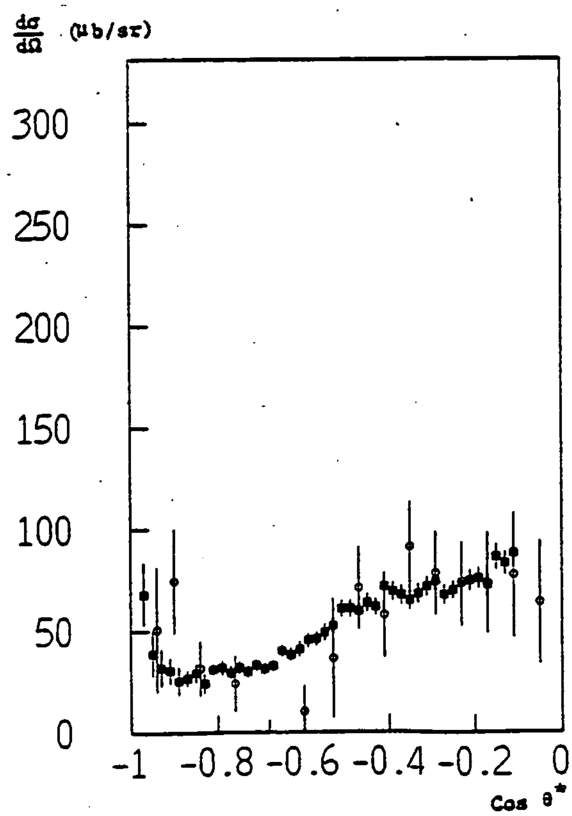

2.25 GEV/C

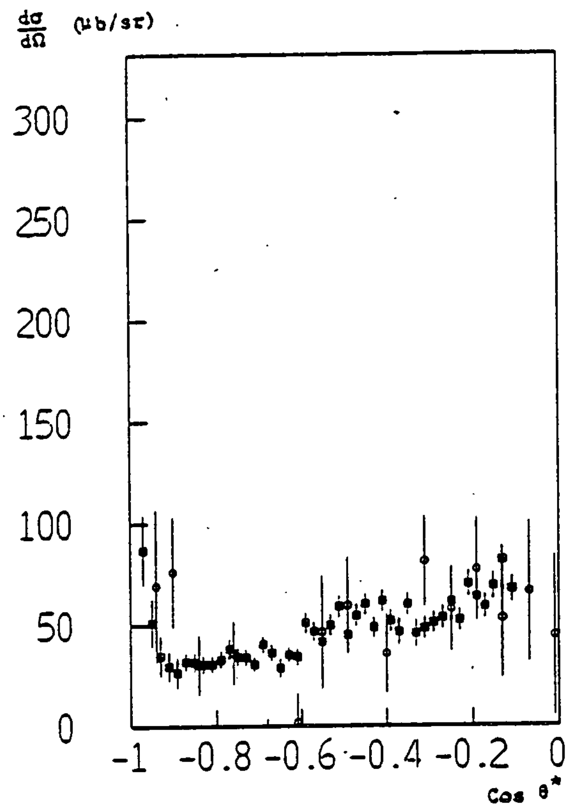

2.29 GEV/C

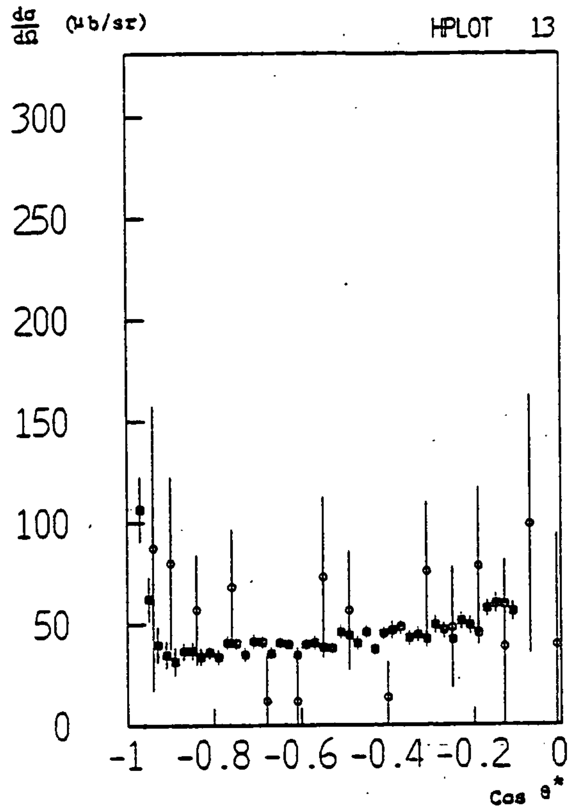

2.34 GEV/C

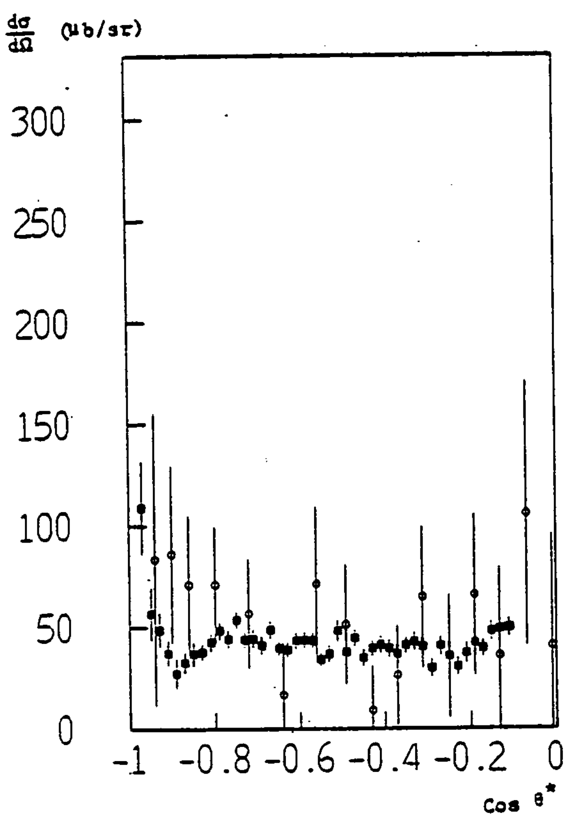

2.38 GEV/C

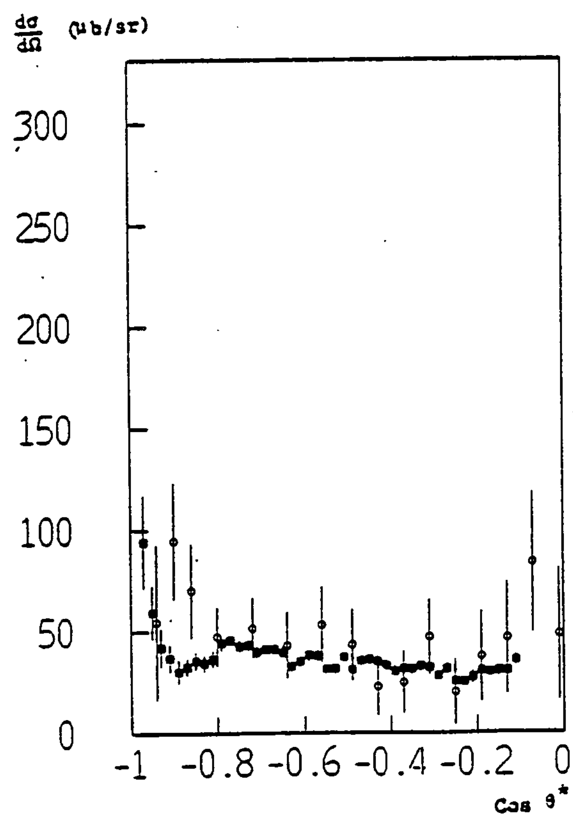

2.43 GEV/C

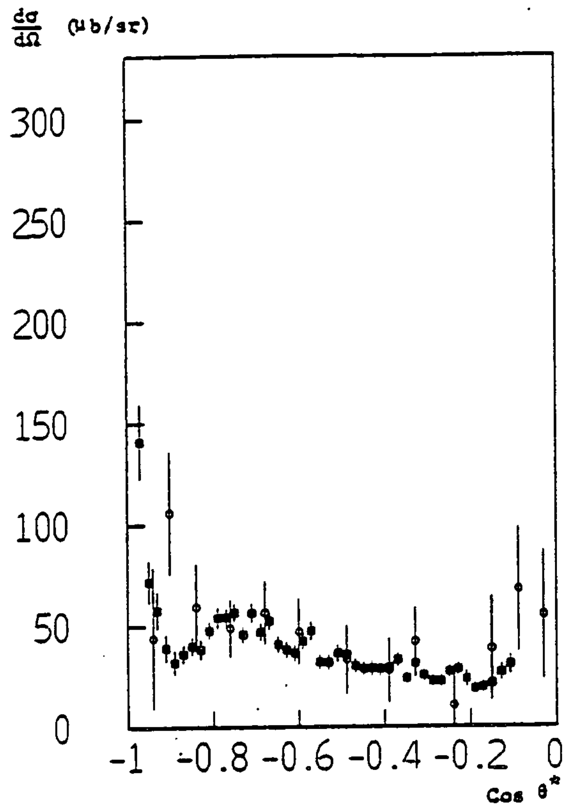

2.48 GEV/C

seen to be in good agreement with the RMS data at all thirteen momenta. Due to the large statistical errors it is almost impossible to make any statement about the relative shapes of the two data samples especially at the higher momenta where the errors are larger and the differential cross sections are fairly flat over a large part of the RMS $\cos\theta^*$ range. This difficulty is reflected in the large errors on the fitted R_1 and R_2 coefficients shown in Figures 6.4.8 and 6.4.9. The zero'th order coefficients, Q_o, which measure the relative normalisation between the two data samples are seen (in Figure 6.4.7) to be in good agreement throughout the momentum range.

Comparison with the Helsinki-Karlsruhe Partial Wave Analysis[13]

The interpolated differential cross sections, obtained from the amplitudes of the Helsinki-Karlsruhe partial wave analysis, are shown superimposed on the thirteen RMS cross sections presented in this thesis in Figure 6.4.5. It can be seen from this figure that there are significant differences between the RMS data and the partial wave analysis. The major discrepancy lies in the region above $\cos\theta^* \approx -0.8$ where the RMS cross sections are consistently lower than, and have a different gradient from the Helsinki-Karlsruhe cross sections. This discrepancy is observed at all momenta with the exception of 1.99 GeV/c. The differences between the RMS data and the analysis show up in the Legendre coefficient plots in two ways. Firstly the RMS Q_o coefficients are consistently lower than those of the partial wave analysis by approximately 20% (see Figure 6.4.7). Despite this discrepancy it can be seen from this plot that the smooth variation of Q_o with momentum predicted by the Helsinki-Karlsruhe analysis is observed by the RMS experiment.

FIGURE 6.4.5: Comparison of the RMS differential cross sections with those of the Helsinki-Karlsruhe partial wave analysis.

KEY

This experiment.

——The Helsinki-Karlsruhe partial wave analysis.

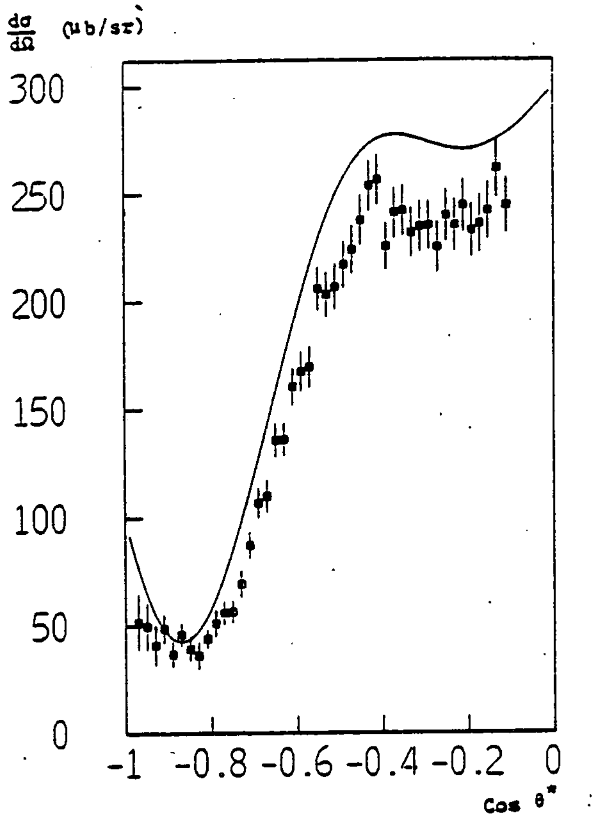

1.91 GEV/C

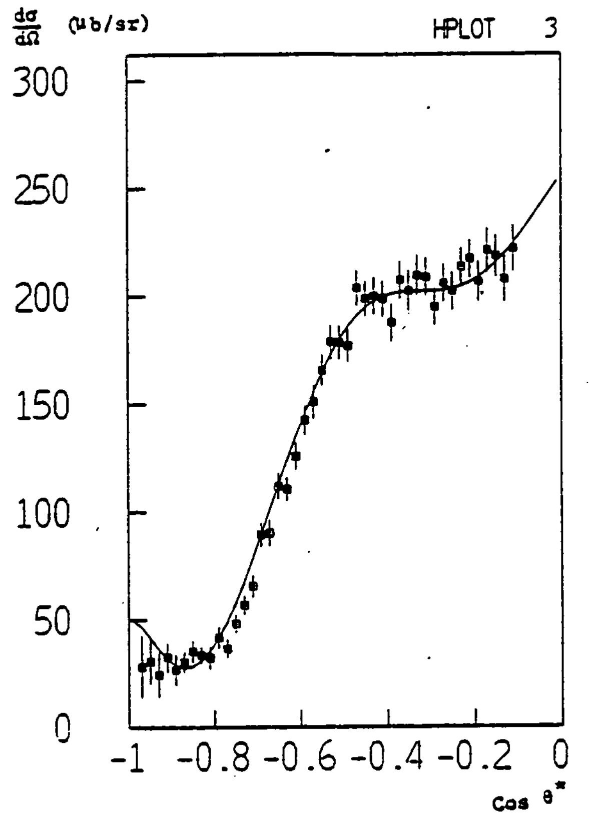

1.99 GEV/C

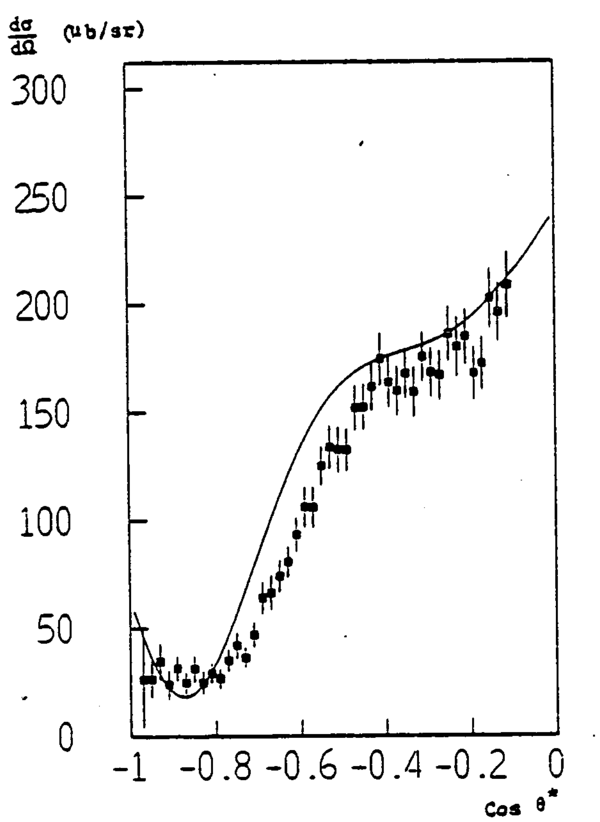

2.01 GEV/C

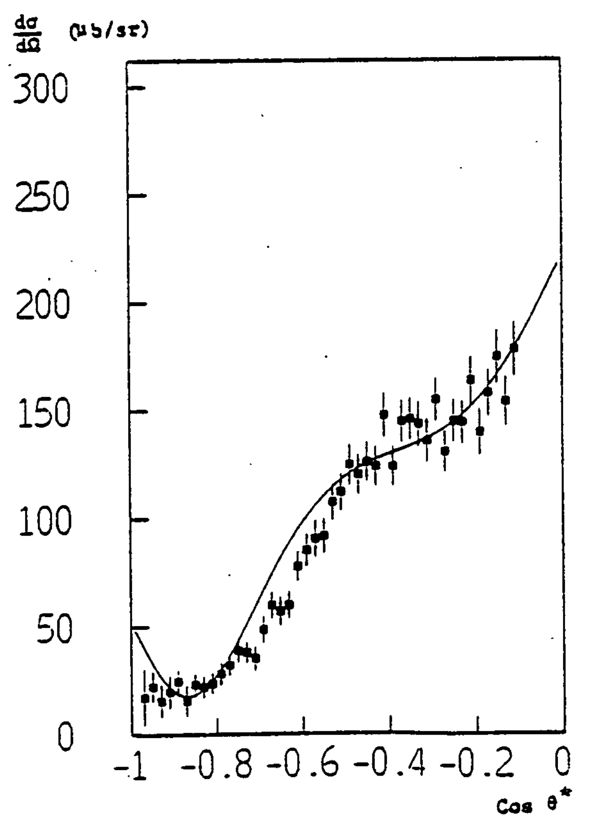

2.08 GEV/C

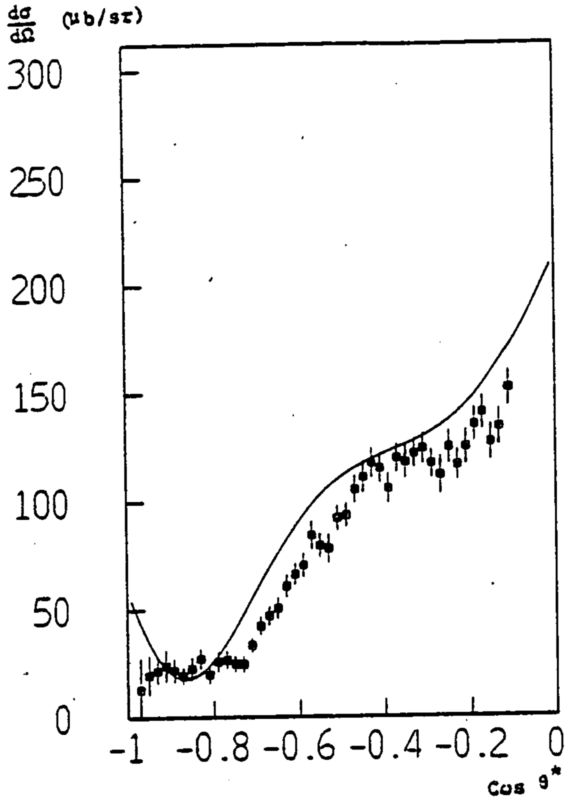

2.10 GEV/C

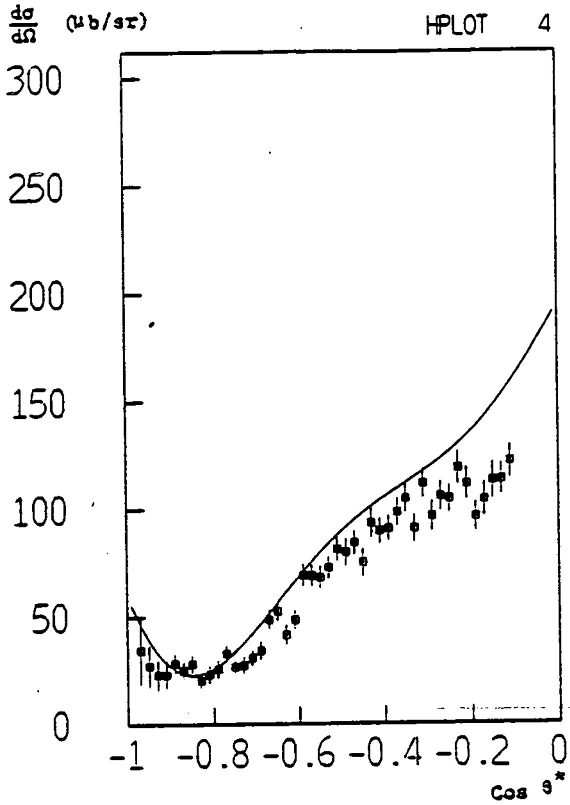

2.16 GEV/C

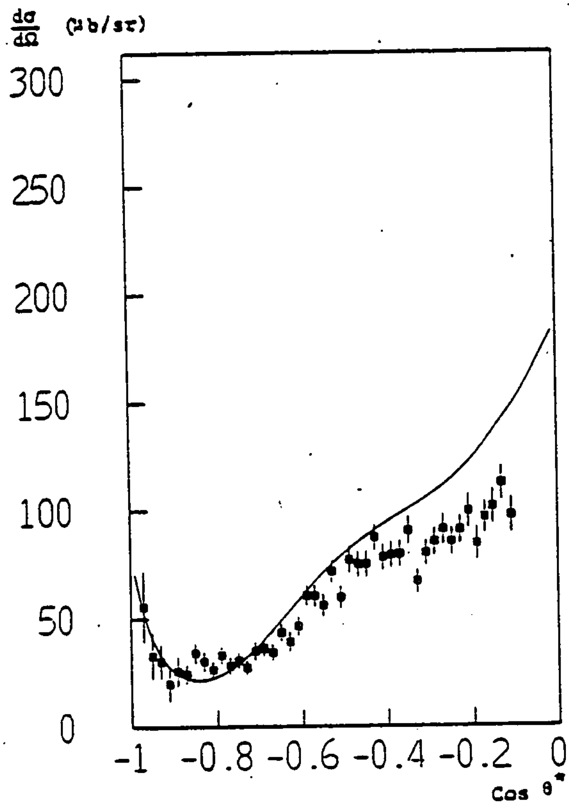

2.20 GEV/C

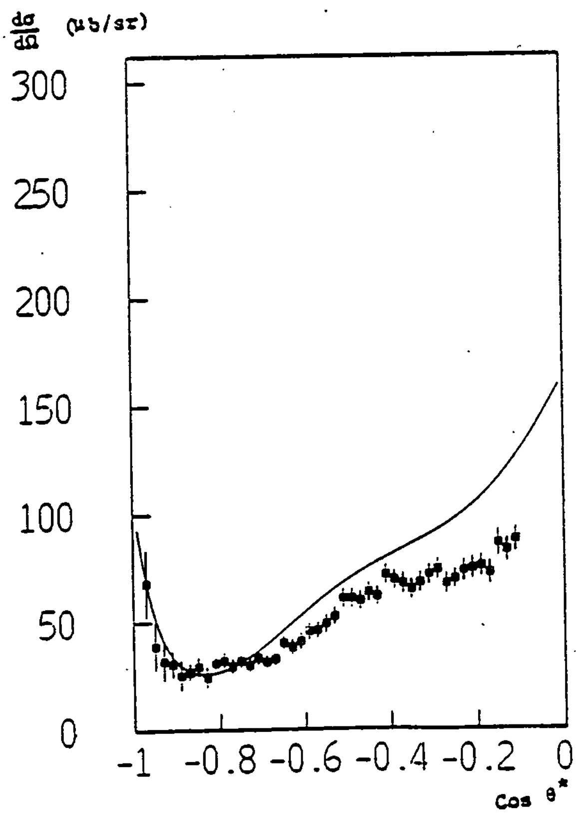

2.25 GEV/C

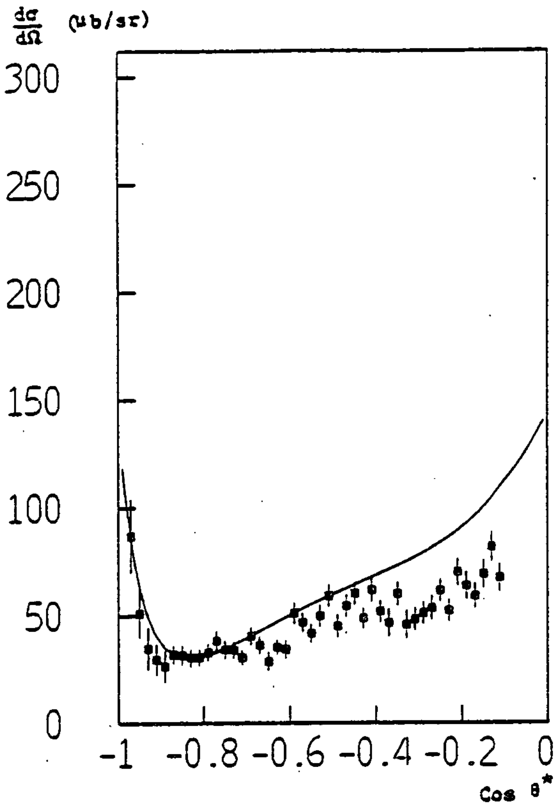

2.29 GEV/C

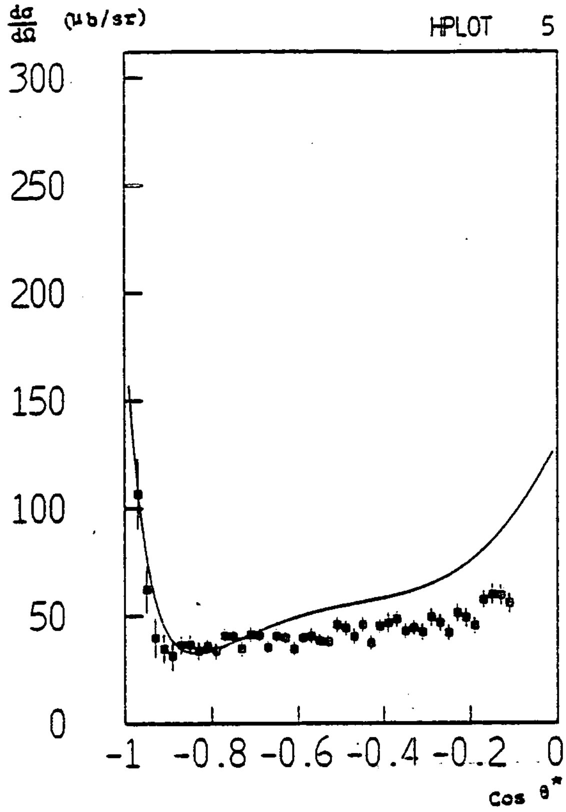

2.34 GEV/C

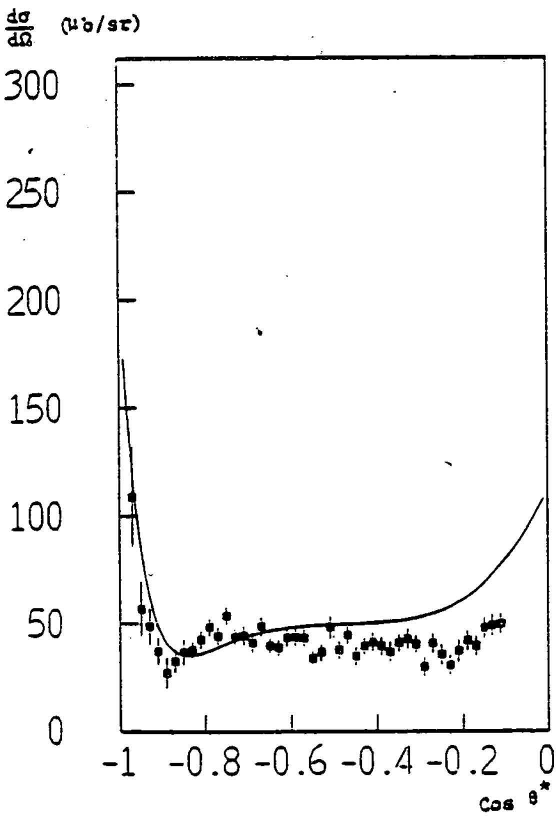

2.38 GEV/C

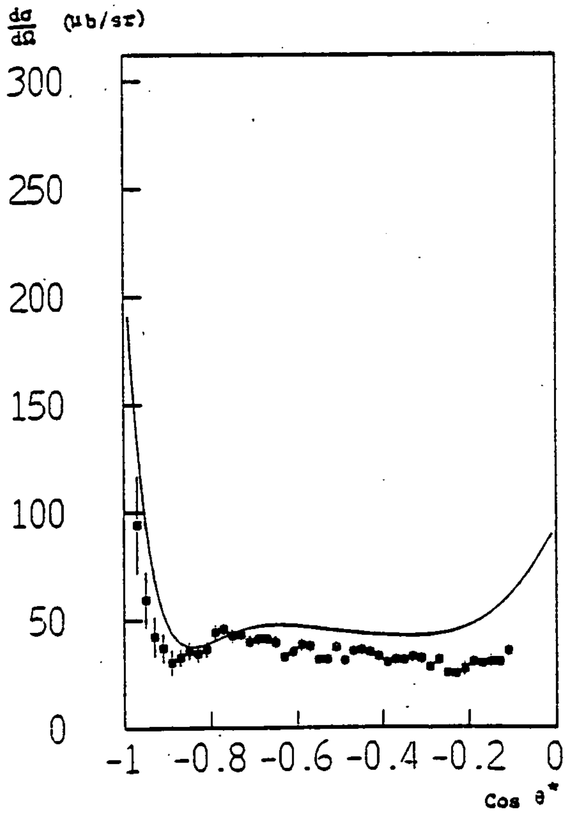

2.43 GEV/C

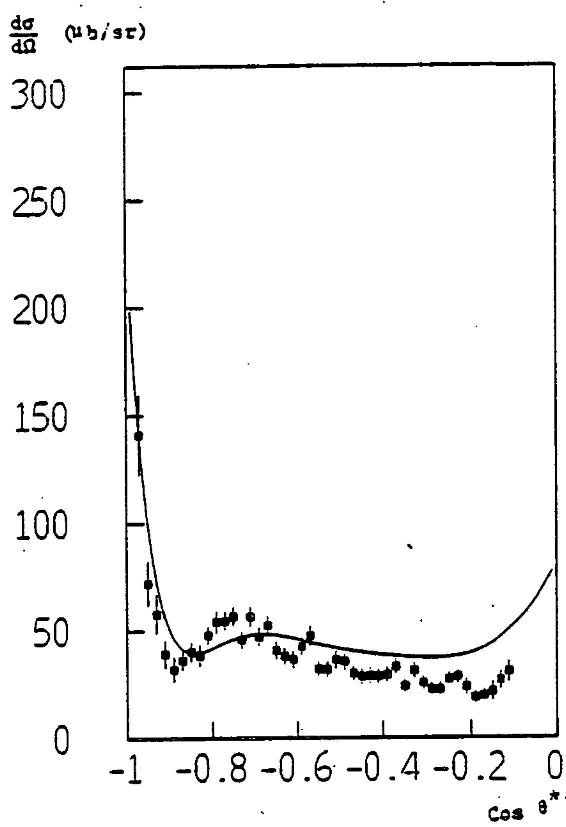
$\frac{d\sigma}{d\Omega}$ (μb/sr)
300
250
200
150
100
50
0
-1
-0.8
-0.6
-0.4
-0.2
0
Cos θ*

2.48 GEV/C

(Note that the RMS data points have a $\pm$ 6% normalisation error associated with them which is not shown in Figure 6.4.7.) Secondly the first order coefficients, R_1, (which are a measure of the gradients of the linear components of the fits) show consistent differences between the RMS experiment and the analysis.

Despite these discrepancies the RMS data is closer to the Helsinki-Karlsruhe partial wave analysis than the data of Abe et al. is. This is perhaps a little surprising since the analysis uses the Abe data as part of its input and, since the Abe experiment is the highest statistics π^+p experiment in this energy region, would be expected to be highly constrained by it. The deviation of the analysis from the data of Abe et al. indicates that theoretical considerations and/or data from other channels are constraining the analysis.

In addition to the discrepancies previously discussed there is also a discrepancy between the RMS data and the partial wave analysis in the extreme backward region ($\cos\theta^* \lesssim -0.9$) where the RMS cross sections are consistently lower than the partial wave analysis cross sections. This discrepancy is probably not significant due to the large uncertainties in the RMS cross sections in this region caused by the linear background subtraction procedure.

Comparison with the CMU-LBL Partial Wave Analysis(24)

The interpolated differential cross sections of the CMU-LBL partial wave analysis are shown superimposed on the thirteen RMS cross sections presented in this thesis in Figure 6.4.6. This figure shows that there are significant differences between the RMS data and the partial wave analysis especially in terms of overall

FIGURE 6.4.6: Comparison of the RMS differential cross sections with those of the CMU-LBL partial wave analysis.

KEY

This experiment.

——The CMU-LBL partial wave analysis.

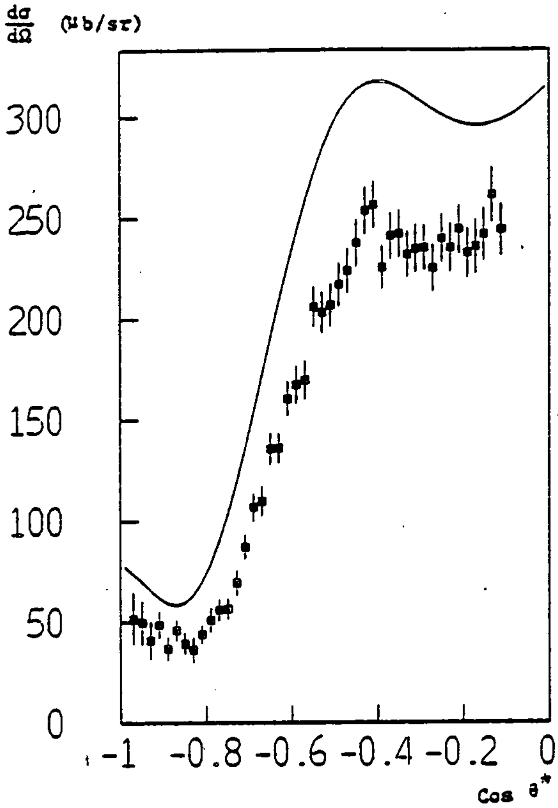

1.91 GEV/C

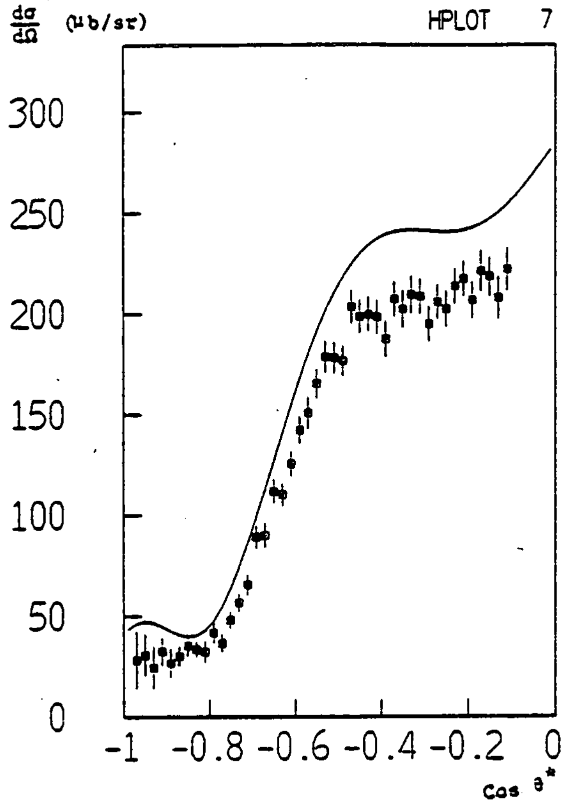

1.99 GEV/C

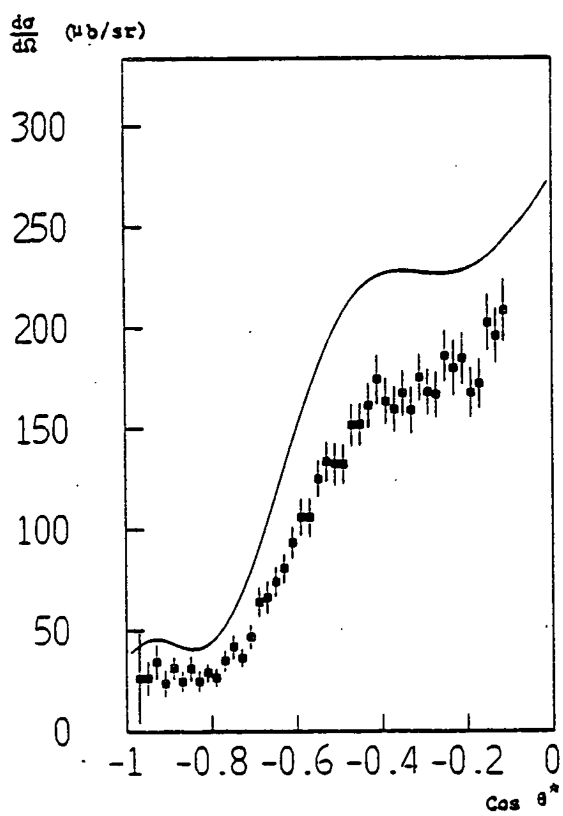

2.01 GEV/C

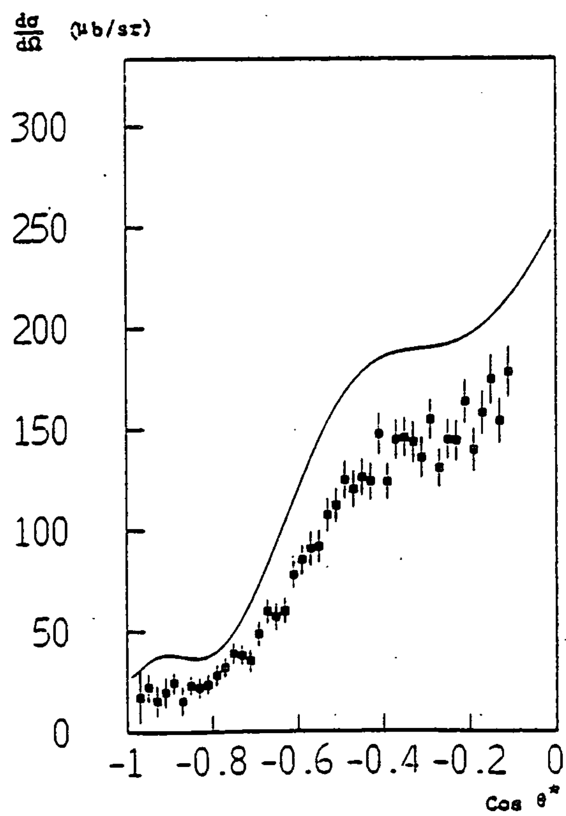

2.08 GEV/C

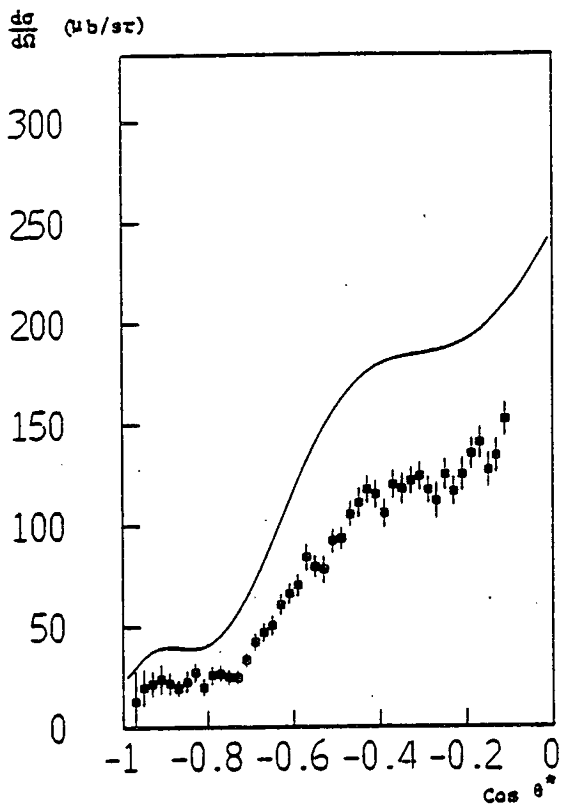

2.10 GEV/C

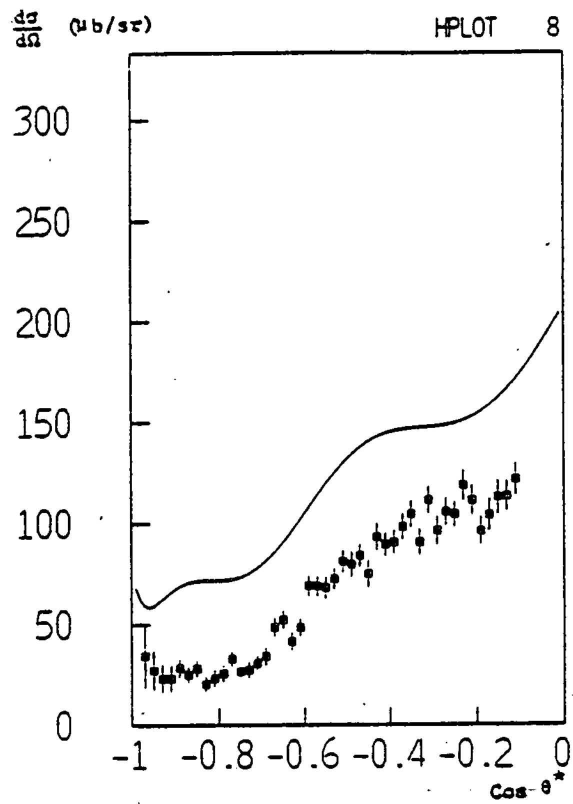

2.16 GEV/C

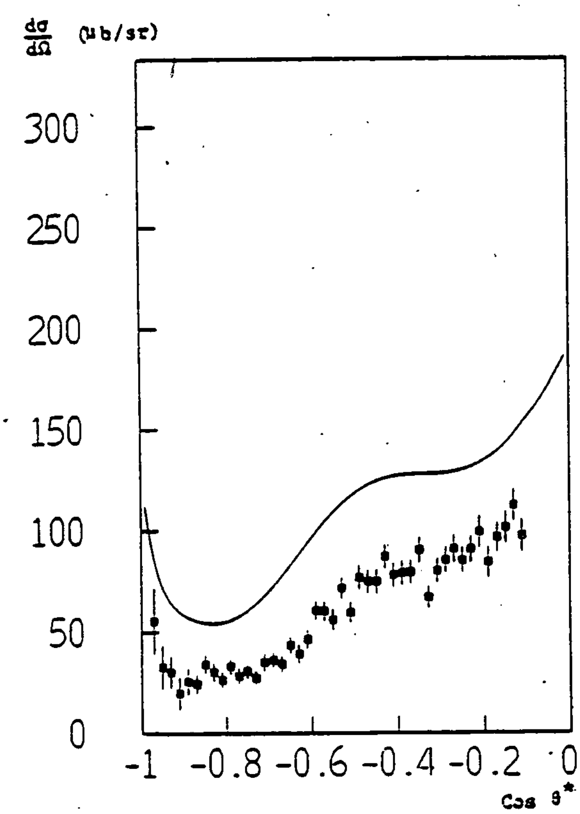

2.20 GEV/C

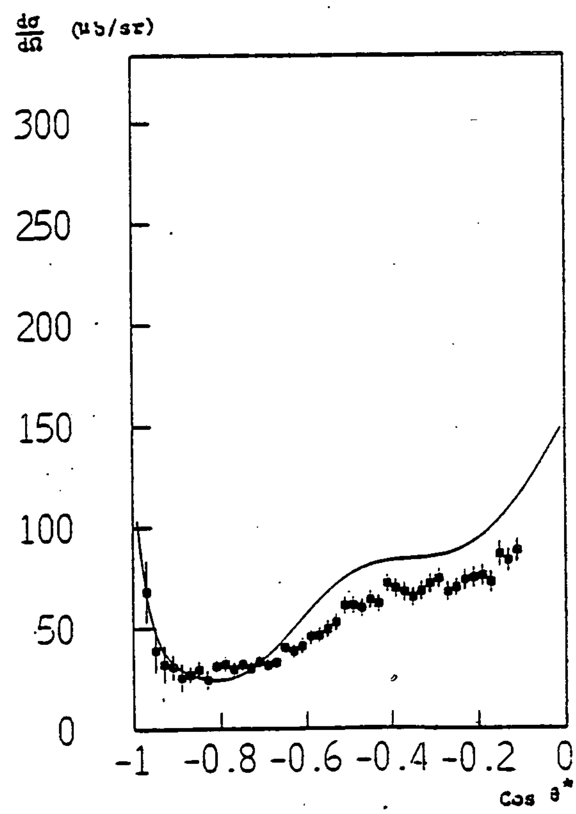

2.25 GEV/C

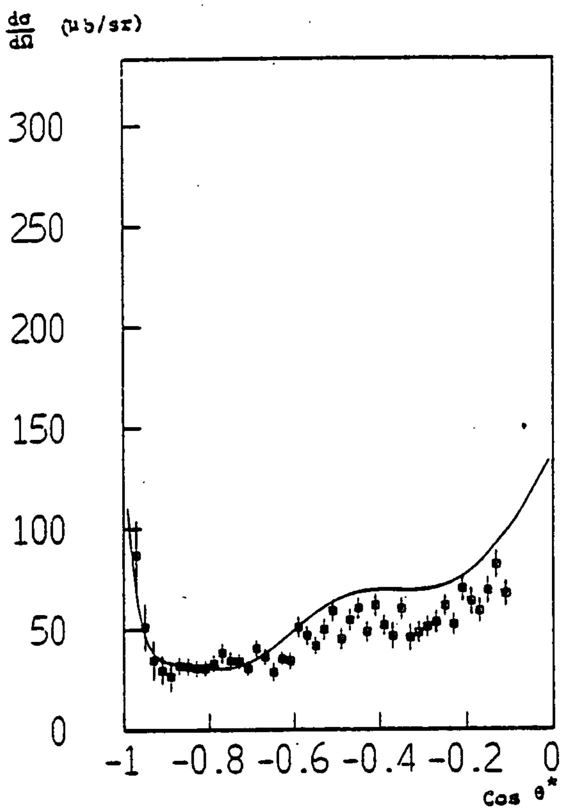

2.29 GEV/C

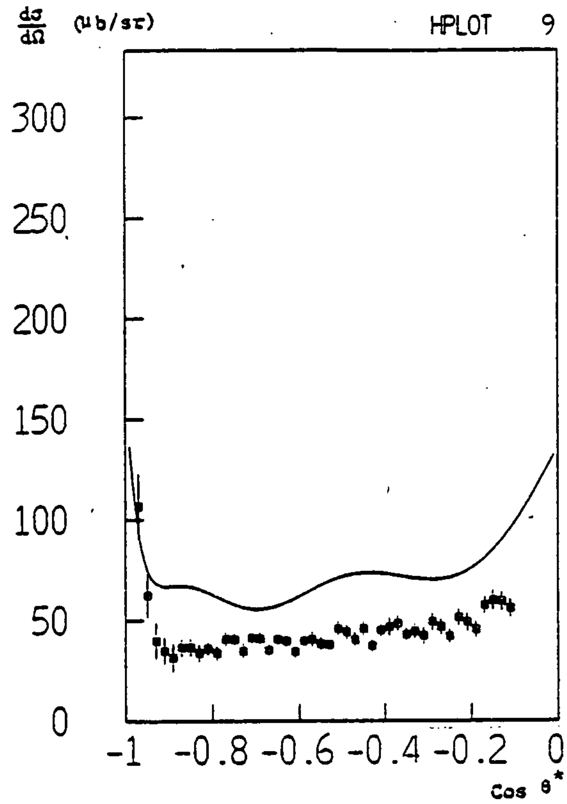

2.34 GEV/C

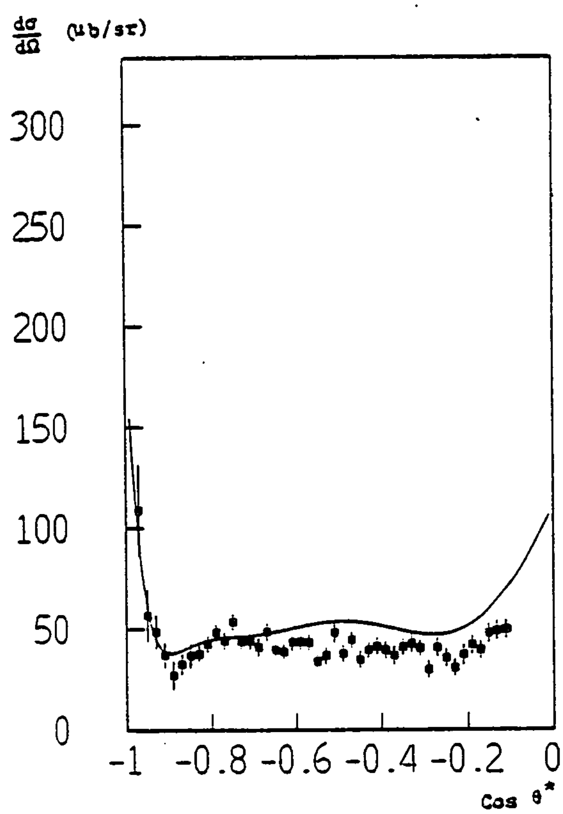

2.38 GEV/C

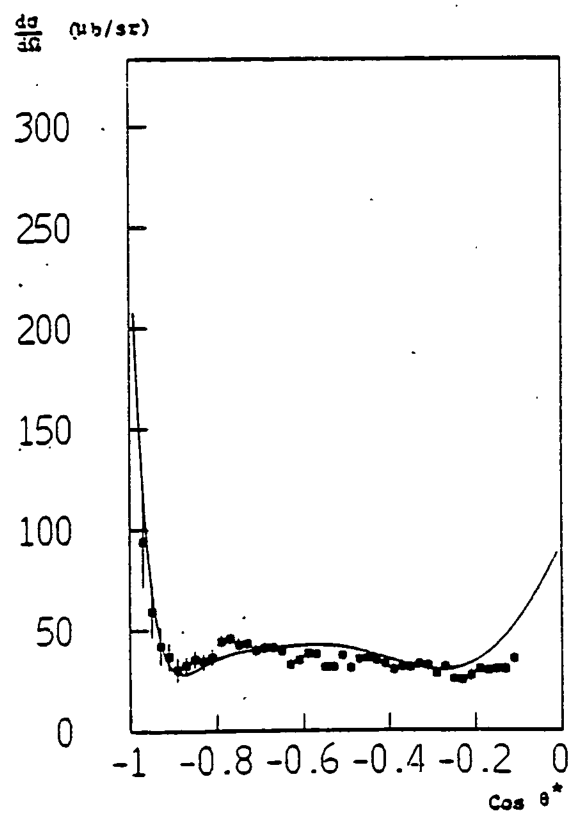

2.43 GEV/C

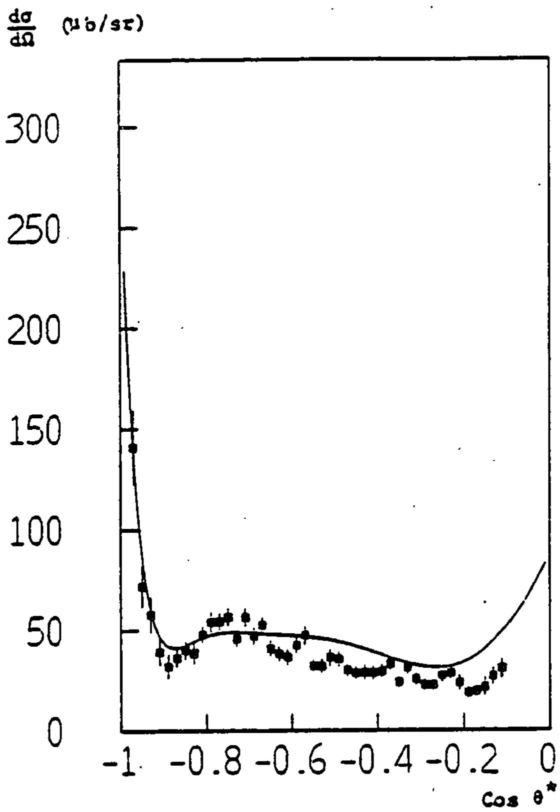
$\frac{d\sigma}{d\Omega}$ (μb/sr)
300
250
200
150
100
50
0
-1
-0.8
-0.6
-0.4
-0.2
0
Cos θ*

2.48 GEV/C

normalisation. These discrepancies are seen to be most serious at the lower momenta.

The normalisation differences show up clearly in the plot of the zero'th order Legendre fit coefficients, Q_o, versus momentum (Figure 6.4.7). It can be seen from this figure that the CMU-LBL cross sections are consistently higher than the RMS cross sections with discrepancies as large as 66% (at 2.16 GeV/c). This figure also shows that the CMU-LBL analysis follows the data of Abe et al. more closely than the Helsinki-Karlsruhe analysis does, thus providing an explanation for the discrepancies with the RMS data.

In addition to the normalisation differences between the RMS data and the CMU-LBL analysis a shape difference was observed in the first order Legendre coefficients, R_1 (Figure 6.4.8). The main difference in the R_1 coefficients was the large dip in the CMU-LBL coefficients at approximately 2.18 GeV/c which was not observed in the RMS data. As in the case of the normalisation differences this discrepancy seems to be caused by the CMU-LBL analysis following the data of Abe et al. more closely than the Helsinki-Karlsruhe analysis does. A similar dip was observed in both the Busza and Bardsley experiments, however these observations should, perhaps, be treated with some caution due to the large statistical errors on the Busza data and the possible effect of the "spuriously" high points in the Bardsley data.

In the extreme backward direction $(\cos\theta^* \lesssim -0.9)$ the RMS data seems to be in better agreement with the CMU-LBL analysis in terms of shape than with the Helsinki-Karlsruhe analysis (Figure 6.4.6). In particular the dip in the extreme backward cross section, in the region of 2.10 GeV/c, seen by the CMU-LBL analysis is in better agreement with the RMS data than is the Helsinki-Karlsruhe analysis. As mentioned previously, however, the uncertainties in the RMS cross sections in this region are rather large due to the linear background subtraction procedure and hence the discrepancy with the Helsinki-Karlsruhe analysis is probably not significant.

FIGURE 6.4.7: The zero'th order Legendre fit coefficients, Q_o, as a function of momentum.

KEY

■ This experiment

Abe et al.

Bardsley et al.

Busza et al.

——The Helsinki-Karlsruhe partial wave analysis

--- The CMU-LBL partial wave analysis.

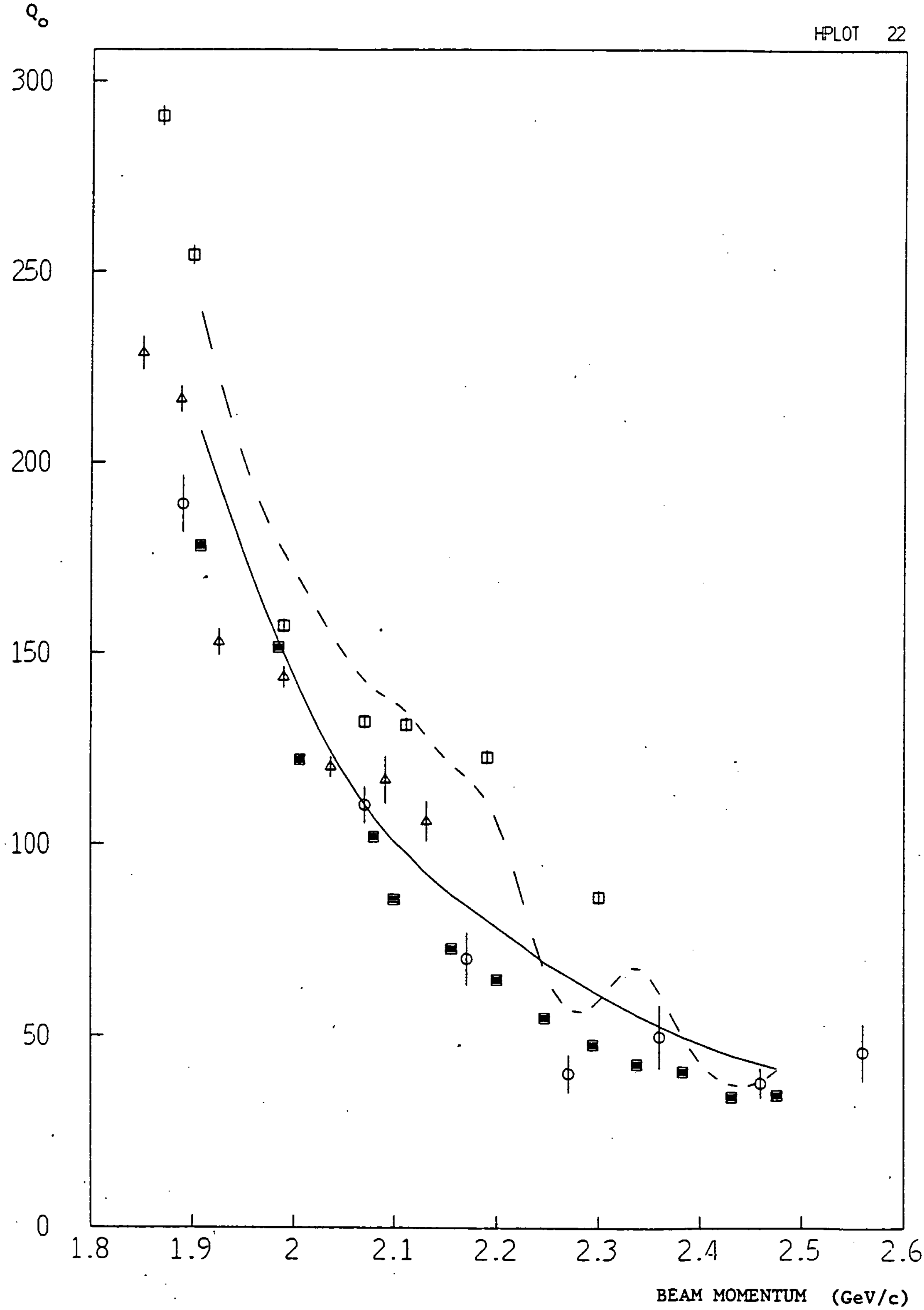

Q_o
HPLOT 22
300
250
200
150
100
50
0
1.8
1.9
2
2.1
2.2
2.3
2.4
2.5
2.6
BEAM MOMENTUM (GeV/c)

FIGURE 6.4.8: The first order Legendre fit coefficients, R_1, as a function of momentum.

KEY

This experiment.

Abe et al.

Bardsley et al.

Busza et al.

——The Helsinki-Karlsruhe partial wave analysis

- - - The CMU-LBL partial wave analysis.

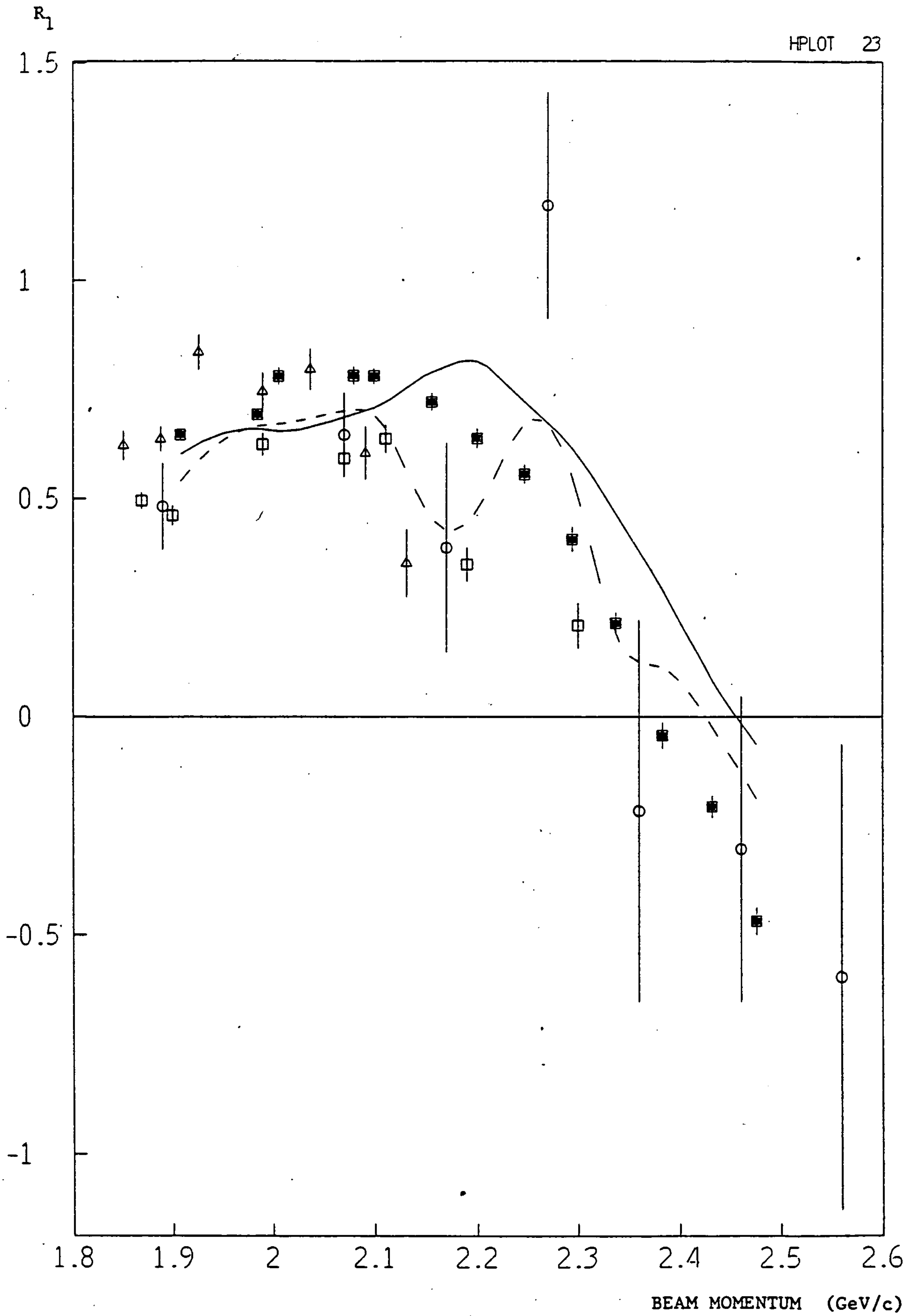

R1
HPLOT 23
1.5
1
0.5
0
-0.5
-1
1.8
1.9
2
2.1
2.2
2.3
2.4
2.5
2.6
BEAM MOMENTUM (GeV/c)

FIGURE 6.4.9: The second order Legendre fit coefficients, R_2, as a function of momentum.

KEY

This experiment.

Abe et al.

Bardsley et al.

Busza et al.

——The Helsinki-Karlsruhe partial wave analysis.

- - -The CMU-LBL partial wave analysis.

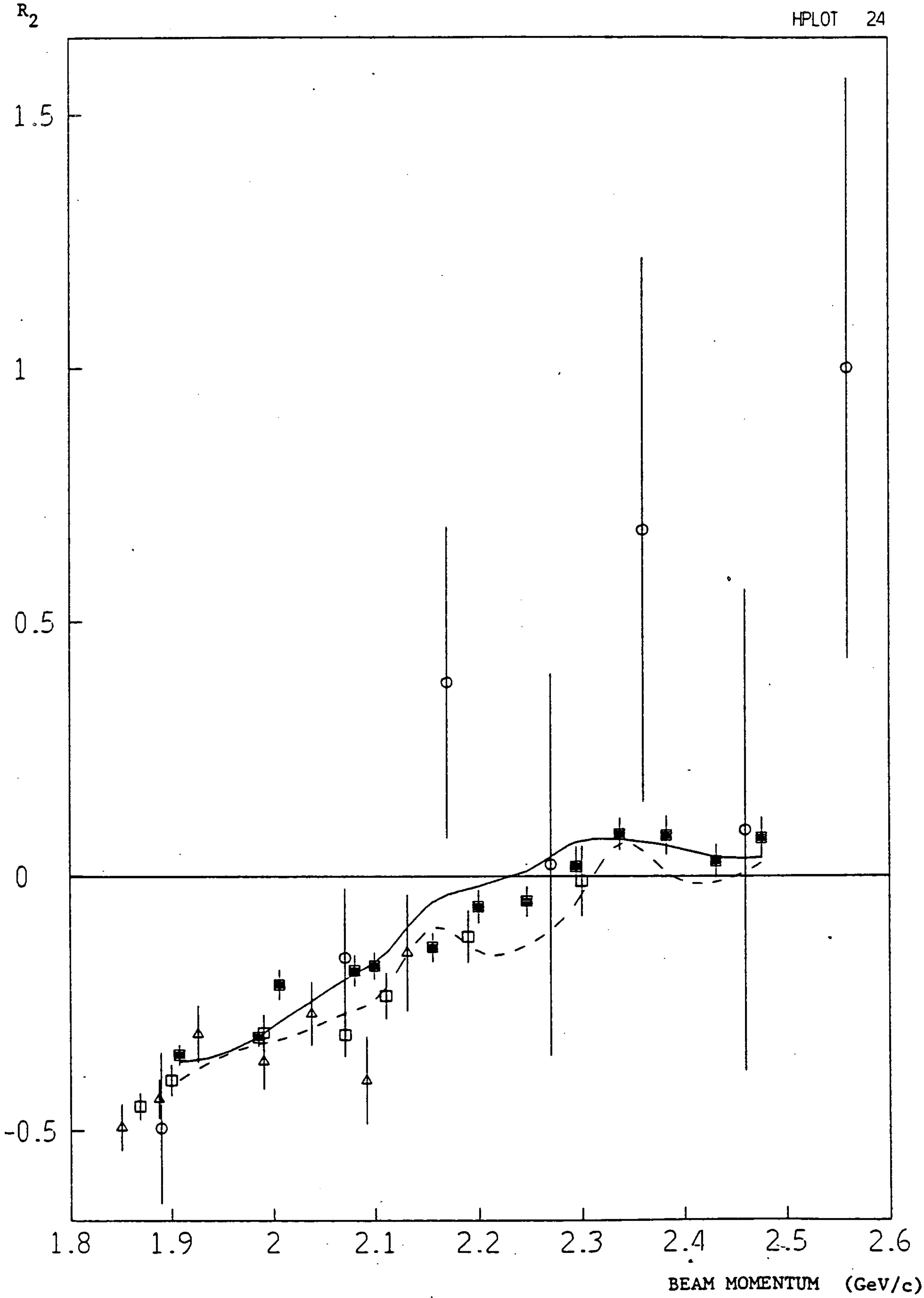

R2
HPLOT 24
1.5
1
0.5
0
-0.5
1.8
1.9
2
2.1
2.2
2.3
2.4
2.5
2.6
BEAM MOMENTUM (GeV/c)

CHAPTER 7

SUMMARY AND CONCLUSIONS

The avowed intent of this experiment was to study the mass spectrum of the Δ^{++} resonance particles, which can be formed in the reactions $\pi^+p \rightarrow K^+\Sigma^+$ and $\pi^+p \rightarrow \pi^+p$, and to resolve some of the discrepancies in the differential cross section measurements of the elastic channel. It is apparent, from the data presented in this thesis, that the RMS experiment will provide a high statistics elastic scattering data set capable of making a major contribution to the existing world data in the elastic channel. This data set will provide new high statistics data in the momentum region from 2.3 to 2.5 GeV/c where no such previous high statistics data exists. It will also provide additional high statistics data in the region from 1.25 to 2.3 GeV/c to help resolve some of the discrepancies between previous experiments in this region. The high quality of the RMS elastic scattering data also lends weight to the belief that the $\pi^+p \rightarrow K^+\Sigma^+$ data collected in the experiment will be of a similar high quality and will provide an important contribution to the world data in the $K\Sigma$ channel.

At the present stage of analysis the elastic data from this experiment has not been incorporated into either of the two major partial wave analyses of the channel and no attempt has yet been made to extract Δ^{++} resonance parameters from the data. Thus the conclusions, which may be drawn from the results presented in this thesis, are limited to the direct comparison of the elastic scattering differential cross sections with the results of other experiments and with the partial wave analyses. An attempt has been made to extract a set of partial wave amplitudes which are consistent with the cross sections presented in this thesis. Details of this analysis are given in Appendix 3 and some preliminary results of the analysis are presented later in this chapter.

From the comparisons drawn in Chapter Six it is evident that the cross sections presented in this thesis are in fairly good agreement with the data of Busza et al. and Bardsley et al. but disagree significantly with the data of Abe et al. This disagreement is mainly in overall normalisation with the Abe data being considerably higher than the RMS data over most of the momentum range. Such a discrepancy could come from several sources. One possible source is the existence of a systematic error in one of the normalisation factors used in either the Abe or the RMS experiment. Such an error would cause a discrepancy to exist in the forward elastic cross section also. By making use of the limited amount of RMS data collected with the downstream Cerenkov counter (V2) switched off, an RMS elastic differential cross section (based on $\sim$ 9400 elastic scattering events) was calculated at 2.10 GeV/c over the full $\cos\theta^*$ range. This differential cross section is shown in Figure 7.1 with a linearly interpolated Abe cross section superimposed. These cross sections were integrated over two $\cos\theta^*$ ranges ($-0.85 \leq \cos\theta^* \leq -0.11$ and $0.6 \leq \cos\theta^* \leq 0.9$) as was the data of Busza et al. The RMS "Cerenkov on" cross section was also integrated over the "backward" $\cos\theta^*$ range ($-0.85 \leq \cos^* \leq -0.11$). The data of Bardsley et al. was not included in this comparison since at this particular momentum Bardsley et al. had very few data points in the "forward" $\cos\theta^*$ range ($0.6 \leq \cos\theta^* \leq 0.9$). The results of this comparison are shown in Table 7.1. It can be seen from this table that all the data samples are in good agreement in the forward direction thus suggesting

FIGURE 7.1: Comparison of the RMS "Cerenkov off" differential cross section at 2.10 GeV/c with the data of Abe et al.

KEY

■ This experiment

□ Abe et al.

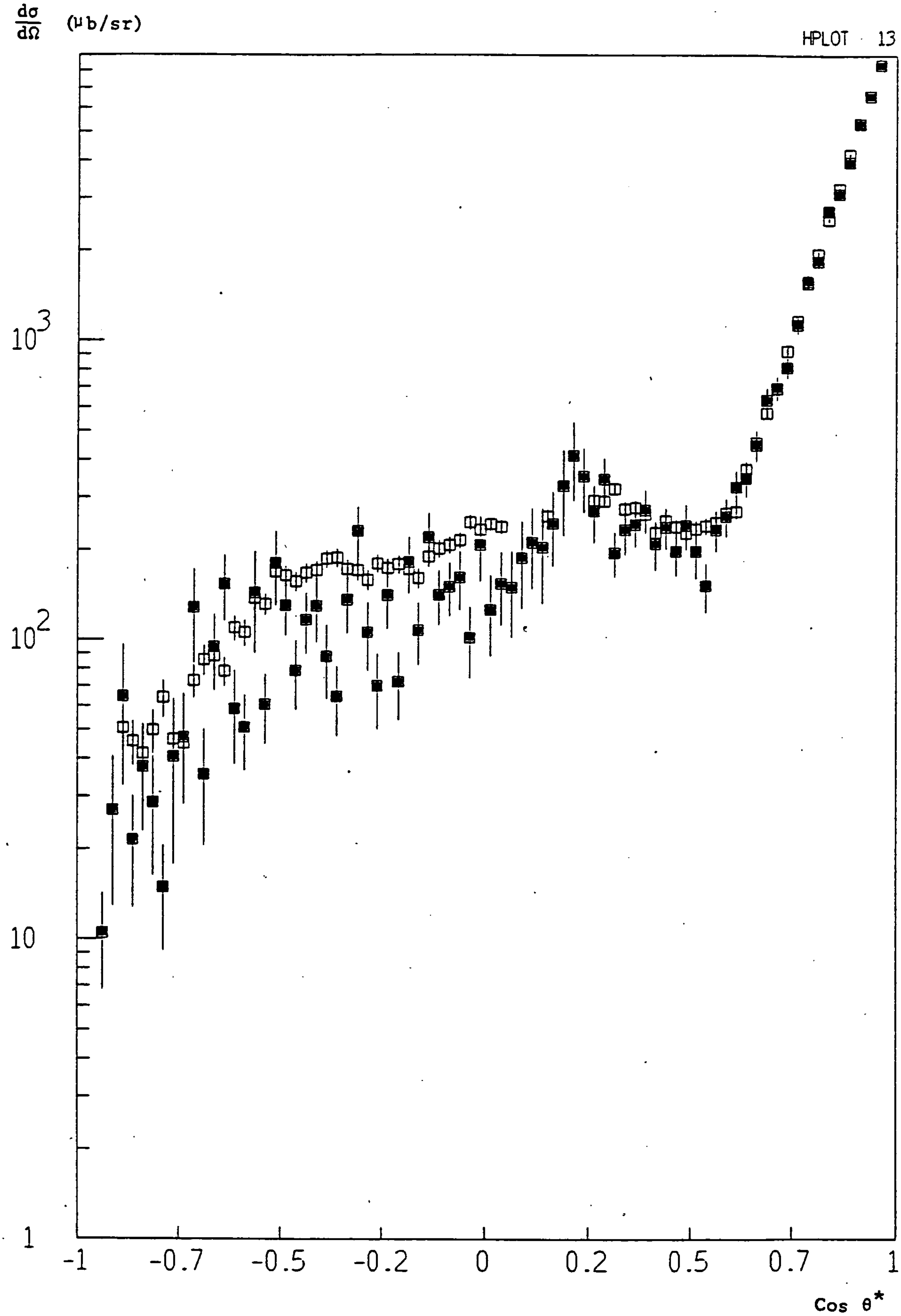

dσ/dΩ (μb/sr)
HPLOT 13
10^3
10^2
10
1
-1
-0.7
-0.5
-0.2
0
0.2
0.5
0.7
1
Cos θ*

Data Sample	Integrated Cross Sections (μb)					
	Backward Region ($-0.85 \leqslant \cos\theta^* \leqslant -0.11$)			Forward Region ($0.6 \leqslant \cos\theta^* \leqslant 0.9$)		
	Cross Section	Statistical Error	Normalisation Error	Cross Section	Statistical Error	Normalisation Error
RMS (Cerenkov Off)	476	±18	±29	2785	±33	±164
RMS (Cerenkov on)	415	± 4	±25	-	-	-
Abe et al.	618	± 7	±19	2832	±12	± 85
Busza et al.	463	±19	Not quoted	2845	±45	Not quoted

TABLE 7.1

Integrated Cross Sections in the "forward" and "backward" Regions at 2.10 GeV/c.

that the discrepancy between the RMS and the Abe data in the backward direction is not caused by an error in a normalisation factor. In addition a comparison can be made between the RMS "Cerenkov off" and Cerenkov on" data, in the backward cos θ^* range, to check that the RMS data is internally consistent. In this comparison the normalisation errors should not be taken fully into account since many (although not all) of the factors which contribute to these errors will have the same effect on both data samples. From Table 7.1 it can be seen that the agreement between the "Cerenkov off" and "Cerenkov on" cross sections is only fair (at approximately the 2 standard deviation level). In the analysis of the "Cerenkov off" data the observed background was somewhat higher than the "Cerenkov on" data background (especially in the backward direction). This background was not studied as intensively as the "Cerenkov on" background had been and thus the background subtraction procedure could have introduced a systematic error into the "Cerenkov off" cross sections which would account for the observed (small) disagreement between the "Cerenkov off" and the "Cerenkov on" cross sections. Thus the disagreement between these two data samples was not thought to be significant. In addition, even if this were not the case, the disagreement was not great enough to explain the discrepancy between the RMS data and the data of Abe et al. Another possible source of the discrepancy between the RMS and the Abe data in the backward direction is a mis-calculation of the acceptance of either of the experiments. This possibility was thought to be unlikely since the acceptances quoted by both experiments seemed to be consistent with their experimental set ups. The mis-identification of scattering events from another channel as elastic scattering events could lead to contamination in the Abe cross sections thus providing a possible explanation for the observed discrepancy. The most likely source of such a contamination is expected to be from the $\pi^+ p \to \pi^+ p\, \pi^o$ channel. Events from this channel formed the major component of the RMS "background" and, since the Abe experiment used an intrinsically inferior measurement method (with no spectrometer magnet to provide momentum measurement), this channel might be expected to cause problems in the Abe experiment. This possible source of contamination was investigated by generating Monte Carlo $\pi^+ p \to \pi^+ p\, \pi^o$ events and applying the Abe elastic selection criteria to these events. This investigation showed that, while $\pi^+ p \to \pi^+ p\, \pi^o$ events probably formed a major component of the Abe background, the background subtraction procedure employed by Abe et al. seemed to correct for such events to a high degree of accuracy. The disagreement between the RMS experiment and the Abe experiment could also be caused by a loss of elastic scattering events in the RMS experiment. No evidence for such a loss could be found. In addition, the good agreement between the RMS data and the Busza and Bardsley data seemed to disfavour this possibility. This was especially true since the method of event selection used in both these experiments was different to that used in the RMS experiment thus making it unlikely that the same error could be made in all three experiments.

The comparison of the RMS differential cross sections presented in this thesis with the two major partial wave analyses of the channel also showed major discrepancies. These discrepancies were, once again, mainly in overall normalisation with the analyses being consistently higher than the RMS data. This effect was to be expected since both of the analyses used the data of Abe et al. as part of their input and were strongly constrained by this data due to the high statistics of the Abe experiment. An attempt was made to extract partial wave amplitudes from the RMS data which were consistent with both the RMS data and the CMU-LBL analysis (as described in Appendix 3). The real and imaginary parts of the amplitudes obtained from this fitting procedure are shown as a function of centre of mass energy in Figure 7.2. The solid lines in this figure represent the fitted amplitudes and the points with error bars represent the original (interpolated) CMU-LBL amplitudes. The nomenclature used to identify the amplitudes in this figure is A 2I 2J where A is the spectroscopic notation symbol representing the orbital angular momentum ($A \equiv S$ for $\ell = 0$, P for $\ell = 1$, D for $\ell = 2$, F for $\ell = 3$, etc.), I is the isotopic spin (always $\frac{3}{2}$ for the $\pi^+ p$ system) and J is the total angular momentum. It can be seen from Figure 7.2 that the RMS data seems to have had little effect on the partial wave amplitudes. This is due to the fact that the fitting procedure has allowed the differences between the data and the partial wave analysis to be absorbed in the renormalisation factors, R, described in Appendix 3. Consequently the partial wave amplitudes have not changed significantly and the fitted amplitudes do not describe the RMS data very well. The renormalisation factors, R, are a measure of how much the RMS data had to be renormalised by to be consistent with the cross sections obtained from the fitted amplitudes. These factors are plotted as a function of beam momentum in Figure 7.3. This figure illustrates the effect of the Abe data on the CMU-LBL partial wave analysis with large renormalisation factors only being necessary, in general, below 2.3 GeV/c where Abe's data has constrained the analysis.

In the energy region of the data presented in this thesis the

FIGURE 7.2: Comparison of the partial wave amplitudes extracted from the RMS data with the CMU-LBL amplitudes.

KEY

┤ The original (interpolated) CMU-LBL amplitudes.

—— The RMS amplitudes.

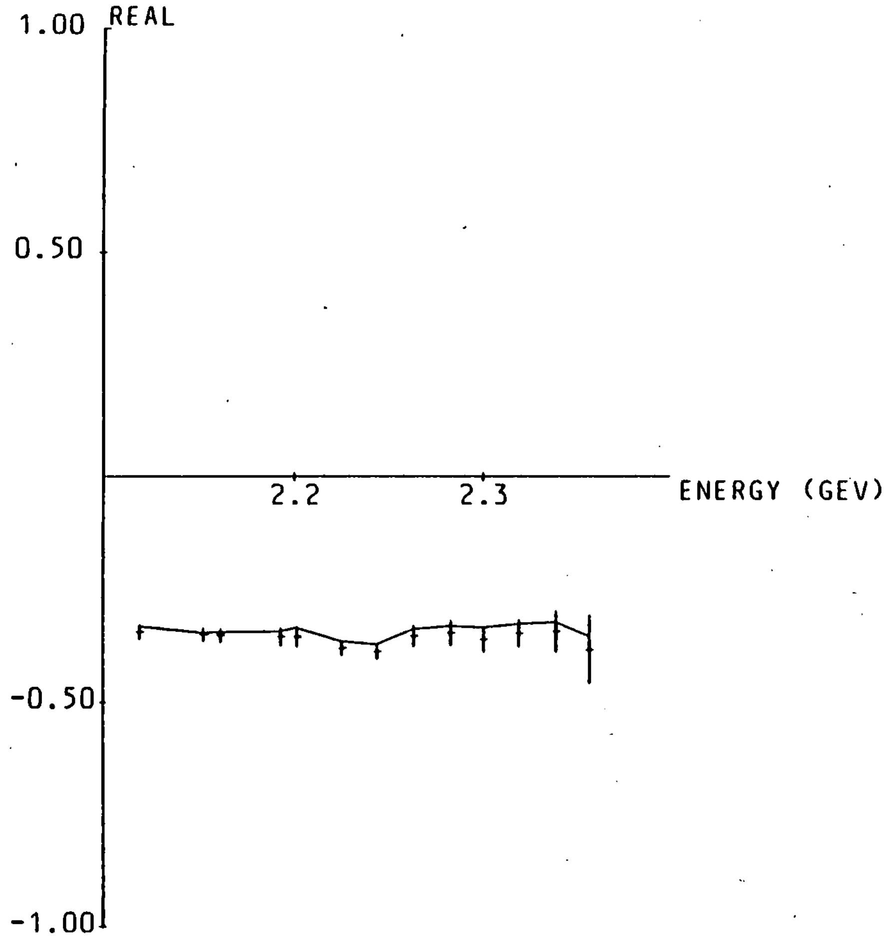
1.00
REAL
0.50
2.2
2.3
ENERGY (GEV)
-0.50
-1.00

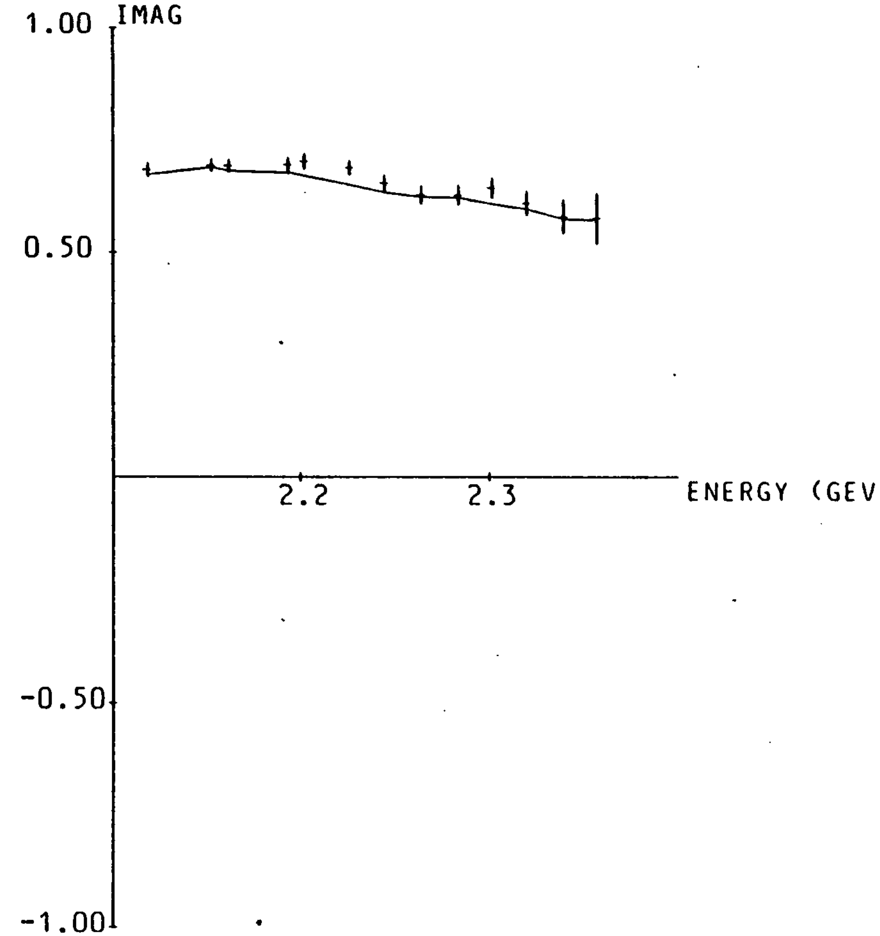
1.00
IMAG
0.50
2.2
2.3
ENERGY (GEV)
-0.50
-1.00

S31

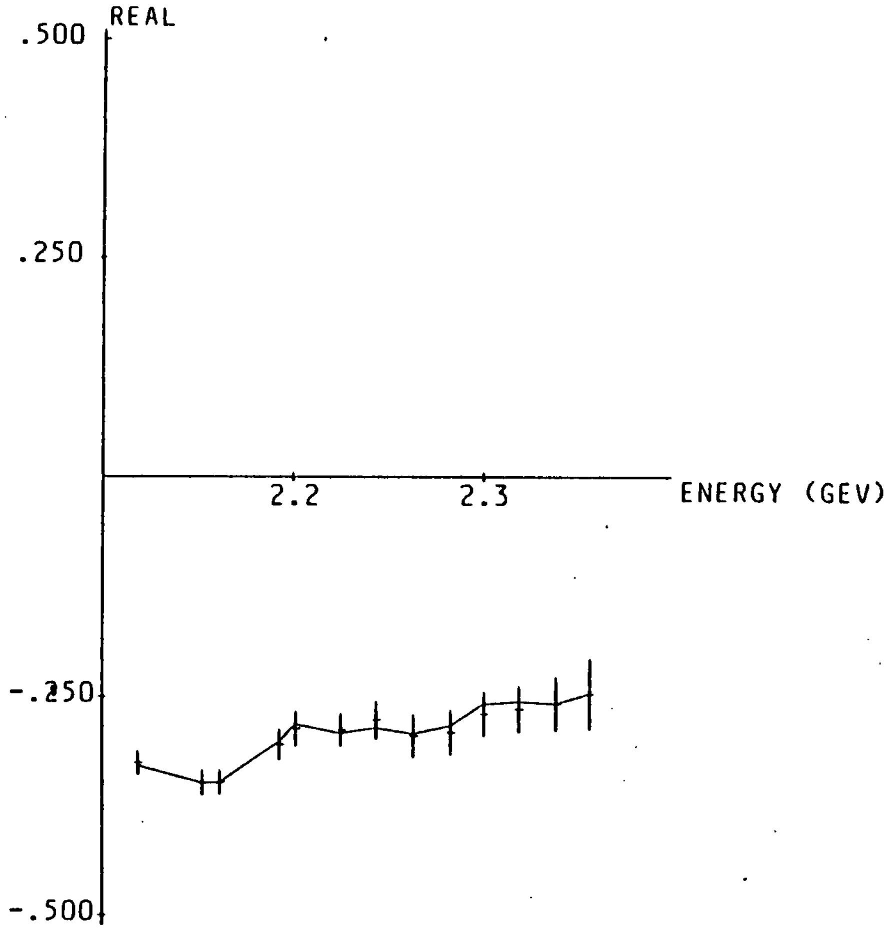
REAL
.500
.250
2.2
2.3
ENERGY (GEV)
-.250
-.500

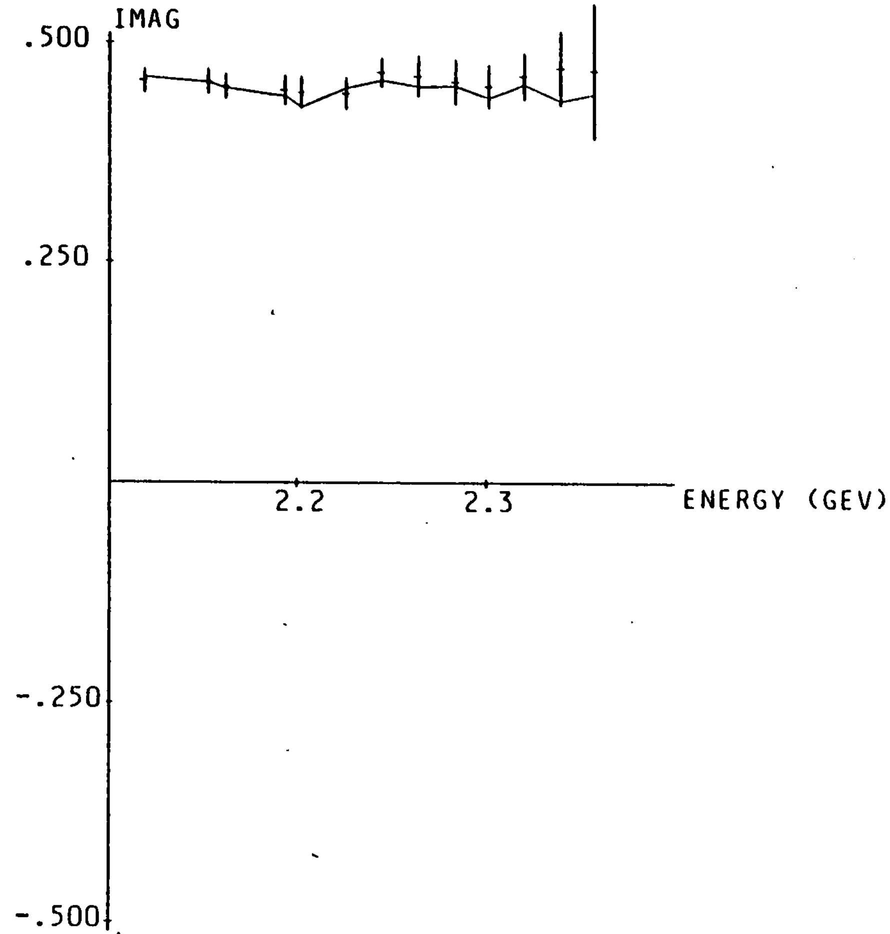
IMAG
.500
.250
2.2
2.3
ENERGY (GEV)
-.250
-.500

P31

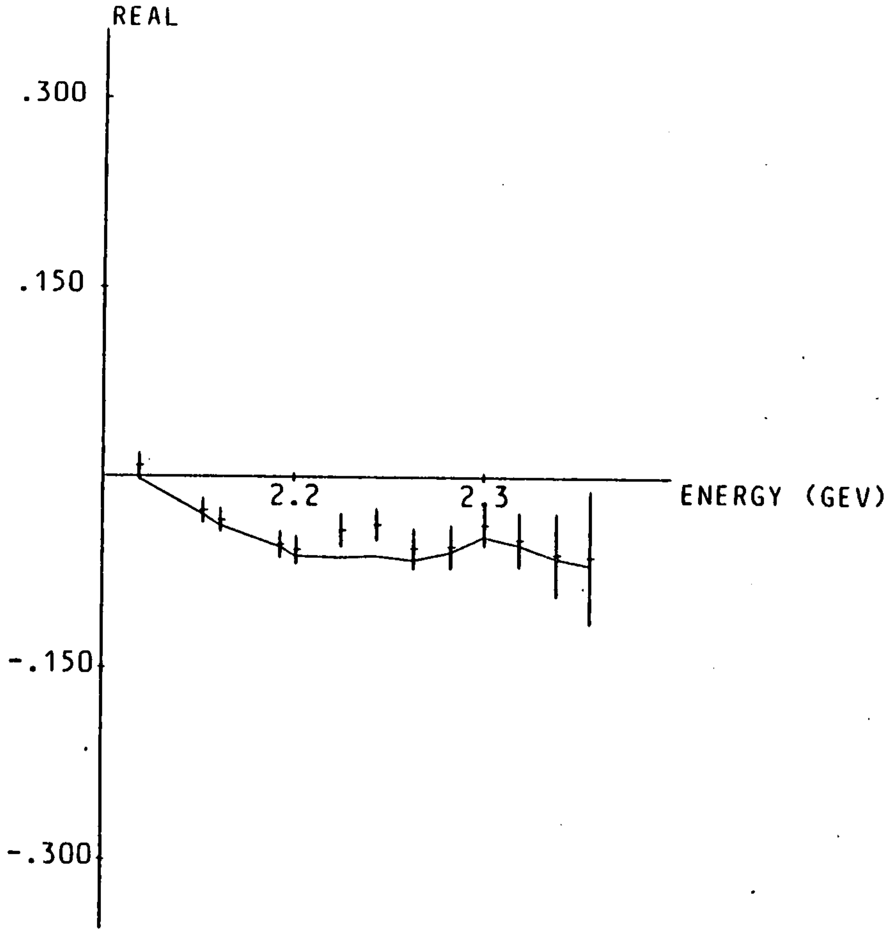
REAL
.300
.150
-.150
-.300
2.2
2.3
ENERGY (GEV)

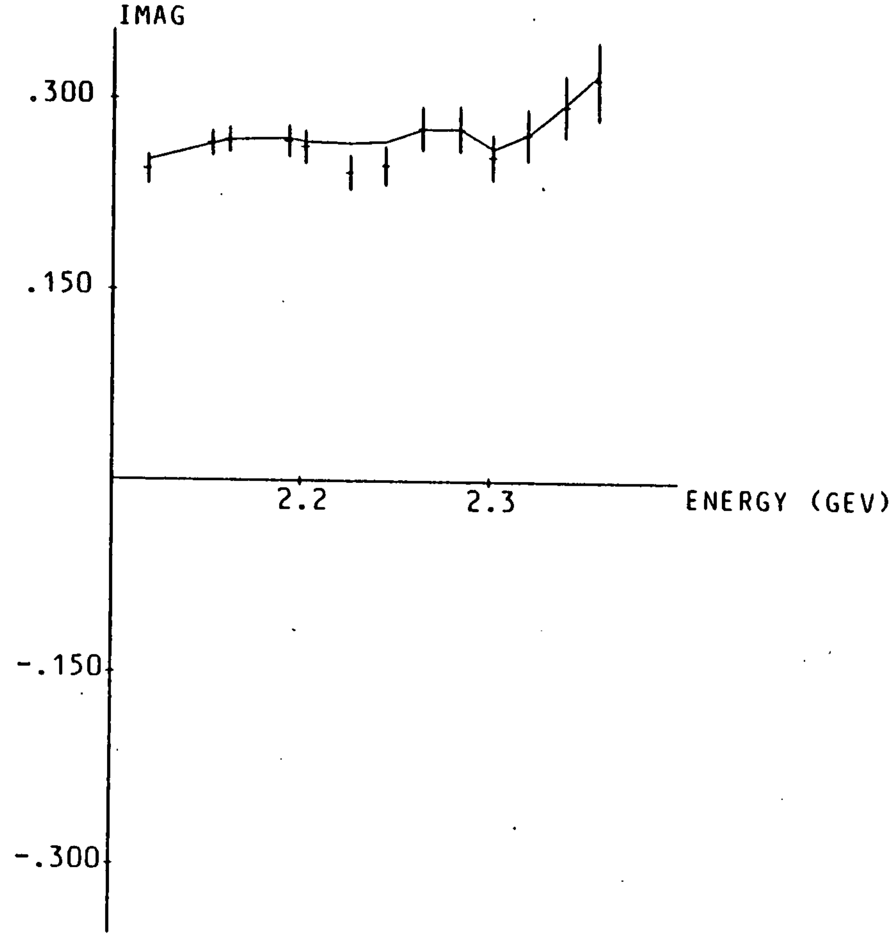
IMAG
.300
.150
-.150
-.300
2.2
2.3
ENERGY (GEV)

P33

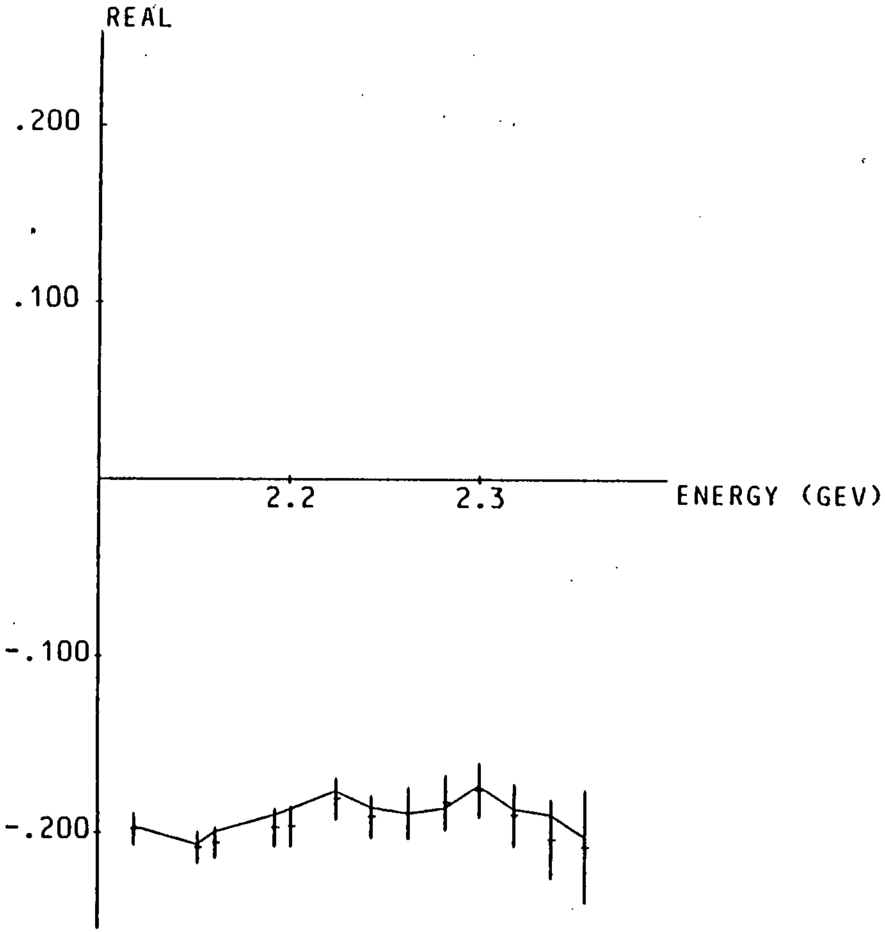
REAL
.200
.100
2.2
2.3
ENERGY (GEV)
-.100
-.200

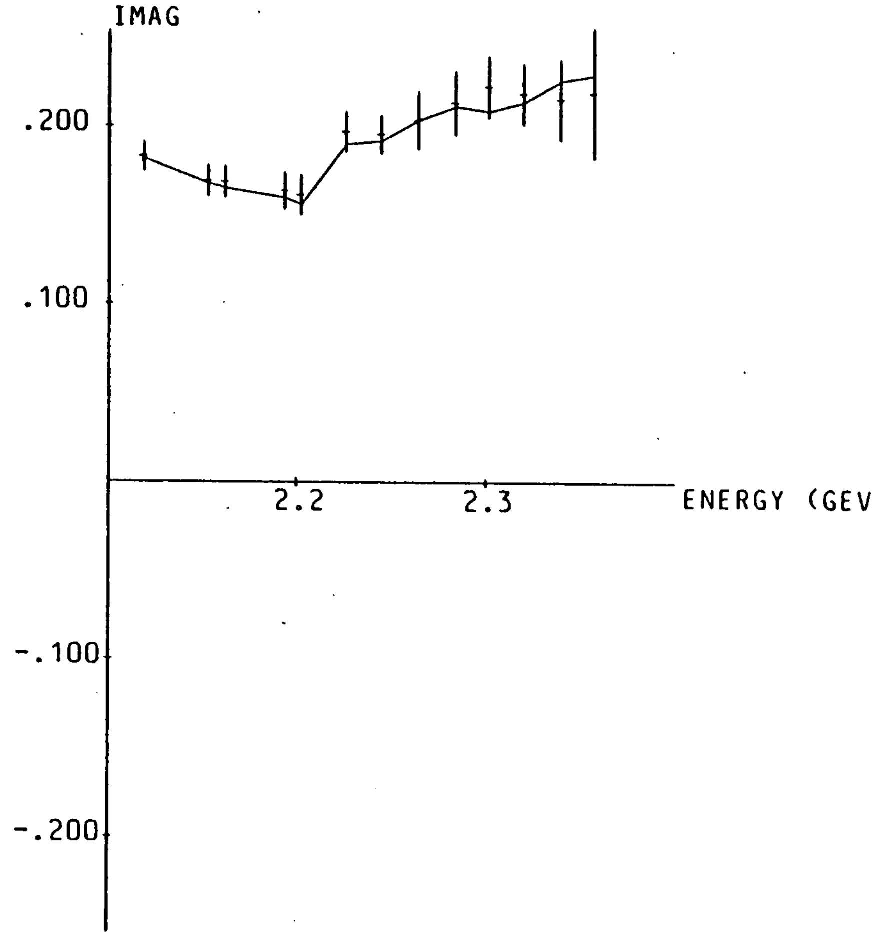
IMAG
.200
.100
2.2
2.3
ENERGY (GEV)
-.100
-.200

D33

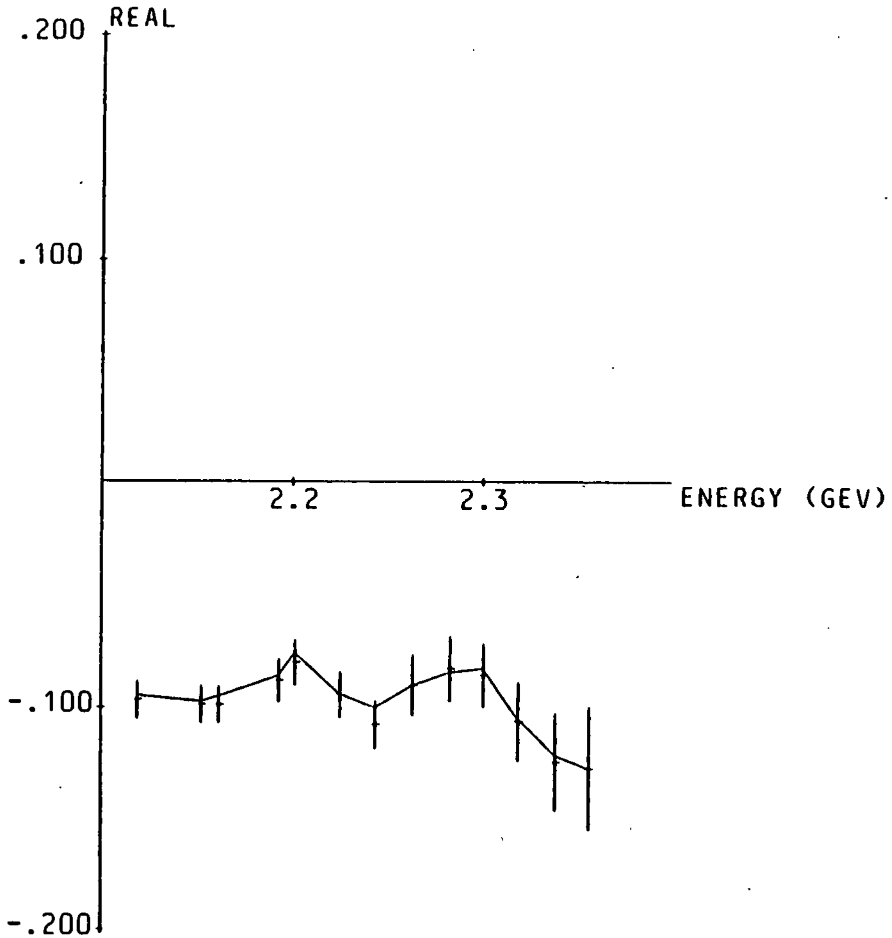
REAL
.200
.100
-.100
-.200
2.2
2.3
ENERGY (GEV)

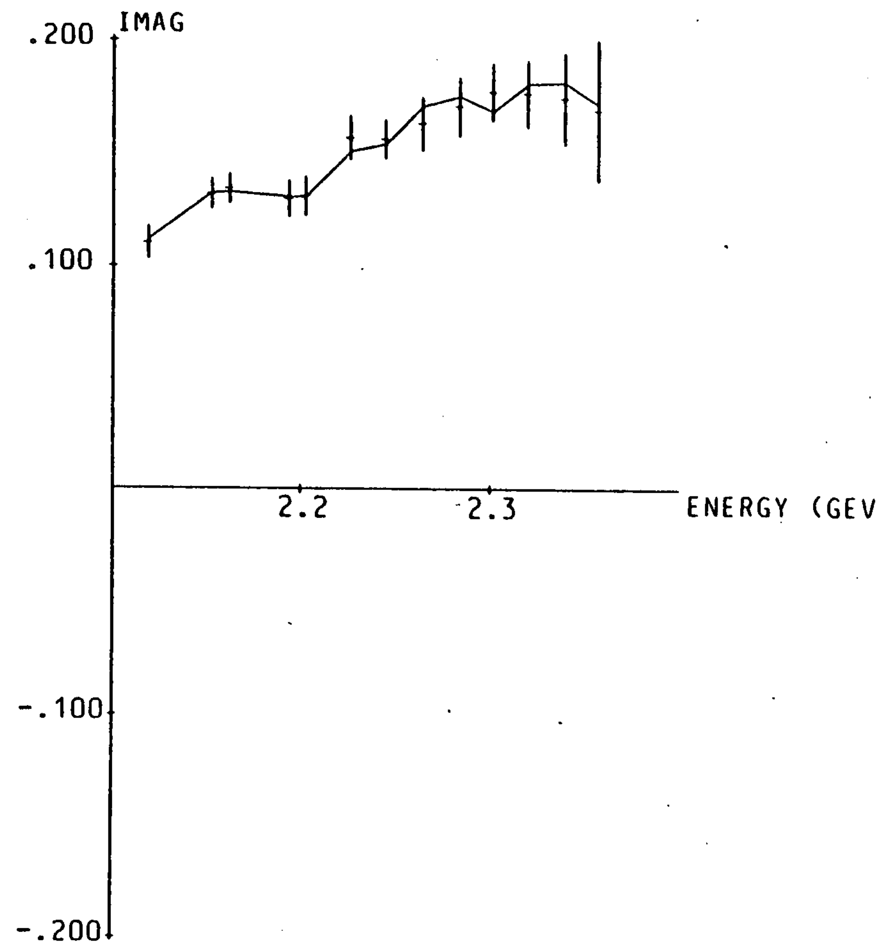
IMAG
.200
.100
-.100
-.200
2.2
2.3
ENERGY (GEV)

D35

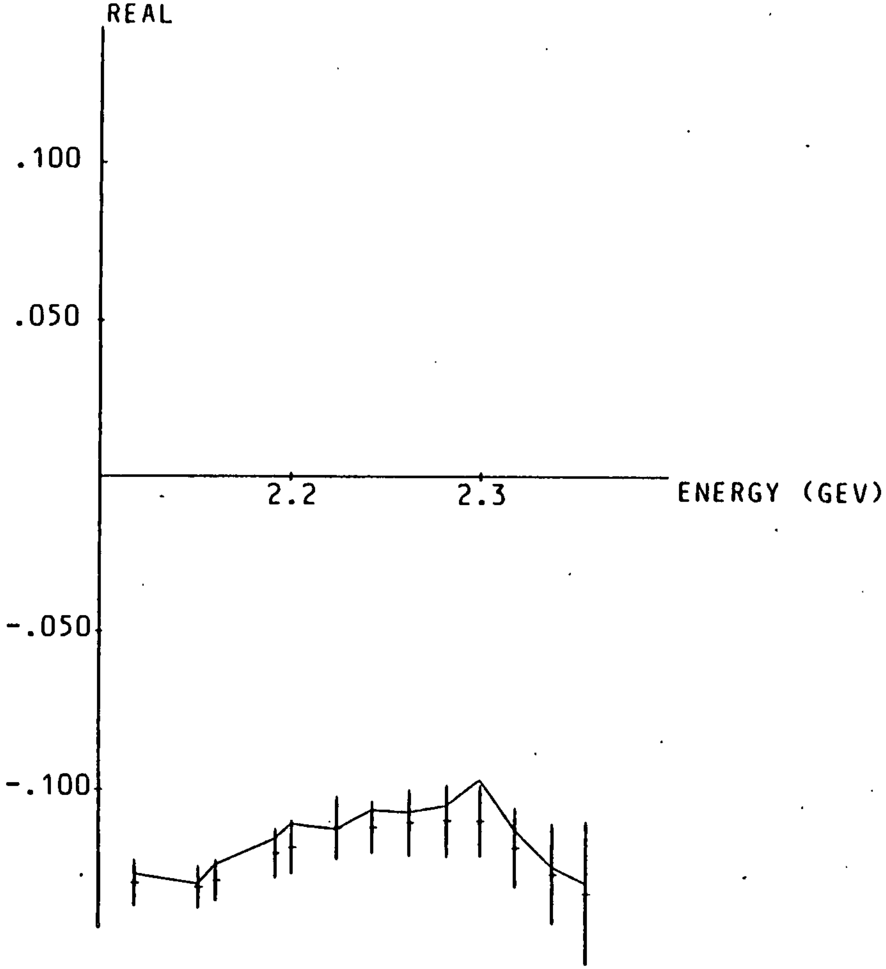
REAL
.100
.050
-.050
-.100
2.2
2.3
ENERGY (GEV)

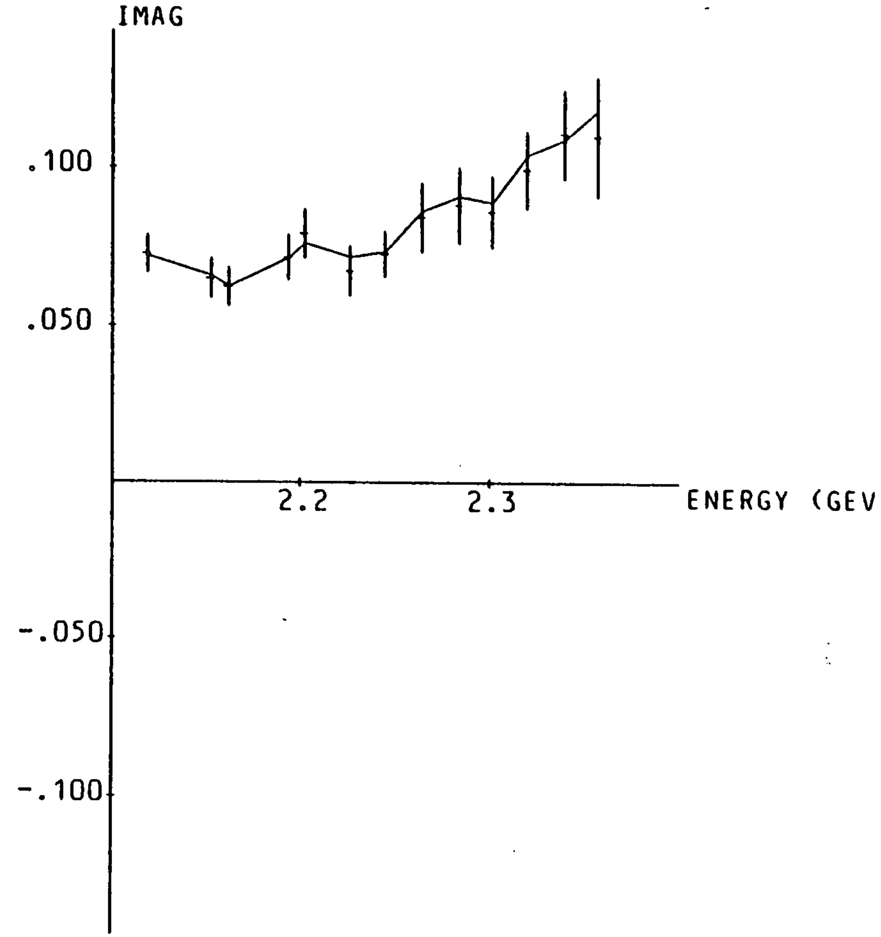
IMAG
.100
.050
-.050
-.100
2.2
2.3
ENERGY (GEV)

F35

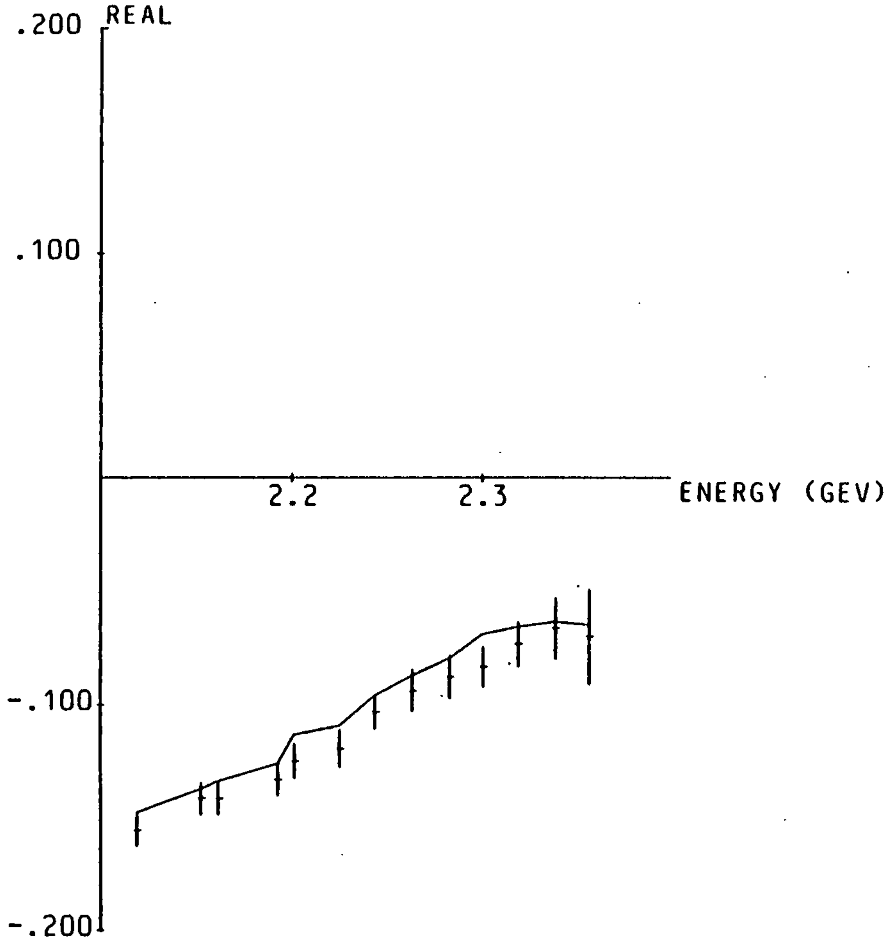

.200
REAL
.100
2.2
2.3
ENERGY (GEV)
-.100
-.200

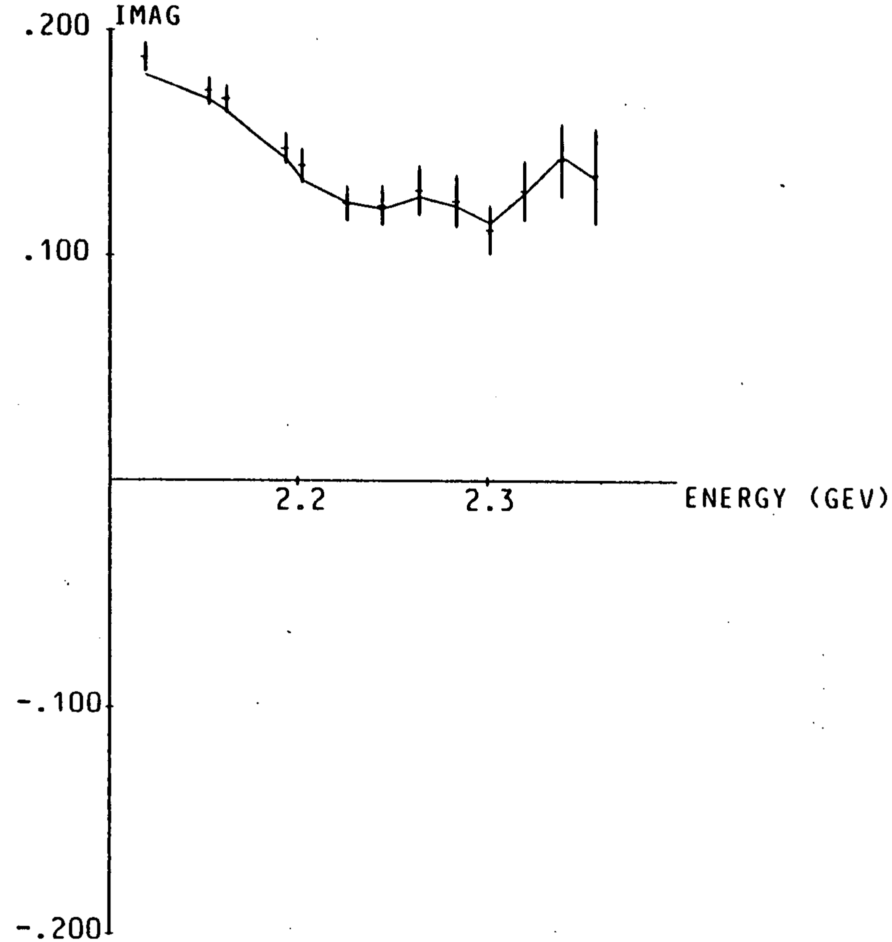

.200
IMAG
.100
2.2
2.3
ENERGY (GEV)
-.100
-.200

F37

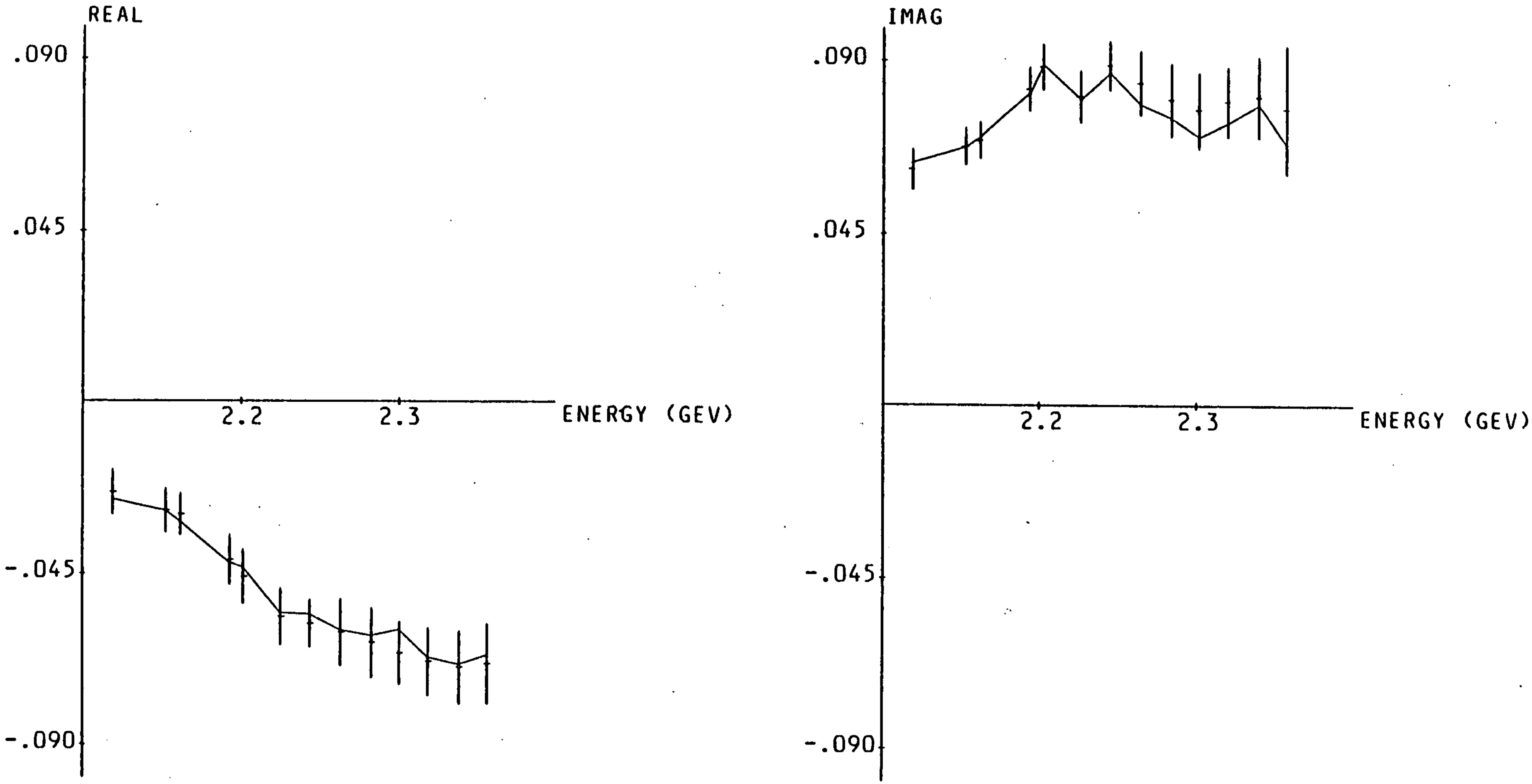
REAL
.090
.045
-.045
-.090
2.2
2.3
ENERGY (GEV)
IMAG
.090
.045
-.045
-.090
2.2
2.3
ENERGY (GEV)

G37

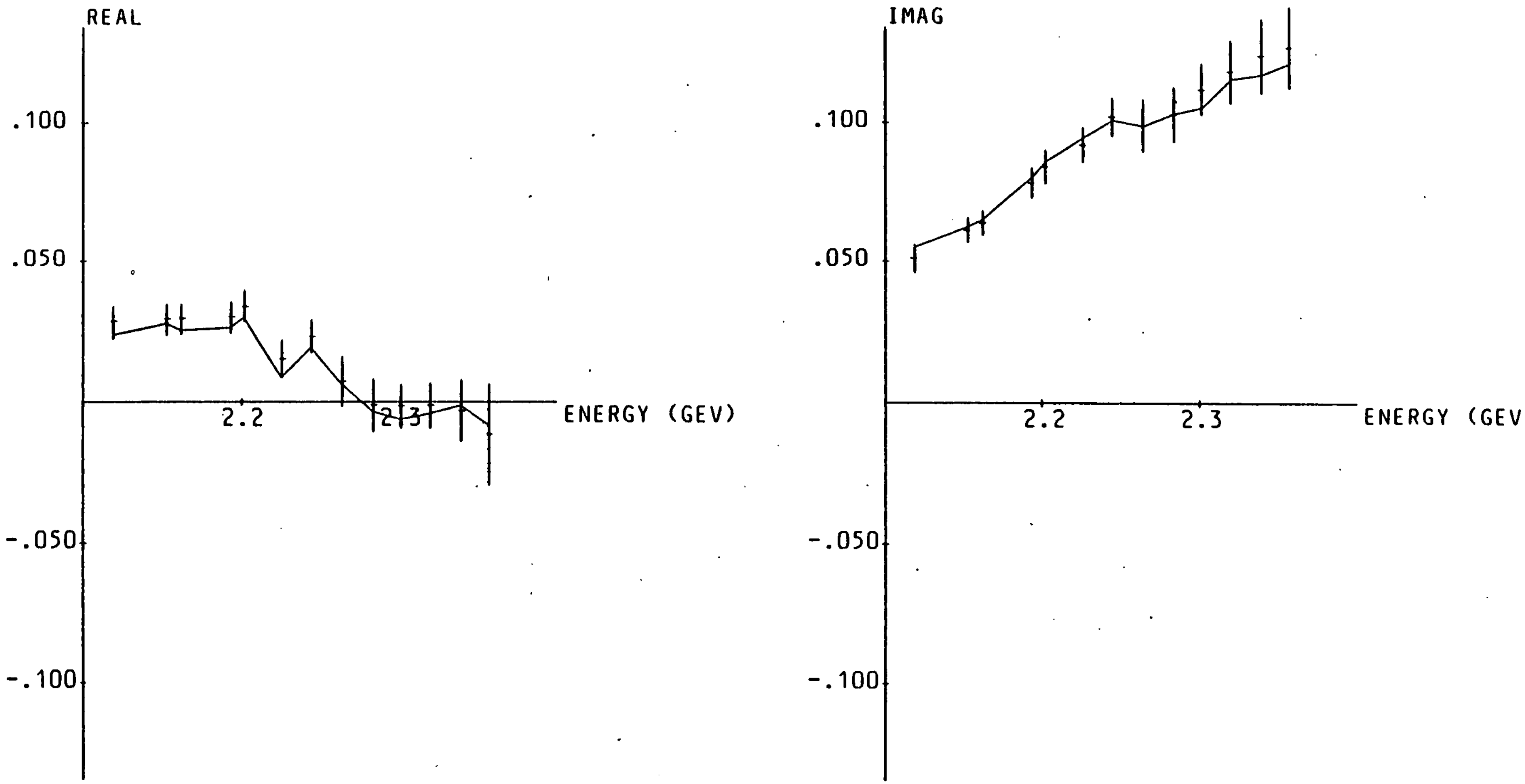
REAL
.100
.050
-.050
-.100
2.2
2.3
ENERGY (GEV)
IMAG
.100
.050
-.050
-.100
2.2
2.3
ENERGY (GEV)

G39

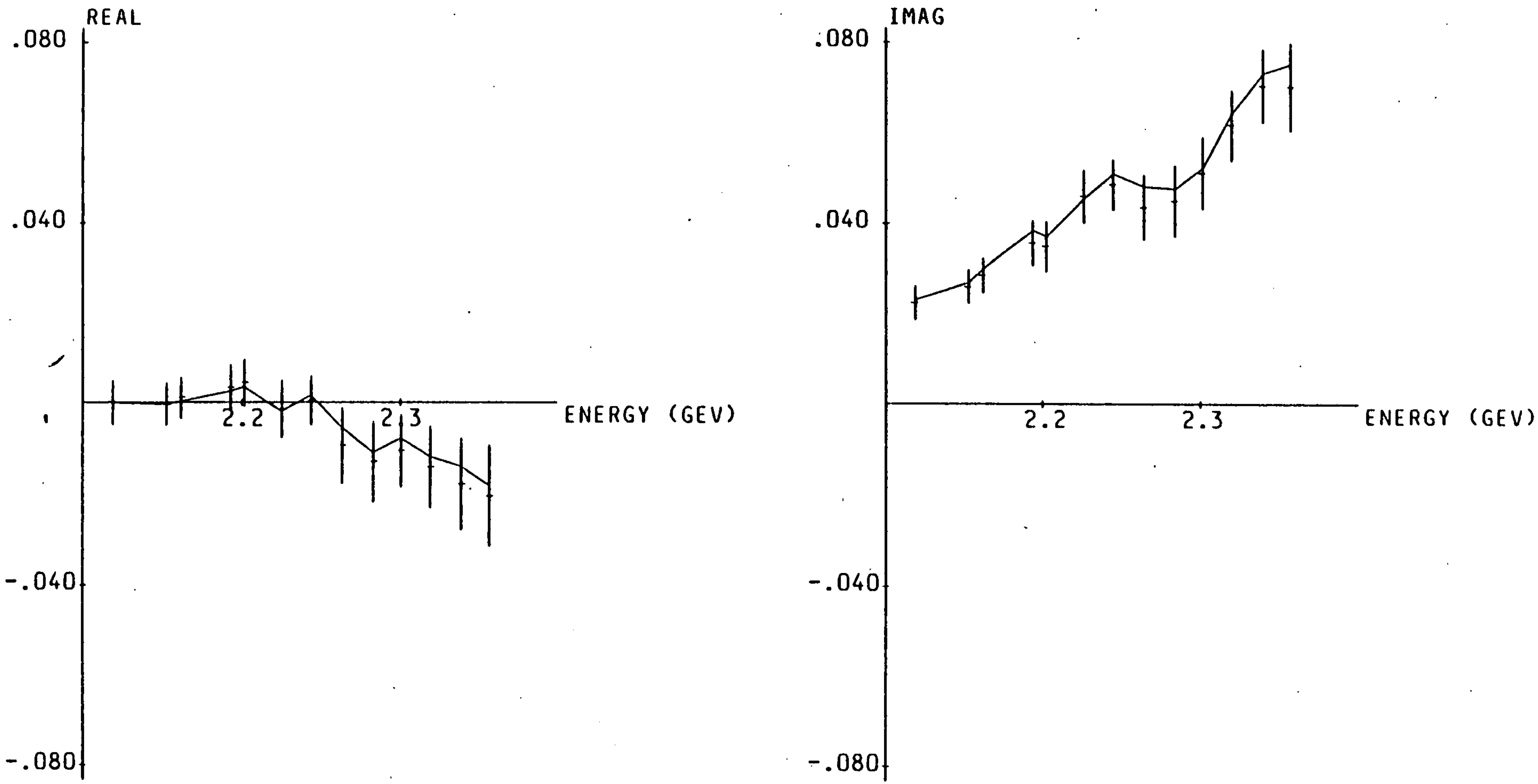
REAL
.080
.040
-.040
-.080
2.2
2.3
ENERGY (GEV)
IMAG
.080
.040
-.040
-.080
2.2
2.3
ENERGY (GEV)

H39

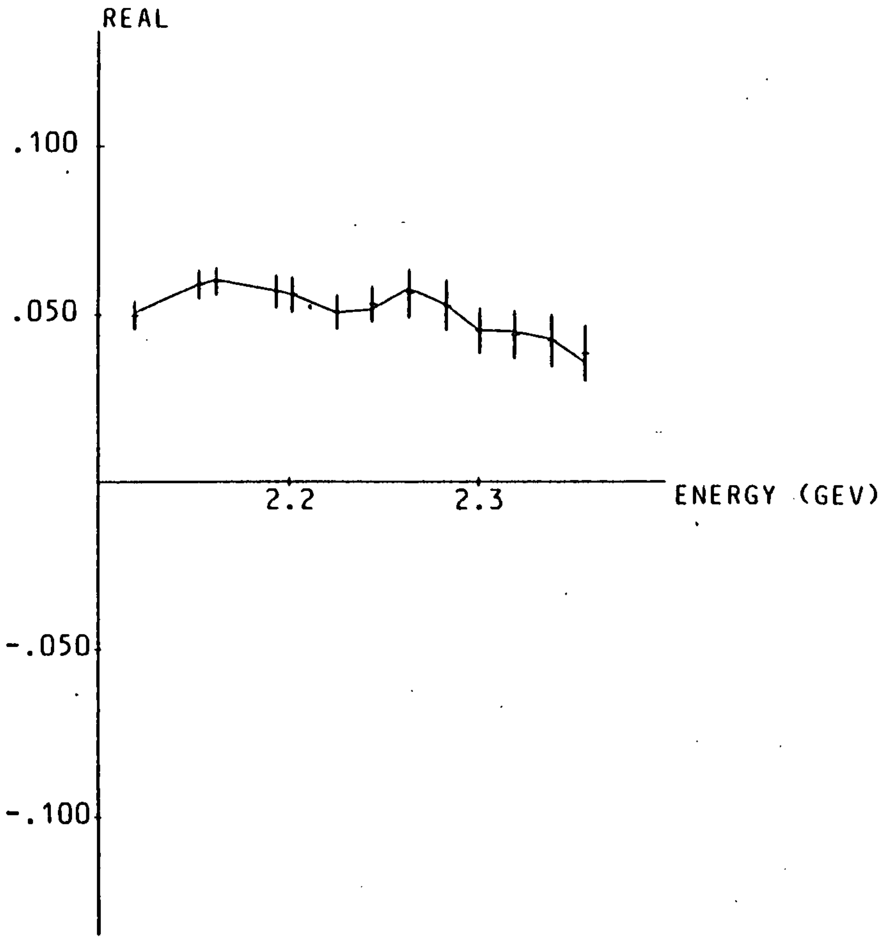
REAL
.100
.050
-.050
-.100
2.2
2.3
ENERGY (GEV)

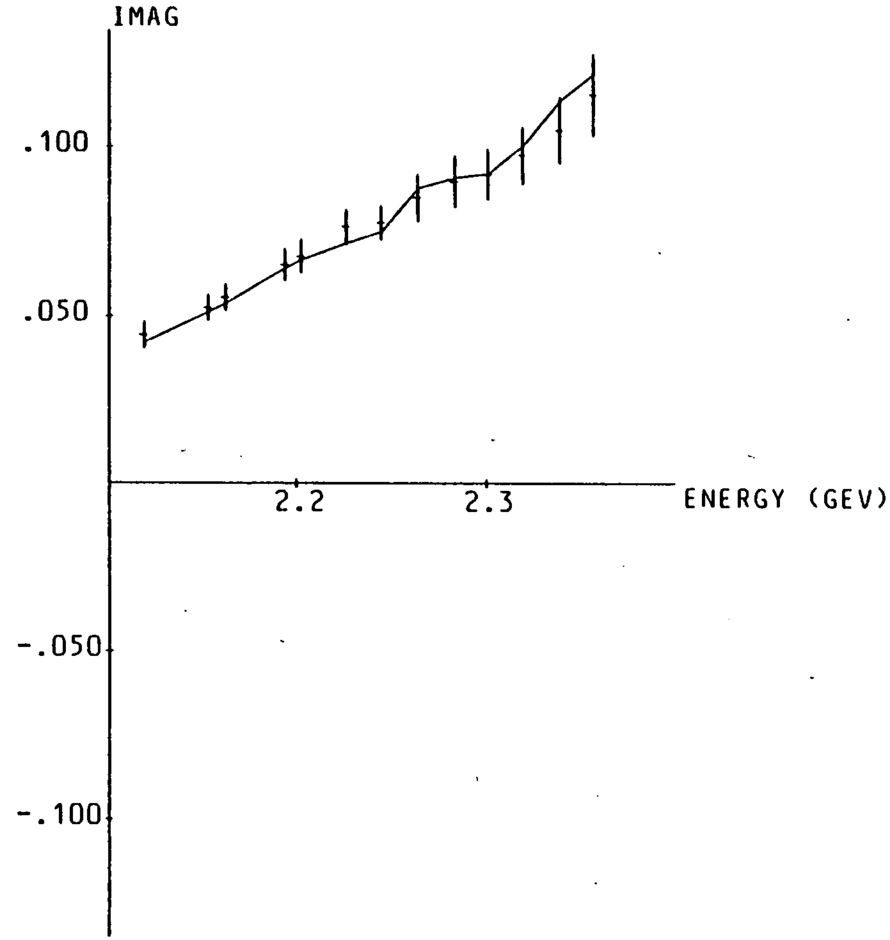
IMAG
.100
.050
-.050
-.100
2.2
2.3
ENERGY (GEV)

H311

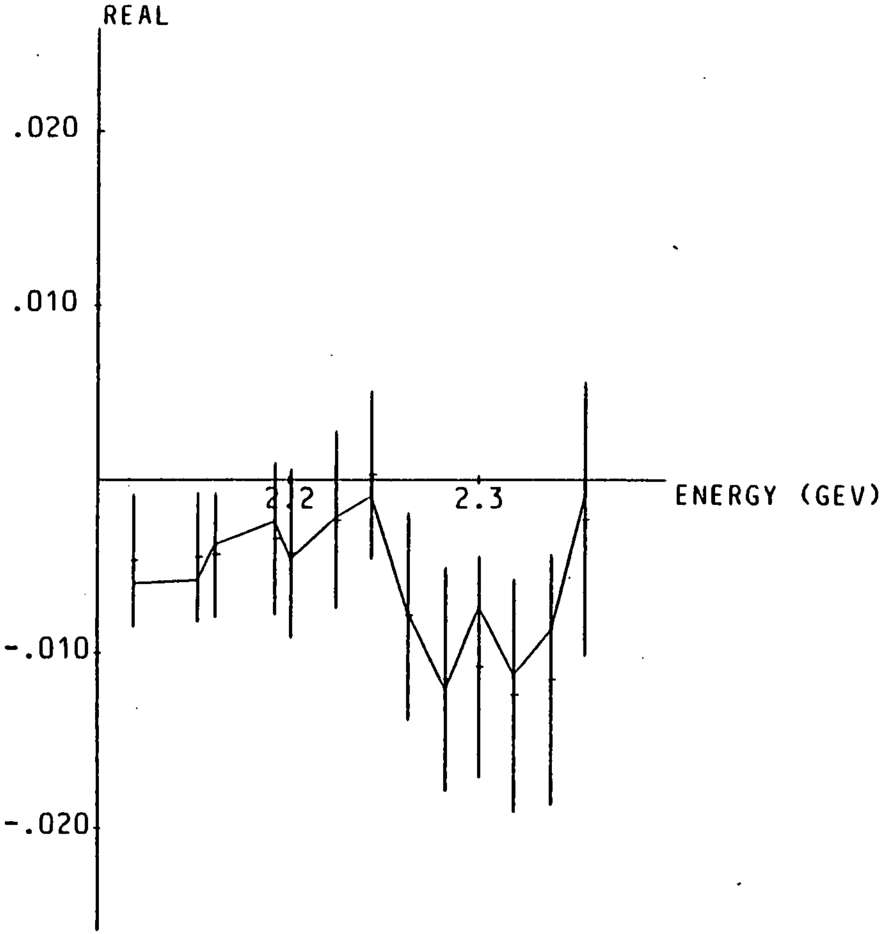
REAL
.020
.010
-.010
-.020
2.2
2.3
ENERGY (GEV)

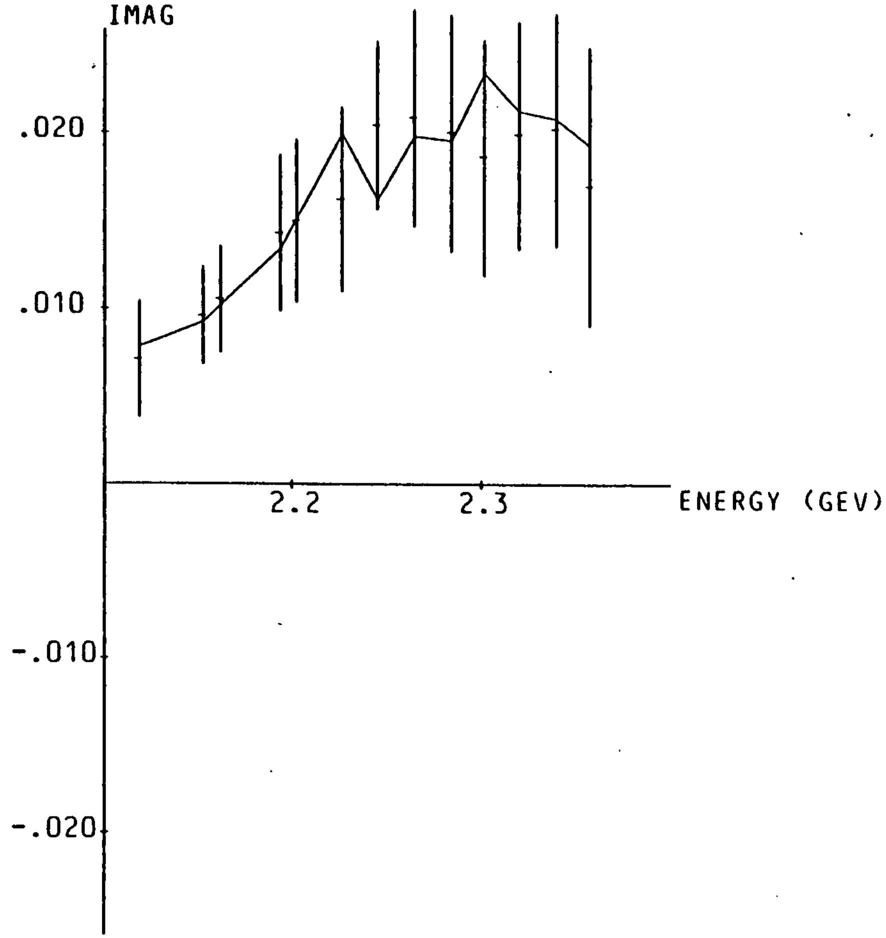
IMAG
.020
.010
-.010
-.020
2.2
2.3
ENERGY (GEV)

I311

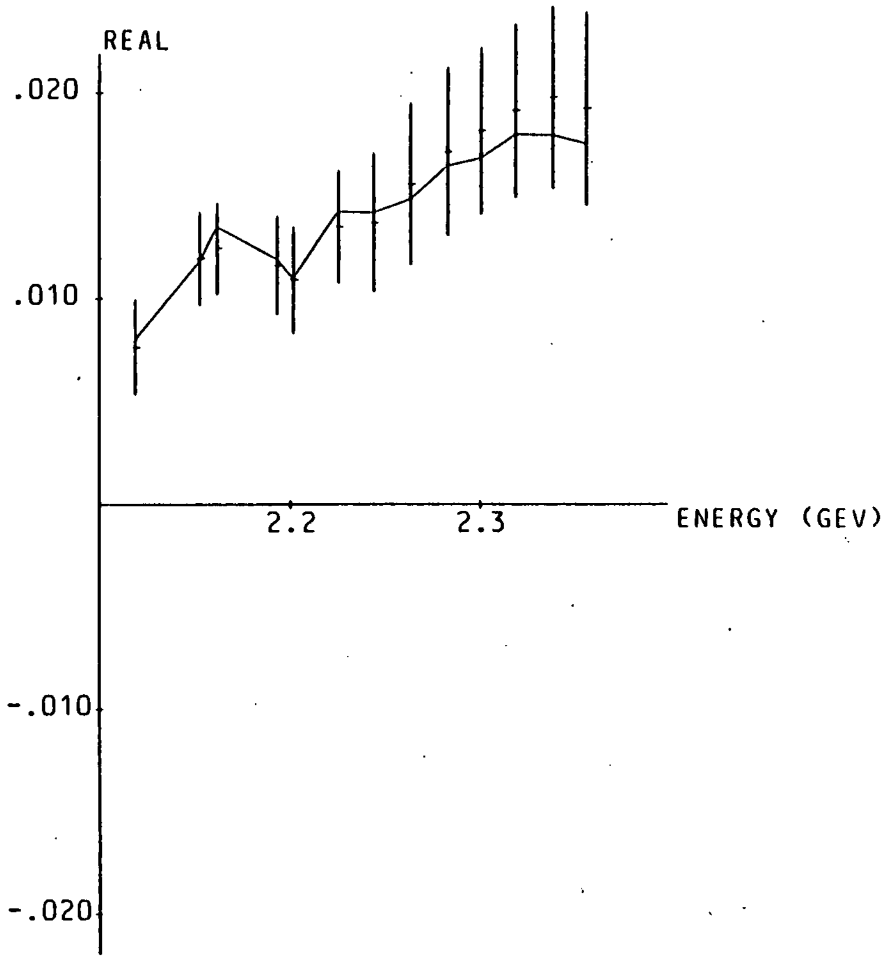
REAL
.020
.010
-.010
-.020
2.2
2.3
ENERGY (GEV)

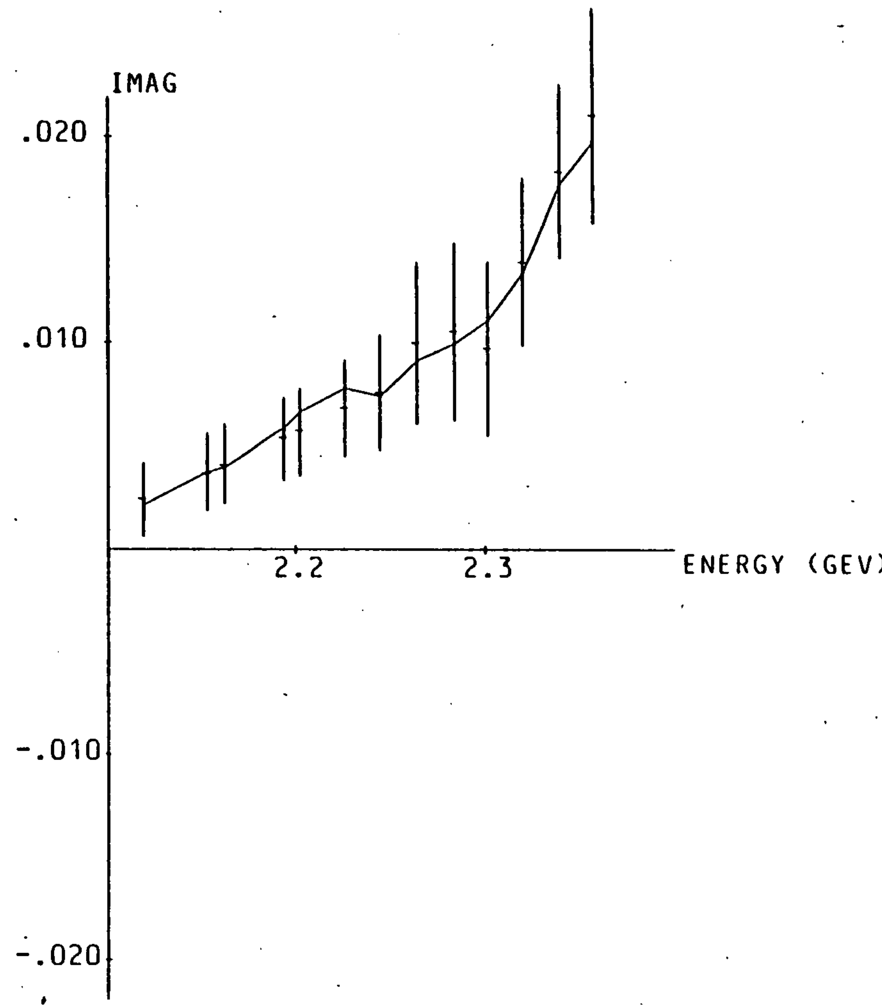
IMAG
.020
.010
-.010
-.020
2.2
2.3
ENERGY (GEV)

I313

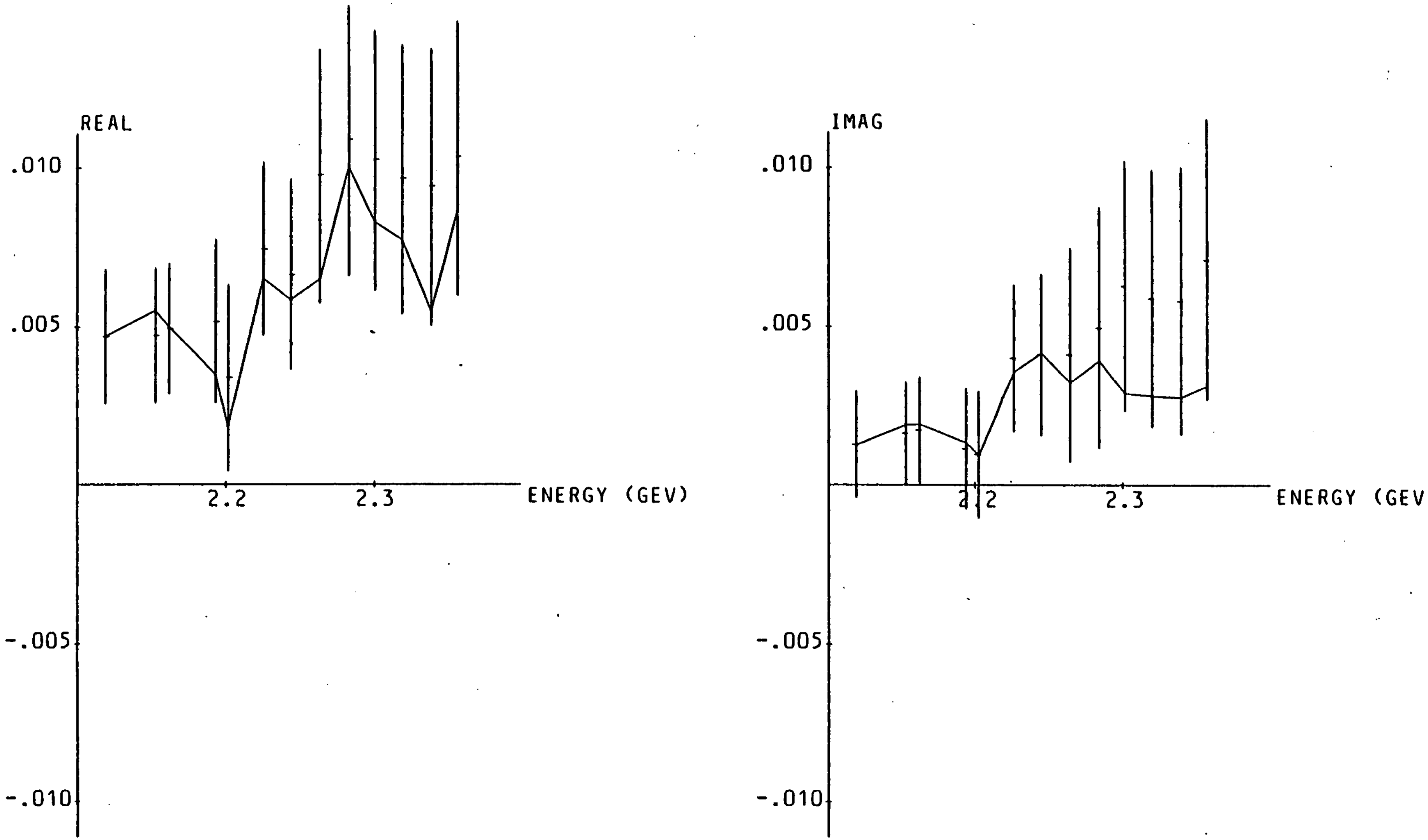

REAL
.010
.005
-.005
-.010
2.2
2.3
ENERGY (GEV)
IMAG
.010
.005
-.005
-.010
2.2
2.3
ENERGY (GEV)

K313

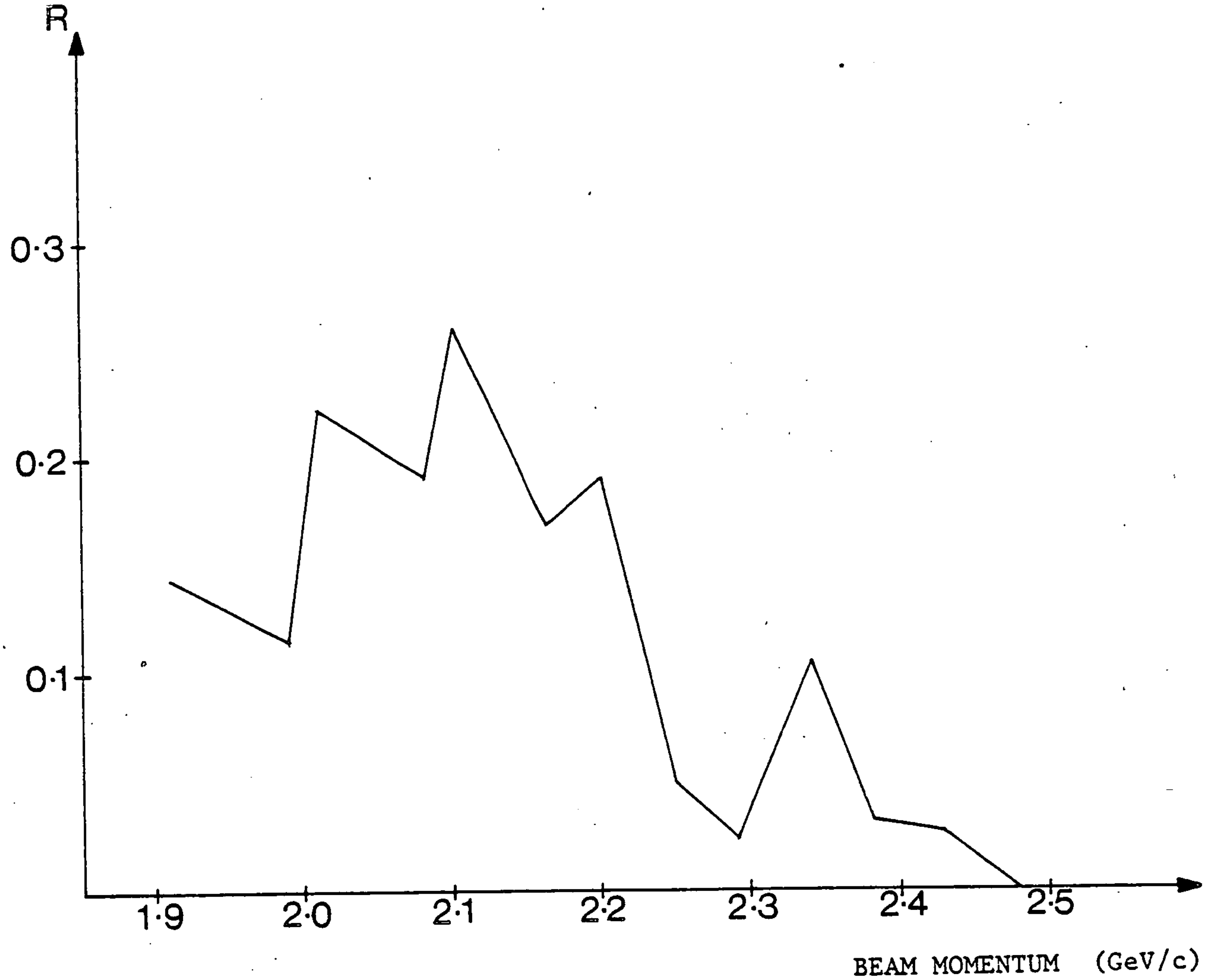

FIGURE 7.3: The renormalisation factor, R, as a function of momentum.

Particle Data Group[25] list the presence of several Δ resonances - the $\Delta(2160)$ (which is a three star resonance whose angular momentum is not well known), the $\Delta(2300)$ (which is a one star resonance in the H39 partial wave) and the $\Delta(2420)$ (which is a three star resonance in the H311 partial wave). The detailed effect of the data presented in this thesis on these resonances has not yet been studied, however, the high quality and fine momentum binning of the RMS data suggest that this data should help to clarify the status and resonance parameters of these resonances.

To summarize then it appears that major discrepancies exist between the backward π^+p elastic scattering differential cross sections of the various experiments which have made measurements in the centre of mass energy range from 2.1 to 2.4 GeV. The data of Busza et al. and Bardsley et al. is in fairly good agreement with the RMS data, however there exist discrepancies between these data sets and the data of Abe et al. This seems to cast some doubt upon the Abe data, however the source of the discrepancies is not known and until such time as a convincing explanation is found the data in this region must remain somewhat uncertain. The magnitude of these discrepancies is rather surprising, since the pion-nucleon system is probably one of the best studied systems in High Energy Physics, and their existence underlines the difficulties in performing even a supposedly "simple" High Energy Physics experiment.

APPENDIX 1

MISSING MASS SQUARED FIT

The data missing mass squared (to the forward track treated as a proton) distribution was fitted using a modified Monte Carlo missing mass squared distribution plus a linear background.

Let the measured data and Monte Carlo distributions be denoted by $d(x_i)$ and $m(y_i)$ respectively where $d(x_i)$ is the number of data events in the bin centred on missing mass squared x_i and $m(y_i)$ is the number of Monte Carlo events in the bin centred on y_i. If the true data and Monte Carlo distributions are $D(x)$ and $M(y)$ respectively then:

$$d(x_i) = \int_{x_i-\delta}^{x_i+\delta} D(x)dx \qquad (1)$$

and

$$m(y_i) = \int_{y_i-\delta}^{y_i+\delta} M(y)dy \qquad (2)$$

where δ is half the bin width.

Assume the true data distribution $D(x)$ is given by:

$$D(x) = p + qx + rM(y) \qquad (3)$$

where p and q are linear background parameters

r is a relative normalisation factor between the data and the Monte Carlo distributions

and y is some function of x.

Let $y = s(x+t)$, then:

$$d(x_i) = \int_{x_i-\delta}^{x_i+\delta} (p + qx)dx + r \int_{s(x_i-\delta+t)}^{s(x_i+\delta+t)} M(y)dy \quad . \tag{4}$$

To calculate the relative normalisation factor r equation (3) was integrated over all x and y to give:

$$r = \frac{\int_{-\infty}^{+\infty} \left[D(x) - (p + qx)\right] dx}{\int_{-\infty}^{+\infty} M(y)dy} \quad . \tag{5}$$

Since the true distributions D and M were unknown equation (5) was approximated by:

$$r = \frac{\sum_i (d(x_i) - (p + qx_i)2\delta)}{\sum_J m(y_J)} \quad . \tag{6}$$

Initially p and q were taken to be zero. Equation (4) may be rewritten as:

$$d(x_i) = p(2\delta) + q(2\delta\ x_i) + rU(x_i:s,t) \tag{7}$$

where
$$U(x_i:s,t) = \int_{s(x_i-\delta+t)}^{s(x_i+\delta+t)} M(y)dy \quad . \tag{8}$$

Since s, t and M are unknown U is also unknown. Let $s = s_o + \Delta s$ and $t = t_o + \Delta t$ where (s_o, t_o) are "guesses" for (s,t) and $(\Delta s, \Delta t)$ are "small" corrections to the initial guesses. Taylor expands U as follows:

$$U(x_i:s,t) = U(x_i:s_o,t_o) + \left.\frac{\partial U(x_i:s,t)}{\partial s}\right|_{s_o,t_o} \Delta s$$

$$+ \left.\frac{\partial U(x_i:s,t)}{\partial t}\right|_{s_o,t_o} \Delta t \qquad (9)$$

Using equation (8) $U(x_i:s_o,t_o)$ is given by:

$$U(x_i:s_o,t_o) = \int_{s_o(x_i-\delta+t_o)}^{s_o(x_i+\delta+t_o)} M(y)\,dy \qquad (10)$$

To calculate $U(x_i:s_o,t_o)$ its dependence upon the true Monte Carlo distribution M must be translated into a dependence on the measured Monte Carlo distribution m. From the set $\{y_J\}$ of Monte Carlo central bin values y_{MIN} and y_{MAX} may be found which satisfy:

$$y_{MIN} - \delta \leq s_o(x_i - \delta + t_o) \ \underline{\text{AND}}\ y_{MIN} + \delta > s_o(x_i - \delta + t_o) \qquad (11)$$

$$y_{MAX} + \delta > s_o(x_i + \delta + t_o) \ \underline{\text{AND}}\ y_{MAX} - \delta \leq s_o(x_i + \delta + t_o)\ . \qquad (12)$$

These quantities can then be used to approximate $U(x_i:s_o,t_o)$ by:

$$U(x_i:s_o,t_o) = \left[m(y_{MIN})\left(\frac{(y_{MIN}+\delta) - s_o(x_i - \delta + t_o)}{2\delta} - 1\right)\right.$$

$$\left. + \left(\sum_{L=MIN}^{L=MAX} m(y_L)\right) + m(y_{MAX})\left(\frac{s_o(x_i + \delta + t_o) - (y_{MAX} - \delta)}{2\delta} - 1\right)\right] \qquad (13)$$

In this equation the integral in equation (10) has been replaced by a summation over the measured Monte Carlo distribution bins. Using equation (13) with (s_o, t_o) replaced by (s, t) approximations for the two derivative terms in equation (9) were obtained:

$$\left.\frac{\partial U}{\partial s}\right|_{s_o,t_o} = m(y_{MIN}) \left(\frac{-(x_i - \delta + t_o)}{2\delta}\right) + m(y_{MAX}) \left(\frac{(x_i + \delta + t_o)}{2\delta}\right) \tag{14}$$

$$\left.\frac{\partial U}{\partial t}\right|_{s_o,t_o} = \frac{s_o(m(y_{MAX}) - m(y_{MIN}))}{2\delta} \tag{15}$$

Using equation (9) equation (7) may be rewritten as:

$$d(x_i) = p[2\delta] + q[2\delta x_i] + \Delta s \left[r \left.\frac{\partial U(x_i:s,t)}{\partial s}\right|_{s_o,t_o} \right] + \Delta t \left[r \left.\frac{\partial U(x_i:s,t)}{\partial t}\right|_{s_o,t_o} \right] + \left[rU(x_i:s_o,t_o) \right] . \tag{16}$$

Given values for the parameters p, q, s_o and t_o all quantities in the square brackets in equation (16) can be calculated. A least squares fit to the data can then be performed which gives estimates for the quantities p, q, Δs and Δt. These can then be used to give better values for the parameters p, q, s_o and t_o and the fit can be iterated until it converges.

This fitting procedure was carried out for all momenta where Monte Carlo data was available. The parameters s and t which were obtained were used to transform the Monte Carlo missing masses as follows:-

$$mm_{FP}^2 \to \frac{mm_{FP}^2}{s} - t \tag{17}$$

where mm_{FP}^2 is the missing mass squared to the forward track treated as a proton.

The missing masssquared to the forward track treated as a π^+, $mm_{F\pi}^2$, is related to mm_{FP}^2 by :

$$mm^2_{F\pi} \quad = \quad mm^2_{FP} \quad + \ C \tag{18}$$

with

$$C \ = \ 2(E_B + m_p)((p_F{}^2 + m_p{}^2)^{\frac{1}{2}} - (p_F{}^2 + m_\pi{}^2)^{\frac{1}{2}}) + m_\pi{}^2 - m_p{}^2 \tag{19}$$

where E_B is the beam energy

m_p is the proton mass

m_π is the π^+ mass

and p_F is the momentum of the forward track.

$mm_{F\pi}{}^2$ was transformed as shown below:

$$mm_{F\pi}{}^2 \quad \rightarrow \quad \frac{mm_{F\pi}{}^2}{s} \quad - \ t + C(1 - \frac{1}{s}) \quad . \tag{20}$$

The missing mass squared distributions used in the fitting procedure were those obtained after all cuts excluding the missing mass squared cut. Thus these distributions were already distorted by the missing mass squared χ^2 cuts which had been applied with $s = 1.0$, $t = 0.0$ effectively. To correct for this the Monte Carlo distribution was reselected using the new values of s and t obtained from the fit and the fit was performed again. This process was iterated until s and t converged.

APPENDIX 2

DETAILS OF THE ACCEPTANCE CALCULATION

The acceptance for this experiment as a function of $\cos\theta^*$ was calculated on a bin by bin basis using Monte Carlo generated events. Before outlining the acceptance calculation in detail it is convenient to define some relevant quantities:-

1) G_i is the number of generated Monte Carlo events in the i'th generated $\cos\theta^*$ bin.

2) H_i is the ϕ weighted number of generated events in the i'th generated $\cos\theta^*$ bin (i.e. $H_i = \frac{2\pi}{\phi_i} G_i$).

3) N_i is the number of selected reconstructed Monte Carlo events in the i'th reconstructed $\cos\theta^*$ bin.

4) W_i is the TOF weighted number of selected reconstructed Monte Carlo events in the i'th reconstructed $\cos\theta^*$ bin.

5) $W_{iJ} \equiv W_i$ for events generated in the J'th bin only.

6) $N_{iJ} \equiv N_i$ for events generated in the J'th bin only.

7) M_i is the number of selected reconstructed data events in the i'th reconstructed $\cos\theta^*$ bin.

8) D_i is the number of acceptance corrected data events in the i'th reconstructed $\cos\theta^*$ bin.

In general M_i is related to D_J as shown below:

$$M_i = \sum_J R_{iJ} D_J \quad . \tag{1}$$

To obtain the true angular distribution of elastic scattering events this equation must be solved for D_J. Now R_{iJ} may be approximated by:

$$R_{iJ} = \frac{W_{iJ}}{H_J} \tag{2}$$

and since the $\cos\theta^*$ resolution of this experiment is comparable to the $\cos\theta^*$ binwidth equation (1) can be reduced to:

$$M_i \approx R_{i,i-1}\, D_{i-1} + R_{i,i}\, D_i + R_{i,i+1}\, D_{i+1} \quad . \tag{3}$$

The acceptance A_i is defined as:-

$$A_i = \frac{M_i}{D_i} \quad . \tag{4}$$

Using equation (3) A_i may be rewritten as:-

$$A_i = R_{i,i-1}\left(\frac{D_{i-1}}{D_i}\right) + R_{i,i} + R_{i,i+1}\left(\frac{D_{i+1}}{D_i}\right) \quad . \tag{5}$$

From equation (5) $(\Delta A_i)^2$ is given by:-

$$(\Delta A_i)^2 = (\Delta R_{i,i})^2 + R_{i,i-1}{}^2(\Delta(\frac{D_{i-1}}{D_i}))^2 + R_{i,i+1}{}^2(\Delta(\frac{D_{i+1}}{D_i}))^2$$

$$+ (\frac{D_{i-1}}{D_i})^2(\Delta R_{i,i-1})^2 + (\frac{D_{i+1}}{D_i})^2 (\Delta R_{i,i+1})^2 . \tag{6}$$

Since D_i is unknown it must be replaced in (5) and (6) by the equivalent Monte Carlo distribution, H_i, to enable A_i and (ΔA_i) to be calculated. This gives:-

$$A_i \approx \frac{W_{i,i-1}}{H_i} + \frac{W_{i,i}}{H_i} + \frac{W_{i,i+1}}{H_i} \tag{7}$$

which implies

$$A_i \approx \frac{W_i}{H_i} \tag{8}$$

and

$$(\Delta A_i)^2 \approx (\Delta R_{i,i})^2 + R_{i,i-1}{}^2(\Delta(\frac{H_{i-1}}{H_i}))^2 + R_{i,i+1}{}^2(\Delta(\frac{H_{i+1}}{H_i}))^2$$
$$+ (\frac{H_{i-1}}{H_i})^2 (\Delta R_{i,i-1})^2 + (\frac{H_{i+1}}{H_i})^2 (\Delta R_{i,i+1})^2 \quad . \tag{9}$$

The acceptance, A_i, was calculated using equation (8) and its statistical error was calculated using equation (9). To evaluate equation (9) the quantities $(\Delta R_{i,J})^2$ and $(\Delta(\frac{H_{i\pm1}}{H_i}))^2$ had to be calculated.

Now $$W_i = C_i N_i \tag{10}$$

where $$C_i = \left< \frac{1.0}{\text{TOF weight}} \right>_i \quad . \tag{11}$$

Thus $$R_{i,J} = \frac{W_{iJ}}{H_J} = \frac{\phi_J}{2\pi} \frac{C_i N_{iJ}}{G_J} \tag{12}$$

and
$$(\Delta R_{i,J})^2 = (\frac{\phi_J}{2\pi})^2 \left[(C_i)^2 \frac{\frac{N_{iJ}}{G_J}(1 - \frac{N_{iJ}}{G_J})}{G_J} + (\frac{N_{iJ}}{G_J})^2 (\Delta C_i)^2 \right] \tag{13}$$

The error on the TOF weight was estimated to be 10% of the correction applied by the weight. Thus if t_i is the mean TOF weight in the i'th bin then:-

$$\Delta t_i = (t_i - 1.0)/10.0 \quad . \tag{14}$$

Since $C_i = \frac{1}{t_i}$ this leads to:

$$\Delta C_i = C_i{}^2(\frac{1.0}{C_i} - 1.0)/10.0 \quad . \tag{15}$$

Combining equations (13) and (15) with $J = i, i\pm1$ the quantities $(\Delta R_{i,i})^2$ and $(\Delta R_{i,i\pm1})^2$ may be calculated. Thus to calculate $(\Delta A_i)^2$ via equation (9) it only remains to calculate $(\Delta(\frac{H_{i\pm1}}{H_i}))^2$.

Now $$\frac{H_{i\pm1}}{H_i} = \left(\frac{\phi_i}{\phi_{i\pm1}}\right) \frac{G_{i\pm1}}{G_i} \qquad (16)$$

and hence

$$\left(\Delta\left(\frac{H_{i\pm1}}{H_i}\right)\right)^2 = \left(\frac{\phi_i}{\phi_{i\pm1}}\right)^2 \frac{\frac{G_{i\pm1}}{G_i}\left(1 + \frac{G_{i\pm1}}{G_i}\right)}{G_i} \qquad . \qquad (17)$$

APPENDIX 3

EXTRACTION OF PARTIAL WAVE AMPLITUDES

Due to the limited angular range of the elastic scattering differential cross sections measured in the RMS experiment and the non-measurement of the polarisation a full partial wave analysis could not be performed based on this data alone. In order to extract partial wave amplitudes from the data it was assumed that the amplitudes of the CMU-LBL analysis were approximately correct and an attempt was made to extract amplitudes which were consistent with both the CMU-LBL analysis and the RMS experiment. Note that the CMU-LBL analysis was used in preference to the Helsinki-Karlsruhe analysis since the CMU-LBL group provided an error matrix on their amplitudes. Before describing the extraction procedure in detail it is convenient to define some relevant quantities:

1) D_i is the RMS elastic differential cross section in the i'th $\cos\theta^*$ bin.

2) ΔD_i is the $\cos\theta^*$ dependent error on the RMS elastic differential cross section in the i'th $\cos\theta^*$ bin.

3) σ_N is the RMS normalisation error (0.06).

4) $\{T_\ell^\pm \equiv V_{4\ell\pm1} + iV_{4\ell\pm1+1}\ ;\ \ell = 0,\ \ell_{MAX}\}$ is the CMU-LBL partial wave amplitudes.

5) G is the error matrix on the CMU-LBL amplitudes.

6) $\{S_\ell^\pm \equiv W_{4\ell\pm1} + iW_{4\ell\pm1+1}\ ;\ \ell = 0,\ \ell_{MAX}\}$ is the parameter amplitudes (to be determined).

7) X_i is the differential cross section in the i'th $\cos\theta^*$ bin as reconstructed from the parameter amplitudes $\{S_\ell^\pm\}$.

8) R is a renormalisation factor (to be determined).

These quantities were used to define a χ^2 as follows:

$$\chi^2 = \chi^2_{DATA} + \chi^2_{PWA} \tag{1}$$

where:

$$\chi^2_{DATA} = \frac{R^2}{\sigma_N^2} + \sum_{\substack{\text{Data}\\ \text{Cos}\theta^*\\ \text{bins}}} \frac{((1.0 + R)D_i - X_i)^2}{(1.0 + R)^2(\Delta D_i)^2} \tag{2}$$

$$\chi^2_{PWA} = \sum_{i=1}^{2+4\ell_{MAX}} \sum_{J=1}^{2+4\ell_{MAX}} (W_i - V_i)G^{-1}_{iJ}(W_J - V_J) \tag{3}$$

The first 14 parameter amplitudes were allowed to vary (with the CMU-LBL amplitudes being used as starting values) as was the renormalisation parameter R and χ^2 was then minimized at each beam momentum independently. This produced a set of partial wave amplitudes at each RMS momentum setting which gave the best combined fit to the RMS data and the CMU-LBL analysis.

REFERENCES

(1) J. Bronowski, The Ascent of Man.

(2) Any standard textbook on the quark model - see, for example, F.E. Close, Quarks and Partons.

(3) N. Isgur, Lectures at the XVI School of Subnuclear Physics, Erice, 1978.

N. Isgur and G. Karl, Phys. Lett. 72B (1977) 109.

N. Isgur and G. Karl, Phys. Lett. 74B (1978) 353.

N. Isgur and G. Karl, Phys. Rev. D18 (1978) 4187.

N. Isgur and G. Karl, Phys. Rev. D19 (1979) 2653.

N. Isgur and G. Karl, Phys. Rev. D20 (1979) 1191.

R. Koniuk, Proceedings of the IV'th International Conference on Baryon Resonances, Toronto, 1980.

(4) See for example:

M. Ferro-Luzzi, Lectures at CERN School of Physics, 1968 (CERN report 68-23).

J. Bowcock and H. Burkhardt, Rep. Progr. Phys. 38 (1975) 1099.

(5) Rutherford experimental proposal PPESP/76/45 (November 1976).

(6) G. Larue, W. Fairbank and A. Hebard, Phys. Rev. Lett. 38 (1977) 1011.

(7) See, for example, R. Horgan and R. Dalitz, Nucl. Phys. B66 (1973) 135.

(8) K.C. Bowler, P. Corvi, A. Hey, P. Jarvis and R. King, Phys. Rev. D24 (1981) 197.

(9) Particle Data Group, Phys. Lett. 75B (1978) 1.

(10) L.R. Scotland's doctoral thesis, Rutherford Laboratory report (HEP/T/88) 1981.

(11) HYDRA systems manual (R. Böck, E. Pagiola, J. Zoll).

REFERENCES (Contd.)

(12) K.J. Peach, RMS internal report "Track geometry in the Rutherford Multi-particle Spectrometer", May 1978.

(13) G. Höhler, F. Kaiser, R. Koch and E. Pietarinen, Handbook of Pion-Nucleon Scattering, Physics Data 12-1, 1979.

G. Höhler et al., Karlsruhe University Preprint TKP 78-11.

(14) I.F. Corbett, RMS internal reports "e^+, μ^+ Contamination in π13", March 1978 and "Normalisation Progress Report" (undated).

(15) Compilation of cross sections ($\pi^{\pm}$ induced reactions), CERN-HERA 79-01.

(16) K. Abe et al., Phys. Rev. D10 (1974) 3556.

(17) D. Bardsley et al., Proceedings of the Oxford Baryon Resonance Conference, 1976.

(18) R. Ott et al., Phys. Rev. D16 (1977) 2699.

(19) W. Busza et al., Phys. Rev. 180(5) (1969) 1339.

(20) K. Jenkins et al., Phys. Rev. D21 (1980) 2445.

(21) M. Albrow et al., Nuclear Physics B25 (1970) 9.

(22) A. Carroll et al., Phys. Rev. Lett. 20(12) (1968) 607.

(23) V. Cook et al., Phys. Rev. 130(2) (1963) 762.

(24) R. Kelly and R. Cutkosky, Phys. Rev. D20 (1979) 2782.

R. Cutkosky et al., Phys. Rev. D20 (1979) 2804.

R. Cutkosky, C. Forsyth, R. Hendrick and R. Kelly, Phys. Rev. D20 (1979) 2839.

R. Kelly and R. Cutkosky, LBL preprint 8551.

R. Cutkosky, C. Forsyth, R. Hendrick and R. Kelly, LBL preprint 8553.

(25) The Particle Data Group, Review of Particle Properties (April 1980 edition).

ACKNOWLEDGEMENTS

I wish to express my thanks to those whose work and help have made this thesis possible.

My especial thanks go to all members of the RMS team, past and present, whose dedication ensured the success of the experiment. In particular I would like to thank my joint supervisors, Dr. D.J. Candlin and Dr. K.J. Peach for their help and encouragement; Dr. S.M. Fisher and Dr. P.J. Litchfield for their work on the data analysis software and Dr. I.F. Corbett, Dr. L. Mapelli and M. Morrisey for their work on the experimental apparatus.

Particular thanks go to Mrs. R. Chester for her patient and accurate typing of this thesis.

Finally I would like to thank Professor R. Cowley, F.R.S., F.R.S.E. and the Physics Department of Edinburgh University for the facilities offered to me during my period of research, and the Carnegie Trust for the Universities of Scotland for their financial support during this period.